Università degli Studi di Genova

Dipartimento di Scienze della Terra dell'Ambiente e della Vita (DISTAV)

PhD in Earth and Environmental Science and Technology (STAT)

XXXVI cycle, curriculum: Earth Science

a.y. 2023-2024

PhD Thesis

Evandro Balbi

Mars as analogue of terrestrial planets and exoplanets: a methodological approach based on geological, geophysical, and astrophysical principles

Academic Tutors:

Prof.ssa Paola Cianfarra

Prof. Gabriele Ferretti

Prof. Silvano Tosi

Table of contents

Structure of the Thesis

Chapter one: introduction, topics, and aims of the thesis.

Chapter two: includes an overview of Mars focussed on the geologic and tectonic evolution of the planet since its formation. Particular emphasis is given to the present-day knowledge about the geo-tectonic setting of Thaumasia Region and Claritas Fossae, that is the area where methods presented in Chapter 3 to 5 are applied.

Chapter three: focuses on the analysis of the geo-tectonic setting of the Claritas Fossae through the combination of kinematic numerical modelling and regional-scale structural mapping. The content of this chapter is shared with a paper published in Icarus Journal as *Balbi, E., Ferretti, G., Tosi, S., Crispini, L., and Cianfarra, P. (2024). Polyphase tectonics on Mars: Insight from the Claritas Fossae. Icarus, 411, 115972* https://doi.org/10.1016/j.icarus.2024.115972.

Chapter four: a clustering analysis workflow is here proposed to objectively investigate complex tectonically controlled regions such as the Claritas Fossae. The content of this chapter is shared with a paper under review on Icarus Journal as *Balbi E., Cianfarra P., Crispini L., Tosi S., and Ferretti G. - Application of Hierarchical-Agglomerative Clustering Analysis to the Geo-Tectonic Investigation of the Claritas Fossae on Mars*.

Chapter five: focuses on lineament domain analysis following a manual and an automatic approach to reconstruct the tectonic evolution of planetary surfaces. The content of this chapter is shared with a paper published in Geoscience Journal as *Balbi, E., & Marini, F. (2024). Lineament Domain Analysis to Unravel Tectonic Settings on Planetary Surfaces: Insights from the Claritas Fossae (Mars). Geosciences, 14(3), 79.* https://doi.org/10.3390/geosciences14030079.

Chapter six: focuses on the ongoing analysis on the spatial and temporal variation of the CO_2 within the atmosphere of Mars aimed at preparing models for investigating terrestrial exoplanets using Mars as analogue. The content of this chapter is shared with two papers: the first published in SPIE Journal as *Ricci D., Tosi S., Balbi E., et al., 2021 – Commissioning and improvements of the instrumentation and launch of the scientific exploitation of OARPAF, the Regional Astronomical Observatory of the Antola Park* https://doi.org/10.1117/1.JATIS.7.2.025003; the second in preparation: *Rainer M., Balbi E., Borsa F., Cianfarra P., Harutyunyan A., and Tosi S., - Spatial and temporal variations of CO2 on Mars*;

Chapter seven: includes the conclusive remarks of this PhD thesis.

Chapter 1

Introduction

From the second half of the 20th Century, rapid and continuous scientific and technological breakthroughs allowed the scientific community to look in ever growing detail at the objects within the Solar System and beyond. The huge amount of data collected by multiple Earth-based and space missions continues to provide vital information, that allowed geoscientists to recognize an enormous variety of geological features shaping the surface of major and minor rocky bodies. Just like the Earth, the surface morphology of planetoids characterised by a rigid outer shell (e.g. terrestrial planets, icy and rocky natural satellites) derives from the contribution and mutual competition of endogenous and exogenous processes. Endogenous processes (e.g. tectonism, volcanism, isostatic adjustments, elastic flexures) shape planetary surfaces yielding the development of peculiar tectonic landforms (Gutiérrez & Gutiérrez 2016; Rossi & Van Gasselt, 2018). On the other hand, erosion, transport and depositional processes (which are active on planets with an atmosphere) together with impact cratering and lava flows in no-atmosphere bodies tend to smooth and obliterate landforms created by endogenous processes. Therefore, Mercury, Venus, Mars, Moon, Io, Enceladus, Ganymede, and Europa, among the others, host multiple geological features that resemble well-known and deeply investigated terrestrial geological settings on Earth. This is the case of structures such as fractures, faults, and folds, and of landforms related to tectonic, volcanic, glacial, or fluvial activity. Nevertheless, in addition to significant similarities, observations and analyses conducted in the last decades have revealed relevant differences among the major rocky and icy planetoids of the Solar System, as well as between them and the Earth. One of the most thrilling aspects concerns the plate tectonics that characterises our planet. Plate tectonics associated to the relative movement of multiple lithospheric plates, seems to be unusual or even unique today in the Solar System (Watters & Schultz, 2010; Platz et al., 2015; Hauber et al., 2018; Stern et al., 2018; Weller & Lenardic, 2018; Palin et al, 2020). Earth is, in fact, the only known planet characterised at present by plate tectonics. Most of the other major rocky/icy planetoids considered geologically active in some way (e.g. Mars, Venus, Io, Titan) are characterised by tectonism related to a single continuous shell (Stern et al., 2018). For this reason, the distinction between *fragmented-lid* and *stagnant-lid* tectonic styles is necessary. Regarding this terminology, "lid" refers to the outermost thermal boundary layer of a planet characterised by conductive geothermal gradient, namely

representing the thermal lithosphere (or thermal lid – Anderson, 1995; Stern et al., 2018). "Fragmented" and "stagnant" refer to the lid's architecture and dynamics, consisting of multiple plates with limited dimensions or a single plate encircling the entire planet/body, respectively. Different types of both fragmented-lid and stagnant-lid tectonics have been distinguished so far in the Solar System. Fragmented-lid tectonics is represented by plate tectonics on Earth and by *ice floe tectonics*, characterised by ice-convection, on Europa and Enceladus (Kattenhorn & Prockter, 2014; Stern et al., 2018). Stagnant-lid tectonics, which is the most represented tectonism, appears with multiple configurations such as i) the *sluggish single lid* of Mars, dominated by one or a few plumes and rift-like structures (Wise et al., 1979; Stern et al., 2018; Hauber et al., 2010); ii) the *corona-dominated style* of Venus, driven by drips and upwelling of many plumes that cause periodic and catastrophic resurfacing (Solomatov & Moresi, 1996; Reese et al., 1999; Grindrod & Hoogenboom, 2006; Gerya, 2014); and iii) the *heat-pipe style* of Jupiter's moon Io, characterised by many plumes (Kirchoff et al., 2011; Moore & Webb, 2013; Bland & McKinnon, 2016; Moore et al., 2017). In all the aforementioned cases, the tectonic activity is expressed on the surface through the brittle and/or ductile deformation of the lid/lithosphere. In the case of a fragmented-lid, the deformation is mostly concentrated at the boundaries between rigid plates, whereas in the case of stagnant-lid it is widespread or, eventually, concentrated in proximity of plumes, upwellings, and/or magma resurfacing areas. Deformation is expressed on the surface through the development of deformation corridors consisting of fold belts, fractures and faults (normal, thrust, strike-slip) network that in some places can affect the entire lithosphere. The identification and the analysis of such structures is of outmost importance for geologists in order to reconstruct the tectonic activity that acts or has acted on a planetary surface, especially in the case of planetoids considered tectonically inactive (e.g. Moon and Mercury) at present. In this way, studying the variety of planetary structures and landforms provides fundamental information on the geologic history of all planets.

Despite the increasing number of planetary missions (that include the use of landers and rovers for direct in situ/local measurements, drilling and sampling), tectonic and geodynamic investigations on planetary rocky and icy planetoids mainly rely on indirect, orbital data. Such studies usually use methodologies developed and successfully applied to unravel the geotectonic setting of key regions on Earth, where access for direct investigations is difficult for climatic, economic, or geopolitical reasons. These methodologies include the study of potential fields (McKenzie et al., 2002; Langlais et al., 2004; Morschhauser et al., 2014; Genova et al., 2016), heat flux (Grott et al., 2005, 2007; Plesa et

al., 2016), and surface geo textures from remotely sensed data (Cianfarra & Salvini, 2014, 2015; Rossi et al., 2018).

In addition to the variety of objects within our Solar System, space exploration also focussed on planets belonging to other planetary systems: the exoplanets. Since 1995, when the first exoplanet was confirmed (namely 51-Pegasi-b, Mayor & Queloz, 1995), the interest in distant alien words has grown exponentially. To date (winter 2023) more than 5000 exoplanets have been confirmed representing different typologies: while some are similar to the terrestrial and gaseous planets of the Solar System, some are very different, such as hot-Jupiters (gaseous planets similar to Jupiter but orbiting much closer to their hosting-star), brown-dwarves (substellar objects 13 to 80 times more massive than Jupiter), or super-Earths (i.e. terrestrial planets 2 to 10 times more massive than Earth) (Howard et al., 2010; Mayor et al., 2011; Fressin et al., 2011; Burke et al., 2015). Although the orbital properties between exoplanetary systems and the Solar System show a good similarity (Martin & Livio, 2015), the existence of typologies of planets not represented in the Solar System is still a matter of discussion. Moreover, the number of discovered terrestrial exoplanets is lower compared to the gaseous ones, whereas both are equally represented in the Solar System. A bias in the currently used observation techniques, which are more sensitive to giant exoplanets close to their hosting-star, is well known (Fressin et al., 2013). Nevertheless, it is not yet clear whether this discrepancy is also influenced by a too low resolution of the available instrumentations or truly to the fact that terrestrial planets like Earth, Venus, Mercury, or Mars are fewer outside the Solar System (Fischer et al., 2015). To answer these questions ever more advanced astrophysical experiments have been planned to better characterise exoplanets and to directly observe them. Indeed, direct observation is very challenging and to date we are (still) not able to produce images of their surfaces. In this way, geologists cannot "directly" analyse the superficial deformations and thus confidently infer the presence of any kind of geologic activity. However, exoplanets are studied by applying different experimental techniques that provide fundamental data for the geological research. One of these methods is the *transit photometry* (Charbonneau et al., 1999) that consists in measuring the variation of the light emitted by a star when an exoplanet passes between the star and the observer. The exoplanet, in fact, by moving gradually from the edge of the hosting star to its central region yields a reduction of the measured number of photons. This results in an inflection of the light curve whose properties provide vital information about the transiting exoplanet. Diameter of the exoplanet, inclination, semi-axis, period of the orbit and gravitational acceleration at the surface can be estimated with the transit photometry. Furthermore, if the radial acceleration of the star is known,

it is possible to infer the average mass density of the planet (Swift et al., 2011). In addition, the spectroscopic analysis of the light reflected or transmitted by the exoplanet can provide insights on the presence and, eventually, on the structure and composition of its atmosphere (Charbonneau et al., 2002). Although these measurements are characterized by a degree of variability/approximation if compared with similar data on the planets of the Solar System, they represent fundamental parameters for the distinction of categories among exoplanets and for the preparation of models on formational processes. Once again, the comparison with analogues of the Solar System is fundamental.

As seen, analogues play a central role in Planetary Geology, and more in general in all the Planetary Sciences. The term "analogue" can be related to a wide range of specific meanings based on the scientific discipline (e.g. structural geology, geomorphology, petrography, biology, astronomy) or even on the academic background of the scientists (Foucher et al., 2021). The definitions commonly used in Planetary Geology refer to the term "analogue" as a terrestrial object (in its most generic meaning) characterised by similar traits (or analogies) with a given extraterrestrial counterpart. In this way, analogues represent a fundamental tool to interpret the nature of the analysed object and to infer the formational causes (Pondrelli et al., 2018; Stern et al., 2018; Foucher et al., 2021). In particular, studies based on both geological and physical approaches on planetoids close to us can provide more information for environmental studies and/or to infer the composition and structure of exoplanets. However, in the study of analogues it must be considered that: i) in complex systems, such as nature, similar effects can be generated by different processes (*Equifinality or Convergence* principle); and ii) the huge variability that exists in nature do not enable the development of two identical features (in other words, two analogues always share important differences - Pondrelli et al., 2018; Foucher et al. 2021). This considered, it is of particular interest the statement made by Pondrelli et al. (2018) according to which the existence of similar traits between features in geology is useful in order to advance hypotheses and to guide the research, rather than providing definitive explanations. In this way, planetary mapping, structural geology, tectonics, and geodynamics, among many others, proved to be core disciplines in the past decades for understanding the origin and the evolution of planetoids characterised by a rigid-outer shell (Watters & Schultz, 2010; Rossi & Van Gasselt, 2018; Klimczak et al., 2021).

As previously discussed, assessing the tectonic processes that affect or have affected the surface of planetoids characterised by a rigid-outer shell is crucial to better understand their origin, evolution, and present-day setting, including the possible development of life. In addition, this can help in

better framing the geologic evolution of terrestrial exoplanets assessing whether the planets have experienced stagnant or fragmented lid tectonics or a combination of them during different stages. The PhD research presented in this thesis has been focussed on developing an original workflow that included the combination of methodologies and approaches usually used in Planetary Sciences. The developed workflow is aimed at providing fundamental geological insights to unravel the tectonic processes that rocky planets/exoplanets (or more in general, planetary bodies characterised by a rigid outer shell) could experience during their evolution. The project has been carried out in a strong multidisciplinary context in which geological, geophysical, and astrophysical principles have been combined to improve the used methods and the reliability of the results. Methodologies and approaches investigated in this thesis and presented in detail in the next chapters include the combination of i) classical geological methods (e.g. remote sensing and structural mapping with kinematic numerical modelling); ii) analytical methods (e.g. clustering analysis, manual and automatic lineament domain analysis), and iii) measurements of the latitudinal variation of the concentration of molecules in planetary atmospheres (e.g. CO2). The original combination of these methodologies has been applied to Mars, considered a good analogue within the Solar System to rocky planets/exoplanets for investigating the geodynamics of crustal processes. The importance of Mars as analogue lies in two crucial aspects. The first one is merely logistic: the proximity of Mars to the Earth combined with its the environmental and atmospheric conditions, contrary to Venus, allowed the conduction in the last decades of numerous fly-by, orbital and ground missions by different space agencies that have collected an extraordinary amount of data (e.g. Snyder & Moroz, 1992; Rossi et al., 2010; Carr, 2013). The second aspect, the most relevant for this thesis, concerns the preserved evidence on the Martian surface of geologic processes (both endogenous and exogenous) from its formation to the present, from the global to the local scale. Mars shows traces of intense tectonic and volcanic activity in areas that share significant analogies with terrestrial counterparts. This evidence has been associated to the early history of the planet but also to more recent times (< 40-100 My - Lucchitta, 1987; Hartmann et al., 1999; Hauber et al., 2011) until the present days (Giardini et al., 2020; Kedar et al., 2021; Stähler et al., 2021; Pieterek et al., 2022, 2023), undermining the previous and long-standing idea of Mars as a geologically inactive planet. In addition, the existence of numerous regional and global scale volcanic and tectonic feature (e.g. Tharsis, Thaumasia) suggests that preferential pathways for fluid migration between the inner planet and its surface and atmosphere may exist. Therefore, analysis on the atmospheric composition and on the variation of peculiar elements/molecules above these regions could provide insights on possible still-

active endogenous processes and on their ability of influencing the atmosphere. These data could then be compared with that of the atmospheres of terrestrial exoplanets to better frame their nature. In this way, the Martian atmosphere can be used as analogue to test and develop original methodologies to be applied in the near future to describe exoplanets. In view of this, Mars represents a key laboratory for geological research on terrestrial planets and the analysis of Mars as "if it was an exoplanet" can provide fundamental clues to create planetary models to be compared with that of terrestrial exoplanets similar in size.

Among the numerous regional and global scale geologic features that shape the surface of Mars, the abovementioned methodologies have been tested and applied in the Claritas Fossae region (hereinafter referred to as CF). This is a N-S elongated system of scarps, depressions, and reliefs that exceeds 1000 km of length and 150 km of width and is included in the wide, complex volcano-tectonic framework of the Thaumasia Region (Dohm & Tanaka, 1999). Although numerous studies refer to the CF as a tectonically controlled area (Hauber & Kronberg 2005; Dohm et al., 2009; Montgomery et al., 2009; Yin, 2012; Vaz et al., 2014; Dohm et al., 2015, 2018; Pieterek et al., 2024), the leading mechanism(s) are still debated since geological evidence of both extensional and strike-slip tectonics exists. Nevertheless, Authors are concordant that this represents a crustal-scale tectonic feature. Therefore, the CF may represent one of the abovementioned preferential pathway for fluid migration between the inner planet and its surface and atmosphere. In this way, the CF represents a key region and a pivotal laboratory in which apply the different methodological approaches investigated in this thesis to unravel tectonics on terrestrial planets and to investigate both the tectonic processes that Mars experienced and how these could have influenced its atmosphere.

Chapter 2

Geological and physiographic setting

2.1 The main physiographic features of Mars at planetary scale

Mars is the fourth planet of the Solar System from the Sun. Its orbit lies between that of Earth and the Main Asteroid Belt, this last separates the four inner, terrestrial planets from the four outer, giant planets. Compared to Earth, Venus, and Mercury, Mars is intermediate in size. Its radius (~3390 km) is in fact nearly half that of Earth (~6370 km) and Venus (~6050 km) but larger than that of Mercury (~2440 km). The dimension (and specifically the volume to surface ratio) yielded the internal energy production related to primordial cooling and radiogenic heat flux to be significant enough to enable geologic, volcanic, and tectonic activity throughout long period of time (differently from Mercury and the Moon) but not so intense to obliterate records of early processes (such as on Earth and Venus) (Golombek & Phillips, 2010). Thus, evidence of the endogenous evolution of the planet from its formation to present remain preserved on the Martian surface and can be analysed at different scales of observation. In addition, although fluvial and glacial valley networks and sedimentary deposits exist that locally shape the oldest terrains, estimated rates of erosion for the entire history of Mars resemble that of low-degradation environments on Earth (from 10^{-6}–10^{-5} m/yr during the Noachian to 10^{-9}–10^{-8} m/yr during the Amazonian - Golombek & Bridges, 2000; Golombek et al., 2006; Vaz et al., 2014). In this way, exogenous processes had negligible impact in shaping the regional scale landscapes and were not able to delete evidence of early geologic history. Preserved evidence of both endogenous and exogenous processes from the formation of the planet to the present allowed geoscientist to reconstruct most of the geologic history of Mars. In this way, a geologic time scale for the Red Planet was developed and it was subdivided in three periods (Carr & Head, 2010): i) Noachian, from 4.1 to 3.7 Gy, ii) Hesperian, from 3.7 to 3.0 Gy, and iii) Amazonian, from 3.0 Gy to present (Figure 2.1). The period prior to 4.1 Gy, namely pre-Noachian, is considered the time interval related to planetary accretion and differentiation. During pre-Noachian, the hemispheric Crustal Dichotomy likely formed (Carr & Head, 2010). This is the most relevant physiographic feature of Mars at planetary scale (black dot-dot-dashed line in Figure 2.2), and it represents a global significant variation in crustal thickness, geological, and geophysical properties between the smoother terrains to the North (Lowlands) and the heavily cratered terrains to the South

(Highlands) (Figure 2.2)(Zuber, 2001; Watters et al., 2007; Andrews-Hanna et al., 2008; Bonnet Gibet et al., 2022).

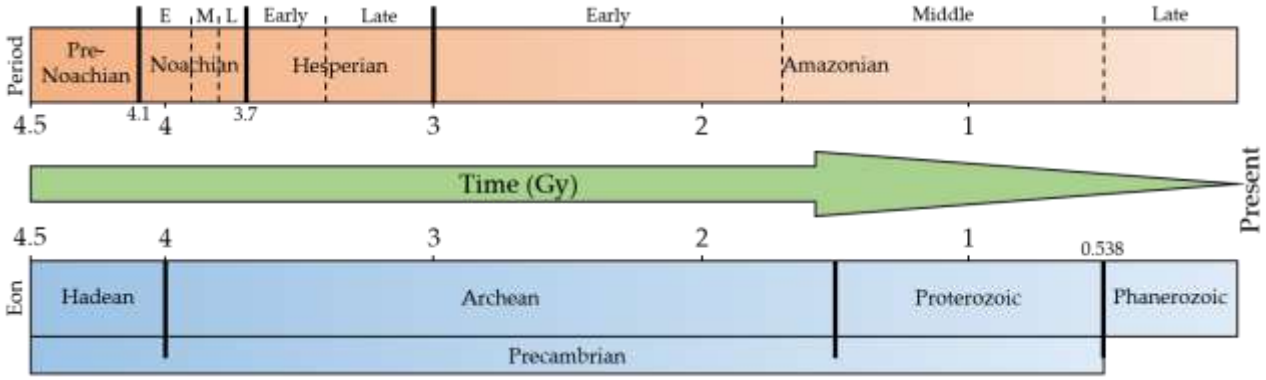

Figure 2.1 - Geologic Time Scale of Mars (upper part) subdivided in Periods compared to that of Earth (lower part) subdivided in Eons.

The surface expression of the Crustal Dichotomy is represented by a difference in elevation between Highlands and Lowlands that exceeds 2500 m and that can be followed for the entire planet with the exception of Tharsis. Here, the position of the crustal dichotomy is still debated, and it is inferred differently if considering geological or geophysical evidence (e.g. Zuber et al., 2000; Andrews-Hanna et al., 2008). In map view, the transition between Highlands and Lowlands is not homogenous being broader in correspondence of the Arabia Terra and narrower proceeding east towards the Elysium Planitia (Frey et al., 1998; Smith et al., 1998, 1999, 2001; Zuber et al., 2000; Watters, 2003a,b). This results in a bi-modal distribution of the elevations by frequency (i.e. hypsometry) similar to Earth but characterised by a wider range of elevations (Aharonson et al., 2001). Therefore, the thickness of the crust shows a bi-modal distribution being on average 58 km in correspondence of the Highlands and 32 km in correspondence of the Lowlands (Neumann et al., 2004). Nevertheless, Martian topographic variations are not uniformly spatially correlated with crustal thickness variations (Watters et al., 2007). The processes that led to this global setting remain unclear and a widely accepted model on the formation of the Crustal Dichotomy still does not exist. To date, three main hypotheses have been proposed: i) endogenous/geodynamic origin driven by first-order mantle convection (Wise et al., 1979; Sleep, 1994; Wenzel et al., 2004); ii) exogenous origin related to one oblique, giant impact or multiple large impacts (Wilhelms & Squyres, 1984; Frey & Schultz, 1988, 1990; Andrews-Hanna et al., 2008; Nimmo et al., 2008); iii) a combination of them (Yin, 2012). However, none of the proposed model seems to be able to fully explain the formation of such structure keeping the debate open (Andrews-Hanna et al., 2008).

The second largest physiographic feature of Mars at planetary scale is the province of Tharsis whose volcano-tectonic evolution influenced the entire western hemisphere (Anderson et al., 2001; Bouley et al., 2018; Anderson et al., 2019; Krishnan & Kumar, 2023). Tharsis appears as a wide bulge/dome that covers nearly 25% of the entire Martian surface (black dashed line in Figure 2.2) (Tanaka et al., 1992; Williams et al., 2008). It is dominated by five giant shield volcanoes: the three Tharsis Montes (from southwest to northeast Arsia, Pavonis, and Ascraeus), Alba and Olympus *montes* (the largest known volcano in the Solar System). Tharsis originated from the emplacement of large volumes of lavas throughout most of the history of the planet from Noachian to Amazonian periods (Anderson et al., 2001; Phillips et al., 2001; Carr & Head, 2010).

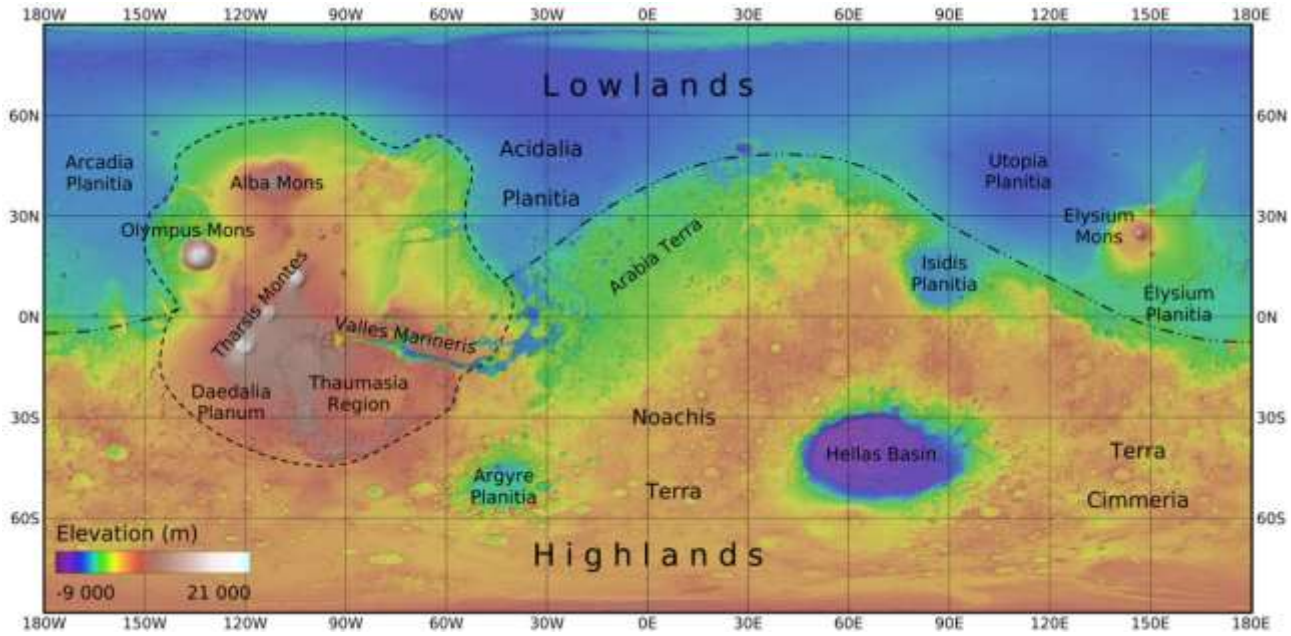

Figure 2.2 - Topographic map of the Martian surface derived from Mars MGS MOLA - MEX HRSC Blended DEM Global v2 with the toponyms of the main physiographic features at regional and global scale. The wide volcanic province of Tharsis is delineated by the black dashed line. The dash-dot-dot line indicates the topographic Crustal Dichotomy expressed on the surface as a difference in elevation exceeding 2500 m between Lowlands and Highlands.

Tectonic deformation related to Tharsis is represented by concentric sets of compressional features (e.g. wrinkle ridges and lobate scarps) and radial sets of extensional features (e.g. elongated depressions, narrow grabens). This indicates an orientation of the stress field characterised by compression radial and tension concentric to Tharsis (Tanaka et al., 1991; Banerdt & Golombek, 2000). Stratigraphic and cross-cutting relationships between tectonic structures and different aged terrains suggest that deformation started during Noachian and continued in different stages till and throughout the Amazonian (Dohm et al., 1999; Hauber et al., 2011; Bouley et al., 2018).

The southern edge of Tharsis is dominated by the Thaumasia Region. This is a wide volcano tectonic province consisting of a central, elevated plateau formed by, from west to east, Syria, Solis, Sinai,

and Thaumasia *plani* (Figure 2.3). The plateau is bounded by a series of regional-scale physiographic features that exceed hundreds of kilometres in length: Valles Marineris and Noctis Labyrinthus to the north, Thaumasia Highlands to the south and southeast, and Claritas Fossae (CF) to the west (Dohm & Tanaka, 1999). The Thaumasia Region is characterised by numerous evidence of intense past tectonic and volcanic activity (e.g. faults, grabens-like morphologies, wrinkle ridges, volcanic edifices, volcanic vents) (Tanaka & Davis, 1988; Tanaka et al., 1991; Anderson et al., 2001; Dohm et al., 2001; Bistacchi et al., 2004; Grott et al., 2007; Nahm & Schultz, 2010; Vaz et al., 2012; Tanaka et al., 2014; Hood et al., 2016; Bouley et al., 2018). In particular, one tectonic and two magmatic regional-scale centres were identified. The tectonic centre consists of the Claritas Rise, a highly tectonically deformed Noachian relief located in correspondence of the crustal/lithospheric weakness zone where also the CF develops (Dohm et al., 2009).

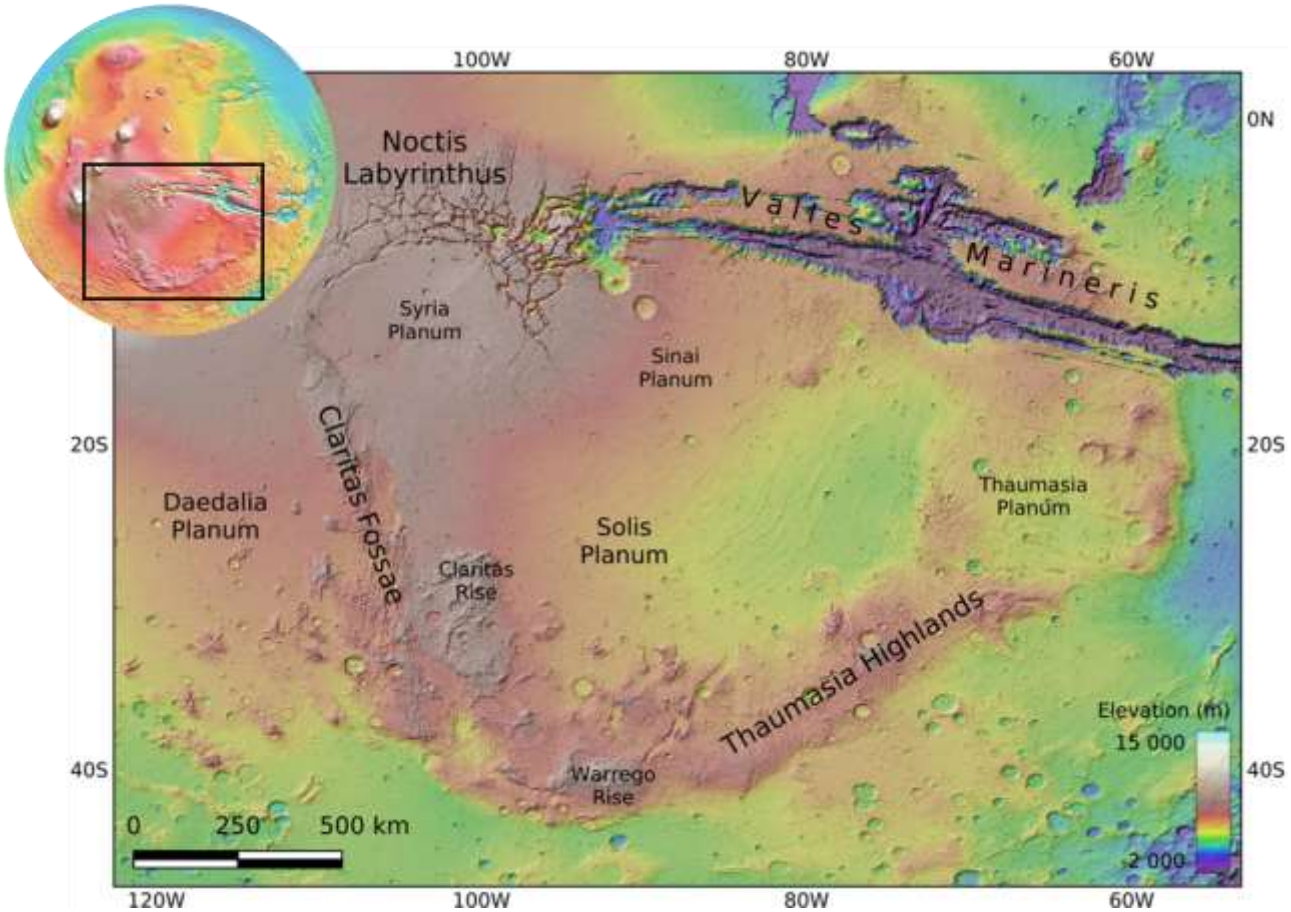

Figure 2.3 - Topographic map of the Thaumasia Region derived from Mars MGS MOLA - MEX HRSC Blended DEM Global v2. Top-left inset shows the location of the Thaumasia Region (black rectangle).

The two magmatic centres are located one in correspondence of Noctis Labyrinthus and Syria Planum to the north (Schultz, 1998; Dohm et al., 2001; Baptista et al., 2008; Hauber et al., 2011; Pozzobon et al., 2023) and the other between the Warrego rise and the double rift system of the

Thaumasia Highlands to the south (Anderson et al., 2001; Grott et al., 2007; Nahm & Schultz, 2010; Hood et al., 2016). Dohm & Tanaka (1999) and Dohm et al. (2001) proposed that tectonic activity at the Thaumasia Region occurred in five phases of faulting between Noachian and Amazonian ages with a main extensional phase developed in Early Hesperian. On the other hand, Smith et al. (2009) grouped the five phases of faulting in two main stages of deformation within a narrower period of time between Late Noachian and Early Hesperian. However, endogenous processes, mechanisms and timing of the multiple proposed tectonic events are still poorly clear. Among the regional scale physiographic features that bound the Thaumasia Region, the CF is of particular interests for studying the evolution of the Thaumasia Region and the tectonics of the Martian crust beneath Tharsis. In fact, the presence of fractured terrains strongly suggest that tectonics actively contributed to form and shape the present-day setting of the CF (Figure 2.4). Evidence of both dip-slip with extensional component and strike-slip tectonics were highlighted (e.g. Hauber & Kronberg, 2005; Montgomery et al., 2009), nevertheless evolutionary models proposed in literature are not mutually exclusive and the mechanism(s) that led to the present-day setting are still debated. Moreover, volcanic activity was proposed likely related to recent times (Pieterek et al., 2024) suggesting that this highly faulted area could act or have acted as a preferential pathway for magma and fluid migration (i.e. interaction between atmosphere, surface, and inner planet).

2.2 Geologic and physiographic setting of the Claritas Fossae

The CF is a highly deformed area characterised by an intricate system of escarpments, graben- and semi graben-like depressions, faults, fractures, and ridges (Figure 2.4) (Hauber & Kronberg, 2005; Vaz et al., 2014). It develops with a nearly N-S orientation for more than 1000 km in total length and 150 km in width between latitudes ~15°S and ~40°S and longitudes ~95°W and ~115°W (Figure 2.3). The CF affects mainly Late to Middle Noachian highland units and Hesperian lava flows (lNh, mNh and lHv, respectively, in Figure 2.4 – geological units and their acronyms follow the Geologic Map of Mars by Tanaka et al., 2014). The eastern boundary of the CF is represented by the Solis Planum, an elevated plateau where lHv crop out. To the west, the limit consists in the relatively less elevated Daedalia Planum where Hesperian volcanic lava flows (Ahv) of Tharsis resurfaced. The long-wavelength topography across the CF (*long-wavelength topography* refers to gently sloping and low amplitude topographic features, such as the hanging-wall roll-over anticlinal of listric/normal faults in extensional setting – Kreslavsky et al., 2017 – spanning distances of hundreds of kilometres. *Short-wavelength topography* refers to rough terrains characterized by the pervasive presence of

depressions, grabens, ridges, and fractures – Watters & Schultz, 2010; Burbank & Anderson, 2013; Klimczak, 2014) is characterised by an elongated and strongly regional-scale, asymmetric valley; namely the Thaumasia Graben (TG) after Hauber & Kronberg (2005). Four regional longitudinal physiographic features are recognized at the CF (Figure 2.4). From west to east they are i) Daedalia Planum; ii) Western Shoulder (WSh), iii) Eastern Scarp (ESc), and iv) Eastern Shoulder (ESh). The Daedalia Planum represents the westernmost part of the study area and marks the boundary of the CF to the west. In our study area, the Daedalia Planum is characterised by a nearly flat topography and by an average altitude that slightly decreases from 6000 m to the north to 4500 m to the south. The WSh is characterised by an articulated short-wavelength (i.e. high-amplitude topographic features of the order of tens of kilometres) topography that develops mainly in mNh and lNh terrains and that changes its characteristics from north to south. From 17°S to about 20°S (box 1, Figure 2.4), a steep scarp with a curved shape in map view exist and it is characterised by a total length of ~230 km, and a maximum elevation change of ~2000 m. This scarp changes its dip that is SE to the north and ENE to the south. It separates a lNh rise to the west from a topographically lower lHv plain to the east. The Noachian-aged rise gently decreases westward towards the Daedalia Planum until it is superimposed by lHv. From about 20°S to 25°S (box 2, Figure 2.4), the WSh is characterised by a smooth, long-wavelength topography that gently dips to the east with a nearly rounded shape. This is a mNh terrain locally etched by a pervasive set of subparallel, NNE–SSW trending scarps and depressions which yield a rugged short-wavelength topography. South of 25°S (box 3, Figure 2.4), the NNE-SSW set of scarp and depression is still present and affects the short-wavelength topography. In this sector, mNh is no longer superimposed by lHv. mNh is here bounded to the west by Noachian volcanic edifice (Nve), early Hesperian volcanic (eHv), and Noachian Highlands edifice (Nhe) units. Moreover, between boxes 2 and 3 three WNW–ESE trending elevated ridges were recognised by Hauber & Kronberg (2005) who interpreted them as the NW continuation of the Thaumasia Highlands that are superimposed by lHv and Ahv further west. The ESc, that is the most prominent morphological feature of the CF, is a west-dipping, NNW–SSE trending steep system of scarps. It exceeds 900 km in length between 17°S and 107°W to the north and 33°S and 103°W to the south affecting lHv and mNh terrains. The ESc marks an elevation change that varies from about 300 m to the north (box 1 in Figure 2.4) to a maximum of 2150 m in the central sector (box 2 in Figure 2.4). To the south (box 3 in Figure 2.4), the elevational change at the ESc decreases from 1000 m to a nearly negligible topographic contrast at the southernmost limit of the study area. In map view, the ESc is rectilinear in the northern and central sectors (boxes 1 and 2 in Figure 2.4), where it offsets

lHv, and is characterised by an en-echelon pattern to the south (box 3 in Figure 2.4), where it offsets mNh. Due to the regional dimensions and morphological characteristics, different authors interpreted the ESc as the superficial manifestation of a major normal dip-slip or strike-slip crustal-scale fault (e.g. Hauber & Kronberg, 2005; Montgomery et al., 2009; Balbi et al., 2022a,b), hereinafter referred to as the Claritas Fossae Fault (CFF).

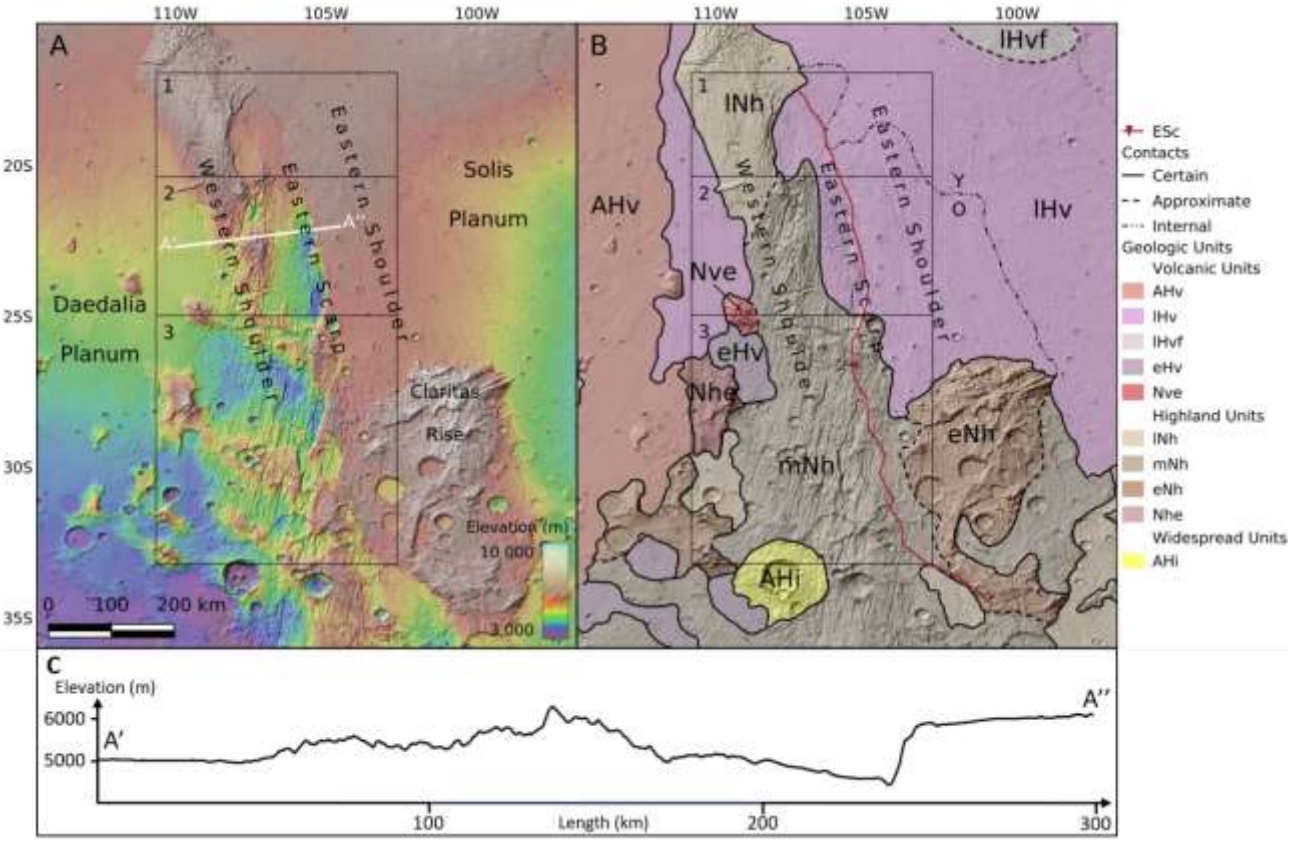

Figure 2.4 - A) Sketch topographic map of the Claritas Fossae (CF) derived from Mars MGS MOLA - MEX HRSC Blended DEM Global v2. Black boxes indicate longitudinal sectors described in the text. White line indicates the trace of the topographic profile shown in C. **B)** geologic Map of the CF from Tanaka et al., 2014. In legenda: trace of the Eastern Scarp (ESc), dip indicated by red triangle; Volcanic Units - AHv: Amazonian and Hesperian volcanic unit; lHv: Late Hesperian volcanic unit; lHvf: Late Hesperian volcanic field unit; eHv: Early Hesperian volcanic unit; Nve: Noachian volcanic edifice unit; Highlands Units - lNh: Late Noachian highlands unit; mNh: Middle Noachian highlands unit; eNh: Early Noachian highlands unit; Nhe: Noachian highlands edifice unit; Widespread Units - AHi: Amazonian and Hesperian impact unit. **C)** across-strike, topographic profile of the CF highlighting the half-graben architecture (namely, the Thaumasia Graben after Hauber & Kronberg, 2005).

The ESh is characterised to the north by the smooth, westernmost part of the Solis Planum where lHv crops out. From 15°S to 26°S, the ESh decreases in elevation from 6500 m (whitish colours in Figure 2.4C) to 5700 m (brownish colours). Thus, the Solis Planum is 500 to 1000 m topographically higher than the Daedalia Planum. South of 26°S, the Claritas Rise represents a more elevated area that exceeds 7000 m, made up of early Noachian highland units (eNh).

2.3 Geotectonic evolution of the Claritas Fossae and open questions

The geo-tectonic evolution of the CF is considered strictly related to that of the Thaumasia Region, thus characterised by intense tectonic activity that likely occurred in different stages between Noachian and Amazonian (Dohm & Tanaka, 1999; Dohm et al., 2001; Smith et al., 2009; Vaz et al., 2014; Tanaka et al., 2014; Pieterek et al., 2024). The numerous structures identified in the area of the CF are characterised by different arrangements that vary from simple, long narrow alignments of lineaments to en-echelon and pull-apart/restraining bend geometries (Dohm & Tanaka 1999, 2001; Hauber & Kronberg, 2005; Montgomery et al., 2009; Tanaka et al., 2014; Bouley et al., 2018). These are evidence that different kinematics contributed to the present-day setting. Extensional and strike-slip kinematics, or a combination of them, have been proposed to explain the formation and evolution of the CF (Dohm & Tanaka, 1999; Hauber & Kronberg, 2005; Montgomery et al., 2009; Balbi et al., 2022a). Dohm et al. (2001) proposed that the development of the CF took place in a long-standing and progressively reducing extensional tectonic setting from Early Noachian to the end of Hesperian age related to the volcano-tectonic activity centred at Tharsis. Several morphological and structural features, such as the overall dimension of the area, the typical half-graben longitudinal asymmetry of the TG (Figure 2.4C), and the numerous fault scarps that affects the valley floor, support this tectonic frame and suggest the existence of a major, normal fault system (Plescia & Saunders, 1982; Tanaka et al., 1991; Tanaka & Davis, 1988; Hauber & Kronberg, 2005; Vaz et al., 2014). These represent remarkable morphological similarities with terrestrial continental rifts, such as the Kenyan Rift or the Icelandic Rift near the Thingvellir National Park, and other Martian rifts, such as the Tempe Fossae (Hauber & Kronberg, 2001, 2005; Hauber et al., 2010). Thus, a crustal-scale normal fault (Figure 2.5A) was proposed by Hauber & Kronberg (2005) to explain the formation of the TG between Late Hesperian and Early Amazonian, in accordance with other timing estimations (Tanaka & Davis, 1988; Tanaka et al., 1991; Dohm et al., 2001; Pieterek et al., 2024). Authors also pointed out that superficial morphological constraints do not allow discriminating between planar or listric geometry of the fault (Hauber & Kronberg, 2005). Nevertheless, the thick crust (estimated between 60 km and 90 km Zuber et al., 2001; Mckenzie et al., 2002; Musiol et al., 2016; Plesa et al., 2018; Taylor et al., 2020; Knapmeyer-Edrun et al., 2021; Plesa et al., 2023), and the lack of regional domal uplift, rift flank uplift, and rift-related volcanism represent significant discrepancies that suggest that classical rift-like processes hardly represent the main formation mechanism (Hauber & Kronberg, 2005).

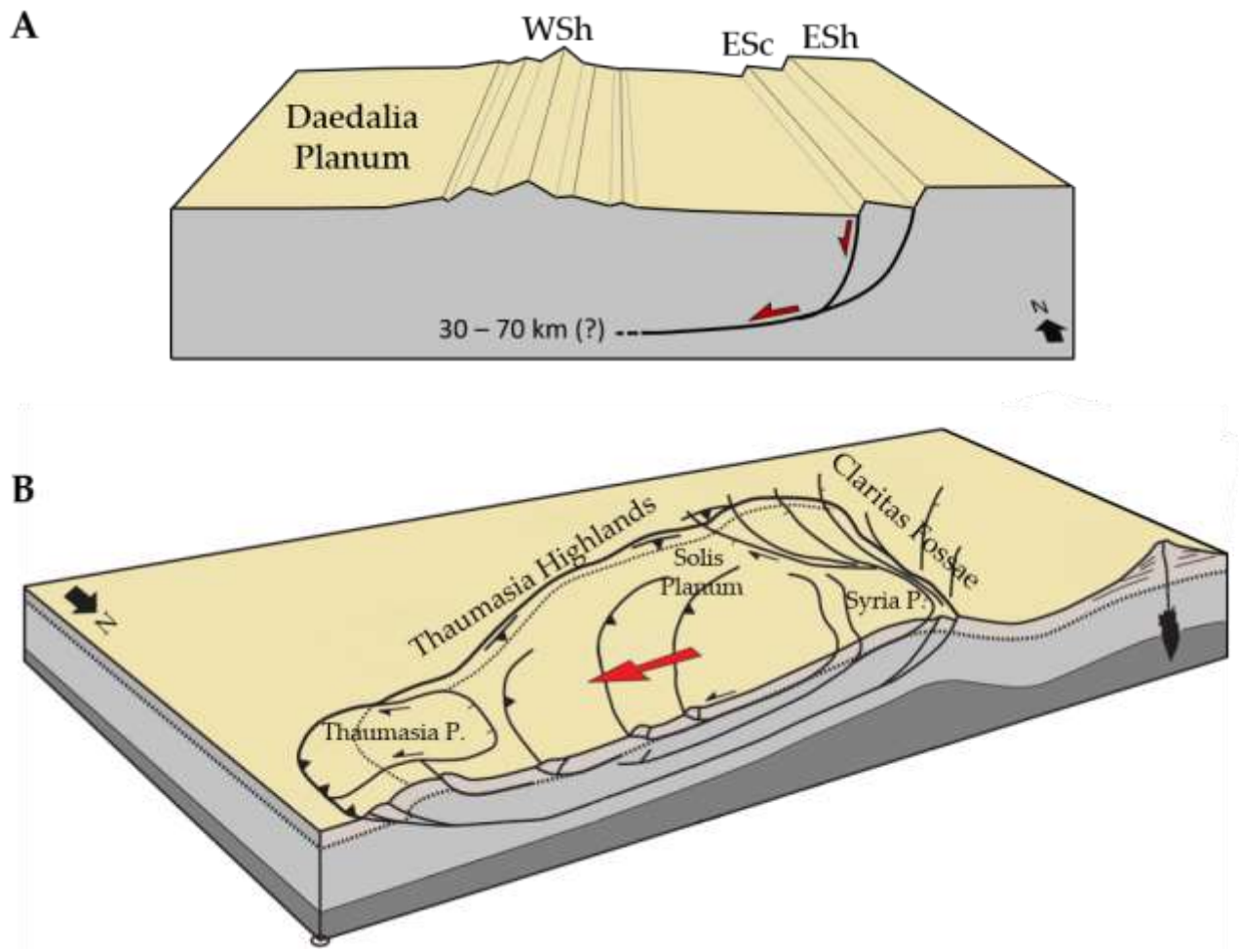

Figure 2.5 - Tectonic models proposed for the formation of the CF: **A)** extensional tectonic model redrawn after Hauber & Kronberg (2005), the asymmetry of the CF/TG results from the activity of a crustal scale listric normal fault inferred reaching 30/70 km of depth (WSh: Western Shoulder; ESc: Eastern Scarp; ESh: Eastern Shoulder). **B)** Right-lateral strike-slip tectonic model redrawn after Montgomery et al., (2009), CF developed as consequence of the mega-gravity slide that originated the present-day setting of the Thaumasia Region.

In addition to the abovementioned evidence of extensional tectonic setting, en-echelon patterns and Riedel-type arrangements of depressions and scarps have been identified at different scales of observation. These have been used by authors to propose the existence of a strike-slip kinematics that acted at the CF (Montgomery et al., 2009; Yin, 2012; Dohm et al., 2015, 2018; Balbi et al., 2022a). Montgomery et al. (2009) interpreted the main scarp of the TG as the result of the combination of R- and P-type structures originated by a right-lateral strike slip kinematics. This developed as a consequence of the gravitational spreading that acted in one to two stages starting from the Late Hesperian (Montgomery et al., 2009; Smith et al. 2009). Within this "mega gravity-slide" model, the CF was interpreted as a trailing imbricate fan with dextral kinematics corresponding to the westernmost margin of the Thaumasia Plateau "microplate" (Figure 2.5B). Dohm et al. (2015, 2018) highlighted geometrical and morphological similarities between the

Thaumasia region and the western US margin. In this setting, the CF represents a strike-slip corridor that resembles the San Andreas Fault. Finally, Yin (2012) described the CF as a right-lateral strike-slip fault zone related to a hemispherical tectonic context ascribed to the episodic slab rollback proposed for the origin of the Tharsis Region.

The compelling evidence of tectonic activity generated a consensus in the scientific community on the tectonic nature of the CF. However, the typology of tectonic deformation and the sequence of events that brought to the present geotectonic setting is still unpuzzled.

Chapter 3

Unravelling the tectonic evolution of tectonically controlled areas through the combination of kinematic numerical modelling and structural mapping

The twofold approach and data included in this chapter are part of a paper published in *Icarus* Journal as *Balbi, E., Ferretti, G., Tosi, S., Crispini, L., and Cianfarra, P. (2024). Polyphase tectonics on Mars: Insight from the Claritas Fossae*. Preliminary results of the presented approach were also part of conference proceedings to national and international congresses: **i)** *Balbi, E., Cianfarra, P., Ferretti, G., Crispini, L., and Tosi, S.: Structural mapping and stress analysis to unravel the polyphasic tectonic history of the Claritas Fossae, Mars. XVIII National Congress of Planetary Sciences, Perugia, Italy, 6-10 Feb 2023;* **ii)** *Balbi, E., Cianfarra, P., Ferretti, G., Crispini, L., and Tosi, S.: The Claritas Fossae region, an example of polyphasic deformation on Mars?, Europlanet Science Congress 2022, Granada, Spain, 18–23 Sep 2022, EPSC2022-1041;* **iii)** *Balbi E., Cianfarra, P., Ferretti, G., Crispini, L., and Tosi, S.: Modelling the extensional tectonic setting of the Claritas Fossae, EGU General Assembly 2022, Vienna, Austria, 23–27 May 2022, EGU22-7683;* **iv)** *Balbi, E., Cianfarra, P., Ferretti, G., Crispini, L., and Tosi, S.: The Claritas Fossae Fault System (Mars): a potential enhanced pathway for fluids exchange between the inner planet and the Martian atmosphere, Chianti Topics: Atmospheres International Congress 2022, Antico Spedale del Bigallo (Fi), Italy, 20 – 22, 2022*; **v)** *Balbi E., Cianfarra P., Ferretti G., Crispini L. &Tosi S., Analysis of tectonic structures on the Martian surface: a contribution to the understanding of the crustal dichotomy – Europlanet Science Congress 2021 (September 13 – 24, 2021), session TP17: Mars surface and Interior, EPSC2021-838*; **vi)** *Balbi E., Cianfarra P., Ferretti G., Crispini L. & Tosi S., Tectonic styles of the Martian crust: insights from Cerberus Fossae and Thaumasia Highlands – 90° Congress of the Italian Geological Society (September 13 – 16, 2021), session S24: The contribution of geology to the knowledge of solar system bodies.*

3.1 Introduction

As discussed in the previous chapter (Section 2.2), the Claritas Fossae (CF) hosts numerous evidence of both dip-slip and strike-slip tectonics. Nevertheless, the relationship between these kinematics and timing of events and possible reactivations is still unclear and multiple scenarios have been proposed to explain the present-day tectonic setting of the CF. To briefly sum up, according to Dohm et al. (2001), the CF developed from the Early Noachian to the end of the Hesperian in a long-standing and progressively reducing extensional tectonic setting related to the volcano-tectonic

activity centred at Tharsis. Hauber & Kronberg (2005) suggested that between Late Hesperian and Early Amazonian a crustal-scale normal fault was responsible for the formation of the TG. In addition, they pointed out that although remarkable morphological similarities exist between the TG and terrestrial continental rifts, the significant differences likely suggest that classical rift-like mechanisms were not the main formational mechanism. On the other hand, Montgomery et al. (2009), Yin (2012), and Dohm et al. (2015, 2018) argued that multiple morphological features (e.g. en-echelon pattern of fractures and faults, Riedel-type arrangements of depressions and scarps, morphological similarities with the western US margin) strongly suggest that strike-slip tectonics have acted and formed the CF. In the present chapter, the kinematic history of the CF is explored to better frame the role of both the normal dip-slip and strike-slip components of tectonic deformation proposed in the literature. For this purpose, the regional-scale topography at the CF (on the order of tens to hundreds of kilometres) is considered as a reference surface resulting from past tectonic activity where minor, negligible changes due to exogenous processes occurred. This represents a reasonable assumption since, although valley networks and periglacial forms have been identified in the CF, erosional estimations at the CF resembles that of low-degradation environments on Earth (Golombek et al., 2006; Vaz et al., 2014). This is the case of hyperarid desertic environments, abyssal plains, and dry/cold ice sheet-bedrock contacts where tectonics/endogenous processes are the main shaping factors (Exon et al., 1997; Burbank & Anderson, 2013; Klimczak, 2014; Maggi et al., 2016; Morelli et al., 2023). To further support the low capability of the Martian exogenous processes in affecting the pre-existing topography, valley networks at the CF have been considered coeval to the stage of faulting occurred in the transition between Noachian and Hesperian ages (Fassett & Head, 2008; Cassanelli & Head, 2019) and the periglacial forms have been related to pre-existing morphologies and/or recent local-scale glacial activity (Rossi & Van Gasselt, 2018). Therefore, the rather homogeneous Martian exogeneous processes poorly altered the morphological contrasts within the study area. In this way, the regional-scale topography is indicative of the tectonic deformation(s) and the strong asymmetry that characterises the CF can be compared to the typical half-graben morphologies resulting from the activity of normal faults with variable dips on Earth (Chorowicz, 2005; Burbank & Anderson, 2013; Hauber & Krionberg, 2005 – Figure 3.1). Half-grabens develop in extensional geodynamic regimes (e.g. the East African Rift system - Atmaoui & Hollnack, 2003; Chorowicz, 2005; Komolafe et al., 2012) and also in strike-slip deformation belts characterised by local extension, such as Lake Baikal (Tapponnier & Molnar, 1979; ten Brink & Taylor, 2002), the

Owen Fracture Zone basin (Rodriguez et al., 2013), and the Dead Sea Fault zone (Ben-Avraham et al., 2008; Smit et al., 2010).

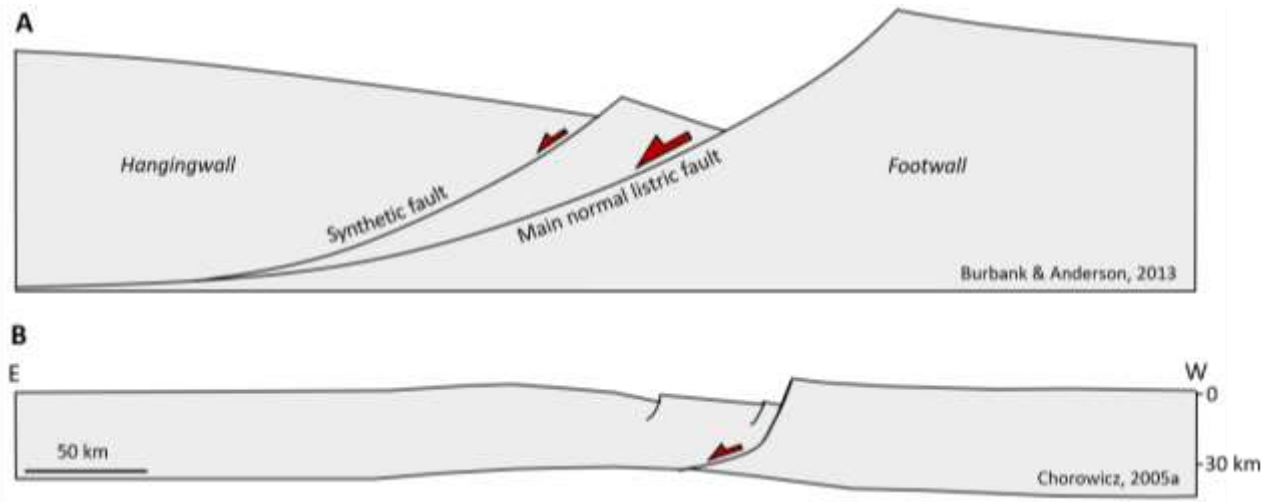

Figure 3.1 - A) Schematic representations in cross-section of the topography outlined by the development of a listric normal fault associated with a synthetic fault. Not to scale, modified after Burbank & Anderson (2013). **B)** Lithospheric section across lake Malawi (redrawn after Chorowicz, 2005) showing how the listric faults control the topography of the East African Rift resulting in a half-graben architecture.

To better frame the kinematic history of the CF an original twofold approach is here followed that combines two methods usually applied for tectonic investigations: i) tectonic numerical modelling, based on the hybrid cellular automata (HCA) technique (Salvini et al., 2001, Salvini & Storti, 2004), and ii) regional-scale structural mapping based on remote sensing data. This last is focussed on the linear and quasi-linear morphotectonic structures that outcrop in the study area and considered as the surficial intersection of subvertical normal dip-slip and strike-slip fault planes. Hereinafter these structures will be referred to as tectonic lineaments. Through the kinematic numerical modelling the dip-slip component is quantified and the geometry of the normal crustal-scale fault that generated the TG is constrained. The strike-slip component of the deformation is highlighted through the structural mapping. The combination of the results of both methods allowed obtaining a more complete kinematic history of the CF and will supply constraints for studies related to the Thaumasia Region on Mars.

3.2 Materials and Methods

3.2.1 Tectonic numerical modelling

Tectonic modelling is performed with the in-house *FORC3* software (v 3.97.2) which implements the HCA (Hybrid Cellular Automata) technique (Salvini et al., 2001; Salvini & Storti, 2004; Cianfarra et al 2009; Silva et al., 2009; Arragoni et al, 2016; Cianfarra & Maggi, 2017). The method consists of

kinematically simulating the superficial morphologies of regions where tectonics is the main shaping factor (e.g. subglacial environments characterised by cold/dry ice-bedrock contact - Maggi et al., 2016; Cianfarra & Salvini, 2016a, 2017) through the activity of one to multiple faults. . HCA follows a forward approach, therefore, the operator configures the initial setting of the model and directly draws the fault(s) according to the tectonic scenario (e.g. extensional, contractional) supposed for the study area. By tuning geometry, position, and displacement of both main and secondary faults with a trial-and-error procedure, the fit between the modelled and the observed topography is progressively improved and refined by the operator. The presented modelling technique considers as assumptions: i) principles of the balanced cross sections (i.e. preservation of areas and lengths and kinematic admissibility and viability, Woodward et al., 1989); ii) crustal-scale visco-elastic behaviour; iii) ductile deformation at the crust-mantle boundary; and iv) the Martian topography as a reference surface for the modelling. The constraints of the model are a) the rheological parameters (i.e. Young's Modulus, Poisson's Ratio, rock density, and resulting rigidity factor) of the Martian crust; b) and the Martian gravity. Modelling results consist of the identification of the characteristics of the main, and secondary faults (i.e. kinematics, fault geometry, position, and displacement) that best reproduce the present day topography. Obtained results allow inferring the thickness of the crust, the tectonic style of deformation (e.g. thick- Vs thin-skin tectonics), and the possible occurrence of rheological contrasts at depth in the Martian crust.

3.2.1.1 Hybrid Cellular Automata (HCA) technique

HCA is a modelling methodology that combines principles of cellular automata and finite element methods. In fact, HCA uses a mesh made of a large number of cells with simplified links (following cellular automata method, Wolfram, 1986) where each point is temporary linked to the surrounding ones trough physical and geometrical laws (following finite element method, Zienkiewicz & Taylor, 1991). In this way, geological layering is replicated through a numerical multilayer that uses a large number of cells that can be visualized as a regular array of linked hinge points and interhinge segments (Figure 3.2A). Layers with similar properties form a mechanical unit whereas a multilayer with multiple mechanical units forms the mechanical stratigraphy (Figure 3.2A). The total number of cells within the model depends on the horizontal nominal cell dimension (625 m in this study) that is selected in order to achieve an accurate representation of the reality. This value, together with the rheology of the mechanical layer(s), controls the geometry of the mechanical stratigraphy and the visco-elastic behaviour of the entire mesh. In fact, HCA reproduces a viscous-elastic material

characterised by ductile behaviour of the regional-scale layering under kinematic conditions. Thus, relative movements between cells are ductile. This yields local dynamic conditions at the scale of the cells and thus elastic behaviour within each cell.

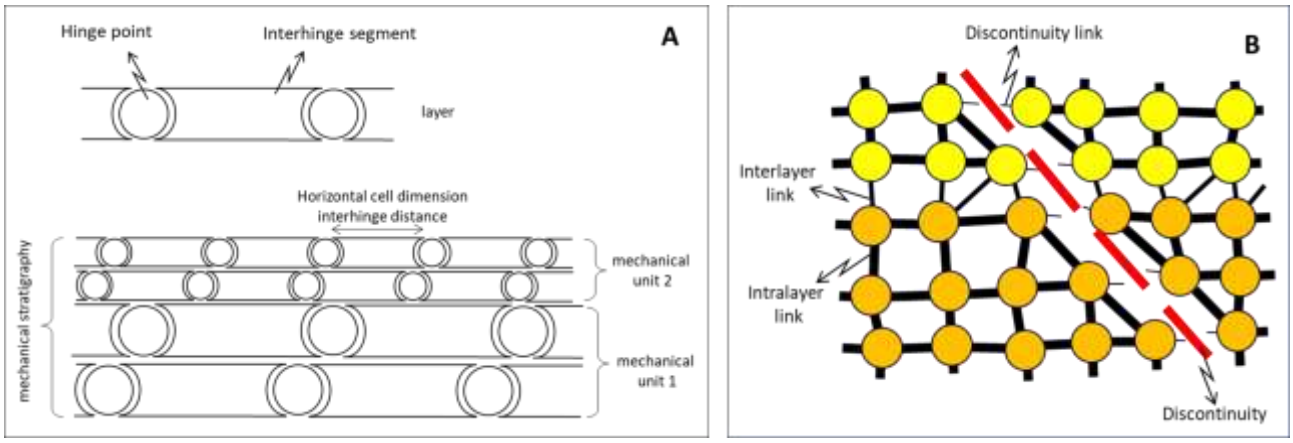

Figure 3.2 - A) schematic representation of layers constituted by hinge points and interhinge segments. Multiple layers form a mechanical units. Multiple mechanical units form the mechanical stratigraphy. **B)** Schematic representation of the three links existing between cells within the mesh: intralayer, interlayer, and discontinuity (redrawn after Salvini & Storti, 2004).

Therefore, the modelling is kinematic since groups of cells (representative of rock volumes) deform plastically during the imposed model kinematics thus maintaining average volume and length and accommodating their sliding and relative movements. The elastic stress (cumulated through time) induced by the overall kinematics within each model cell include the contribution of i) torsion induced fibre stress *sf* (Turcotte & Schubert, 2014) given by:

$$sf = \frac{Eh}{[2(1-\nu^2)]\frac{d^2a}{dt^2}} \qquad \text{(Eq. 1)}$$

where E is the Young modulus, ν is the Poisson ratio, h is the layer thickness, a is the layer dip. $Eh/[2(1-\nu^2)]$ is proportional to the rigidity factor (Turcotte & Schubert, 2014); ii) flexural slip induced stress, which relate to the rheology of the mechanical layer and the amount of relative displacement among adjacent layers. This latter can be derived from the linear stress/strain equation (Turcotte & Schubert, 2014) in which the maximum shear stress is directly proportional to *E* and *e* (elastic deformation) and inversely proportional to *(1+ν)*; and iii) stress induced by the slip along discontinuities, that is computed by comparing the failure conditions for each cell at each model step with the strength of each cell derived from the classical Coulomb failure criterion (Turcotte & Schubert, 2014).

Therefore, according to the finite element principles, for small step of deformation links among adjacent cells obey to first-order geometrical and physical laws (i.e. following linear elasticity within each cell), and, according to the cellular automata principles, cells are free to migrate within the mesh. Forward modelling is accomplished by steps small enough to provide negligible differences (i.e. differences below the horizontal nominal cell dimension) in the resulting geometric/physical law computations thus allowing to use first order (i.e. linear) relations between adjacent cells. Therefore, the new position of a cell at each step can be computed by considering only the neighbouring cells. In this way, the small pace accompanying the cell movement eases the propagation of the dislocation (movement/deformation) within the HCA mesh with a precision (approximation) of the order of 1 m that thus represents the resolution of the model.

The in-house *FORC3* software (Salvini et al., 2001; Salvini & Storti, 2004) used in this work is a 2D implementation of HCA. Layered rocks are simulated by a polygon where all cell movements are constrained. In this way, cells are unable to move in or out of the polygon during the model evolution. Within the polygon, groups of cells are related with homogeneous links. Three types of geometric links exist within the mesh (Figure 3.2B): i) intralayer, ii) interlayer, and iii) discontinuity. Intralayer relations are link between cells belonging to the same layer and consist of rigid relationships derived from average volume and surface preservation conditions, physical boundary conditions (e.g. overburden, gravity), and rock rheology. Interlayer links regulate the relationships among adjacent/different layers. These relations take into account the weaker rheology of interlayer material, physical boundary conditions, and volume preservation conditions, while partial freedom is given to surface variations. Discontinuity relations correspond to the presence of ruptures such as faults. No kinematic links exist across them but physical boundary conditions and slip-induced stresses. This approach guaranteed the overall preservation of volumes and surfaces. The resulting code is fast, allowing the results to be checked in near real time.

3.2.1.2 Modelling and constraints

The forward approach used by the HCA tectonic modelling includes several attempts of tuning fault geometry, position, displacement, and crustal thickness to progressively improve the fit between the observed and modelled final topography. In the case of this thesis, the Martian topography at the CF is replicated in correspondence of four georeferenced topographic profiles (described in detail in the next Section 3.2.1.3) oriented nearly perpendicular to the main CF strike. Profiles are traced where the highest topographic offset at the Esc between WSh and ESh exists (box 2 in Figure 2.4). In

this way, fault displacement is simulated in cylindrical conditions allowing reproducing the true fault and morphology dips. The Martian crust is modelled as a series of 2D sections of layered material with the same length as the topographic profiles (500 km). Rheological parameters used as constraints for the modelling are derived from literature (Table 3.1). It should be noted that, at the used scale/precision (i.e. 1 m), rheological parameters are not critical and their variation within reasonable ranges (Poisson's Ratio: 0.2–0.3; Young's Modulus: 40–120 GPa, Musiol et al., 2016; Taylor et al., 2020; Crane & Rich, 2023) produces differences smaller than 1%, thus negligible in the resulting kinematic model (Cianfarra & Maggi, 2017). Used ranges consider the Martian crust relatively porous and permeable to fluid/magma storage and migration with the possible occurrence of fractured rock volumes (Plesa et al., 2018; Heap et al., 2020; Taylor et al., 2020; Plesa et al., 2023). The thickness of the crust considered for tuning the model ranges from 60 to 90 km and is derived from the estimations proposed using analytical models and gravitational admittance analysis in the CF region (Zuber, 2001; Mckenzie et al., 2002; Knapmeyer-Endrun et al., 2021; Plesa et al., 2018; Taylor et al., 2020; Plesa et al., 2023).

	Value	**References**
Gravity	3.7 m/s^2	-
Horizontal cell dimension	625 m	-
Profile length	500 km	-
Range of crustal thickness	60 - 90 km	Zuber et al., 2001; Mckenzie et al., 2002; Plesa et al., 2013; Musiol et al., 2016; Taylor et al., 2020; Knapmeyer-Edrun et al., 2021; Plesa et al., 2023
Rock Density	2900 kg/m^3	Neumann et al., 2004; Pauer & Breuer, 2008; Plesa et al., 2013; Baratoux et al., 2014; Musiol et al., 2016; Taylor et al., 2020; Knapmeyer-Endrun et al., 2021; Plesa et al., 2023
Range of Young's module	40 - 120 GPa	Taylor et al., 2020; Heap et al., 2020; Crane & Rich, 2023
Range of Poisson's ratio	0.2 - 0.3	Musiol et al., 2016; Taylor et al., 2020; Crane & Rich, 2023

Table 3.1 - Modelling constraints used to reproduce the topography along the four profiles through the *Forc3* software.

As discussed in Section 3.1, the asymmetric morphology of the CF resembles tectonically controlled morphostructures developed in extensional/transtensional regimes, both on the Earth and on other planetary surfaces (e.g. Hauber & Kronberg, 2001, 2005; Chorowicz, 2005; Cianfarra & Maggi, 2017). Therefore, we consider i) the ca. 1000 m topographic offset between ESh and Solis Planum to the east and Daedalia Planum to the west as the result of tectonic activity, and ii) the ESc as the superficial manifestation of a crustal scale normal fault. Thus, the initial setting of the four modelled profiles

includes the location of the model top in correspondence with the mean elevation of the highest long-wavelength topography (i.e. ESh–Solis Planum), and a west-dipping crustal fault with normal kinematics and with the upper tip placed in correspondence of ESc. With a trial-and-error procedure, fault tip position, fault displacement and fault geometry are slightly changed to progressively improve the fit between each model and the Martian topography. A second synthetic fault is added to that models characterised by a more articulated morphology and where the activity of a single fault does not allow achieving a good fit. Thus, we begin with a simplified setting and, when necessary, we introduce a more complex tectonic setting to simulate reliable geological scenarios. Careful tuning of fault(s) geometry included the comparison of each modelled profile with the adjacent ones to better constrain the along-strike fault(s) geometry and displacement. The results from this comparison are then used to improve the fit of adjacent profiles in a feedback-forward modelling process. As an example, Figure 3.3 and Appendix A.1.1 show the different morphologies of the hangingwall that can be obtained by varying fault displacement (Figure 3.3A) and the geometry of the fault (e.g. dip, position of the tip, Figure 3.3B).

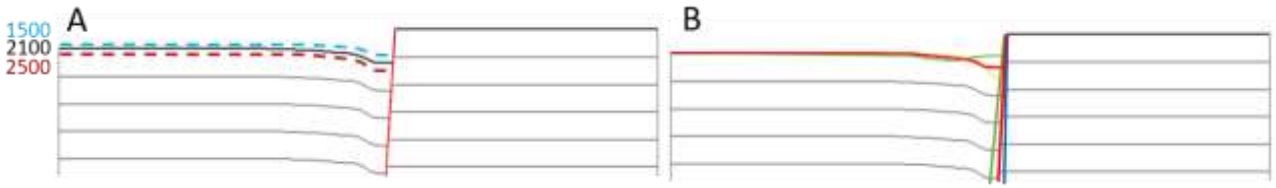

Figure 3.3 - A) different displacements (considering dip-slip normal kinematics) and **B)** different dip of the fault led significant variation in the resulting modelled morphologies. Vertical exaggeration 10:1.

The accuracy of each model is evaluated by quantifying the mean misfit that is expressed through the standard deviation (σ), given as:

$$\sigma = \sqrt{\frac{1}{N-1}\sum_{i=1}^{N}(x_i - \bar{x})^2} \qquad \text{(Eq. 2)}$$

Where:

- N is the total number of simulated/modelled data point,
- $(x_i - \bar{x})$ is the residuals between the modelled and observed topography,
- x_i is the i^{th} data point of the model,
- $\bar{x}$ is the reference Martian topographic value at the i^{th} data point that matches with x_i.

Models with lower σ have a better fit. Thus, σ provides an evaluation of the average deviation of the modelled topography from the reference and represents the Maximum Permissible Error of the

model. Models are considered confident approximations of the reality when the *a* is lower than the used horizontal cell dimension (625 m in this study case).

3.2.1.3 Topographic Profiles

As discussed in Chapter 2, the surface expression of the crustal-scale tectonic feature, namely the CFF, likely responsible for the development of the regional, longitudinal asymmetry of the CF is the ESc. Therefore, the four topographic profiles used as reference surface to conduct the kinematic numerical modelling (P1 to P4, Figure 3.4) are perpendicular to the main strike of the ESc.

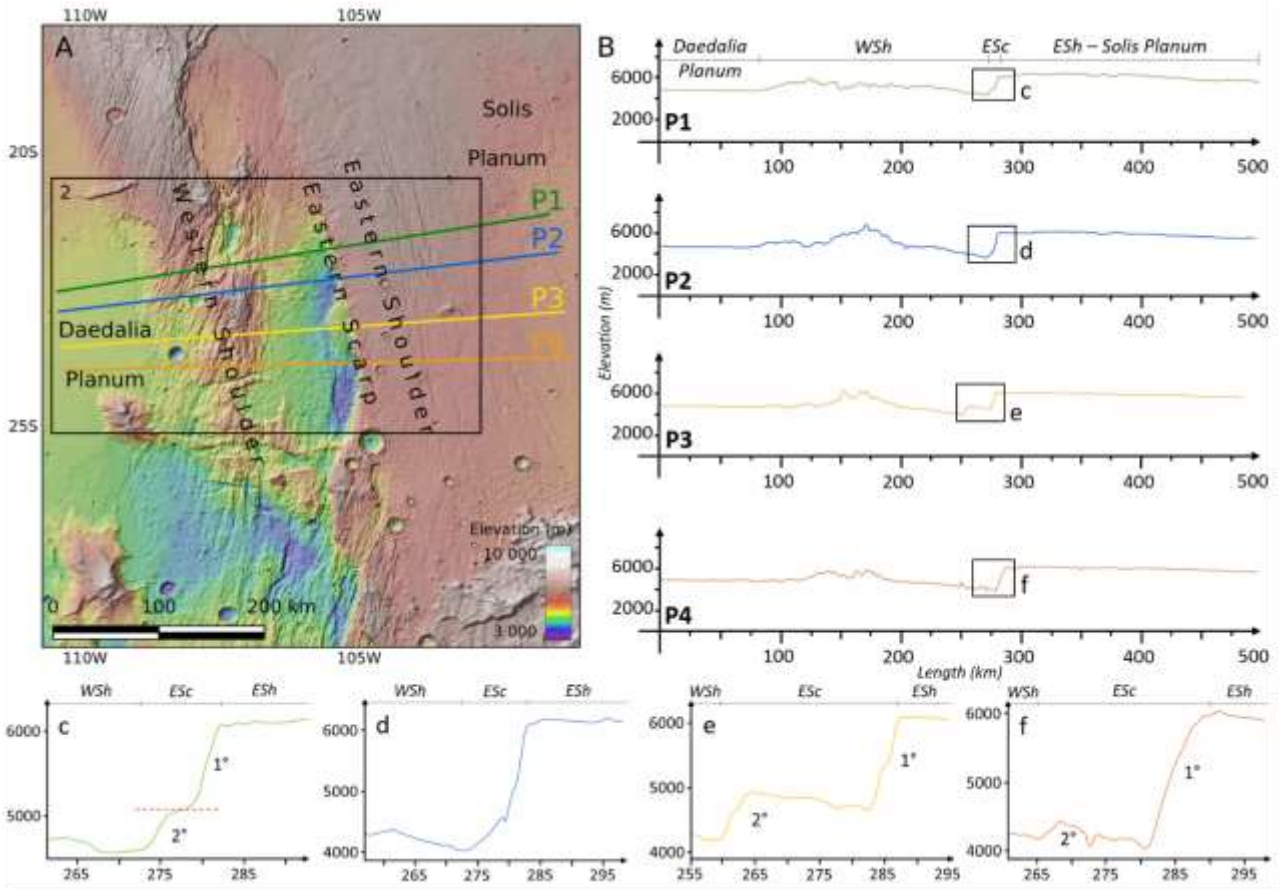

Figure 3.4 - A) Traces of the four topographic profiles in the central sector of the CF (Box 2 refers to Figure 2.4) derived from the Mars MGS MOLA – MEX HRSC Blended DEM Global v2; **B)** Profiles from P1 to P4, black boxes indicate close-ups of the ESc shown in lower part of the figure (**c**, **d**, **e**, and **f**; 1° and 2° refer to the segments of the scarp described in the text). Acronyms of the three longitudinal morphological areas refer to Western Shoulder (WSh), Eastern Scarp (ESc), and Eastern Shoulder (Esh).

In particular, they are focused between 20°S and 25°S (box 2, Figure 3.4) where the highest morphological offset at the ESc occurs indicating this as the area most affected by tectonic processes. The four topographic profiles derive from the Mars MGS MOLA-MEX HRSC Blended DEM Global v2 (spatial resolution 200 m/px - Fergason et al., 2018) and have a length of 500 km to reproduce the long wavelength topography of the CF and to investigate geometry and characteristics of the entire

crustal-scale CFF. The four topographic profiles reproduce the regional asymmetry that characterises the CF. Moreover, they highlight morphological features that characterise the Daedalia Planum, WSh, ESc and ESh from north to south (i.e. from P1 to P4). Specifically, in the westernmost part of the profiles, the Daedalia Planum is characterised by a flat landscape with a mean elevation of 4900 m that gently decreases from P1 to P4. The WSh is characterised by a regional dip towards east which progressively increases as it approaches the ESc. Closely spaced (5–10 km) depressions and scarps significantly affect the short-wavelength topography of the WSh resulting in a rugged landscape that changes in the four profiles. The boundary between the ESc and WSh is represented by the point of lowest elevation of each profile (between 4500 m and 4000 m) located at the base of the scarp. The ESc, that is clearly distinguishable as a steep, W-dipping scarp in each profile, is characterised by a step in P1 and P3 whereas in P4 a less elevated secondary scarp exists to the west of the ESc, between 250 and 275 km along the profile. The ESh is characterised in the four profiles by a smooth landscape with a mean elevation of approximately 6000 m that progressively decreases southwards. Thus, the less elevated Daedalia Planum to the west and the higher Solis Planum to the east describes an elevation change of approximately 1000 m.

3.2.2 Structural Mapping

Structural mapping is coupled with the kinematic numerical modelling to explore the strike-slip component of deformation. Due to the regional/crustal scale of the CFF, the regional signature of the deformation associated with the tectonic activity needs to be investigated. In this way, structural mapping is focussed only on the most prominent and regionally developed morphotectonic structures with regional dimensions (i.e. tens to hundreds of kilometres of length) occurring in the study area. Structures with dimensions ranging from hundreds of meters to a few kilometres are considered related to local-scale deformation and therefore negligible for the purpose of the study.

3.2.2.1 Selected Image Datasets

In order to filter out small and faint structures that are considered the effects of local-scale causes, image datasets with spatial resolution of the order of hundreds of metres are selected. These datasets are: i) the Mars MGS MOLA – MEX HRSC Blended DEM Global v2, with spatial resolution of 200 m/px, that assembles the Digital Elevation Model (DEM) derived from the MOLA, instrument belonging to the NASA's Mars Global Surveyor (MGS), and the High-Resolution Stereo Camera (HRSC), belonging to the ESA's Mars Express (MEX) (Fergason et al., 2018), and ii) the THEMIS

Day/NightIR Controlled Mosaic v2, with spatial resolution of 100 m/px, that assembles the acquisitions performed during day and night by the Thermal Emission Imaging System (THEMIS) aboard the 2001 Mars Odyssey orbiter (Christensen et al., 2004; Edwards et al., 2011). Both datasets are freely available at PDS (Planetary Data System). They represent the best compromise between scale and resolution and provide a synoptic view of the study area.

3.2.2.2 Enhancement Image Processing

Selected datasets are processed in the geographic information system (GIS) environment based on the open-source software QGIS 3.18_Zurich. They are firstly georeferenced and co-registered and then subscenes of the study area are extracted. Subscenes correspond to an area of about 1 500 000 km^2 between 15°S and 40°S, and 95°W and 115°W. With the aim of easing the visual identification of the morphotectonic regional scale structures outcropping in the study area, subscenes are enhanced following an *ad hoc* image processing based on the methodology presented in Lucianetti et al. (2017). Firstly, first-order directional derivatives are applied to the original subscene of the Mars MGS MOLA – MEX HRSC Blended DEM Global v2. In this way, eight "shadow" (*sensu* Wise et al., 1985) images are prepared corresponding to as many synthetic lighting conditions (i.e. every 45° of azimuth and a common elevation of 45°). This is a fundamental step that allows reducing the bias related to the use of a single lighting condition that tends to enhance the visibility of structures nearly perpendicular to the synthetic lighting direction, to add some small rotation to the features in the image, and to reduce those nearly parallel (Wise et al., 1985; Watters & Schultz, 2010). High-pass Laplacian filter is then applied to the shadow images. The combination of high-pass spatially filtered subscenes with the corresponding shadow images and the application of lookup table stretching (i.e. widening the range of possible brightness values of the image pixels) allows the enhancement of tone contrast (Drury, 2004). Laplacian filtering and look-up table stretching are applied also to the two subscenes of the THEMIS Day/NightIR Controlled Mosaic. The ten enhanced subscenes derived from both image datasets are then used for photogeological interpretation.

3.2.2.3 Photogeological Interpretation and Creation of the Structural Database

Structural mapping is conducted through the photogeological Interpretation of the enhanced image mosaics in the GIS environment (QGIS_3.18_Zurich). In particular, pattern of aligned pixels associated with tonal contrast and corresponding to sharp, elongated topographic elements with negative and/or positive relief are visually identified (Watter & Schulz, 2010; van Gasselt & Nass,

2011; Hargitai, 2019; Morelli et al., 2022 - see Appendix A.1.2 for the details of the mapped features). Regional scale morphotectonic structures (length greater than 20 km) outcropping in the study area are traced by systematically inspecting the ten derived enhanced subscenes (i.e. eight MOLA shadow images and two THEMIS images). In particular, structures evident in no less than six MOLA shadow images and one THEMIS image are included in the final structural database. This allow excluding faint structures or partially overlapping doubles providing robustness to the resulting database that is thus representative of the solely crustal deformation. Identified morphotectonic structures are digitised by tracing polylines and drawing vertices by clicking on a fixed map scale of 1:5 000 000 on the screen. Polylines are stored in a dedicated vector layer where the following attributes calculated for each structure are included: i) coordinates of the tips, ii) coordinates of the centroid, iii) length in meters, iv) azimuthal direction, and v) sinuosity (S). In particular, S is computed as the ratio between the real length of the feature and the Euclidean distance between its tips. Straight features are characterised by $S = 1$; deviation of straightness yields $S > 1$, and in the case of circular (infinite loop) or infinitely long features, S increases to $+\infty$ (Leopold et al., 1964).

3.2.2.4 Geostatistical analysis

Geostatistical analysis is conducted on the mapped morphotectonic structures. This consisted of azimuthal analyses of their orientation by frequency and cumulative length performed with the dedicated statistic tool implemented in the freeware *Daisy3* software (v. 5.58.3.231121, Rome, Italy). A polymodal procedure is followed including the best fit with a family of Gaussian curves that represent independent azimuthal groups within each system (Wise et al., 1985; Salvini et al., 1999; Cianfarra & Salvini, 2016b; Maggi et al., 2016). Identified Gaussian peak(s) correspond to preferential orientation/azimuthal set characterised by statistical parameters including mean azimuth and angular standard deviation (*sd*). Histograms derived from azimuthal analysis by frequency and cumulative length are normalised to their highest values. In this way, histograms are smoothed to reduce the statistical noise component by a selected number of moving weighted averages (Wise & Mccrory, 1982). Afterwards, histogram peaks are fitted with a function sum of Gaussian curves following the methodology proposed by Wise et al. (1985) and by applying a best-fit algorithm derived from Frazer & Suzuki (1966). Finally, mean azimuth, height, and azimuthal width at half height of the calculated Gaussian curves are used to recast histograms/Gaussian fits into rose-diagrams. In this way, the existence of multiple preferred orientations can be easily detected (see Appendix A.1.3 for details).

3.3 Results

3.3.1 Kinematic Numerical Modelling

Numerical modelling conducted on the four topographic profiles reproduces the present-day, regional-scale topography at CF with high accuracy (Figure 3.5 and Table 3.2). The best fit between the observed and the synthetic topography (i.e. $\sigma < 625$ m) is achieved through the activity of a west-dipping, crustal-scale normal fault that reaches the base of the crust at 80 km of depth. In the four models, this master fault preserves the same geometry characterised by a dip that decreases from the Martian surface to the base of the crust resembling a listric shape. In particular, the dip is 47° from the surface to 30 km of depth, 37° from 30 to 50 km, and then 33° down to the base of the crust at 80 km. The displacement varies across four profiles being 1200 m in model M1, 2100 m in M2, 1500 m in M3, and 1900 m in M4.

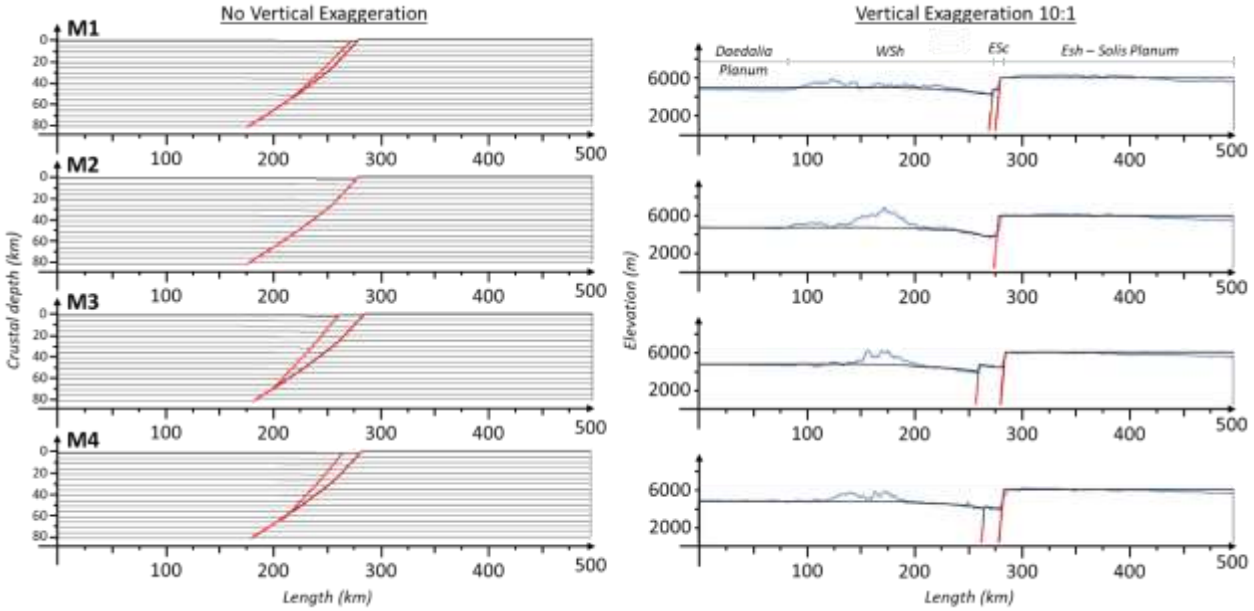

Figure 3.5 - Results of the tectonic numerical modelling. On the left, models with no vertical exaggeration show the geometry of the crustal-scale main fault that reaches the base of the crust at 80 km of depth and of the synthetic faults. On the right, models with vertical exaggeration 10:1 show the fit between the modelled (black line) and the Martian topography (blue line). In profiles P1, P3 and P4 the main listric fault is associated with a synthetic normal fault whose tip is in correspondence with the step of the ESc.

In models M1, M3, and M4, the best fit is achieved by associating to the master fault a secondary, synthetic fault with the tip located in correspondence with the step of the ESc. Also this secondary synthetic fault required a specific tuning to find out the best fault geometry, position, and displacement to reproduce the present day Martian topography. This is mostly related to the different morphologies that characterise the steps of the ESc in the three profiles (see Figure 3.4). In

particular, the dip of the synthetic faults in the three models commonly decrease with depth following the master fault. Synthetic faults slightly change in geometry but branch from the master fault at various depths that are 65 km in M1, 70 km in M3, and 60 km in M4. The displacement of the synthetic faults increase from 500 m in M1 to 600 m in M3 and then decrease to 200 m in M4. Therefore, the total displacement, calculated as the sum of the displacements of both master and synthetic faults, is 1700 m in M1 and 2100 m in the other three models. These values resemble that of the elevation changes of the ESc in the corresponding profiles (P1: 1500 m; P2: 2150 m; P3: 2100 m; P4: 1950 m - Table 3.2).

	Main Fault Displacement	**Synthetic Fault Displacement**	**Total Displacement (Height of the Esc)**	**Mean misfit (m)**
M1	1200	500	1700 (1500)	215
M2	2100	-	2100 (2150)	313
M3	1500	600	2100 (2100)	210
M4	1900	200	2100 (1950)	145

Table 3.2 - Modelled displacements for main and synthetic faults. The total displacement, calculated as the sum of the displacement of each fault, resembles the morphological offset of the ESc along the profiles. The mean misfit (Equation 2) is lower than the horizontal cell dimension (625 m) in each profile, demonstrating the accuracy of the performed models.

The accuracy σ of the presented models is lower than the horizontal cell dimension (625 m). In fact, the mean misfit between the observed and the synthetic topography is 215 m in M1, 313 m in M2, 210 m in M3, and 145 m in M4. These values testify that models successfully reproduce with high precision the Martian topography from the Daedalia Planum to the Esh/Solis Planum. Nevertheless, the fit throughout the entire length of the models does not remain constant. In correspondence with the WSh, the misfit increases remaining below 625 m in models M1 and M4 and exceeding the horizontal cell dimension in M2 and M3. Specifically, the mean misfit in M1 is 370 m between 100 and 150 km, and it is 540 m between 130 and 180 km in M4. Local mean misfits of 1146 m between 150 km and 190 km and of 838 m between 170 km and 190 km characterise M2 and M3, respectively. This local higher misfit may be related to a more complex tectonic setting in which the modelled dip-slip component adds to a horizontal component of the motion. The possible occurrence of this last component and its relationship with the normal dip-slip modelled kinematics is explored through structural mapping.

3.3.2 Structural Mapping

Photogeological interpretation of the enhanced subscenes allowed the identification of 251 linear and quasi-linear morphotectonic structures (Figure 3.6). They represent single or several linked scarps that maintain the same azimuthal direction for a minimum of 20 km and are associated with elevation changes in the order of hundreds of meters.

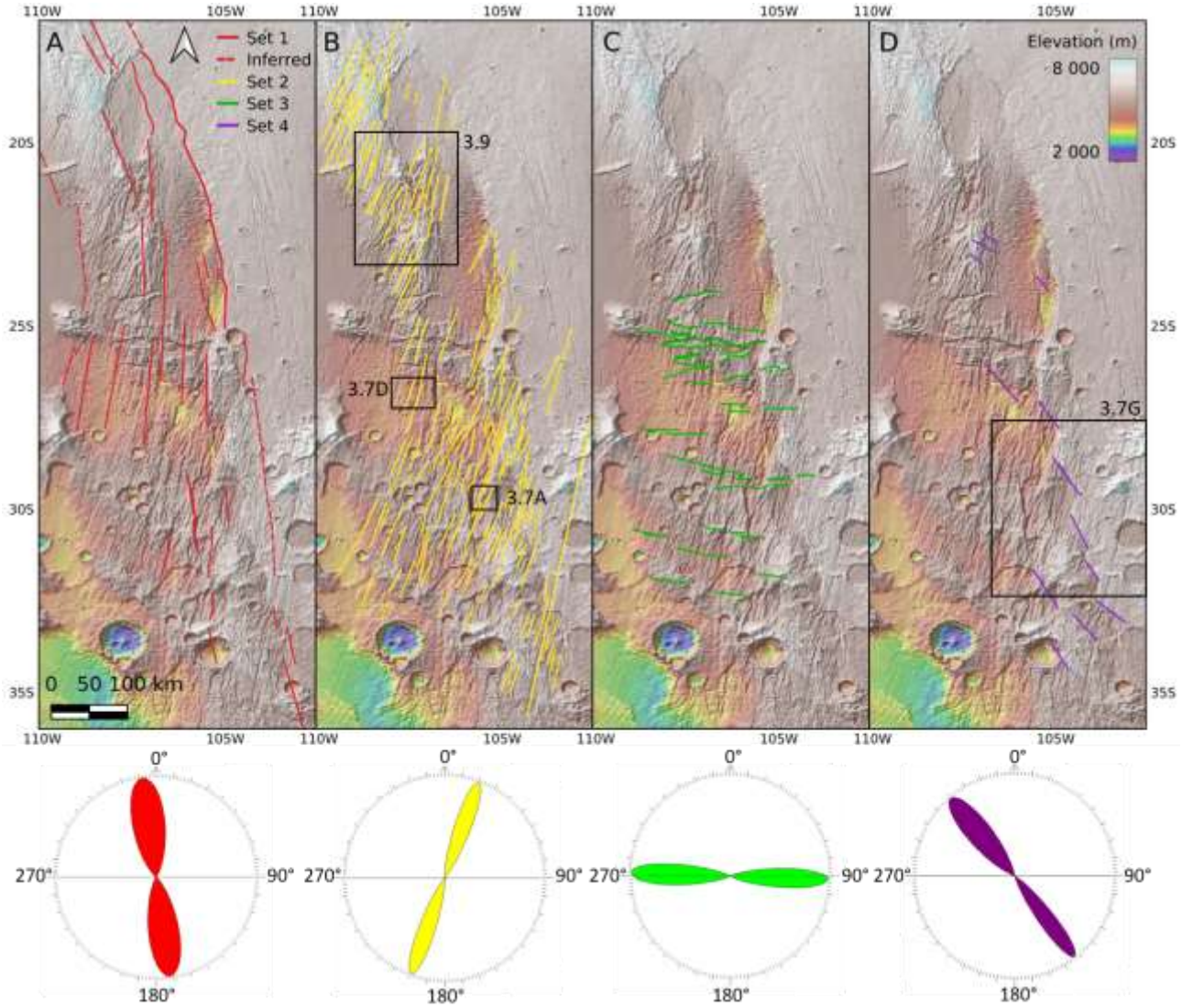

Figure 3.6 - Sketch maps of the four identified sets in the area of the CF: **A)** Set 1, **B)** Set 2, **C)** Set 3, and **D)** Set 4. The black boxes indicate close-ups in Figures 3.7 and 3.9. Below, wind rose diagram with the petals representing the Gaussian peaks (i.e. the uni-modal azimuthal distribution) resulting from the azimuthal analyses of the mapped structures. The width of each petal represents the sd (see Table 3). Note that the azimuthal distance among the found sets is larger than the sd of their Gaussian peaks, making the identification of the sets robust. The rose diagrams are subdivided into two semicircles which show the results by frequency (upper) and cumulative length (lower).

Mapped structures occur in correspondence of i) elongated, straight graben-like depressions, ii) elongated reliefs, iii) a combination of i and ii, and iv) the juxtaposition of regions with different surface roughness resulting in different image textures (Appendix A.1.2 shows examples of the

identified structures as they appear in high-resolution CTX and THEMIS images). Most of the 251 mapped structures (92%) occur in the correspondence of Noachian terrains and only 22 affect the lHv or eHv terrains. These lasts also include some strands of the ESc. Evidence of apparent offsets and en-echelon arrangements were identified, suggesting normal overall dip-slip and strike-slip kinematics (Figure 3.7). Thus, mapped structures can be considered as the intersection with the Martian surface of subvertical normal dip-slip and strike-slip fault planes (i.e. tectonic lineaments). On the basis of the azimuthal trends and characteristics (e.g. length and spatial distribution), mapped structures can be grouped in four sets of tectonic lineaments (Figure 3.6 and Table 3.3). Each set is characterized by low *sd* of the azimuth both by frequency (upper part of the rose diagrams in Figure 3.6) and cumulative length (lower part of the rose diagrams in Figure 3.6), indicating little variation in the overall directions within the entire study area. Consequently, the angular relations (calculated at an acute angle) between the sets remain constant. The four identified sets are:

Set 1 (red, Figure 3.6A) includes 32 faults spatially distributed throughout the study area. Faults of Set 1 are characterised by prominent scarps with mean length of 125.6 km and mean S of 1.00 (i.e. straight elements). The main trend of Set 1 is 352° for both frequency and cumulative length, with *sd* values that are 13° and 12°, respectively (red rose diagram in Figure 3.6 and Table 3.3).

	n°	**Main Azimuth by frequency *(sd)***	**Main Azimuth by cumulated length *(sd)***	**Mean Length (km)**	**Sinuosity**
Set 1	32	352° *(13°)*	352° *(12°)*	125.6	1.00
Set 2	167	20° *(6°)*	20° *(7°)*	55.5	1.00
Set 3	39	272° *(8°)*	271 *(8°)*	48.1	1.01
Set 4	13	320° *(10°)*	323 *(7°)*	48	1.00

Table 3.3 - Table summarizing the characteristics of the identified sets: number of mapped structures for each set, main azimuth by frequency and cumulated length with the Standard Deviation (*sd*) in brackets, mean length and mean sinuosity.

Set 2 (yellow, Figure 3.6B) includes 167 faults associated with straight scarps and graben-like elongated depressions with mean length of 55.5 km. Structures belonging to Set 2 are clustered mainly on the hanging wall of the modelled CFF. They have kilometric spacing resulting in a relatively high number of structures per unit area compared with the other sets. Set 2 is characterised by a main trend of 20° for both frequency and cumulative length analysis (*sd*: 6° and 7°, respectively).

The acute angle between Sets 1 and 2 is constant and it is 28° on average. The faults of Set 2 show dextral components of offsets, as evidenced by crater rims, en-echelon patterns with restraining bands, and local pull-apart basins (Figure 3.7A-C).

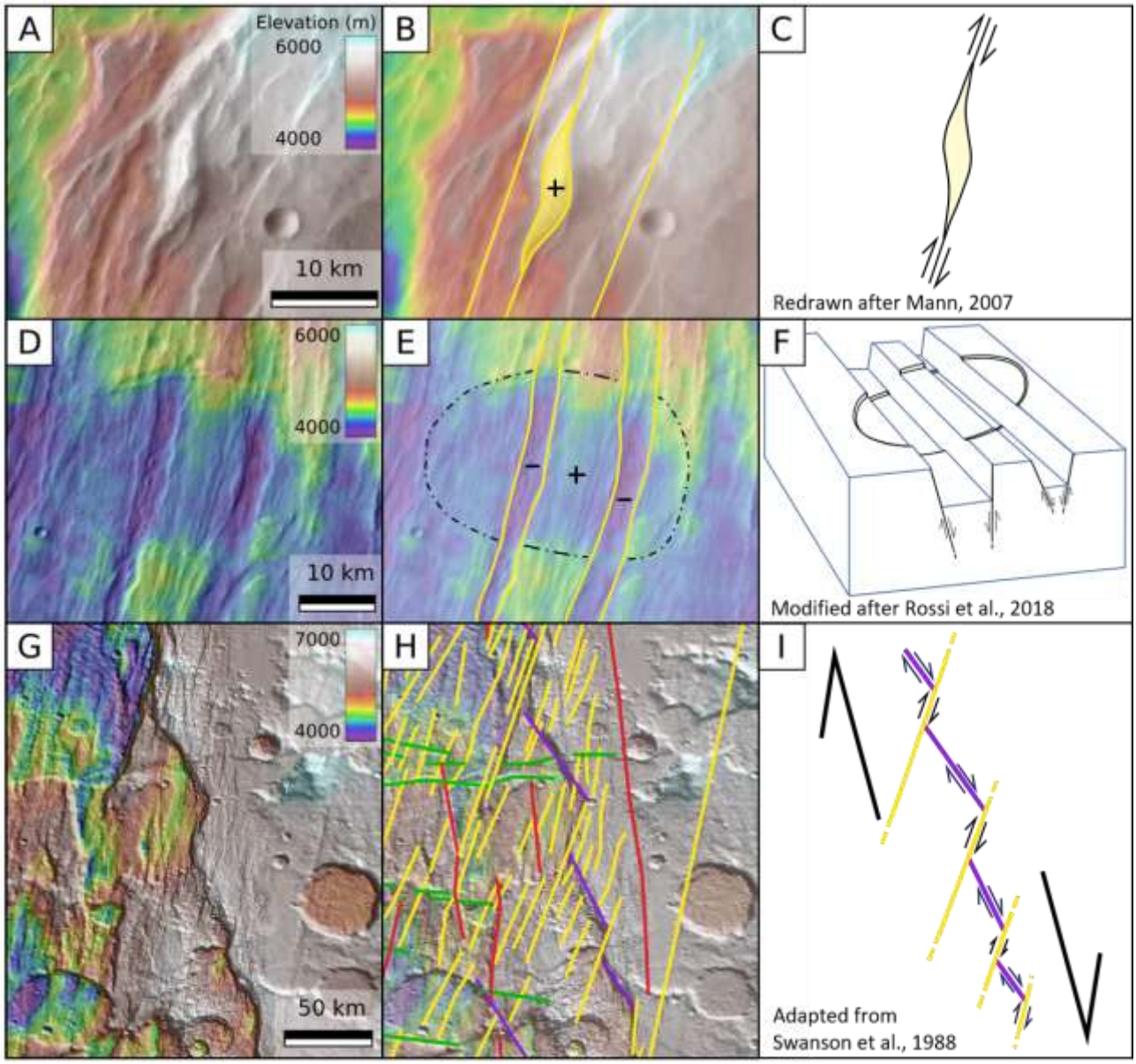

Figure 3.7 - Kinematic evidence related to Sets 2 and 4. The presence of both right-lateral strike-slip and normal dip-slip components associated with Set 2 is suggested by the presence of overlap structures such as left-stepping contractional step-overs **(A-C)** and grabens **(D-F)** that deform and offset crater rims (+ and – indicate positive and negative relative topography, respectively – THEMIS IRDay images). In **(G-I)** evidence of Set 4 abutting Set 2 that accommodates dextral kinematics (MOLA shadow image, direction of the light 45°). In **(I)** external, thicker arrows indicate regional kinematics. Images are north oriented.

This evidence is consistent with right-lateral strike-slip kinematics. Evidence of graben-like depressions are present as well indicating the existence of extensional components of the deformation with WNW–ESE orientation (Figure 3.7D-F). Some of these faults were interpreted as

apparent Riedel-shear (R-shear) structures part of an NNW–SSE oriented shear system developed under a dextral transtensional tectonic regime (Montgomery et al., 2009).

Set 3 (green, Figure 3.6C) includes 39 faults associated with straight, prominent scarps characterised by a mean length of 48.1 km. Set 3 is characterised by main azimuthal trend of 272° (*sd*: 8°) by frequency and a 271° (*sd*: 8°) by cumulative length. Faults belonging to Set 3 mainly occur in the central and southern sectors of the hanging wall of the CFF with spacing ranging from kilometres to tens of kilometres (boxes 2 and 3 in Figure 2.4). Between 24°S and 27°S, a cluster of structures of Set 3 bound wide graben-like depressions characterised by elevation change up to 500 m, suggesting extensional kinematics. Set 3 has a constant angular relationship with Set 1 of 80° on average.

Set 4 (purple, Figure 3.6D) includes 13 faults associated with straight scarps characterised by mean length of 48 km. The main trend of Set 4 is 320° (*sd*: 10°) by frequency and 323° (*sd*:7°) by cumulative length. In the southern sector of the CF, structures belonging to Set 4 show an en-echelon, right-stepped arrangement and abut Set 2 faults (Figure 3.7G-I). Set 4 maintains a constant angular relationship with Set 1 of 32° on average. This set was described by Montgomery et al. (2009) as apparent P-shear structures developed within a regional NNW-SSE right-lateral transtension.

3.4 Discussion: Claritas Fossae tectonic model

The CFF is the regional tectonic lineament that characterised the geological and structural evolution of the western boundary of the Thaumasia Region. The area of the CFF represents the envelope of main fault strands associated with secondary faults, resulting in an elongated N-S trending corridor of deformation where the CF develops. The nowadays geotectonic setting at the CF may be the result of the contribution of two components of deformation associated with the CFF: strike-slip and dip-slip tectonics. The occurrence of these two components is suggested by multiple evidence indicating a complex or poly-phase tectonic history.

3.4.1 Dip-slip Tectonics

In the present work, the dip-slip component of the deformation that acted at the CFF and its influence on the topography were reproduced through the kinematic numerical modelling. Fault attributes (geometry, displacement, and location of the upper tip) and thickness of the crust represented the most significant parameters to be set for achieving the best model accuracy. Performed models highlight that the regional-scale, long-wavelength topography of the CF is the result of the activity of a crustal listric normal fault locally associated with synthetic normal faults.

The normal dip-slip displacement of approximately 2000 m confirms that the modelled fault exceeds hundreds of kilometres in length (Walsh & Watterson, 1988). This is compatible with the resulting modelled listric fault that affects the entire Martian crust up to 80 km of depth which is the inferred crustal thickness. Similarly to what happens for the Earth where crustal faults develop as shear zones at depth (Storti et al., 2003), we assume that the modelled normal CFF fades down into an increasingly broad shear zone and the modelled displacement at depth (crustal-mantle boundary) occurs through a ductile shear. Lack of abrupt changes in fault trajectory/dip at depth is compatible with a rather homogeneous, rigid crust in this region of Mars. In this way, whether minor vertical rheological layering, mechanical contrasts, or strength anisotropies existed, they could not affect the overall geometry at the depth of the crustal faults. The modelled crustal thickness of 80 km is in line with previous estimations (e.g. Hauber & Kronberg, 2005; Plesa et al., 2023). Knapmeyer-Endrun et al. (2021) proposed two scenarios for the crustal thickness and structure on Mars on the basis of seismic data from InSight mission. Specifically, they favoured the thick-crust seismic model (about 80–90 km and average density of 2900 kg/m^3) in the area of Tharsis proposing the existence of present-day melting related to an ascending plume. Our results fit this thick-crust model that thus could represent a reliable setting for the CF area. Plesa et al. (2023) on the basis of geophysical modelling and Hauber et al. (2011) using evidence of young lava flows on the surface supported the occurrence of present-day partial melts in the crust of the Tharsis region. Moreover, volcanism has been highlighted by different authors in the areas of Noctis Labyrinthus and Syria Planum (Hauber et al., 2011; Pieterek et al., 2022; Pozzobon et al., 2023), and Ulysses Fossae (Brož & Hauber, 2012). In the CF Pieterek et al. (2024) reported the existence of mounds of volcanic origin without significant lava flows. The crustal dimension of the CFF replicated through the modelling highlighted that this deformation zone may represent a preferential pathway for magma (and fluid) migration. In addition, the existence of secondary faults and fractures and their intersection with the main fault strands may locally increase crustal secondary permeability further favouring eventual upwellings. The modelled initial dip angle of the CFF at the Martian surface ranges between 47° and 51°. These values are similar to the average dip angles of 46.8° ± 9.8° estimated by Vaz et al. (2014) for normal faults in the area of the CF. The obvious logistical problems in collecting direct measurements of normal faults dip on Mars led authors to usually assume 60° as average dip angle of Martian normal faults (Vaz et al., 2014). This is the value predicted by Anderson (1951) and by the Mohr-Coulomb failure criterion for most rocks (Jaeger et al., 2007; Schultz et al., 2009) and used to estimate the extensional strain on Mars. Specifically, in the area of the CF Hauber & Kronberg (2005) estimated

along a series of topographic profiles across the TG crustal extension between 0.5 and 4.5 km and strain between 1% and 3%. Considering the lower values of the normal-fault dip derived from our model, along the same topographic profiles extension and strain are between 0.8 and 7.2 km and between 1.6% and 4.8%, respectively, with 47° of dip angle, and between 0.7 and 6.3 km and between 1.4% and 4.2% with 51° of dip angle. This highlights an underestimation of the extensional strain at the CF between 40% and 60%, in line with what was predicted by Vaz et al., (2014). This suggest that the estimates of extensional strain on Mars could be reconsidered.

3.4.2 Strike-slip Tectonics

Spatial distribution and angular relations between identified sets are consistent with models of strain partitioning and shear fracture orientation within idealized shear zones (Swanson, 1988; Storti et al., 2006). In particular, mapped structures are compatible with either transtensional strike-slip tectonics (Figure 3.8A) or fault-parallel extension/contraction conditions (e.g. Storti et al., 2006, Figure 3.8B, C).

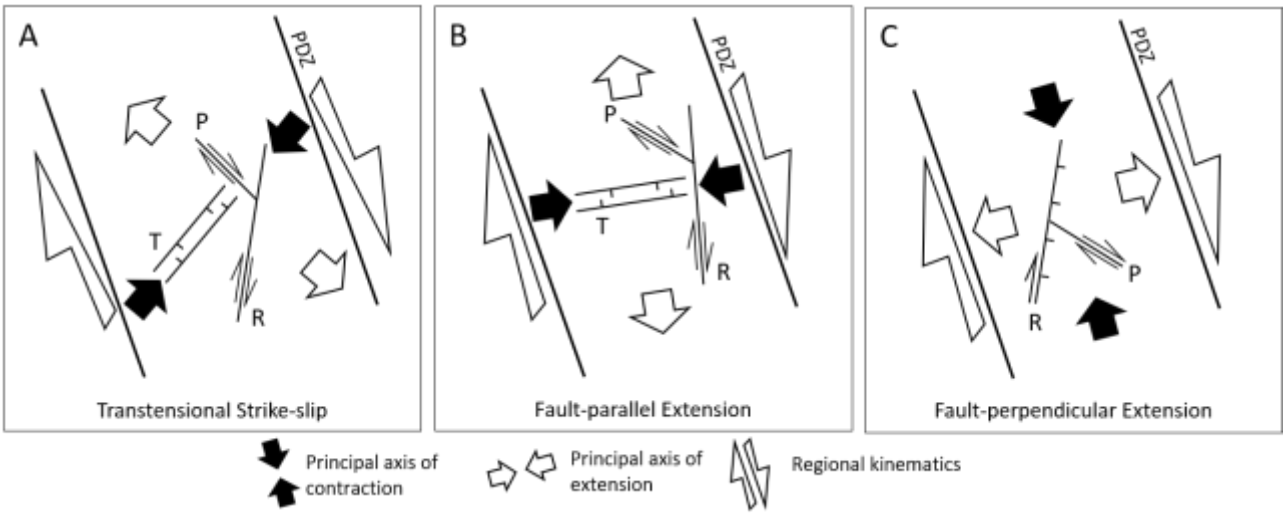

Figure 3.8 - Sketch on the type of structures that can occur within a right-lateral shear zone (PDZ: Principal Displacement Zone, redrawn after Storti et al., 2006). The orientation of the kinematic stress field within the shear zone influences the arrangement of the structures. Figures shows examples of the different arrangements of R, P and T structures within right-lateral shear zones in the cases of **A)** transtensional strike-slip kinematics, **B)** strike-slip kinematics characterised by fault-parallel extension, and **C)** strike-slip kinematics characterised by fault-perpendicular extension sets.

The four identified sets are consistent with the Riedel shear model (Riedel, 1929) where the main shear zone (or principal displacement zone - PDZ) is parallel to Set 1. Structures belonging to Set 2 characterised by right-lateral kinematics and extensional components represent R-shear structures. Extensional structures of Set 3 correspond to T-structures, and those of Set 4 to P-shear structures accommodating the kinematics in the overlapping zones of R-shear (Swanson, 1988; Montgomery et

al., 2009; Fossen, 2016). This architecture is compatible with an NNW-SSE trending right-lateral strike-slip shear zone. Set 2 and Set 3 form average angles with the main shear zone/PDZ that are larger than that of 15° and 45° that form R-shear and T-structures in a classical Riedel-type model. Different studies highlighted that the existence of normal/extensional or reverse/contractional dip-slip component associated with the main strike-slip can affect the angles between each set and between the sets and shear zone (Cianfarra & Salvini, 2015; Donzé et al., 2021). In the case of this work, the angle of 28° between Set 2/R-shear and Set 1/PDZ (28°) may be related to a right-lateral transtensional regime. This is consistent with the highlighted extensional components associated with Set 2 that adds to the pre-existing strike-slip component. On the other hand, the angle of 80° between Set 3/T-structures and Set 1/PDZ is compatible with the principal axes of extension, induced by the regional kinematics, nearly parallel to the shear zone (Storti et al., 2006; Swanson, 1988).

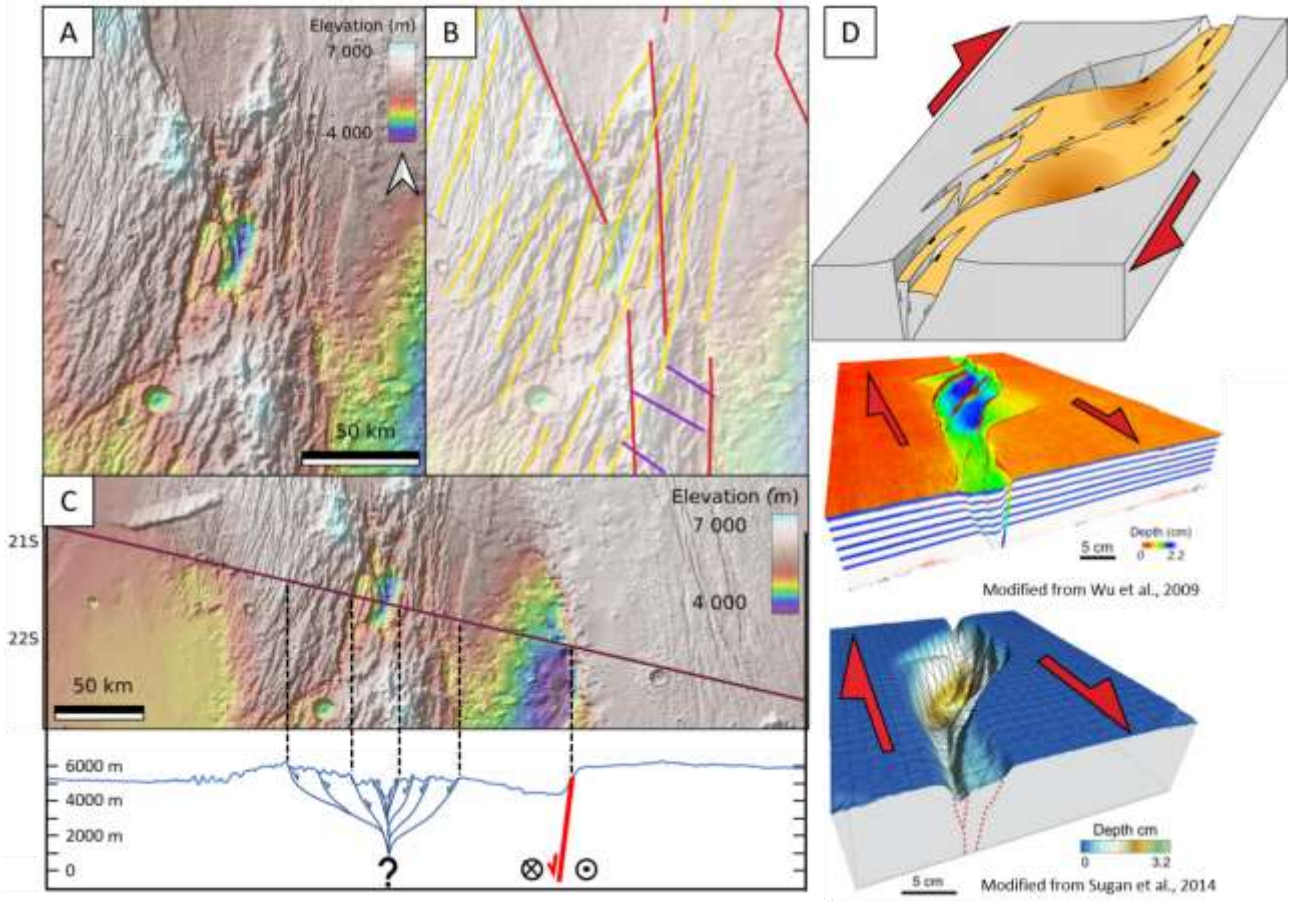

Figure 3.9 - A) Topographic sketch map of the basin that affects the WSh between 20°S–22°S. **B)** Sketch of the structural map (Figure 5) showing the intersection in the area of the structure of Sets 1 and 2. **C)** Across the strike topographic profile of the basin. The morphology resembles that of a terrestrial pull-apart basin developing in transtensional tectonic environments. **D)** Analogical models of pull-apart basin in dextral strike-slip corridor characterised by a percentage of transtension.

Evidence of strike-slip regional tectonics is provided also by the existence of several local depressions that alternated with local relief along the NNW–SSE strike of the CFF. Figure 3.9A shows the basin that persists over the WSh between 20°S-22°S. This is a NNE-SSW oriented depression that exceeds 100 km in width and 80 km in length and originated by the activity of faults belonging to Sets 1 and 2 (Figure 3.9B). This basin marks an elevation change of approximately 2000 m from its westernmost border to its most depressed part, and approximately of 1500 m from its most depressed part to its easternmost limit (Figure 3.9C). Visualizations in map view and in sections highlight morphologies resembling that of terrestrial pull-apart basins related to right-lateral strike-slip tectonics with a percentage of transtension. Figure3.9D highlights these similarities showing a comparison between the Martian basin and the digital models of the Vienna Basin (Wu et al., 2009) and Cynarcik Basin in Turkey (Sugan et al., 2014) occurring in a dextral strike-slip regime with 5% of percentage of transtension.

3.4.3 Claritas Fossae Tectonic Model

The highlighted deformations developed along the shear zone of the CFF are compatible with two tectonic scenarios. The first scenario includes a single transtensional tectonic event responsible for the formation of both the asymmetry of the CF valley and the mapped sets (Scenario 1 in Figure 3.10A). The second scenario (Scenario 2 in Figure 3.10B) involves a tectonic evolution made of two events: i) an older right-lateral strike-slip event responsible for the development of the Set1/PDZ, Set 2/R-shear, Set 3/T-structures, and Set 4/P-shear followed by reactivation in a right-lateral transtensional regime. The first event is characterised by extension related to regional kinematics nearly parallel to the main shear zone in which the four sets develop. In the second event extension is nearly orthogonal to the main shear zone adding to the regional extensional setting, resulting in an overall transtensional tectonics. The dip-slip normal component in this second event yields the asymmetry of the CF valley through the activity of the listric crustal fault. Although both the proposed scenarios are reliable, constraining the timing of the deformation provided important insights. The four identified sets persist almost exclusively over the WSh and the southern part of the CF (Box 3 in Figure 2.4) where middle and late Noachian age terrains (mNh, lNh) crop out (Figure 3.11). Structures belonging to Sets 1 and 2 are superimposed by Late Hesperian volcanic units (lHv) both to the west and east of the WSh in the central and northern sectors of the CF (boxes 1 and 2, Figure 2.4). Moreover, to the west of the WSh a few structures belonging to Set 1 persist also over early Hesperian volcanic units (eHv).

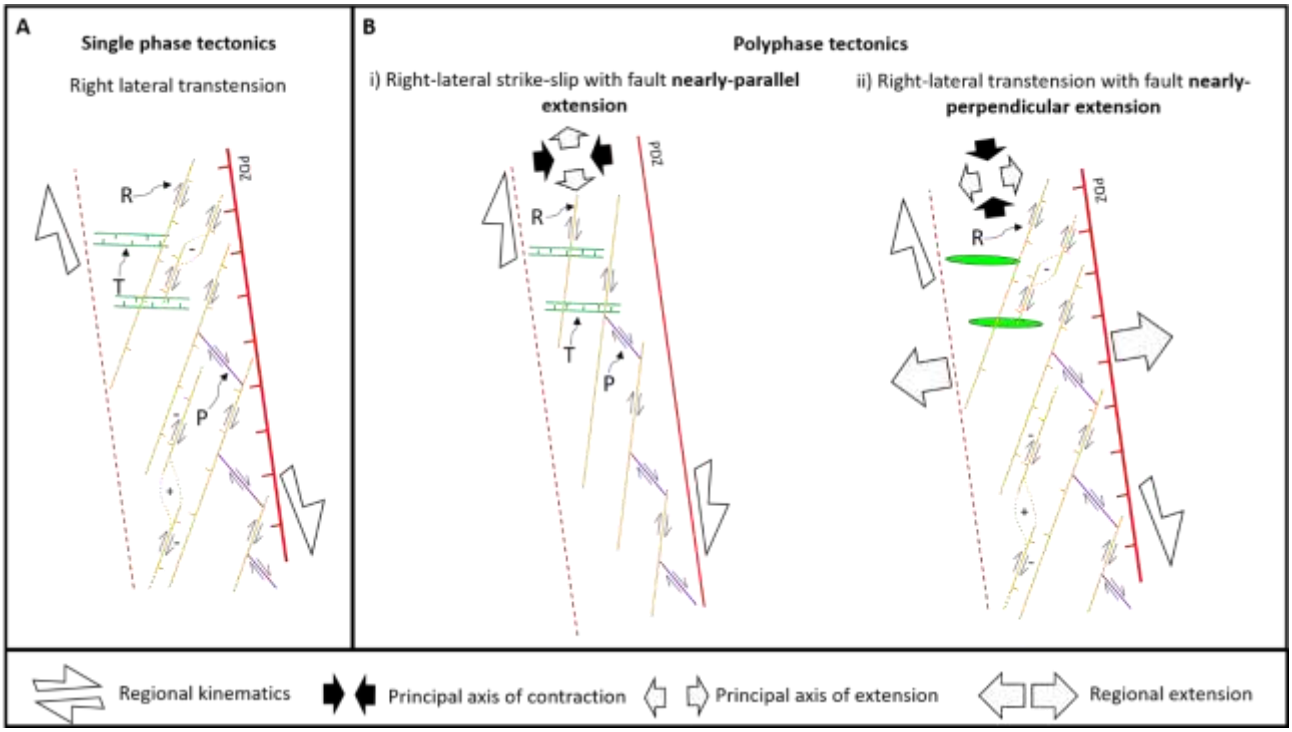

Figure 3.10 - Two proposed tectonic scenarios for the formation of the CF. **A)** Scenario 1: Single tectonic event characterised by right-lateral transtension. R (Set 2), T (Set 3), and P (Set 4) formed coeval to the PDZ (Set 1). **B)** Scenario 2: Polyphase tectonics characterised by i) Noachian-Early Hesperian right-lateral strike-slip tectonics with fault-parallel extension (R, T and P formed); ii) Late Hesperian/Early Amazonian-? transtensional reactivation of the CFF with a significative extensional component that led to the formation of the listric fault and the variation of the angular relationships between sets. During this phase, R were reactivated with transtensional kinematics.

In this way, the development of the four sets can be constrained before the onset of the late Hesperian age. However, the ESc clearly cut and offset lHv in the central and northern sectors of the CF constraining the development of the modelled listric fault after Late Hesperian/Early Amazonian. Therefore, the proposed polyphase evolution (Scenario 2) represents the most reliable scenario. In particular, presented evidence suggests that the first event of strike-slip deformation likely occurred in the Noachian and continued until the Early Hesperian. This is in accordance with the estimations on the beginning of the deformation within the CF (e.g. Dohm & Tanaka, 1999; Dohm et al., 2001). The second, transtensional event then started after Late Hesperian/Early Amazonian yielding the development of the crustal, listric normal fault and thus the half-graben morphology. This second event is accordance with the formation mechanisms proposed by Hauber and Kronberg (2005) for TG and with the timing proposed in the literature (Tanaka & Davis, 1988; Tanaka et al., 1991; Dohm et al., 2001; Hauber & Kronberg, 2005; Montgomery et al., 2009; Smith et al., 2009; Pieterek et al., 2024). In addition to these considerations on the timing of the deformations, it must be considered that the CFF likely formed at a relatively shallow crustal depth under Andersonian stress conditions (e.g. one principal component of the stress acting vertical/perpendicular to the planetary surface). In

this way, the formation of an oblique-slip fault in a single transtensional tectonic event is unlikely. This adds to the insight derived from the timing of the deformation further favouring the poly-phased tectonic evolutionary model.

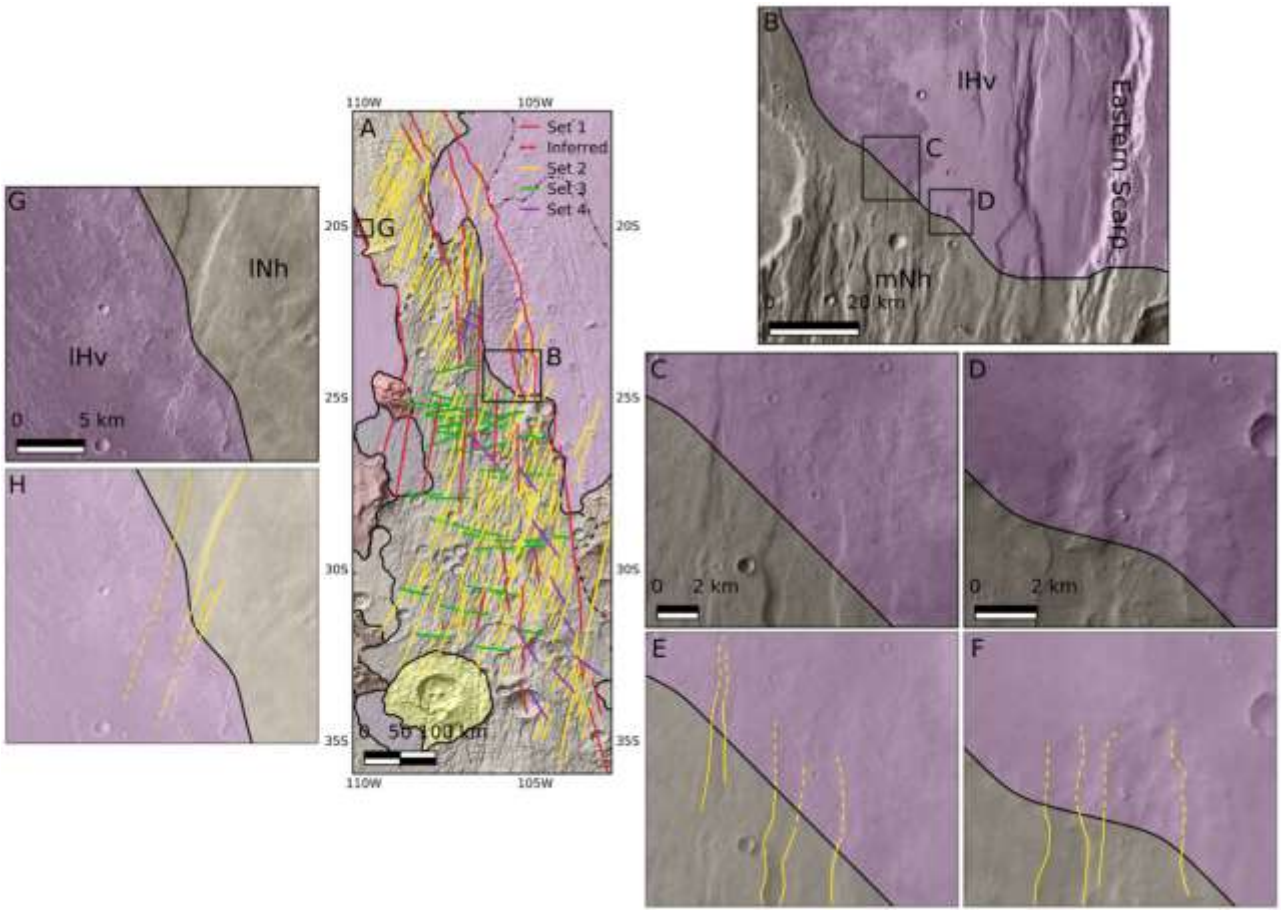

Figure 3.11 - A) the four identified sets with the geologic map from Tanaka et al., 2014. Structures belonging to the sets develops in Noachian terrains and are overlapped by the late Hesperian lavas. **B)** the Eastern Scarp cuts and offsets both Noachian and late Hesperian terrains suggesting its formation after the emplacement of lHv.

To conclude, it is important to note that the presented geotectonic setting for the CF strongly resembles the spatial distribution of deformation that develops on the Earth in extensional/transtensional tectonic regimes and strike-slip deformation belts (e.g. Storti et al., 2003; Hauber & Kronberg, 2005). For instance, the East African Rift system (EAR – Figure 3.12) shares significant similarities with the CF both in map view and regional topography. Similarly to the CF, the half-graben architecture of the EAR and the development of structures associated with the main shear zone have been interpreted by authors as the result of the contribution of extensional and dextral strike-slip kinematics (Atmaoui & Hollnack, 2003; Chorowicz, 2005; Komolafe et al., 2012).

To conclude, the proposed polyphase tectonic model agrees with previous studies and provide a more complete kinematic history of the CF in the frame of the tectonic evolution related to Tharsis. In particular, the approach here presented highlights a regional strike-slip component that adds to

the regional extension. The first identified event is in line with the peak of the Tharsis related tectonic deformation whose activity has been dated to late Noachian-Early Hesperian (Anderson et al., 2001; Bouley et al., 2018). The second, younger transtensional reactivation agrees with the Late Hesperian to Early Amazonian peak of extensional strain highlighted in literature (Bouley et al., 2018; Andrews-Hanna & Broquet, 2023). The used kinematic tectonic modelling does not allow favouring/supporting isostatic compensation model or flexural elastic deformation associated to the Tharsis induced stress. Nevertheless, results supply constraints for future geodynamic modelling of steady-state mantle evolution or first-order mantle circulation (mantle plume/upwelling) accounting for the planetary cooling.

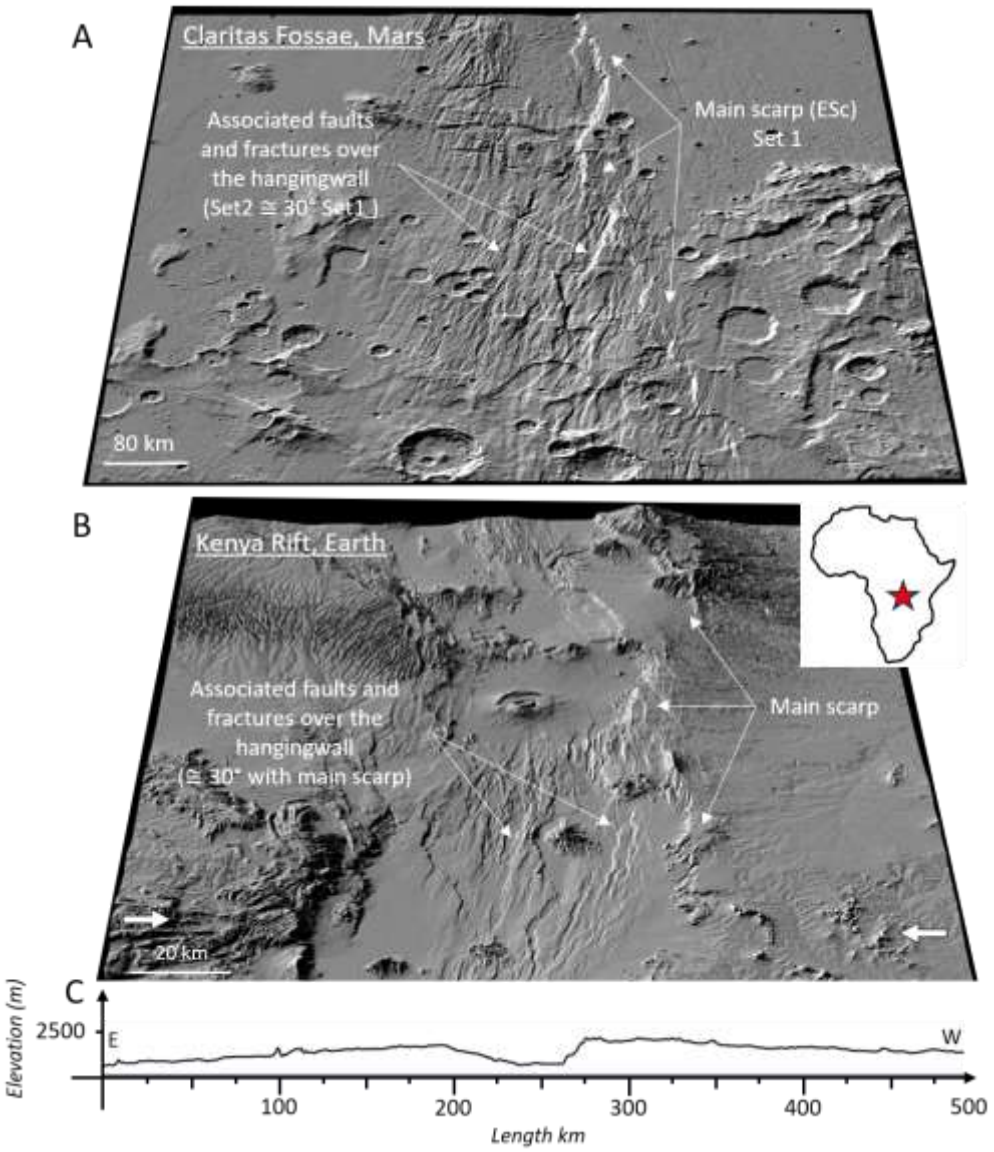

Figure 3.12 - Topographic 3D perspective view (north oriented) of the CF **(A)** and of the Kenya Rift **(B)** showing their morphological similarities (30x vertical exaggeration). The topographic profile across the Kenya Rift **(C)** shows the half-graben morphology resulting from the activity of the listric faults of the rift. Note the striking similarity with the topographic profiles across the CF shown in Figure 3.4 and used for the modelling.

3.5 Conclusions

The twofold approach presented in this Chapter combining kinematic numerical modelling and structural mapping allowed addressing a series of issues concerning the geotectonic evolution of the CF. In particular, this approach highlighted that the deformation corridor of the CFF is the result of the contribution of both strike-slip and normal-dip-slip tectonics. Results are in overall agreement with previous studies but confirms and provides a more complete kinematic history of the CF. Moreover, results provide constraints for geodynamic modelling of planetary cooling through different models of mantle dynamics (e.g. steady-state, first order circulation). A polyphase tectonic scenario with two events of deformation is here proposed. The first right-lateral strike-slip event started in the Noachian age with kinematics characterised by fault-parallel extension and ended in the Early Hesperian. The second event started between Late Hesperian and Early Amazonian and involved the reactivation of the CFF in dextral transtensional regime characterised by a fault-perpendicular extension. In this way, regional-scale structural mapping allowed the identification of the right-lateral strike-slip deformation. During this second event, a crustal scaled, listric normal fault developed leading to the formation of the present regional half-graben morphology. In this way, the spatial distribution and angular relations among the four identified sets of faults indicated different orientations of the stress field within the CFF over time. On the other hand, kinematic numerical modelling was effective in reproducing the listric and synthetic faults responsible for the formation of the half-graben morphology. This provided important constraints about the thick-crust architecture beneath this region. Moreover, the initial dip derived from our modelling (47°-51°) is lower than the value generally used for strain estimations (60°) suggesting that extensional strain on Mars could have been underestimated. Specifically, our results suggest an underestimation between 40% and 60% at the CF. Future strain investigations could combine the here presented double approach with morphometric analyses of the topography to better constrain normal fault dips and their possible local and regional variations.

The presented approach proved to be an effective tool to unravel the geo-tectonic evolution of tectonically controlled areas on planetary surfaces. Moreover, if coupled with modelling of geophysical data, it can provide vital insights on volcano-tectonic deformations both on Mars and other planetary surfaces.

Chapter 4

Application of Hierarchical-Agglomerative Clustering analysis to geo-tectonic investigations

The methodological approach and data presented in this chapter are included in a paper submitted to *Icarus* Journal and entitled *Balbi E., Cianfarra P., Crispini L., Tosi S., and Ferretti G. - Application of Hierarchical-Agglomerative Clustering Analysis to the Geo -Tectonic Investigation of the Claritas Fossae on Mars*. The methodological approach and preliminary results here presented were also part of conference proceedings to international congress: *Balbi E., Cianfarra P., Tosi S., Crispini L. & Ferretti G. - Clustering analysis to unravel polyphase tectonics settings on planetary surfaces: the case of the Claritas Fossae, Mars. SIMP, SGI, SOGEI, AIV Joint Congress, Potenza, Italy, 18-22 Sept 2023.*

4.1 Introduction

The identification and categorisation of different types of tectonic lineaments (e.g. faults, fractures, thrust, graben, semigraben, escarpments) represents a highly informative approach to unravel the deformation of tectonically controlled regions on the Earth (Ouillon et al., 1996; Mazzarini & D'Orazio, 2003; Mazzarini et al., 2007; Mazzarini & Isola, 2010; Cianfarra & Salvini, 2014; Fransceschini et al., 2020; Mazzarini & Isola, 2021, 2022; Ceccato et al., 2022; de Arruda Passos et al. 2022) and on other planetary surfaces (Wise et al., 1979; Anguita et al., 2001; Plescia, 2003; Rossi et al., 2018; Anderson et al., 2019; Rossi et al., 2020; Lucchetti et al., 2021; Perrin et al., 2022; Man et al., 2023). Classification and clustering methods are the most used approaches in Earth Science to objectively categorise geological features (more in general referred to as objects) with similar characteristics (Ansari et al., 2009; Paasche & Eberle, 2009; Yang et al., 2019; Aghaee et al., 2021; Faraj Ortiz, 2021). Classification methods group objects in predefined target classes. Clustering methods sort objects in a number of groups such that each group includes the most similar objects and is homogeneous and distinct from the others according to specific attributes (Kaufman & Rousseeuw, 1990; Arabie et al., 1996; Mirki, 2013; Schwenker & Trentin, 2014). In this way, clustering methods represent a powerful tool for finding groups in data in a systematic way (Kaufman & Rousseeuw, 1990). They are conventionally categorised in partitioning, hierarchical, arbitrary origin, and mutual similarity methods based on the adopted cluster model (Sneath & Sokal, 1973; Gordon, 1999). Among them, hierarchical methods are increasingly being used in multivariate data analysis in

many fields (e.g. artificial intelligence, ecology, economics, geosciences, marketing, medical research, political science) including tectonic investigations (Mazzarini, 2004; Davey et al., 2013; Šilhavý et al., 2016; Takahashi et al., 2019; Prabhakaran et al. 2021; Kaas et al., 2023). This approach deals with all possible clusters in a single run, and it is able to reproduce the hierarchical structure of data, classify multivariate populations and identify groups or clusters (Mojena, 1977). Hierarchical methods operate by initially grouping the most similar objects into clusters. Then, new clusters are created by connecting the next most similar object(s). The resulting progressive similarity levels at which objects are merged is represented by a dendrogram. Hierarchical methods include two main techniques: agglomerative and divisive. Agglomerative Hierarchical techniques start with each object as a separate cluster (i.e. n objects = n clusters) and progressively merge clusters until all objects are included in a single cluster. Conversely, Divisive Hierarchical techniques start with the entire population of n objects merged into a single cluster that is subsequently split until n clusters remain.

In this chapter, an Agglomerative Hierarchical Clustering workflow is proposed to the geo-tectonic investigation of the CF. The primary aim is to develop an analytical and statistical clustering workflow that provides objective insights into the geo-tectonic evolution of complex, tectonically controlled regions on planetary surfaces. In particular, the presented clustering procedure calculates the dissimilarity among tectonic lineaments based on a series of attributes with geological relevance (azimuthal direction, length, and position). The analysed database includes the 251 tectonic lineaments presented in Chapter 3, identified in the area of the CF through classical regional-scale structural mapping and interpreted as morphotectonic structures subdivided in four azimuthal set. The subdivision of clusters obtained though the developed clustering workflow is consistent with the tectonic polyphasic model presented in Chapter 3 that is characterized by strain partitioning and shear fracture orientation within a right-lateral strike-slip deformation corridor (Storti et al., 2006; Balbi et al., 2024).

4.2 Materials and Methods

The structural dataset including the 251 tectonic lineaments identified in the CF region represents a valuable testing dataset to evaluate the efficacy of the developed clustering workflow in geo-tectonic investigations. This dataset includes a limited number of objects (but enough for statistical validity) identified with classical, validated methodological approach. Moreover, the distribution in four sets identified through the geostatistical analysis of the azimuth of the tectonic lineaments represents a

key distribution to be replicated to validate the proposed workflow. Refer to Chapter 3, Section 3.2.2 for details regarding the structural mapping and the dataset, and Section 3.3.2 for the results of structural mapping and geostatistical analysis.

4.2.1 Clustering analysis workflow

The workflow presented in this chapter is based on an Agglomerative Hierarchical Clustering method. The clustering procedure is conducted by computing the dissimilarity (or distance as explained later) between i) objects as a function of their attributes (or characteristics), thus obtaining a dissimilarity matrix, and ii) clusters as a function of the pairwise dissimilarities of the objects. In this way, the general scheme of the agglomerative clustering procedure consists of an initial step with n single clusters which represent the n input objects. Then, the dissimilarity among all objects/clusters is computed to iteratively join them in pairs on the basis of the minimal dissimilarity value. This step ends when a single cluster including all the original input objects remains. The stagewise clustering is graphically represented by the dendrogram in Figure 4.1 that shows the distribution of the clusters iteratively produced through the adopted method on the used dataset. Clusters pass from 251 at the base of the dendrogram (i.e. n objects = n clusters) to 1 single cluster which includes the entire dataset on the top. In the case of the application here presented, azimuthal direction, length, and centroid position are used as attributes to calculate the dissimilarity between the tectonic lineaments and thus to cluster them. The three attributes are calculated as follow: i) *azimuthal direction* is the angle (0°-180°) between the north and the fictitious linear feature connecting the extremes of the mapped structure; ii) *length* is the curvilinear length of the mapped structure; iii) *position* is the Euclidean distance between the centroid (defined by latitude and longitude) of the mapped structure and the planetocentric coordinate system's origin (latitude 0° and longitude 0°) defined in Duxbury et al. (2002).

Different algorithms to calculate the dissimilarity between objects exist. The most used are "Euclidean", "Maximum", "Manhattan", "Canberra", "Binary", "Gower", and "Minkowski" (for details see Kaufman & Rousseeuw, 1990). These functions calculate the dissimilarity in different ways. For instance, Euclidean calculates the dissimilarity between objects as the root sum-of-squares of differences, Manhattan sums the absolute values of differences, and Gower, used in this application, calculates the dissimilarity through the general dissimilarity coefficient (Gower, 1971). Similarly, different criterion to calculate the dissimilarity between two clusters exist. These are: "the single linkage": the dissimilarity is the closest distance between any two points in each cluster; "the

complete linkage": the dissimilarity is the maximal distance between any two points in each cluster; "the average linkage": the dissimilarity is the average distance between the points in the two clusters; and "the centroid linkage": the dissimilarity is the distance between the centroids (or the barycenters) of the clusters in Euclidean space (Müllner, 2013).

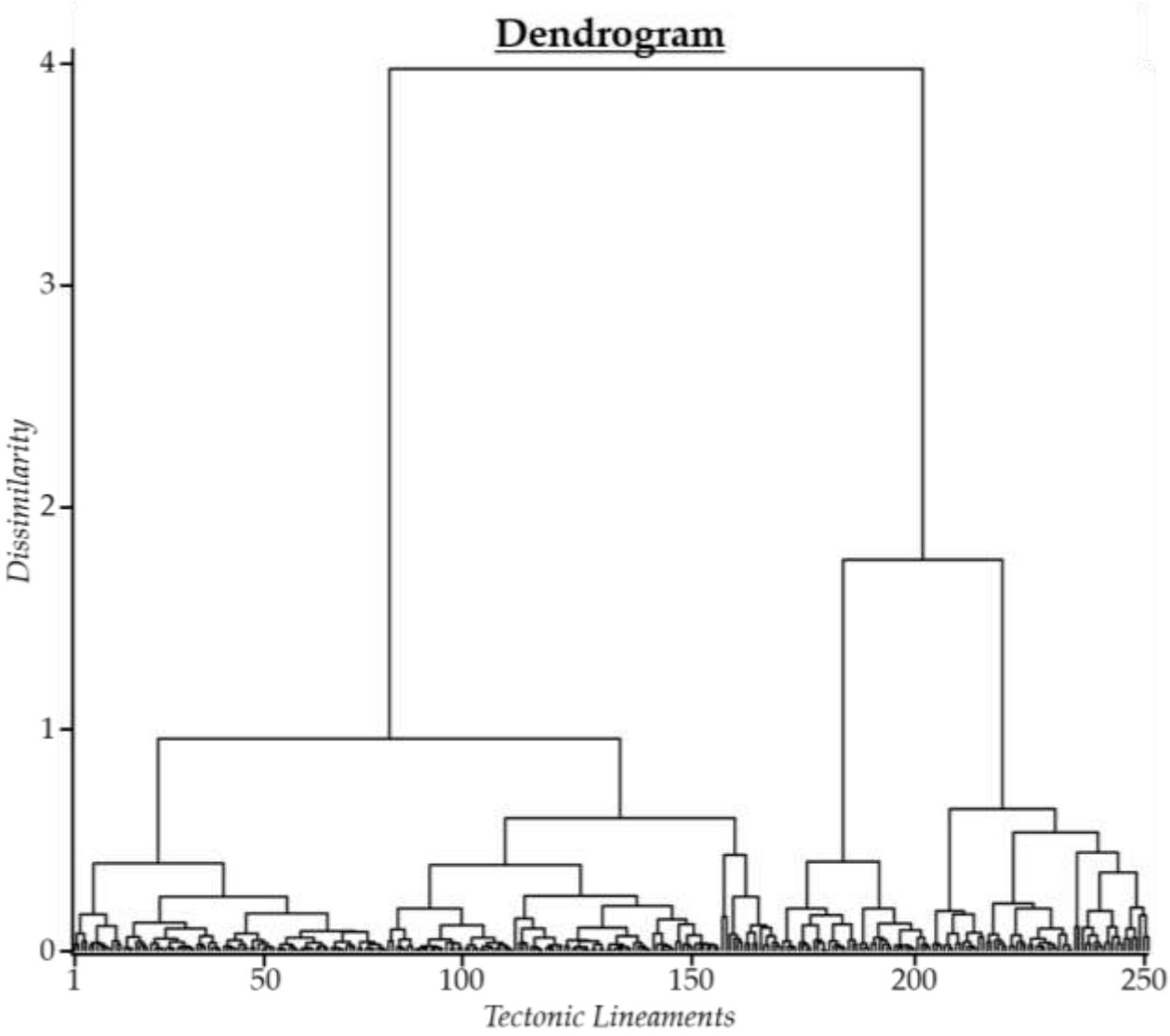

Figure 4.1 - The dendrogram shows the clustering path for the analysed tectonic lineaments. X-axis indicates the number of objects (251). Y-axis indicates the dissimilarity at which two single objects, or two clusters are merged in a new cluster.

The clustering procedure used in this chapter utilises the *"daisy"* function from the R package *"cluster"* (Struyf et al., 1997) and the *"hclust"* function from the R package *"fastcluster"* (Müllner, 2013). The *"daisy"* function computes the dissimilarity matrix by employing the *"Gower"* function and assigning a specific weight to each attribute of lineaments in the dataset. Hierarchical clustering is executed using the *"hclust"* function which employs the *"Ward.D2"* agglomeration method (Murtagh & Legendre, 2014) based on Ward's (1963) clustering criterion.

The last step of the presented workflow consists of the stopping rule necessary to select the "best" number of clusters based on the clustering criterion distribution associated with each hierarchical level. This work, following Rousseeuw (1987) and Kaufman & Rousseeuw (1990), guides the choice of the "best" number of clusters through the computation of silhouette width *(s)*. For each object i in cluster A, $s(i)$ is defined as follows:

$$s(i) = \frac{b(i)-a(i)}{max\{a(i),b(i)\}} \quad \text{(Eq. 3)}$$

where:

$a(i)$ is the average dissimilarity of i to all other objects of A

and:

$$b(i) = \min_{C \neq A} d(i, C) \quad \text{(Eq. 4)}$$

where for any cluster C distinct from A, $d(i, C)$ denotes the average dissimilarity between object i and its neighbouring objects in C.

The average silhouette width of a cluster is derived from the mean of the silhouette values, $s(i)$, for all objects i within a cluster. An $s(i) \cong 1$ suggests that the objects are well-clustered, whereas $s(i) \cong 0$ indicates that objects are positioned between two clusters. A negative $s(i)$ implies that the objects likely be placed in the wrong cluster. The average silhouette width for the entire dataset, denoted as $\bar{s}(k)$, is calculated by averaging the $s(i)$ values for all objects $i = 1, 2, \dots, n$, where n represents the total number of objects in the dataset. $\bar{s}(k)$ can be used to estimate the "best" number of clusters, k. From a mathematical point of view, the "best" number of cluster can be defined by the value of k for which $\bar{s}(k)$ is as high as possible. In particular, $1 > \bar{s} > 0.71$ indicates strong (robust) structure, $0.70 > \bar{s} > 0.51$ reasonable structure, $0.50 > \bar{s} > 0.26$ weak structure, and $0.25 > \bar{s} > 0$ no substantial structure (Kaufman and Rousseeuw, 1990). Note that the choice of k is one of the most challenging aspects of cluster analysis, for which no unique solution exists.

In summary, the general outline of the clustering workflow proposed in this study is as follows:

a) *Input data preparation*: Clustering is applied to the 251 tectonic lineaments identified in the CF through structural mapping (Chapter 3). Attributes associated with each structure and used for clustering analysis are azimuth, length, and centroid position. The input data are

displayed as a matrix with dimension $n \times p$, where n is the number of observations (i.e. 251) and p is the number of attributes (i.e. 3).

b) *Scaling observations*: Each attribute of the observations is corrected by subtracting the mean and dividing by the standard deviation of the entire vector.

c) *Dissimilarity matrix calculation*: The computation of all pairwise dissimilarities between observations in the dataset is performed in R environment using the *"daisy"* function, selecting metric *"Gower"*. The weight for each attribute is specified by a vector of length p (the number of attributes used in the clustering).

d) *Hierarchical clustering*: Clustering is implemented using the *"hclust"* function with the agglomeration method *"Ward.D2"*. In this step, different values of k (the number of clusters) are considered as a stopping rule.

e) *Validation of consistency within clusters of data*: The *"silhouette"* technique (Rousseeuw, 1987) is used to examine the clustering configuration. For each value of k the average silhouette width $\bar{s}$ is computed and the "best" number of clusters is chosen.

4.3 Results

Numerous tests were conducted on the 251 tectonic lineaments using azimuth, length, and position as attributes. Among these, four are presented as representative of the tests carried out to verify the performance of the proposed clustering workflow. Three consider a different combination of the attributes, each assigning a weight of 1 to the considered attributes: 1) *azimuth* only; 2) *azimuth and length*; and 3) *azimuth, length and position*. The fourth test evaluates the three attributes together (as the third test) by assigning double weight to azimuth compared to length and position.

For each of the four tests, results obtained considering a range of clusters k from 3 to 6 (k being the stopping rule in the hierarchical clustering workflow) are presented. Clusters formed with $k > 6$ are overly fragmented and demonstrate significantly very low $\bar{s}(k)$ (< 0.25) thus with no substantial structure, following Kaufman & Rousseeuw (1990). Therefore, 16 outputs from the clustering workflow are presented below without considering the geologic implications that will be explored in the Discussion Section of this Chapter (Section 4.4). In the text, clusters are denoted as follows: *Cluster2-Azimuth+Length-k4*. Here, the first suffix refers to the name of the cluster (Cluster2 in this

example), second to the attribute(s) considered (azimuth and length), and third to the number of clusters (k value) selected for that specific test (4).

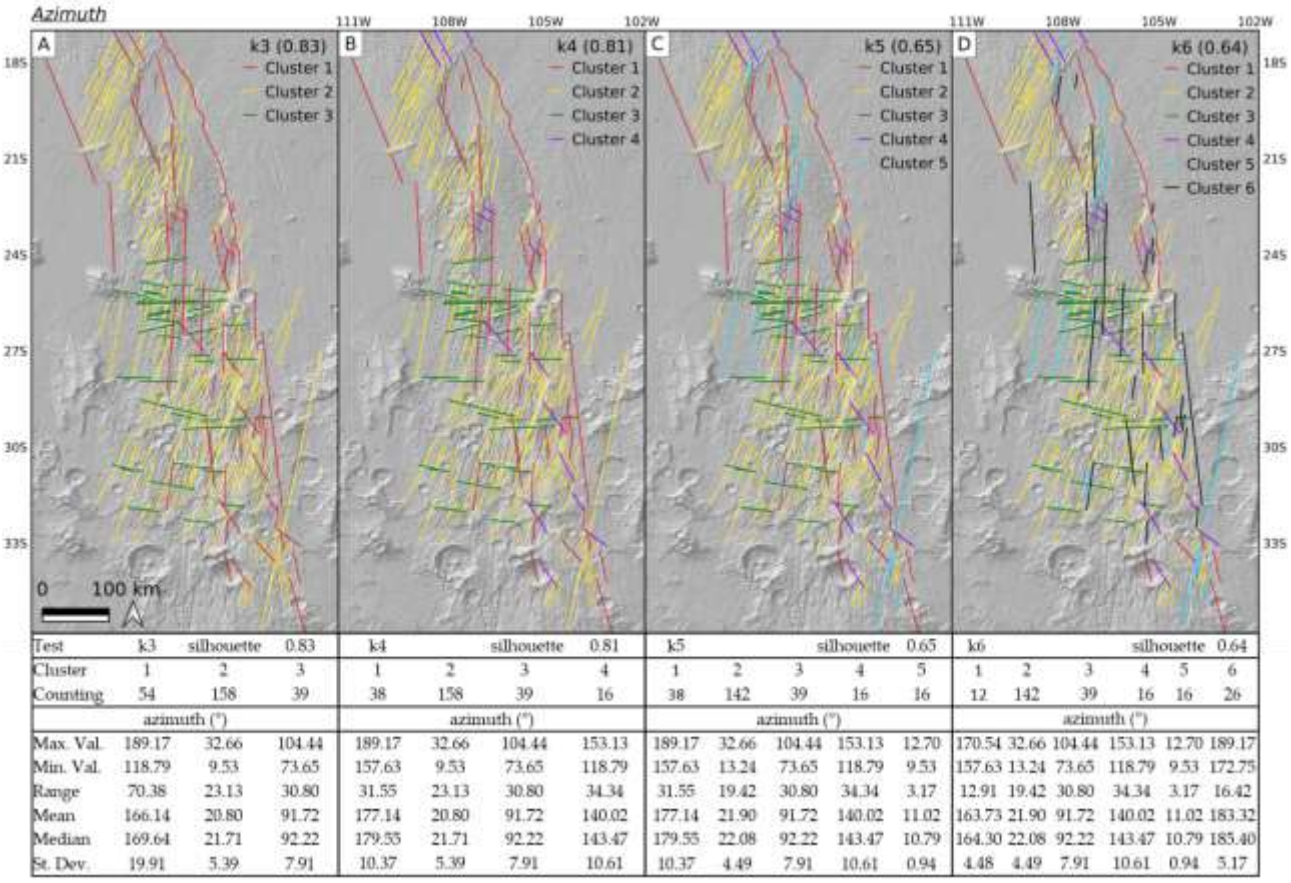

Test	k3	silhouette	0.83	k4		silhouette	0.81	k5		silhouette	0.65	k6		silhouette	0.64
Cluster	1	2	3	1	2	3	4	1	2	3	4	5	1	2	3	4	5	6
Counting	54	158	39	38	158	39	16	38	142	39	16	16	12	142	39	16	16	26
	azimuth (°)			azimuth (°)				azimuth (°)					azimuth (°)					
Max. Val.	189.17	32.66	104.44	189.17	32.66	104.44	153.13	189.17	32.66	104.44	153.13	12.70	170.54	32.66	104.44	153.13	12.70	189.17
Min. Val.	118.79	9.53	73.65	157.63	9.53	73.65	118.79	157.63	13.24	73.65	118.79	9.53	157.63	13.24	73.65	118.79	9.53	172.75
Range	70.38	23.13	30.80	31.55	23.13	30.80	34.34	31.55	19.42	30.80	34.34	3.17	12.91	19.42	30.80	34.34	3.17	16.42
Mean	166.14	20.80	91.72	177.14	20.80	91.72	140.02	177.14	21.90	91.72	140.02	11.02	163.73	21.90	91.72	140.02	11.02	183.32
Median	169.64	21.71	92.22	179.55	21.71	92.22	143.47	179.55	22.08	92.22	143.47	10.79	164.30	22.08	92.22	143.47	10.79	185.40
St. Dev.	19.91	5.39	7.91	10.37	5.39	7.91	10.61	10.37	4.49	7.91	10.61	0.94	4.48	4.49	7.91	10.61	0.94	5.17

Figure 4.2 - Results considering only the azimuth as attribute. A) k3: three clusters, average silhouette width for the entire dataset ($\bar{s}$): 0.83; B) k4: 4 clusters, $\bar{s}$: 0.81; C) k5: 5 clusters, $\bar{s}$: 0.65; D) k6: 6 clusters, $\bar{s}$: 0.64. In the tables below statistical parameters for each cluster are shown.

Figure 4.2 reveals the clustering results using azimuth as the sole attribute and varying k values (i.e. $k = 3, 4, 5, 6$). Notably, the average silhouette widths $\bar{s}$ of the resulting groups of clusters consistently exceeds 0.5 for all k. Thus, following Kaufman & Rousseeuw (1990), from a statistical point of view *Azimuth-k3* and *-k4* tests are characterised by a strong/robust structure $1 > \bar{s} > 0.71$ and *Azimuth-k5* and *-k6* by a reasonable structure $0.70 > \bar{s} > 0.51$. *Azimuth-k3* test (Figure 4.2A) identifies 3 clusters that include 54, 158 and 39 tectonic lineaments each characterised by average azimuth of 166°, 21° and 92°, respectively. Setting $k = 4$ (*Azimuth-k4 test*, Figure 4.2B), clusters 2 (yellow) and 3 (green) remain unchanged compared to *-k3* test. On the other hand, *Cluster1-Azimuth-k3* (red) divides in *Cluster1-Azimuth-k4* (red) and *Cluster4-Azimuth-k4* (purple). These newly formed clusters contain 38 and 16 tectonic lineaments with average azimuths of 177° and 140°, respectively. In *Azimuth-k5* test ($k = 5$, Figure 4.2C), *Cluster2-Azimuth-k5* (yellow, comprising 142 tectonic lineaments with average azimuth of 22°) and *Cluster5-Azimuth-k5* (cyan, comprising 16 lineaments with average azimuth of

11°) represent two subsets of *Cluster2-Azimuth-k4*. With $k = 6$ (Figure 4.2D), *Cluster1-Azimuth-k5* (red) is subdivided in *Cluster1-Azimuth-k6* (red) and *Cluster6-Azimuth-k6* (black), characterised by 12 and 26 lineaments and mean azimuths of 164° and 183°.

In general, the tests carried out by considering azimuth as the sole attribute reveal that, by increasing k, the proposed workflow is able to identify subsets of tectonic lineaments with progressively lower values of standard deviation (*sd*) and range of the azimuth. This testify a grouping process that becomes more selective and accurate by the statistical point of view always maintaining a reasonable structure of the clusters ($\bar{s} > 0.5$). Cluster 3 is the only cluster that remains unchanged in the four tests, likely due to its mean azimuth strongly different compared to the other clusters.

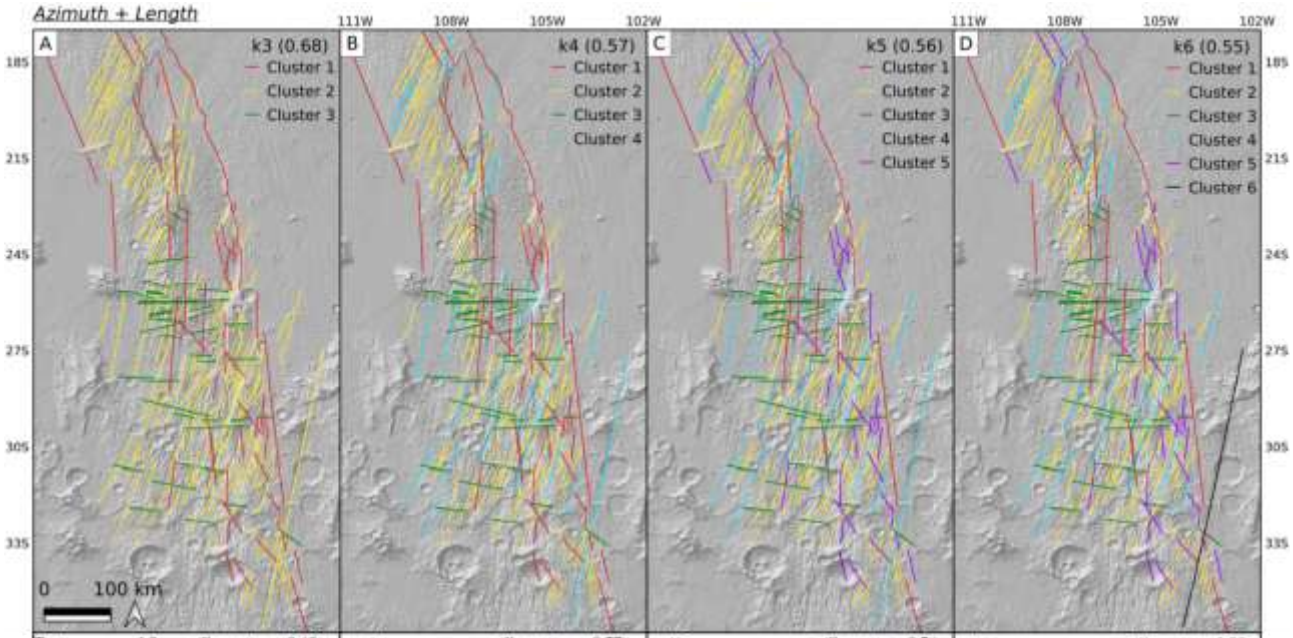

Test	k3	silhouette	0.68	k4		silhouette	0.57	k5			silhouette	0.56	k6				silhouette	0.55
Cluster	1	2	3	1	2	3	4	1	2	3	4	5	1	2	3	4	5	6
Counting	50	158	43	50	133	43	25	14	133	43	25	36	14	133	43	24	36	1
	azimuth (°)			azimuth (°)				azimuth (°)					azimuth (°)					
Max. Val.	189.17	32.66	126.95	189.17	32.66	126.95	27.84	185.42	32.66	126.95	27.84	189.17	185.42	32.66	126.95	27.84	189.17	*12.17*
Min. Val.	137.78	9.53	73.65	137.78	10.40	73.65	9.53	157.63	10.40	73.65	9.53	137.78	157.63	10.40	73.65	9.53	137.78	*12.17*
Range	51.39	23.13	53.30	51.39	22.26	53.30	18.31	27.80	22.26	53.30	18.31	51.39	27.80	22.26	53.30	18.31	51.39	*0.00*
Mean	169.56	20.80	94.67	169.56	21.32	94.67	18.06	172.42	21.32	94.67	18.06	168.44	172.42	21.32	94.67	18.30	168.44	*12.17*
Median	173.12	21.71	94.49	173.12	21.80	94.49	19.80	175.22	21.80	94.49	19.80	169.64	175.22	21.80	94.49	19.89	169.64	*12.17*
St. Dev.	16.42	5.39	11.94	16.42	5.17	11.94	5.66	8.93	5.17	11.94	5.66	18.41	8.93	5.17	11.94	5.65	18.41	*0.00*
	length (km)			length (km)				length (km)					length (km)					
Max. Val.	474.43	518.18	155.81	474.43	80.11	155.81	518.18	474.43	80.11	155.81	518.18	103.30	474.43	80.11	155.81	178.99	103.30	*518.175*
Min. Val.	16.63	16.85	20.02	16.63	16.85	20.02	72.02	112.78	16.85	20.02	72.02	16.63	112.78	16.85	20.02	72.02	16.63	*518.175*
Range	457.80	501.33	135.79	457.80	63.26	135.79	446.16	361.65	63.26	135.79	446.16	86.67	361.65	63.26	135.79	106.98	86.67	*0*
Mean	90.95	59.30	46.69	90.95	46.49	46.69	127.46	189.64	46.49	46.69	127.46	52.58	189.64	46.49	46.69	111.18	52.58	*518.175*
Median	59.48	50.48	37.65	59.48	47.98	37.65	105.88	152.50	47.98	37.65	105.88	52.61	152.50	47.98	37.65	105.65	52.61	*518.175*
St. Dev.	82.04	46.57	27.33	82.04	14.52	27.33	84.06	96.69	14.52	27.33	84.06	21.26	96.69	14.52	27.33	27.09	21.26	*0*

Figure 4.3 - Results considering azimuth and length as attributes. A) k3: 3 clusters, average silhouette width for the entire dataset ($\bar{s}$): 0.68; B) k4: 4 clusters, $\bar{s}$: 0.57; C) k5: 5 clusters, $\bar{s}$: 0.56; D) k6: 6 clusters, $\bar{s}$: 0.55. In the tables below show the statistical parameters for each cluster for both azimuth and length are shown. *Cluster6-k6* includes an insufficient number of lineament for reliable statistical analysis of the attributes.

Figure 4.3 illustrates the results of the clustering workflow using azimuth and length as attributes. Such as in Azimuth tests, the average silhouette width $\bar{s}$ of the resulting groups of clusters consistently exceeds 0.5. Specifically, $\bar{s}$ is between 0.51 and 0.70 thus indicating reasonable structure for all k (Kaufman & Rousseeuw, 1990). Clustering obtained considering *Azimut+Length-k3* (Figure 4.3A) are mostly the same of *Azimuth-k3* test (Figure 4.2A) with minor differences in the number of tectonic lineaments included in clusters 1 (50) and 3 (43). Accordingly, marginal variation in the statistical parameters of the azimuth for both clusters of *Azimut+Length-k3* exist. The mean lengths of the three clusters is 91 km, 59 km, and 47 km, respectively, but they exhibit a substantial range between the longest and shortest lineaments, along with considerable *sd* that is almost comparable with the mean. Such as in the Azimuth test, both range and *sd* decrease with an increasing k. Differently, considering *Azimut+Length-k4 test* (Figure 4.3B), Cluster 1 remain unchanged whereas *Cluster2-Azimuth+Length-k4* (yellow) and *Cluster4-Azimuth+Length-k4* (cyan) derive from *Cluster2-Azimuth+Length-k3* (yellow). These new clusters differ in mean azimuth by a value smaller than their *sd* (mean azimuth: 21° and 18°; *sd*: 5° and 6°) but include tectonic lineaments characterised by significantly different mean lengths: 46 km (*sd*: 15 km) for *Cluster2-Azimuth+Length-k4* and 127 km (*sd*: 84 km) for *Cluster4-Azimuth+Length-k4*. Particularly, it can be observed that *Cluster2-Azimuth+Length-k4* has been "cleaned" of the longest structures. This has led to a significant reduction of the *sd* compared to *Cluster2-Azimuth+Length-k3* (more than one third, 15 km Vs 47 km) despite a relative smaller reduction of the values of mean length (59 km Vs 47 km). Considering $k = 5$ (Figure 4.3C), *Cluster1-Azimuth+Length-k5* (red) and *Cluster5-Azimuth+Length-k4* (purple) represent two subsets of *Cluster1-Azimuth+Length-k4*. In particular, *Cluster5-Azimuth+Length-k4* (purple) counts 36 tectonic lineaments with mean azimuth of 168° and mean length of 53 km somewhat resembling Cluster 4 *in Azimuth-k4*, *k5* and *k6* (Figure 4.2B-D). Figure 4.3D shows the clustering obtained with $k = 6$, *Azimuth+Length-k6* test. New *Cluster6-Azimuth+Length-k6* (black) includes a single lineament, specifically the longest lineaments of the dataset.

Results obtained considering Azimuth and Length as attributes are in general agreement with results of the Azimuth tests. Both grouping are comparable and share similarities (for instance cluster 3 remain unchanged in both the series of tests). Nevertheless, including length as attributes allowed to further constrain the clustering and highlight new subsets of the mapped tectonic lineaments.

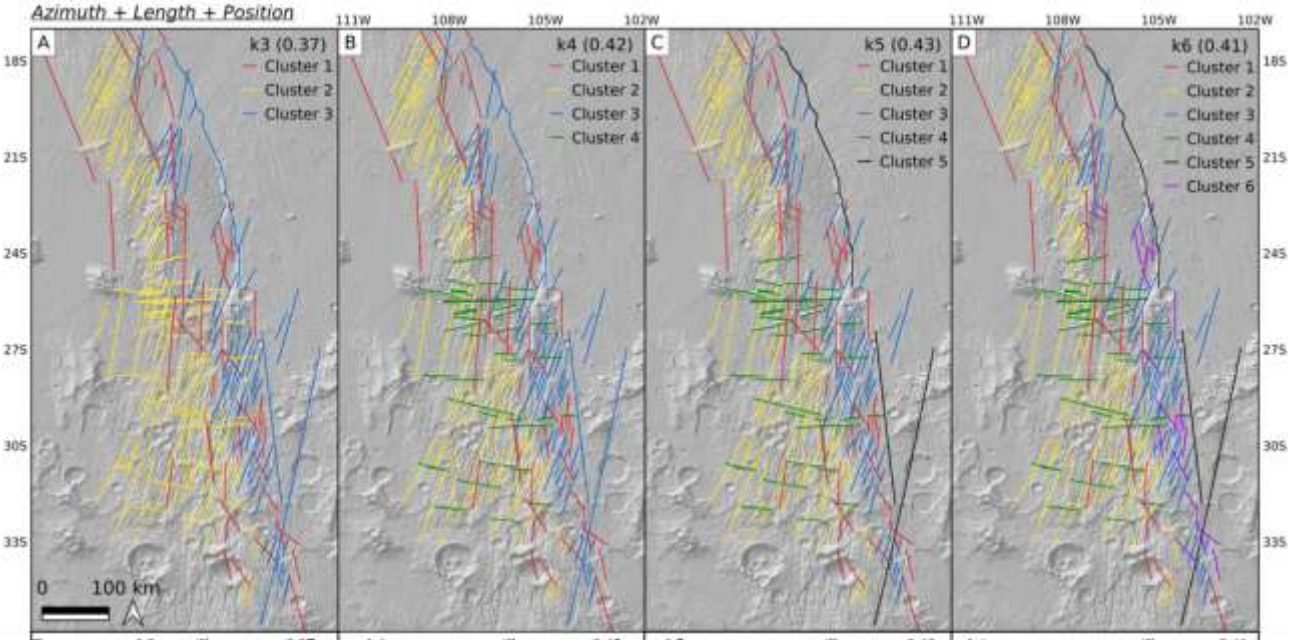

Test	k3	silhouette	0.37	k4		silhouette	0.42	k5			silhouette	0.43	k6				silhouette	0.41
Cluster	1	2	3	1	2	3	4	1	2	3	4	5	1	2	3	4	5	6
Counting	52	135	64	52	96	64	39	52	96	61	39	3	26	96	61	39	3	26
	azimuth (°)			azimuth (°)				azimuth (°)					azimuth (°)					
Max. Val.	189.17	104.44	173.49	189.17	32.66	173.49	104.44	189.17	32.66	28.78	104.44	173.49	189.17	32.66	28.78	104.44	173.49	188.95
Min. Val.	118.79	9.53	9.73	118.79	9.53	9.73	73.65	118.79	9.53	9.73	73.65	12.17	138.89	9.53	9.73	73.65	12.17	118.79
Range	70.38	94.92	163.76	70.38	23.13	163.76	30.80	70.38	23.13	19.05	30.80	161.32	50.28	23.13	19.05	30.80	161.32	70.16
Mean	166.05	42.47	22.92	166.05	22.46	22.92	91.72	166.05	22.46	18.32	91.72	116.32	169.64	22.46	18.32	91.72	116.32	162.47
Median	169.64	25.42	18.83	169.64	22.79	18.83	92.22	169.64	22.79	18.75	92.22	163.29	174.85	22.79	18.75	92.22	163.29	168.17
St. Dev.	20.26	31.96	26.59	20.26	4.99	26.59	7.91	20.26	4.99	4.92	7.91	73.76	15.43	4.99	4.92	7.91	73.76	23.59
	length (km)			length (km)				length (km)					length (km)					
Max. Val.	239.82	165.41	518.18	239.82	165.41	518.18	155.81	239.82	165.41	178.99	104.44	518.18	239.82	165.41	178.99	104.44	518.18	85.23
Min. Val.	16.63	20.02	16.85	16.63	21.55	16.85	20.02	16.63	21.55	16.85	73.65	317.57	23.70	21.55	16.85	73.65	317.57	16.63
Range	223.19	145.39	501.33	223.19	143.85	501.33	135.79	223.19	143.85	162.14	30.80	200.61	216.12	143.85	162.14	30.80	200.61	68.60
Mean	74.73	55.05	71.99	74.73	57.86	71.99	48.14	74.73	57.86	54.05	91.72	436.72	106.35	57.86	54.05	91.72	436.72	43.12
Median	57.48	49.91	47.33	57.48	53.90	47.33	38.14	57.48	53.90	45.30	92.22	474.43	99.95	53.90	45.30	92.22	474.43	38.68
St. Dev.	51.61	26.41	89.30	51.61	25.16	89.30	28.10	51.61	25.16	33.73	7.91	86.13	55.15	25.16	33.73	7.91	0.57	16.90
	position			position				position					position					
Max. Val.	112.21	113.32	109.47	112.21	113.32	109.47	112.90	112.21	113.32	109.47	112.90	108.016	112.21	113.32	109.47	112.90	108.02	109.65
Min. Val.	107.58	108.25	106.74	107.58	109.47	106.74	108.25	107.58	109.47	106.74	108.25	107.893	108.84	109.47	106.74	108.25	107.89	107.58
Range	4.63	5.08	2.73	4.63	3.85	2.73	4.65	4.63	3.85	2.73	4.65	0.124	3.36	3.85	2.73	4.65	0.12	2.07
Mean	109.31	110.60	108.64	109.25	110.71	108.64	110.33	109.25	110.71	108.67	110.33	107.946	109.98	110.71	108.67	110.33	107.95	108.52
Median	109.15	110.51	108.77	109.11	110.53	108.77	110.46	109.11	110.53	108.81	110.46	107.928	109.79	110.53	108.81	110.46	107.93	108.55
St. Dev.	1.06	0.94	0.58	1.03	0.85	0.58	1.10	1.03	0.85	0.57	1.10	0.052	0.88	0.85	0.57	1.10	0.05	0.52

Figure 4.4 - Results considering azimuth, length, and position as attributes. A) k3: three clusters, average silhouette width for the entire dataset ($\bar{s}$): 0.37; B) k4: 4 clusters, $\bar{s}$: 0.42; C) k5: 5 clusters, $\bar{s}$: 0.43; D) k6: 6 clusters, $\bar{s}$: 0.41. In the tables below statistical parameters for each cluster for azimuth, length, and position are shown. Cluster5-k5 and -k6 include an insufficient number of lineaments for reliable statistical analysis of the attributes.

Figures 4.4 and 4.5 show the results obtained considering all the three attributes together (azimuth, length, and centroid position) by setting to 1 the weight of each of them (Figure 4.4) and weighting twice the azimuth with respect to the others (Figure 4.5). With the exception of *2Azimuth+Length+Position-k3* (Figure 4.5A), $\bar{s}$ in these tests is between 0.26 and 0.50 indicating by the statistical point of view a weak structure of the groups of clusters (Kaufman & Rousseeuw, 1990). Among all the presented tests, the clustering obtained with *Azimuth+Length+Position-k3* test (Figure 4.4A) is the only one that does not identify the E-W oriented, green cluster that in this test is identified only for *k4*, *k5*, and *k6*. Nevertheless, the most significant difference among tests in figures

4.4 and 4.5 and the previous ones involves Cluster 2 (yellow) that no longer includes tectonic lineaments with mean azimuth of about 20° and homogenously distributed in the whole study area. *2Azimuth+length+position-k3* (Figure 4.5A) once again is the exception since it is identical to *Azimuth-k3* (Figure 4.2A) and similar to *Azimuth+length-k3* (Figure 4.3A).

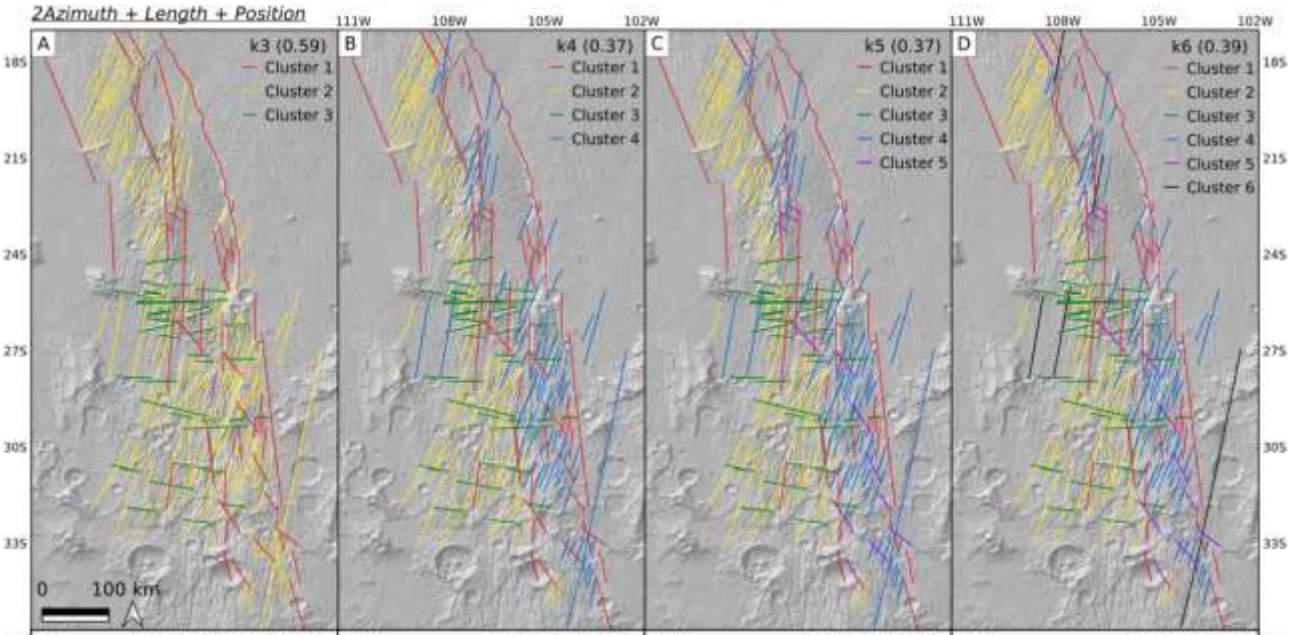

Test	k3	silhouette	0.59	k3		silhouette	0.37	k5			silhouette	0.37	k6				silhouette	0.39
Cluster	1	2	3	1	2	3	4	1	2	3	4	5	1	2	3	4	5	6
Counting	54	158	39	54	80	39	78	40	80	39	78	14	40	80	39	73	14	5
	azimuth (°)				azimuth (°)				azimuth (°)					azimuth (°)				
Max. Val.	189.17	32.66	104.44	189.17	32.66	104.44	28.78	189.17	32.66	104.44	28.78	153.13	189.17	32.66	104.44	28.78	153.13	12.17
Min. Val.	118.79	9.53	73.65	118.79	11.54	73.65	9.53	150.83	11.54	73.65	9.53	118.79	150.83	11.54	73.65	9.73	118.79	9.53
Range	70.38	23.13	30.80	70.38	21.13	30.80	19.25	38.34	21.13	30.80	19.25	34.34	38.34	21.13	30.80	19.05	34.34	2.64
Mean	166.14	20.80	91.72	166.14	22.57	91.72	18.99	175.82	22.57	91.72	18.99	138.47	175.82	22.57	91.72	19.56	138.47	10.64
Median	169.64	21.71	92.22	169.64	22.77	92.22	19.89	178.58	22.77	92.22	19.89	140.93	178.58	22.77	92.22	20.17	140.93	10.46
St. Dev.	19.91	5.39	7.91	19.91	4.96	7.91	5.20	11.62	4.96	7.91	5.20	10.47	11.62	4.96	7.91	4.87	10.47	0.86
	length (km)				length (km)				length (km)					length (km)				
Max. Val.	474.43	518.18	155.81	474.43	133.53	155.81	518.18	474.43	133.53	155.81	518.18	74.15	474.43	133.53	155.81	178.99	74.15	518.18
Min. Val.	16.63	16.85	20.02	16.63	21.55	20.02	16.85	16.63	21.55	20.02	16.85	22.17	16.63	21.55	20.02	16.85	22.17	105.25
Range	457.80	501.33	135.79	457.80	111.98	135.79	501.33	457.80	111.98	135.79	501.33	51.98	457.80	111.98	135.79	162.14	51.98	412.92
Mean	86.63	59.30	48.14	86.63	57.85	48.14	60.79	99.66	57.85	48.14	60.79	49.41	99.66	57.85	48.14	50.37	49.41	213.00
Median	58.54	50.48	38.14	58.54	55.73	38.14	47.33	61.48	55.73	38.14	47.33	50.90	61.48	55.73	38.14	44.76	50.90	149.94
St. Dev.	80.46	46.57	28.10	80.46	20.91	28.10	62.77	89.35	20.91	28.10	62.77	17.07	89.35	20.91	28.10	29.85	17.07	153.96
	position				position				position					position				
Max. Val.	112.21	113.32	112.90	112.21	113.32	112.90	112.05	112.21	113.32	112.90	112.04	110.28	112.21	113.32	112.90	110.01	110.28	112.04
Min. Val.	107.58	106.74	108.25	107.58	109.68	108.25	106.74	107.58	109.67	108.25	106.74	108.02	107.58	109.67	108.25	106.74	108.02	108.02
Range	4.63	6.58	4.65	4.63	3.65	4.65	5.31	4.63	3.65	4.65	5.31	2.26	4.63	3.65	4.65	3.27	2.26	4.03
Mean	109.20	109.91	110.33	109.20	110.86	110.33	108.93	109.19	110.86	110.33	108.93	109.22	109.19	110.86	110.33	108.86	109.22	109.97
Median	109.05	109.99	110.46	109.05	110.64	110.46	108.98	108.98	110.64	110.46	108.98	109.26	108.98	110.64	110.46	108.97	109.26	109.47
St. Dev.	1.04	1.25	1.10	1.04	0.80	1.10	0.79	1.15	0.80	1.10	0.79	0.65	1.15	0.80	1.10	0.67	0.65	1.46

Figure 4.5 - Results considering azimuth, length, and position as attributes, and weighting twice the azimuth. A) k3: three clusters, average silhouette width for the entire dataset ($\bar{s}$): 0.59; B) k4: four clusters, $\bar{s}$: 0.42; C) k5: 5 clusters, $\bar{s}$: 0.37; D) k6: 6 clusters, $\bar{s}$: 0.39. In the tables below statistical parameters for each cluster for azimuth, length and position are shown. Cluster6-k6 included an insufficient number of lineaments for reliable statistical analysis of the attributes.

In Azimuth+Length+Position and 2Azimuth+Length+Position tests, tectonic lineaments with mean azimuth of 20° are included in two clusters with different spatial distribution (i.e. yellow and blue in Figure 4.4A-D and 4.5B-D) that represents subsets of the Cluster 2 in Azimuth and Azimuth+Length tests. In particular, the blue cluster (Cluster 3 in Figure 4.4A-D and Cluster 4 in

Figure 4.5B-D) includes the tectonic lineaments located in the easternmost part of the study area whereas the yellow cluster (Cluster 2 in figures 4.4A-D and 4.5B-D) is located to the west, at different mean distance from the ESc (Eastern Scarp, that is the main scarp of the CF. See Chapter 2, Section 2.2 for details). The blue cluster is characterised in both tests (Figures 4.4 and 4.5) by mean azimuth between 18° and 23° and mean length between 50 km and 72 km, values that slightly differ from Clusters 2 (mean azimuth 21°-23° and mean length 55-58 km). In this way, the position of the centroids used as attribute represent a significant discriminating factor to identify subsets of the dataset otherwise not visible considering only azimuth or azimuth and length.

In addition to the above-mentioned subdivision, *Azimuth+Length+Position-k5* and *-k6* tests (Figure 4.4C) group in a single cluster (i.e. *Cluster5-Azimuth+Length+Position-k5* and *-k6*) the three longest mapped lineaments. Moreover, in *Azimuth+Length+Position-k6* Cluster 6 (purple) includes tectonic lineaments whose mean azimuth and length somewhat resemble that of *Cluster4-Azimuthk4*, *-k5* and *-k6*, and *Cluster5-Azimuth+Length-k5* and *-k6.* A similar cluster is identified also when weighting twice the azimuth with respect to length and position (Figure 4.5C, D). It should be also noted that the subdivision in clusters obtained with *2Azimuth+Length+Position-k5* test resemble that of *Azimuth-k4* (Figure 4.2B) with the obvious exception of the blue cluster.

To sum-up, results obtained considering the azimuthal direction as sole attribute are those characterised by the greatest values of the average silhouette width $\bar{s}$. Specifically, the highest $\bar{s}$ is obtained with *azimuth-k3* (0.83), that is the test that considers the lowest number of attributes (one) together with the lowest number of clusters (three). By increasing the number of clusters and by adding new attributes, $\bar{s}$ slightly decreases up to the lowest value of 0.37 obtained in the cases of *Azimuth+Length+Position-k3* and *2Azimuth+Length+Position-k4* and *-k5.* In all the four main tests it can be observed that the first three clusters found with *k3* divide in new clusters when increasing k. This represents an increasingly refined subdivision of the dataset based on the attribute(s) considered. This is witnessed by the values of *sd* and range of the attribute(s) that decrease as the number of clusters increases. In the case of Azimuth tests, for instance, from *k4* to *k6* three other preferential azimuthal directions are highlighted splitting Cluster 1 and Cluster 2. In this way, the *sd* of Cluster 1 decreases from 19.91° to 4.48°, and the *sd* of Cluster 2 decreases from 5.39 to 4.49. However, as discussed later in Section 4.4, the new subdivisions do not always reflect meaningful information or reliable geological scenarios. Therefore, the expertise of the operator in interpreting the geological significance of the results is crucial.

4.4 Discussion

4.4.1 Methodological consideration

The workflow based on the Agglomerative Clustering Analysis presented in this Chapter has been applied to the tectonic lineaments occurring in the area of the CF with the aim of grouping them on the basis of their characteristics. Operationally, this application necessitated two fundamental settings: i) selection of attributes for performing the clustering, and ii) determination of the optimal number of clusters (k) to stop the analysis. Results were found to be highly dependent on these settings, especially to the choice of attributes, including their weighting. For instance, the azimuth alone (Figure 4.2) led to identify clusters characterised by very low values of *sd* regardless of the number of clusters k. On the other hand, considering azimuth, length, and position together (Figure 4.4) enabled the identification of subsets of tectonic lineaments with different spatial distributions in the study area and the isolation of the population with the longest mean length. In addition, the used workflow proved to be significatively responsive to the different weight assigned to one attribute compared to the others. Weighting twice the azimuth greatly influenced the distribution of the resulting clusters (Figure 4.5), further highlighting the importance of attribute selection and weighting in the proposed method. Consequently, attribute selection should be driven by the aim of the analysis, the geological properties of the objects of the study, and the most relevant geo-tectonic characteristics of the area under investigation. Here, the geological expertise of the operator plays a pivotal role and cannot be overtaken or neglected.

The number of clusters k is the other crucial parameter. k can be objectively evaluated through the average silhouette width $\bar{s}$ that can be used *"a posteriori"* to assess the robustness of the chosen cluster structure in a sort of trial-and-error procedure (Kaufman & Rousseeuw, 1990). Therefore, the optimal value of k should be chosen by analysing the geological relevance of the resulting clustering distribution thus exploring the geologic information that it provides. In this application, results indicated that $\bar{s}$ generally decreased with an increasing number of attributes and clusters, passing from 0.83 considering 1 attribute and 3 clusters (*Azimuth-k3*, Figure 4.2A) to 0.37 considering 3 attributes alongside an increasing number of clusters (*Azimuth+Length+Position-k3*, Figure 4.4A; *2Azimuth+Length+Position-k4* and *-k5*, Figure 4.5B, C). Values of $\bar{s}$ related to Azimuth+Length+Position and 2Azimuth+Length+Position tests are below the threshold of 0.50 suggested by Kaufman & Rousseeuw (1990) for identifying reasonable cluster structure. Nevertheless, although the Azimuth tests show the most robust results (i.e. the highest $\bar{s}$), these tests

reveal a previously unidentified subdivision of tectonic lineaments whose relevant geological meaning is explored in the next Section.

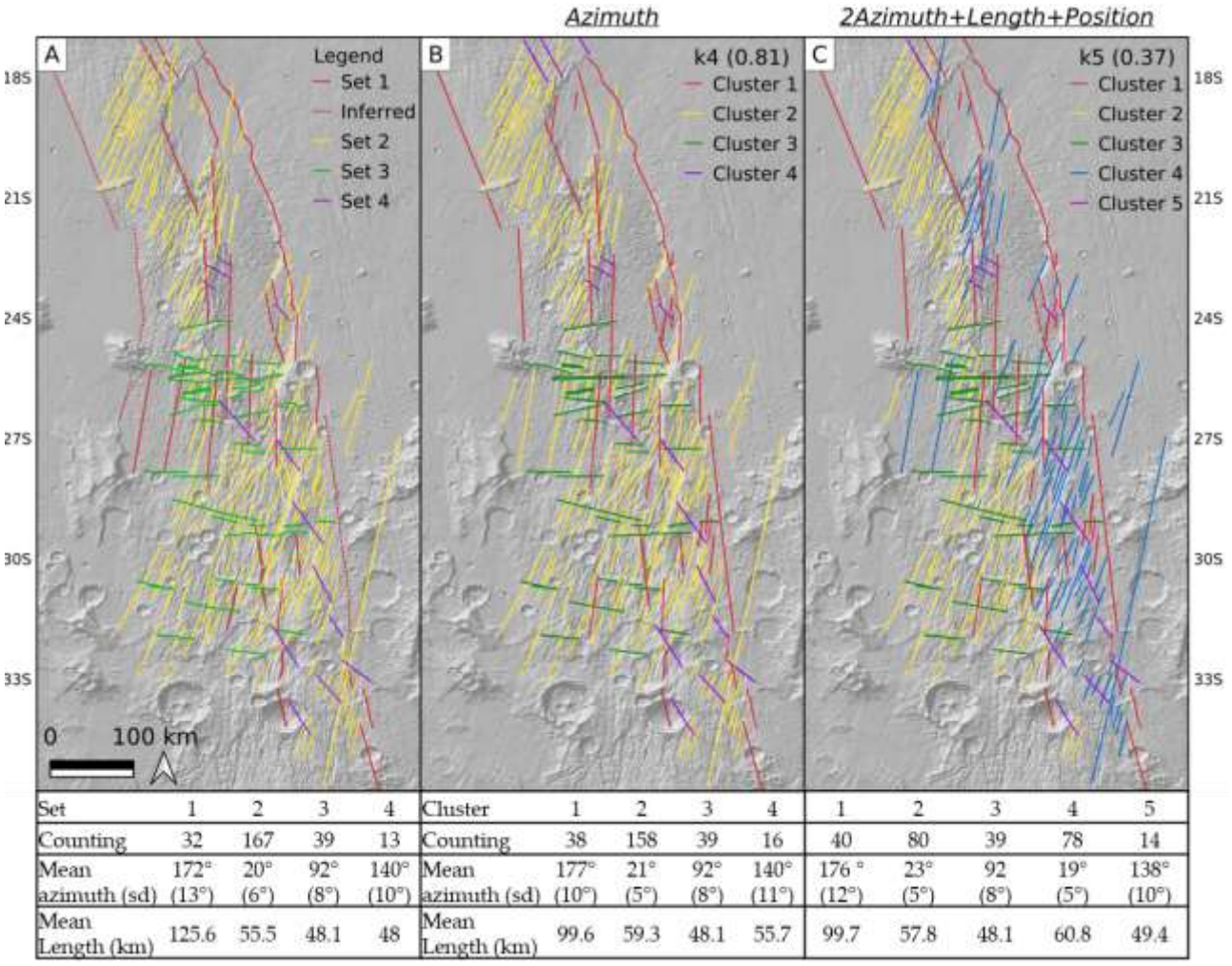

Set	1	2	3	4
Counting	32	167	39	13
Mean azimuth (sd)	172° (13°)	20° (6°)	92° (8°)	140° (10°)
Mean Length (km)	125.6	55.5	48.1	48

Cluster	1	2	3	4
Counting	38	158	39	16
Mean azimuth (sd)	177° (10°)	21° (5°)	92° (8°)	140° (11°)
Mean Length (km)	99.6	59.3	48.1	55.7

	1	2	3	4	5
	176 ° (12°)	23° (5°)	92 (8°)	19° (5°)	138° (10°)
	99.7	57.8	48.1	60.8	49.4

Figure 4.6 - A) Sets obtained through the geostatistical analysis of the mapped tectonic lineaments presented in Chapter 3. **B)** Clusters distribution obtained with *Azimuth-k4* test. Distribution of sets and clusters in A and B is substantially identical as shown by the differences in mean azimuth lower than the *sd*. **C)** Clusters distribution obtained with *2Azimuth+Length+Position-k5* test. Set2 is subdivided in two subsets (Cluster2, yellow, and Cluster4, blue) with different spatial distributions. Note that the mean azimuth of the clusters remain unchanged.

4.4.2 Geological implications

The proposed clustering workflow proved to be able to i) reproduce with very high accuracy the results derived from classical geostatistical azimuthal analysis presented in Chapter 3, and ii) obtain new tectonic insight on the CF. To ease the comparison between sets presented in Chapter 3 and clusters, the same colours assigned to the four sets (replicated in Figure 4.6A) are used for that clusters that best represent the sets (i.e. red *Set 1*/*Cluster 1*; yellow *Set 2*/*Cluster 2*; green *Set 3*/*Cluster 3*; purple *Set 4*/*Cluster4*. To facilitate the reader hereinafter sets and clusters will be renamed with the colours used in Figure 4.6 together with the value of *k* used for the corresponding test; e.g.

Cluster1-Azimuth-k4 of Figure 4.6B becomes *Red-k4* and *Cluster2-2Azimuth-Length-Position-k5* in Figure 4.6C becomes *Yellow-k5*). The subdivision of the clusters obtained through the *Azimuth-k4* (Figure 4.6B) test is substantially identical to that of the sets. In particular, the *Green* and *Purple* sets (Figure 4.6A) and clusters (Figure 4.6B) perfectly match by both number of grouped tectonic lineaments and value of mean azimuth. *Red* and *Yellow* sets and clusters are characterised by minor variations in the number of tectonic lineaments still maintaining differences in terms of mean azimuth lower than the *sd*. This strengthen the tectonic interpretation discussed in Chapter 3 (Section 3.4) of a model of strain partitioning consistent with a NNW–SSE oriented right-lateral strike-slip deformation corridor. In the proposed tectonic scenario sets/clusters represent: *Red*, the main shear zone; *Yellow*, R-shear structures; *Green*, T-Structures; and *Purple*, P-shear structures (Figure 3.10). The recognition of this azimuthal distribution of the tectonic lineaments in four sets/clusters by both approaches strengthen their reliability.

Significant geological information derive by the *2Azimuth-Length-Position-k5* test as well. The distribution of the clusters obtained considering the three attributes together with the azimuth weighted twice and 5 clusters (Figure 4.6C) shows two subsets of the *Yellow-k4* cluster (Figure 4.6B) characterised by different spatial distributions. These are: *Yellow-k5* and *Blue-k5* clusters in Figure 4.6C. Differences in terms of mean azimuth and length between these two clusters are lower than the values of *sd*. This prevented to identify them considering only azimuth and length as attributes or classical geostatistical methods. In this way, the position of the tectonic lineaments represents the discriminating factor to identify this subdivision. In fact, the blue and yellow clusters are clearly separated and, most important for geological investigations, they are located at different distances from the ESc. In particular, *Yellow-k5* is more distant and *Blue-k5* is closer. As discussed in the introduction section, the ESc is considered by different authors as the superficial manifestation of a crustal-scale fault (e.g. Hauber & Krolnber, 2005; Montgomery et al., 2009; Balbi et al., 2024). Therefore, the different position of these clusters with respect to this regional-scale scarp could suggest their development at different distances from the main fault zone of the CF. In order to verify the geological significance of these two clusters, the Length-Spacing (or L/S) ratio can be used. This parameter involves the length (L) of the structure considered and its perpendicular distance, or spacing (S), to the most adjacent and nearly parallel structure belonging to the same cluster. L/S is nondimensional and scale-independent and reflects the fracture infilling process that represents the nucleation of new faults/fractures between two pre-existing faults/fractures in evolving brittle deformation conditions (Lachenbruch, 1961; Durney & Kisch, 1994; Bai & Pollard, 2000a, 2000b;

Tavani et al., 2006). L/S is then used to determine the spatial frequency of tectonic lineaments derived from crustal tectonic stresses and is proportional to the intensity of brittle deformation (Salvini, 2013; Cianfarra & Salvini, 2016a; Rossi et al., 2018, 2020). Highly deformed areas are characterized by close-spaced fractures/faults yielding higher L/S values than low-deformed areas. Therefore, L/S decreases with the distance from fault zones (Cianfarra et al., 2022). In the case of *Yellow-k5* and *Blue-k5* (Figure 4.6C), L/S is 3.33 and 3.53, respectively. This significant difference reflects the distance of the clusters from the ESc (i.e. Cluster 2 further from and Cluster4 closer to the scarp, Figure 4.7) suggesting that the deformation in the study area increases by approaching the scarp. It should be noted that the spatial distribution of Cluster4-2Azimuth-Length-Position-k5 is not homogenous. The number of tectonic lineaments belonging to this cluster drastically changes between the northern and the southern part of the study area. In this way, the computed L/S ratio should be affected by this different distribution. By re-calculating L/S exclusively in the southernmost part of the CF, where both clusters are homogenously distributed, values of 2.83 for *Yellow-k5* and 3.49 for *Blue-k5* are obtained. Thus, although absolute values effectively change, especially for the yellow cluster, L/S of *Blue-k5* remains relatively higher. In this way, the subdivision shown in Figure 4.6C indicates: i) two areas characterized by different intensity of brittle deformation; ii) the deformation increases by approaching the ESc that thus likely represents the area in which the deformation has concentrated the most. This is in accordance with the proposed tectonic model presented in Chapter 3 (Figure 3.10) and with the development of a crustal-scale normal fault whose superficial manifestation is represented by the ESc (Figure 3.5). These results prove that even if the most robust results from the mathematical point of view (i.e. the clustering showing the highest $\bar{s}$ value) are obtained considering the azimuth alone, also clusters obtained using the three attributes together (with the lowest values of $\bar{s}$) provide significant geologic information. Therefore, $\bar{s}$ proved to be a fundamental parameter to guide the analysis. Nevertheless, the choice of the attributes and their weights, and of the number of clusters should follow the geological expertise of the operator and cannot be based only on purely objective criteria.

As discussed in Chapter 3, a crustal-scale fault zone such as that proposed for the CFF could represent a preferential pathway for magma and fluid migration. In this way, the two areas characterised by different brittle deformation highlighted through the clustering workflow suggest that the secondary permeability could increase by approaching the ESc. A confirmation may be represented by the distribution of mounds (i.e. positive topographic landforms) possibly related to volcanic origin identified by Pieterek et al., (2024) in the central part of the CF. These mounds are

more numerous and closely spaced near the main scarp of the CF, aligning with the area influenced by *Blue-k5*.

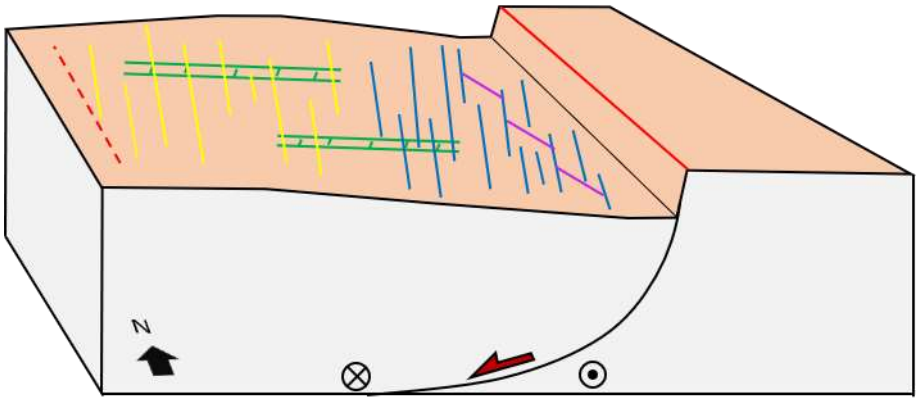

Figure 4.7 – Schematic representations of the distribution of the clusters identified through the *2Azimuth-Length-Position-k5* test (Cluster1, red; Cluster2, yellow; Cluster3, green; Cluster4 blue; Cluster5, purple). In particular, clusters 2 and 4 represent two subsets of Set2/Cluster2 in Figure 4.6A and B. They are located at different distance from the ESc and characterised by different spacing (lower for Cluster4). This led two different values of L/S indicative of different intensity of brittle deformation between the two clusters.

In addition to the abovementioned considerations, the spatial distribution of *Yellow-k5* and *Blue-k5* also implies temporal considerations. Specifically, the transition between the two areas distinctly affected by *Blue-k5* (Figure 4.6C) corresponds with the transition between the Late Hesperian lavas (lHv) to the north and the middle Noachian Highlands units (mNh) to the south (Figure 4.8A-C). Similarly to what discussed for the distribution of the azimuthal sets (Section 3.3.3 and Figure 3.11), the majority of the tectonic lineaments belonging to both *Yellow-k5* and *Blue-k5* occurs in correspondence of Late (lNh) to Middle Noachian Highlands units suggesting that these clusters formed before the emplacement of the Late Hesperian lavas. This consideration can be extended to lineaments belonging to *Green-k5* and, partially, to that of *Red-k5*. Specifically, *Red-k5* includes lineaments outcropping at the lithological contact between Noachian and Hesperian terrains and the main scarp of the CF that cuts and offsets the Hesperian lava flows. This suggests a reactivation of the main fault zone of the CF and consequently of some of the identified sets/clusters after the emplacement of the Late Hesperian lava flows. In this way, results of the presented clustering workflow favour the polyphase tectonic model hypothesis characterised by a Noachian right-lateral strike-slip event and a Late Hesperian/Early Amazonian transtensional reactivation presented in Chapter 3.

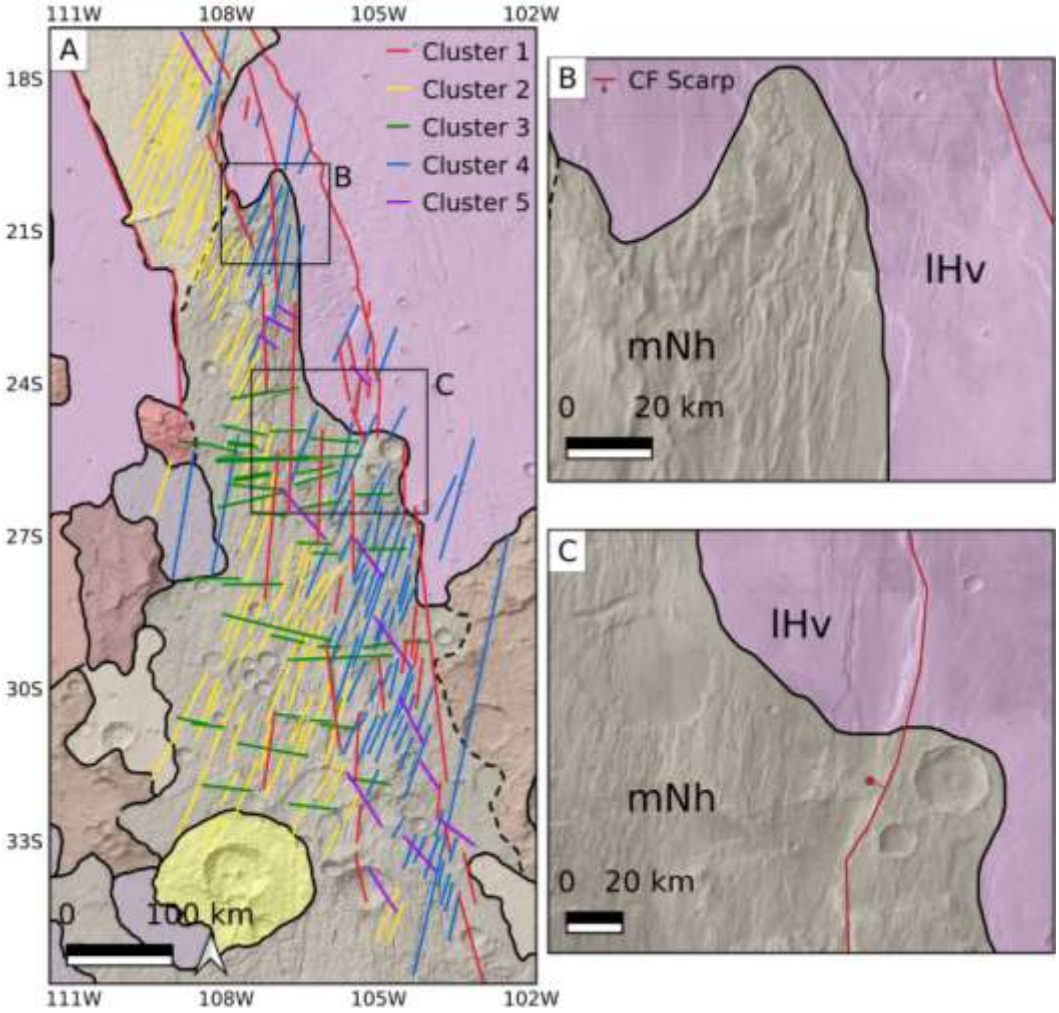

Figure 4.8 - A) Sketch map showing the position of the clusters of tectonic lineaments derived from the *2Azimuth-Length-Position-k5* test with respect to the geologic units from Tanaka et al., (2014). Clusters mainly affect late to middle Noachian Highlands units (mNh). **B)** and **C)** show Late Hesperian lavas (lHv) overlapping tectonic lineaments belonging to all clusters and the ESc (belonging to Cluster 1) that cuts and offsets lHv. These temporal constraints agree with the polyphase tectonic scenario presented in Chapter 3.

4.5 Conclusions

The proposed clustering workflow proved a valuable tool to objectively categorize objects based on their characteristics. This approach is particularly worthwhile when dealing with complex databases containing hundreds or thousands of objects, such as tectonic lineaments, each with numerous attributes. The application to the CF allowed verifying the effectiveness of the proposed method in investigating complex, tectonically controlled regions. In particular, this clustering procedure has demonstrated its capability to both replicate results obtained by classic geostatistical methods and identify previously unrecognised areas characterised by varying intensities of deformation, yielding significant tectonic and geological considerations. With azimuth, length, and position as attributes,

the cluster analysis identified subsets of tectonic lineaments whose distribution has been useful to provide significant insights on the geo-tectonic evolution of the CF.

The proposed clustering workflow is guided by two crucial parameters: the attributes used for grouping objects (in the case of this study azimuth, length and position of the centroids) and the optimal number of clusters to stop the routine. The attributes represents a mindful choice that has to be driven by the aim of the analysis and scale/resolution at which it is conducted. In the case of this study, the goal of revealing the regional scale tectonics at the CF necessitated focusing on characteristics of the mapped tectonic lineaments representative of regional/crustal deformation (e.g. orientation, length, position) rather than parameters related to local-scale causes (e.g. morphometric characteristics). The other challenging aspect of the proposed method is assessing the optimal number of clusters. This choice can be guided by the Silhouette index that allows evaluating the statistical consistency of the clustering results. Nevertheless, the final decision on when to stop the analysis rests with the operator who must validate the geological reliability of the resulting distributions of the clusters. Therefore, both aspects crucially rely on the fundamental role of the operator, whose geological expertise remains essential in setting and conducting the analysis and cannot be neglected in favour of a merely objective procedure.

When the attributes to be used and the number of clusters are adequately tuned, the proposed clustering workflow proved to be a useful tool to provide new insights into the analysis of tectonic lineaments in complex areas such as the CF. In the case of this study, considering all available attributes, the cluster analysis has successfully identified groups of tectonic lineaments. The distribution of these groups was extremely useful for recognising different deformation conditions and strengthen the polyphase tectonic model of the CF.

The performance of the proposed workflow is promising. As a future perspective, this method will be applied to more complex areas characterised by a higher number of tectonic lineaments. This could be the case of Noctis Labyrinthus, the whole Thaumasia Region or the entire Tharsis region, where tectonic lineaments have a higher range of variability and cluster them with classical methods could be extremely challenging and subject to operator biased interpretations.

Chapter 5

Lineament domain analysis through manual and automatic approaches

This chapter presents the methodological approach and dataset included in a paper published in *Geoscience* Journal as *Balbi, E., & Marini, F. (2024). Lineament Domain Analysis to Unravel Tectonic Settings on Planetary Surfaces: Insights from the Claritas Fossae (Mars).*

5.1 Introduction

In the present Chapter the term "lineament" is used with a different meaning compared to that of "tectonic lineaments" used in Chapter 3 and 4. Whereas before "tectonic lineaments" has been used to refer to geological elements recognised on the Martian surface (e.g. scarps, reliefs, semi-graben etc…), here "lineament" refers to geo-texture reflecting elongated, subparallel alignments of tonal contrasts in satellite images. In the following the use of the term "lineament" and its geological meaning is discussed.

Regionally sized lineaments (length of the order of hundreds to thousands of kilometers) record the signature of the tectonic deformation, and thus they represent a powerful tool to unravel the geotectonic evolution of the surface of terrestrial planets with a rigid outer shell. Azimuthal and spatial analysis of lineaments provides fundamental insights to applied studies, such as characterization of hydrothermal fluid circulation (Kerrich et al., 1997; Pischiutta et al., 2013) and groundwater fractured reservoirs (Sander et al., 2007; Gleeson & Novakowski, 2009; Kouider et al., 2023), assessment of hydrocarbon potential in oil fields (Lee & Morris, 2010; Enoh et al., 2021), characterization of areas with high landslide susceptibility (Ramli et al., 2010; Yusof et al., 2021), and investigation of the structural setting of seismically and volcanic active regions (Pardo et al., 2009; Moustafa et al., 2022), as well as to unravel the tectonic evolution of different planetary surfaces (Dzurisin et al., 1978; Wise et al., 1979; Chabot et al. 2000; Aydin, 2006; Vaz, 2011; Rossi et al., 2018, 2020; Cardinale et al., 2023). Nevertheless, it is not easy to give a precise definition of lineaments. During the last decades, quoting Wise et al. (1985) "*definitions and theories on the origin of lineaments have been as numerous as the lines themselves"* (see also O'Leary et al., 1976 for a review on the various definition of lineaments since Hobbs, 1904). In the present study, lineaments are considered as geo-texture reflecting elongated, subparallel alignments of tonal contrasts in satellite images. Lineaments are tens to hundreds of km long, cluster in azimuthal family set called domains, and persist over

wide regions (hundreds to thousands of square kilometers) forming lineament swarms. This description resembles the lineaments definition given by Wise et al. (1985). The most significative aspect of this class of lineaments is given by their membership in large populations. Therefore, this kind of lineament texture analysis does not focus on the geo-tectonic meaning of a single lineament, instead it is based on the characteristics of the entire domain. The inclusion, omission or misinterpretation of one or a few lineaments does not affect the tectonic meaning of the entire population. Wise et al. (1985) suggested that lineament swarms originated through weathering and erosional etching of subtle features produced by extension of the brittle upper crust above a deeper layer behaving in an overall more ductile fashion. Following Wise et al., (1985) lineament domains represent the surface manifestation of crustal stress trajectories. Specifically, under Andersonian stress conditions, the main lineament domain develops perpendicularly to the least horizontal compression ($\sigma 2$ in compressional regimes, and $\sigma 3$ in extensional and strike-slip regimes) and parallel to the maximum horizontal compression ($\sigma 1$ in compressional and strike-slip regimes, and $\sigma 2$ in extensional regimes). Thus, lineaments may be figured as the intersection with the topography of virtual vertical planar surfaces striking parallel to maximum horizontal compression ($\sigma 1$ or $\sigma 2$). In this way, the characteristics and spatial distribution of lineament domains and swarms have been observed reflecting crustal geodynamic effects on different planetary surfaces (e.g. Earth: Mazzarini & Salvini, 1994; Pischiutta et al., 2013; Lucianetti et al., 2017; Ganymede: Rossi et al., 2018; Mars: Binder et al., 1972; Wise et al., 1985; Heller & Janle, 1999; Vaz et al., 2012). In a single region, multiple lineament domains may exist thus producing the structural/topographic grain of the region. These lineament textures reflect the structural architecture of the crust that in some cases is partially hidden by thick sedimentary, volcanic, or ice covers. Nevertheless, the dynamic adjustment of such covers (including sediment compaction and ice flow) preserves on their surface the record of the bedrock architecture. In this way, smoothed signature may be detected and analysed from satellite images (Cianfarra & Salvini, 2014).

In the present Chapter, lineament domain analysis is conducted to explore the tectonic setting of the CF by means of an independent dataset in order to strengthen the tectonic interpretations proposed in the previous chapters based on different methodological approach. Lineament detection is performed following a manual and an automatic approach. In particular, the automatic analysis, performed with *SID* software (v. 3.06-2, Rome, Italy) (Cianfarra & Salvini, 2015), is conducted to validate the results of the manual detection and thus to improve the reliability of the dataset. Data obtained by both methods are statistically analysed by means of *Daisy3* software (v. 5.58.3.231121,

Rome, Italy) (Salvini et al., 1999). Results are compared with findings presented in the previous Chapter 3 and 4.

5.2 Materials and Methods

A twofold approach consisting of the combination of a manual and an automatic method is followed for the detection of lineaments.

5.2.1 Manual lineament detection and statistical analysis

Lineaments outcropping in the study area are visually identified through geologic interpretation of satellite image mosaics. Lineaments appear as patterns of aligned pixels reflecting linear anisotropies in the image texture. To ease their identification, an ad hoc image enhancement is conducted on the Digital Elevation Model (DEM) derived from the acquisitions of the Mars Orbiter Laser Altimeter (MOLA) aboard the Mars Global Surveyor (MGS), namely the Mars MGS MOLA DEM 463m v2 dataset (Neumann et al., 2001, 2003). This dataset is characterised by 463 m/px of spatial resolution, that represents the best compromise between scale and resolution providing a synoptic view of the study area yet preserving the signature of regionally sized tectonic features. In the geographic information system (GIS) environment based on the open-source software QGIS_3.30_s-Hertogenbosch, from the original dataset a subset of the study area is extracted. It represents an area of 1060 x 1080 km in the latitude interval 20° - 35°S and longitude interval 100° - 115°W. The subset image is resampled at the spatial resolution of 1000 m/px. In this way, the image is filtered to exclude elements and morphologies related to local effects that we consider negligible for the regional aim of this study. Shaded relief images are derived from the resampled subset image according to four, low angle (20°), synthetic lighting conditions trending 45°, 90°, 135° and 180° (Figure 5.1). The combination of their analyses allows the reduction of the bias induced by the use of a single direction of the light for which lineaments nearly parallel to the direction of the light tend to be hidden and those nearly perpendicular emphasized (Wise et al., 1985; Pischiutta et al., 2013; Pinheiro et al., 2019; Watters & Schultz, 2010). Linear texture enhancing of each shadow images included: i) the application of Laplacian filter to emphasize higher spatial frequency related to the presence of tectonic texture; ii) lookup table stretching to enhance the tone contrasts and ease the manual identification of lineaments (Drury, 2004). Lineaments detection is conducted in GIS environment (QGIS_3.30_s-Hertogenbosch) through the systematic visual inspection of each enhanced, shadow image and following suggestions provided in Wise (1982). Thus, four distinct

lineament datasets are derived. Due to the regional purpose of the present work, only lineaments corresponding to pixel alignments that maintain the same azimuthal direction for no less than 20 km are traced. Identified lineaments are digitized by manually tracing linear elements by drawing vertices by clicking on a fixed map scale of 1:10.000.000 on screen (cylindrical projection). The linear, digital elements are stored in four dedicated vector layers. The following attributes are calculated for each lineament: length, azimuthal direction, coordinates of the extremes and of the centroids. The four derived datasets are then grouped into a single database.

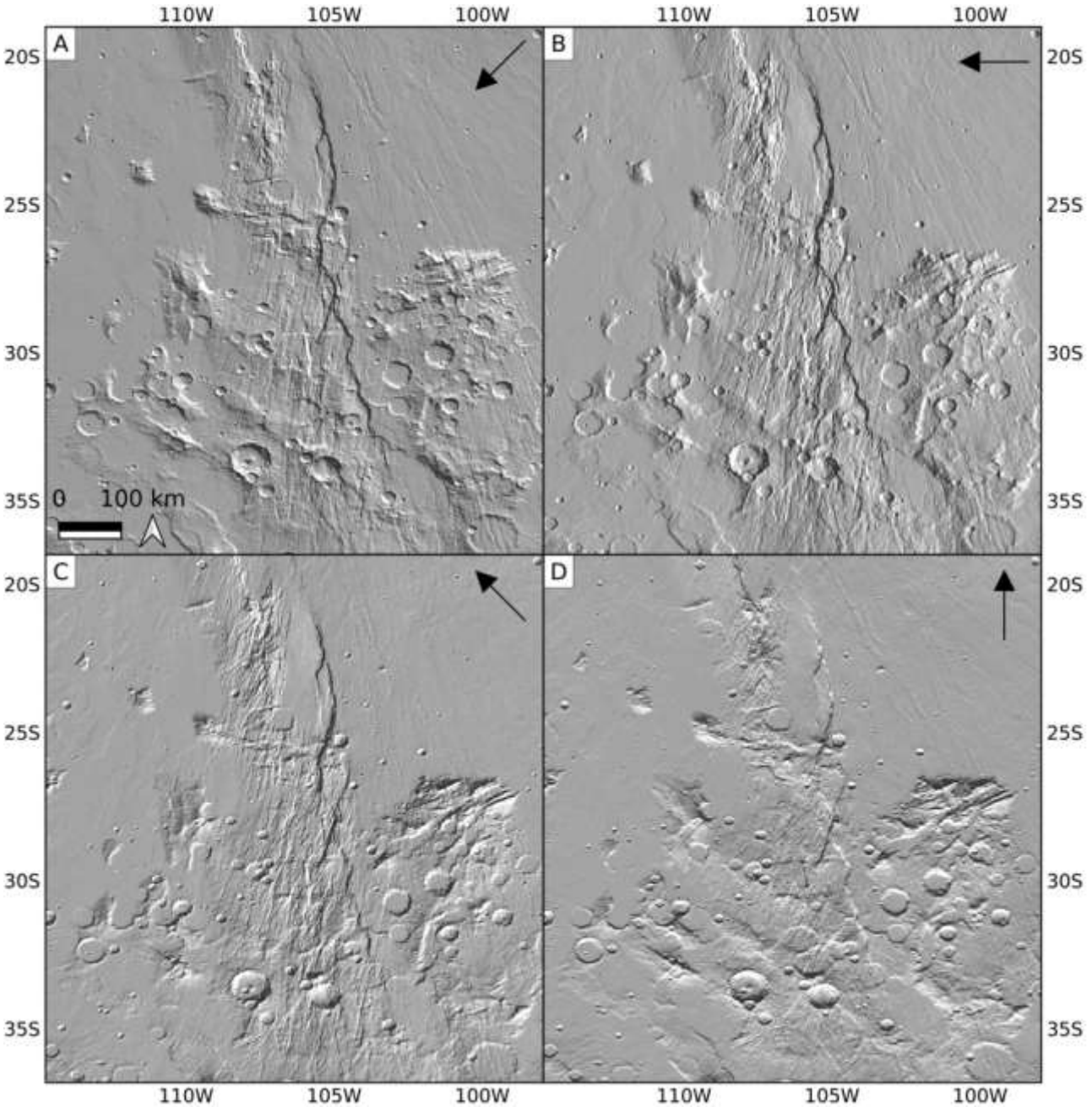

Figure 5.1 – The four shadow images used for the manual lineament detection. Maps are in cylindrical projection. Black arrows indicate the direction of the light **A)** 45°, **B)** 90°, **C)** 135°, **D)** 180°.

This database is statistically analysed using the *Daisy3* software. *Daisy3* allows conducting an azimuthal analysis by frequency and by cumulative length following the approach presented in Wise et al. (1985). This analysis includes the polymodal Gaussian fit aimed at identifying the main azimuthal orientations (i.e. lineaments domains, *sensu* Wise et al., 1985). The statistical analysis includes several steps: i) histograms of the azimuth by frequency and by cumulative length of the identified lineaments are prepared and are normalized to their highest value; ii) peak(s) of the histograms are fitted with a sum of Gaussian curve functions using a best-fit algorithm derived from Frazer &Suzuki (1966); iii) results are plotted as rose diagrams that represents as "petals" the recognized unimodal (single azimuthal set) or polymodal (multiple azimuthal sets) distribution of lineament domains. In this way, each domain can be described by its gaussian/statistical parameters, such as main azimuth, standard deviation, and relative height. In particular, the value of the standard deviation (*sd*), calculated from the width of the petals/gaussian measured at half height, is related to the azimuthal scattering of the lineament domain. Two adjacent domains can be easily identified when their angular distance (i.e. distance between their modes) is higher than their *sd* and thus the corresponding Gaussian peaks show minimal or null overlap. In other word, overlap between adjacent domains is less likely with low values of *sd*.

5.2.2 Automatic lineament detection and statistical analysis

Criticism about lineament detection relies on the magnitude of its potential for observer bias (Wise, 1982). In fact, manual lineament identification may be conditioned by subjective factors of operator as enthusiasm for drawing lines or former knowledge of the study area that can produce a biased data set. For this reason, the automatic detection is performed to strengthen the objectivity of the dataset manually traced. The *SID* software (v. 3.06-2, Rome, Italy) is used to find out alignment of adjacent pixels contrast in the pre-processed DEM (Mars MGS MOLA DEM 463m v2) of the Martian surface by systematic search for all possible digital combinations of segment directions within a given range of parameters. According to the used parameters the algorithm can identify faint, discontinuous lineaments characterized by alignments of adjacent pixels contrast separated by null pixels. The software search for lineaments according to a set of parameters defining the characteristics of the linear pattern. These parameters include: i) the minimum and maximum length in pixel unit of a lineament; ii) the width of lineament measured in pixel unit perpendicularly to its strike; iii) the dimension of the moving smoothing window along the potential lineament to override the discontinuities in pixel distribution; iv) the minimum length of each lineament segment; v) the

maximum distance between lineament segments that belong to the same lineament; and vi) the pixel density along the lineaments.

In this study a set of parameters is selected to find out lineaments longer than 30 km and 3 km wide. The ad-hoc image enhancement of the four shadowed images (prepared ad described in the previous section) includes: i) Laplacian filtering (to emphasize the higher spatial frequency related to the presence of linear texture); ii) threshold slicing (to select pixels contributing to the image texture related to the presence of lineaments and in order to reduce the meaningful pixel number to ~10% of the image); iii) and LIFE filtering (that allowed reduction of random noise in the raster image – Gardner, 1970). The resulting images are then automatically processed with *SID* to recognize lineament pattern. The detected lineaments from each analysis are cumulated into a database that is successively statistically analysed through the *Daisy3* software to find out lineament domains with the same procedure previously described.

5.3 Results

Photogeological interpretation of the four shadow images allowed the visual identification of 735 lineaments (Figure 5.2A). The polymodal Gaussian fit highlighted that the identified lineaments cluster around two preferential orientations thus defining two domains of lineaments (*sensu* Wise et al., 1985 - Figure 5.2B).

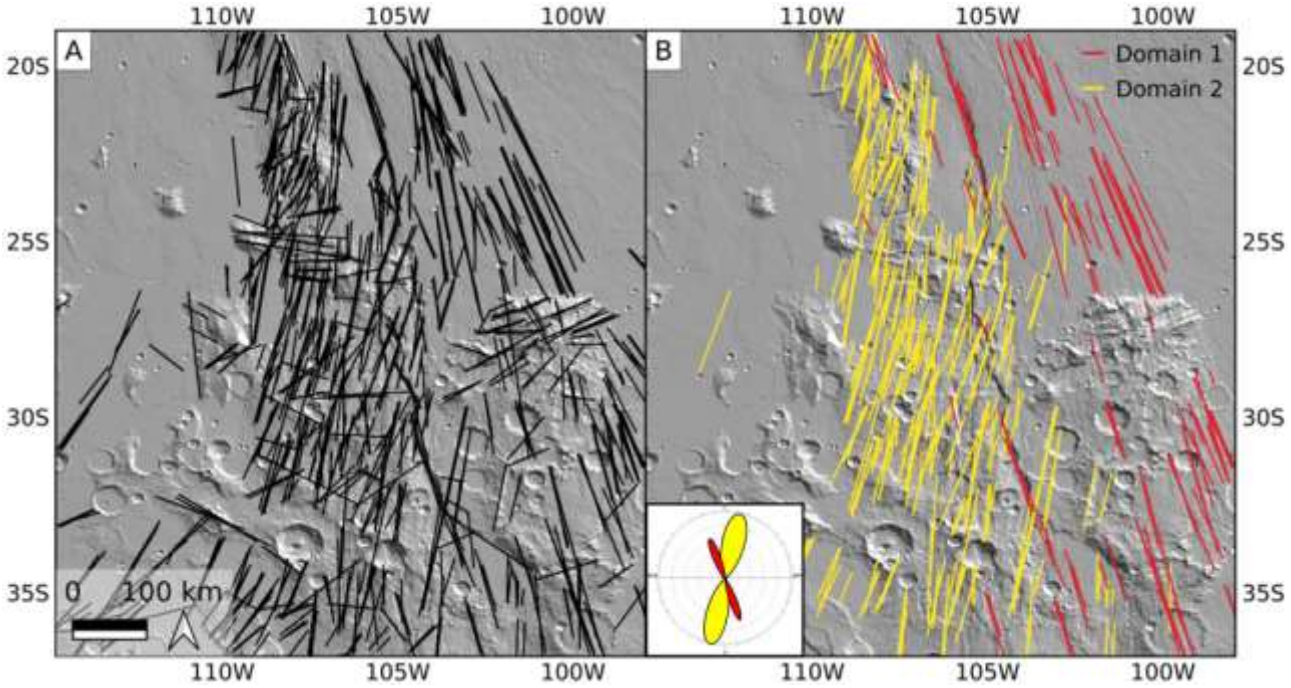

Figure 5.2 - A) The entire population of manually detected lineaments. **B)** The two lineament domains of the CF identified through the polymodal gaussian fit analysis. Rose diagram on the bottom left is the same of Figure 5.3A.

The two lineament domains are clearly highlighted by both the analyses by frequency and by cumulative length (upper and lower part of the rose diagrams in Figure 5.3A, B). They are: i) Domain 1 (red in Figure 5.2B) which includes 139 lineaments with main azimuthal direction of 339.35°(NNW-SSE)), sd: 6.03°; and ii) Domain 2 (yellow in Figure 5.2B) which counts 381 lineaments with main azimuthal direction of 13.39° (NNE-SSW), sd: 11.91°. The angular difference between the two Gaussian peaks is 34.04° that is well above the standard deviation of both the domains. This indicates that the analysis identified and separated two Gaussian peaks that represents two lineament domains. In addition, Figure 5.2B clearly shows that Domain 1 and 2 are characterized by different spatial distribution. Domain 1 is localized in the western part of the study areas whereas Domain 2 is localized in the eastern.

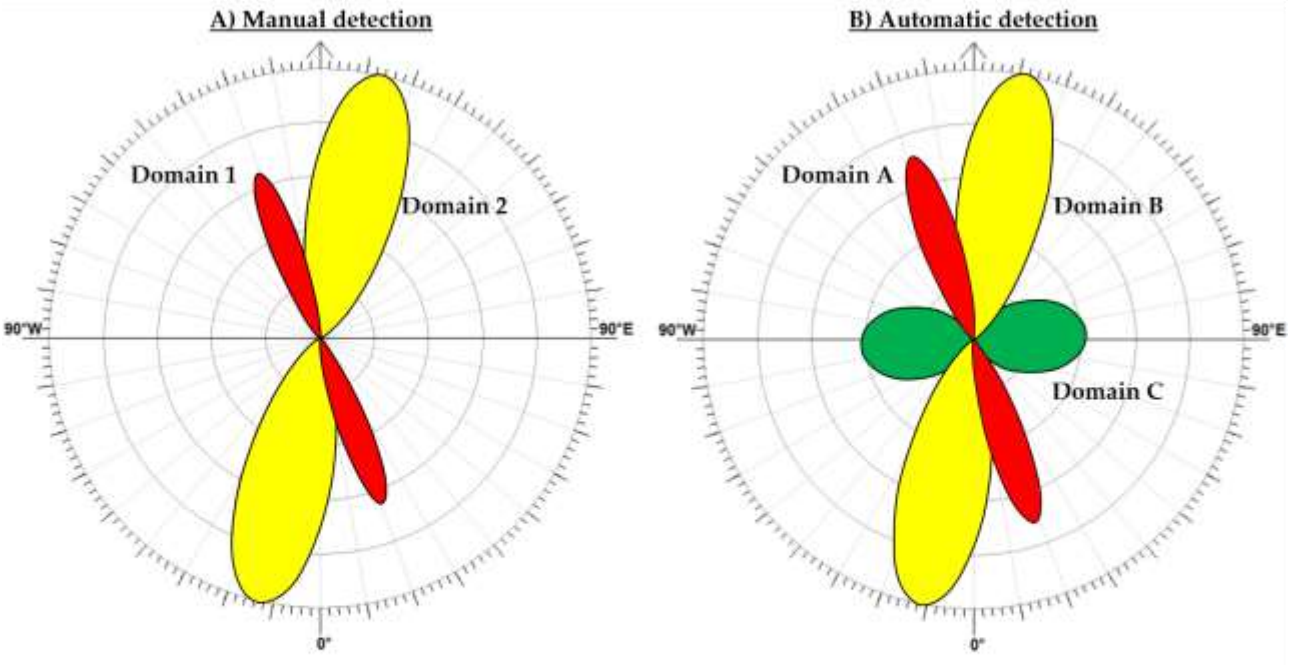

	Gaussian Parameters			
Domain	n°	Nor H	Max H	Azimuth (*sd*)
1	139	64.89	15.32	339.64° (6.03°)
2	381	100.00	23.60	13.17° (11.91°)

	Gaussian Parameters			
Domain	n°	Nor H	Max H	Azimuth (*sd*)
A	116	71.35	13.60	341.40° (7.61°)
B	228	100.00	19.06	11.26° (12.75°)
C	189	41.47	7.91	86.87° (26.29°)

Figure 5.3 - Results of the polymodal Gaussian fit of the **A)** manually detected (tot. 735) and **B)** automatically detected (tot. 824) lineaments. Petals in the wind rose diagrams represent the Gaussian peaks resulting from the azimuthal analyses by frequency (upper part of the diagram) and by cumulative length (lower part) of the lineaments. Width of each petal corresponds to the standard deviation (*sd*). **Tables** below include the statistical parameters of each domain as derived from the polymodal Gaussian fit analyses.

Automatic lineament domains analysis identified 824 lineaments. The polymodal Gaussian fit highlighted three Gaussian peaks corresponding to three lineament domains (Figure 5.3B) that are: Domain A (red in Figure 5.3B) which includes 116 lineaments with main azimuthal direction of

341.40°(NNW-SSE), *sd*: 7.61°; Domain B (yellow in Figure 5.3B) which counts 228 lineaments with main azimuthal direction of 11.26° (NNE-SSW), sd: 12.75°; and, the minor peak, Domain C (green in Figure 5.3B) which includes 189 lineaments with main azimuthal direction of 86.87° (E-W), sd: 26.29°. Domains A and B are characterised by azimuthal trends strongly that resemble the domains 1 and 2 identified through the manual approach. The strong azimuthal similarity is shown in Figure 5.3 and confirms the reliability of the manually traced lineaments. Therefore, in the following discussion and tectonic interpretations the manual lineaments dataset is considered representative of analysis conducted in this study. Rose diagrams in Figure 5.3 show that azimuthal differences between domains 1 and A, and 2 and B are lower than 2°. Therefore, also the mean angular distance between domains A and B, that is 29.86°, is nearly the same of that between domains 1 and 2 (34.04°) with a difference lower than 5°.

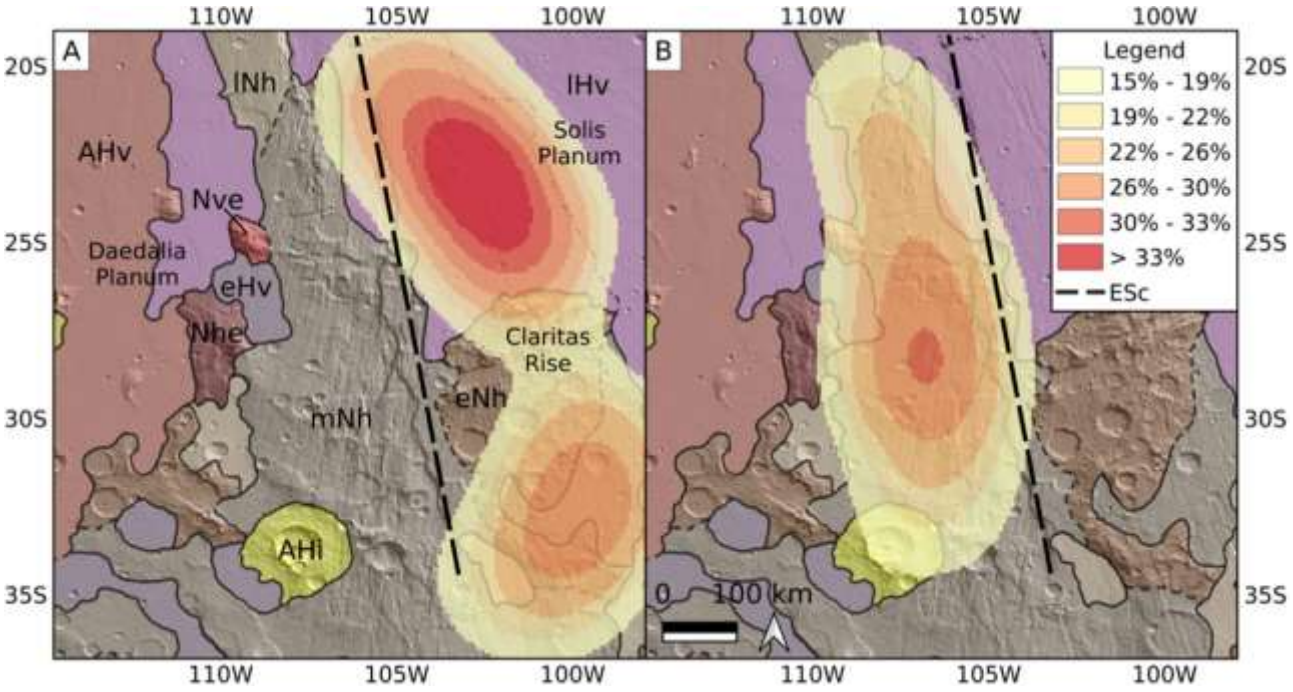

Figure 5.4 - Density maps of **A)** NNW-SSE/red Domain and **B)** NNE-SSW/yellow Domain on the geologic map of the CF from Tanaka et al., 2014 (acronyms of geologic units refer to Figure 2.4). Black dashed line indicates the azimuthal trend of the ESc.

To sum up, results of the lineament domain analysis highlighted that two prevailing regional lineament domains characterise the area of the CF. They are the i) NNW/red Domain, corresponding to domains 1 (manual analysis) and A (automatic analysis), and ii) NNE/yellow Domain corresponding to domains 2 and B. These two main lineament domains persist over two distinct areas separated by the ESc as better highlighted with density maps in Figure 5.4. Density maps are obtained in GIS environment (QGIS_3.30_s-Hertogenbosch) through the plugin *"Heatmap"* that uses

the kernel density estimation algorithm to generate a density raster from a vector point layer as input. The density of the points is calculated as a function of the number of points in a position. The more points are present at specific location, the larger the density values. In this case, centroids of the manually detected lineaments are used. Density map in Figure 5.4A shows that the NNW Domain is located to the east of the ESc (black dashed line) and is characterised by two areas of higher concentration of lineaments. The main concentration is located to the north of the Claritas Rise, where lHv crops out. The second concentration is to the south and persists on the Early to Middle Noachian terrains. In correspondence of the Claritas Rise, a spatial density minimum of lineaments belonging to the NNW Domain is present. On the other hand, density map in Figure 5.4B highlights an almost homogenous distribution of the NNE Domain to the west of the ESc, in correspondence of middle Noachian terrains. A restricted area with higher concertation can be observed around 28°S and 103°W.

5.4 Discussion

Figure 5.2B and 5.4 clearly show that the transition between the two main domains identified in the aera of the CF (i.e. NNW/red and NNE/yellow domains) is sharp and occurs in correspondence of the ESc. As discussed in the previous chapters, the ESc represents the superficial manifestation of a crustal-scale fault characterised by polyphase tectonics. The lineament domain analysis highlighted that the NNW Domain includes some strands of the ESc and shares with the scarp the same azimuthal trend (Figure 5.2B). In this way, the NNW Domain resembles Set1, identified through the structural mapping in Chapter 3, and Cluster1, identified through the Clustering workflow in Chapter 4. Set1/Cluster1 have been interpreted as parallel to the Principal Displacement Zone (PDZ) of the deformation corridor corresponding to the CF. Similarly, the NNW lineament domain can be related to the CFF. On the other hand, the NNE Domain resemble Set2 and Cluster2 that have been interpreted as belonging to the deformation associated to the main shear zone (i.e. R-shear structures). According to Wise et al. (1985), the main lineament domain develops under Andersonian stress conditions perpendicularly (parallel) to the least (maximum) horizontal compression. In this way, considering the NNW Domain as the main lineament domain and an extensional tectonic scenario as that reproduced through the kinematic numerical modelling, the extension should be nearly ENE-WSW oriented. Nevertheless, the spatial distribution and angular relationship of sets and clusters have suggested that the CF likely never experienced a single, pure extensional kinematics. This is supported also by the existence of the NNE Domain and by the

angular relationship with the main NNW Domain. The low values of standard deviation that characterize both the NNE and NNW domains indicates small azimuthal variability of the identified lineament families. Thus, the angular relationship, that is ~34°, is maintained for the entire extent of the CF (>1000 km of length and >150 km of width). In pure strike-slip tectonic regimes the angle between the main fault/shear corridor and the maximum horizontal compression induced by the regional kinematic conditions is 45°. This angle reduces (increases) in the case of transtensional (transpressional) kinematics. It is 0° in pure extensional tectonic regimes and 90° in pure compressional settings (Cianfarra & Salvini, 2015; Rossi et al., 2018 - Figure 5.5). In this way, the variation of the fault kinematics yield the rotation of the angle of the intra-fault/shear corridor stress field resulting in a different orientation of the related lineament domain. In the case of our study, the angle of ~34° between the NNW and NNE domains suggests that the identified domains developed in a transtensional tectonic regime.

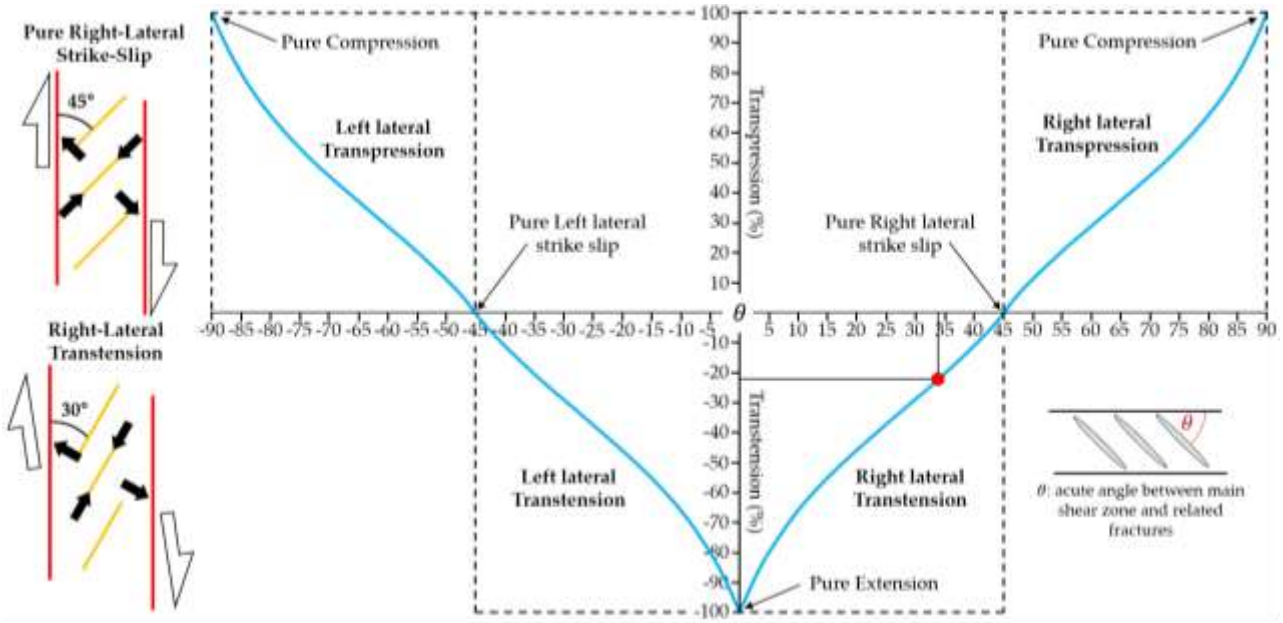

Figure 5.5 - To the left, schematic representation of pure strike-slip and transtensional regimes (redrawn after Rossi et al., 2018) in which the red lines represent the kinematic elements (i.e. boundaries of the shear corridor, NNW Domains) and the orange lines the dynamic elements (i.e. intra-corridor fractures, NNE Domain). **To the right**, the diagram shows different angular relationships as derived from different orientation of the internal stress field. The different angles are shown on the X-axis whereas the percentage of extension/compression is shown on the Y-axis. The acute angle measured clockwise between shear corridor and fractures is 45° in pure strike slip-regime and decreases (increases) in the case of transtensional (transpressional) regime. In this study, the angular relationships of ~34° between the two identified domains indicates that they formed under a right-lateral transtensional regime with ~20% of extensional component.

This can be visualised in the diagram presented in Figure 5.5 in which the acute angle θ between the shear corridor and the related fractures is used to quantify the transtensional/transpressional component in a strike-slip deformation corridor. In the case of this study, the angle of ~34° refer to

a right-lateral transtensional regime characterised by a ~20% of extensional component. Additional information can be derived from the he polymodal Gaussian fit analysis that can be used to determine the relative age of the identified domains (Salvini et al., 1979; Cianfarra & Salvini 2014). In particular, the ratio between the values of the normalized Gaussian height NorH and standard deviation sd (values for both domains are shown in tables in Figure 5.3) is indicative of the sharpness of the peaks or, in other words, of the azimuthal scattering of lineaments belonging to the same domain with respect to their frequency (Lucianetti et al., 2017). Exogenous processes that act on areas deformed by tectonic/endogenous processes tend to increase through time the azimuthal scattering of the original unaltered linear geometries thus increasing the standard deviation of the domain. Therefore, higher values of NorH/sd relate to relatively younger lineament domains (Salvini et al., 1979; Cianfarra & Salvini 2014; Lucianetti et al., 2017). In the case of this study, lineament domain analysis highlighted values of the ratio NorH/sd higher for the NNW Domain (NNW: 10.76 and NNE: 8.39). This indicates that the NNW domain is relatively younger compared to the NNE domain. This is supported also by the spatial distribution of the domains as highlighted by the density maps that show the NNW Domain developing on both the Noachian and Late Hesperian terrains whereas the NNE Domain persisting only over the Noachian terrains. This evidence suggests the formation of NNE Domain in the Noachian age and the NNW domain after the onset of the late Hesperian age. This is in disagreement with the coeval or nearly coeval growth of both domains in a single tectonic stage whereas it can be better explained by a tectonic evolution characterised by multiple events.

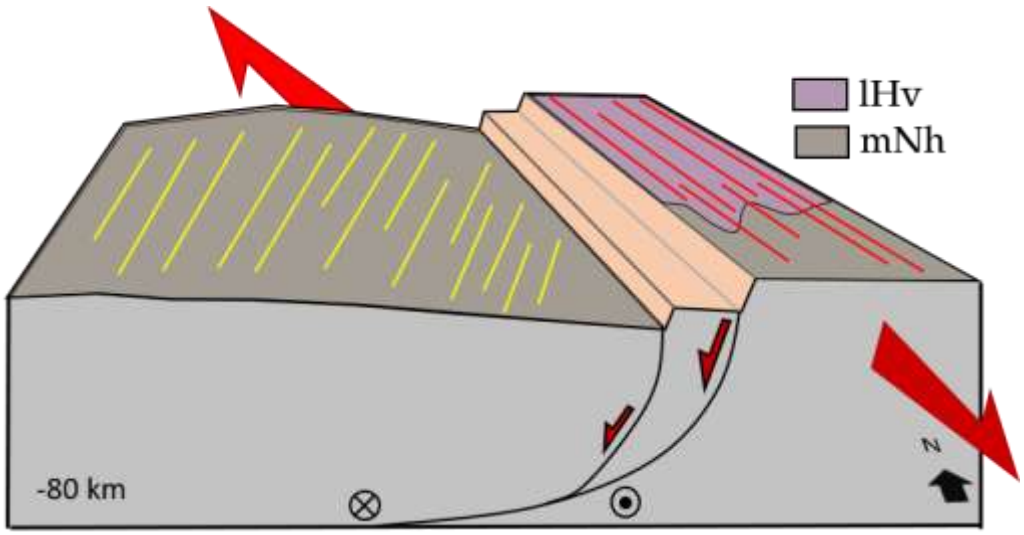

Figure 5.6 - Tectonic sketch showing the proposed right-lateral transtensional tectonic event started in after the emplacement of late Hesperian lavas (lHv) as highlighted by the lineament domain analysis. The normal fault that generates the scarp is redrawn following the results of the kinematic numerical modelling presented in Chapter 3.

In this multi-phase tectonic scenario, a first right-lateral transtensional event led to the development of both the Domains during the Noachian age. A subsequent event occurred after the emplacement of the Late Hesperian lavas, likely reactivating the NNW domain thus explaining its younger relative age (Figure 5.6). The timing of these events is in line with the beginning of the tectonic deformation at the CF in the Noachian age proposed by different authors (e.g. Dohm & Tanaka, 1999; Dohm et al., 2001), and with the event that yielded the development of the TG between Late Hesperian and Early Amazonian (Hauber & Kronberg, 2005). This tectonic reconstruction is in line with the model presented in Chapter 3 and 4 as yielded by the combination of kinematic numerical modelling and structural mapping, and by the clustering workflow.

5.5 Conclusions

In this Chapter lineament domain analysis has been successfully applied to provide important insights on the tectonic evolution of the CF. Two lineament domains have been identified whose spatial distribution and angular relationship suggest their development in a polyphase tectonic frame. A right-lateral transtensional tectonic regime during the Noachian age and a reactivation between Late Hesperian and Early Amazonian have been highlighted. Results are in accordance with findings resulting from kinematic numerical modelling and structural mapping (Chapter 3) and confirmed with the clustering analysis (Chapter 4). In this way, lineament domain analysis proved to be a powerful tool to investigate the evolution of tectonically controlled regions on planetary surfaces.

Chapter 6

Mars as an exoplanet analogue

As stated in Chapter 1 (Introduction), Mars represents a key laboratory for geological research on terrestrial planets and exoplanets. In the previous chapters, methods usually applied in geological and geophysical studies have been successfully combined to better frame the tectonic setting of the CF. More in general, the presented workflow proved to be able to provide an in depth knowledge about the evolution and present-day setting of tectonically controlled regions. This is crucial to better characterize terrestrial planets. Nevertheless, with the aim of creating models to be compared with data obtained from exoplanetary research, a link between geological/geophysical investigations and astronomical/astrophysical techniques is vital to achieve an ever more detailed characterization of exoplanetary systems. In this way, in the present chapter Mars is analysed from a different perspective, and in particular "as if it was an exoplanet". Therefore, the question to be answered is not focussed anymore on getting ever more precise or accurate data or achieving ever more detailed geo-tectonic reconstructions. Instead, the question should be "what would Mars look like if it was an exoplanet?" or, in more scientific terms, "what kind of data would we get if we observed Mars with the same techniques used in exoplanetary studies?". Mars is then here analysed through astronomical techniques usually applied in exoplanetary research to obtained data as similar as possible to that we would obtain from exoplanets similar in size. This chapter includes the content of two papers: the first published in SPIE Journal as *Ricci D., Tosi S., Balbi E., et al., 2021 – Commissioning and improvements of the instrumentation and launch of the scientific exploitation of OARPAF, the Regional Astronomical Observatory of the Antola Park*; the second in preparation and entitled *Rainer M., Balbi E., Borsa F., Cianfarra P., Harutyunyan A., and Tosi S., - Spatial and temporal variations of CO2 on Mars.*

6.1 Short introduction to exoplanets and exoplanetary systems

The existence of planets orbiting stars different from the Sun, namely extrasolar planets or more commonly exoplanets, was confirmed in 1995 when the first exoplanet orbiting a solar-like star (51-Pegasi-b) was detected by Mayor & Queloz (1995). Since then, thousands of exoplanets have been identified orbiting in thousands of exoplanetary systems and far large numbers are considered promising candidates (a continuously updated catalogue of exoplanets can be viewed at https://exoplanets.nasa.gov/discovery/exoplanet-catalog/). During these decades of exoplanetary

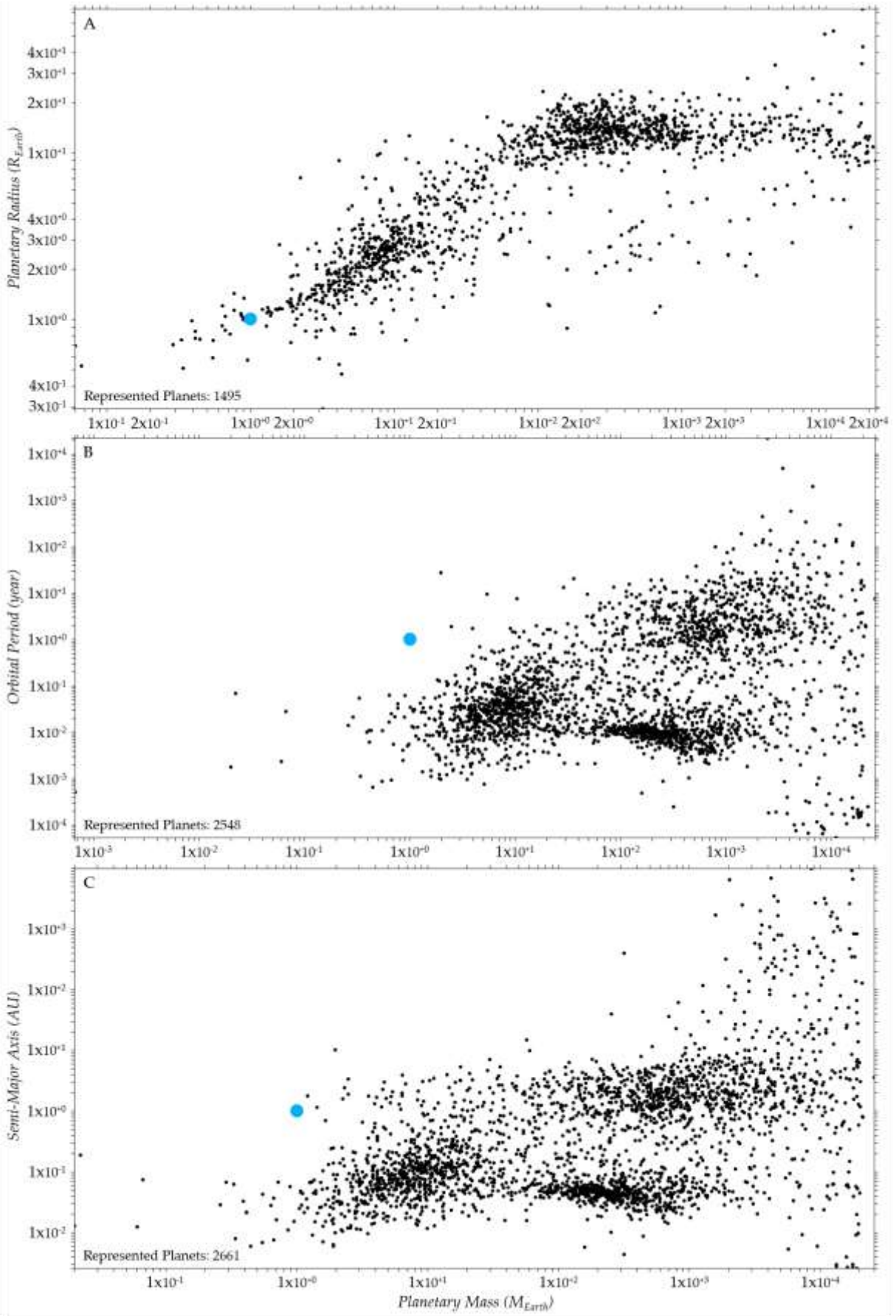

Figure 6.1 - Plots show the huge diversity of exoplanets discovered (confirmed) until January 2024 by comparing the mass of the exoplanets with **A)** radius, **B)** orbital period, and **C)** semi-major axis of the orbit. The blue dot shows the position of the Earth in the graphs. Axes are in logarithmic scale. Plots are derived from https://exoplanet.eu/plots.

research, analogies but also significant differences with the Solar System have been highlighted questioning the anthropocentric paradigm of the Solar System as a "standard" (Martin & Livio, 2015). For instance, although terrestrial and gaseous planets exist also in other planetary systems, categories not represented in the Solar System have been highlighted, such as: gaseous exoplanets with mass similar to that of Jupiter orbiting closer to their host-star than Mercury to the Sun (namely, hot Jupiters – Fortney et al., 2021; Mansfiel et al., 2021); substellar objects 13-80 times more massive than Jupiter (namely, brown dwarfs – Basri, 2000; Bate et al., 2002; Showman et al., 2020); terrestrial planets with mass 2-10 times greater than Earth (namely, super-Earth or mini-Neptune Howard et al., 2010; Mayor et al. 2011; Burke et al., 2015; Edwards et al., 2020). Other types have been only theoretically predicted and will guide future research efforts such as exoplanets totally covered of water or magma oceans (Olson et al., 2020; Howell et al., 2020; Chao et al., 2021). The huge diversity of exoplanets detected so far is well shown in the plots in Figure 6.1 where the mass of the exoplanets is related with the radius and orbital period of the planet, and with the semi-major axis of the orbit. Exoplanets are highly scattered in all the plots and a great abundance of exoplanets with mass and radius several order of magnitude greater than that of the Earth is clearly shown (Figure 6.1A). In this way, the amount of terrestrial exoplanets (relatively lower mass and radius) seems to be lower compared to the gaseous. In addition, exoplanets more massive than the Earth appear to be more common closer to their host-star (Figure 6.1B, C). These represent significative discrepancies with the Solar System where gaseous and terrestrial planets are equally represented and clearly separated. A bias in the currently used observation techniques which are more sensitive to giant exoplanets close to their hosting-star is well known (Fressin et al., 2013). In this way, the present-day effort of the ever more advanced astrophysical experiments in exoplanetary research is focussed in clarifying if these discrepancies are related to a resolution threshold of the available instrumentations. The other possible explanation is that terrestrial planets are truly less common beyond the Solar System (Fischer et al., 2015).

In the last decades, various methods have been developed and have been constantly improving to detect and study exoplanets. These methods allow deriving a series of parameters of the orbit (e.g. semi-major axis, eccentricity, inclination), of the planet (e.g. radius, mass, density) and of its atmosphere if present (e.g. composition, temperature, layering). These parameters are fundamental to characterize the observed exoplanet and distinguish between different categories. Radial Velocity, Transit Photometry, Gravitational Microlensing, Direct Imaging, and Astrometry are among the

most widely used methods for exoplanets detection (Mason, 2008; De Pater & Lissauer, 2015; Perryman, 2018).

- *Radial Velocity*: This is the first method used to detect exoplanets and was successful for the identification of 51-Pegasi-b. It is based on the Doppler shift induced on the star's visible light spectrum by the presence of an orbiting planet (Figure 6.2A). The planet, in fact, causes an orbital motion of the star around the centre of mass of the system that yields a blueshift of the spectrum when the star moves towards the observer and a redshift when it moves away. Radial Velocity is most sensitive to massive exoplanets orbiting close to the star (e.g. hot Jupiter) and it is able to estimate the mass of the planet (related to the mass of the star), period and eccentricity of the orbit.
- *Transit Photometry*: This method measures the drop of the starlight induced by an exoplanet that transits between the star and the observer (Charbonneau et al., 1999 - Figure 6.2B). The inflection of the light curve yields estimates the diameter of the exoplanet and inclination, semi-axis, and period of the orbit of the transiting exoplanets. If the exoplanet can be detected by both Transit Photometry and Radial Velocity, and the radius and mass of the host star are known, the mean density of the planet and the gravitational acceleration on the surface can be estimated as well. Moreover, based on spectrographic measurements it is possible to infer the presence of the atmosphere and the existence of atmospheric layering can be detected thanks to the different opacity of the atmosphere in the various wavelengths. Transit photometry is sensitive to massive exoplanets with short-period orbit (e.g. hot Jupiters). An example of exoplanet detected with Transit Photometry with a local astronomical observatory is shown in Figure 6.3.
- *Gravitational Microlensing*: This method is based on the gravitational bending of the light yielded by the presence of a massive object (namely the lens) between the source and the observer (Figure 6.2C). According to Einstein's general theory of relativity, in fact, the more massive is an object the more the spacetime is distorted. Consequently, the path of the electromagnetic radiation (light) is bent. Moreover, the light of the source is significantly amplified, and multiple copies of the same source can be viewed. If the lens is represented by a star hosting one or multiple exoplanets, these can be distinguished in the measured light curve as peculiar blip(s). With Gravitational Microlensing, different parameters of the orbit can be estimated also for earth-like planets. Unfortunately, the lensing event is not repeatable, and the exoplanets detected in this way are usually too far to be observed with

any of the other techniques, so any information on the system is derived by a single lensing event.

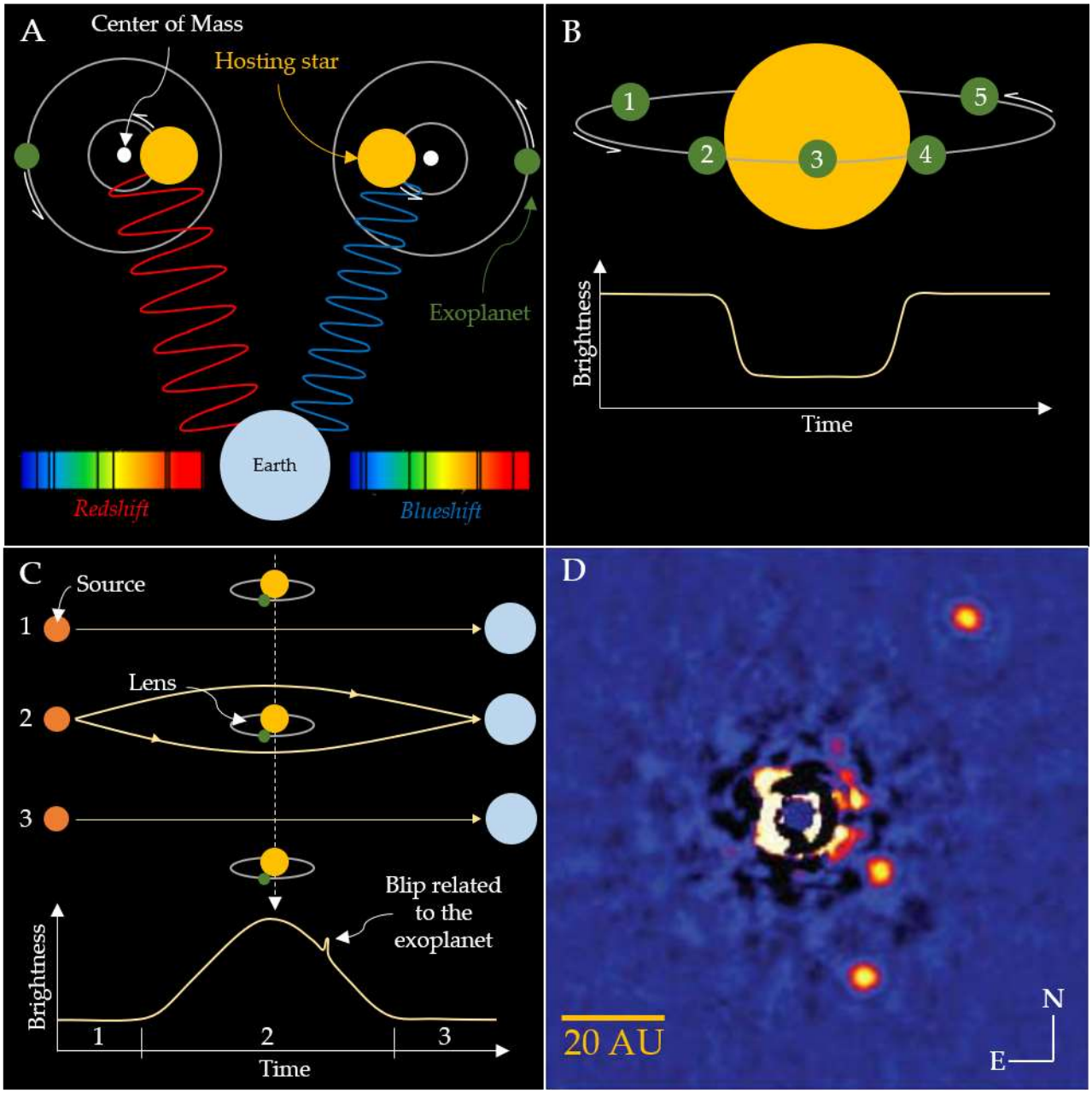

Figure 6.2 - **A)** Radial Velocity measures the Doppler shift induced on the visible part of the spectrum of light coming from the star by an orbiting exoplanet; **B)** Transit Photometry analyses the variation of the intensity of the starlight yielded by the transit of an exoplanet. The orbit of the transiting exoplanet needs to lie on or close to the equatorial plane of the Earth to be observed; **C)** Gravitational Microlensing allows detecting an exoplanet orbiting around the star that acts as lens. The exoplanet causes a peculiar blip on the light curve of the magnified source. **D)** Example of three exoplanets orbiting HR8799 observed through high contrast near-infrared Direct Imaging (modified from Marois et al., 2010).

- *Direct Imaging*: This represents (to date) the only existing direct method and consists in detecting exoplanets as point sources of light (Figure 6.2D). The most challenging aspect of this approach lies in the brightness of the Star that is several orders of magnitude greater than that of the planets, which reflect the light of the host star. To cope with this issue, the

emission of the host star is obscured through a dedicated mask and exoplanets are usually observed in the thermal infrared where the star-planet contrast is more favourable. Particularly bright exoplanets and exoplanets orbiting at several AU (Astronomical Unit, 1AU: Sun-Earth distance, i.e., 150 million of km) from the star are more likely to be observed with Direct Imaging.

Combining all the information from the various observation techniques to build models of formation, evolution and composition of planetary systems is a supreme, holistic example of interdisciplinary science in which physics, astronomy, chemistry, geology, and ultimately even biology, must combine in order to obtain a synoptic, robust and reliable theory capable of describing at the same time our own solar system and the newly discovered planetary systems.

6.1.1 OARPAF astronomical observatory: a local source for exoplanets data taking

As part of this PhD project, I participated in the efforts to commission and prepare the data taking software tools for a local facility that is currently routinely used for exoplanet measurements (Ricci D., Tosi S., Balbi E., et al., 2021). The Regional Astronomical Observatory of the Antola Park (OARPAF, Figure 6.3A) is an 80 cm optical telescope. It is installed in the Comune di Fascia (GE), Liguria, Northern Italy, at 1480 m a.s.l. in an area characterised by extremely small light pollution. Scientific and outreach activities at OARPAF are managed by the interdepartmental Observations and Research in the Science of Astronomy (ORSA) group that includes researchers from the department of Physics (DIFI), Mathematics (DIMA), Chemistry and Industrial Chemistry (DCCI), Informatics, Bioengineering, Robotics and System Engineering (DIBRIS), Telecommunications, Electric, Electronic and Naval Engineering (DITEN), and Earth, Environmental and Life Sciences (DISTAV) of the University of Genova. Following the growing scientific interest in astronomical studies and in the facility, ORSA established important scientific collaborations with the Italian National Institute for Astrophysics (INAF) and the National Institute for Nuclear Physics (INFN).

OARPAF is equipped with an 80 cm alt-azimuthal Cassegrain–Nasmyth T0800-01 telescope manufactured by ASTELCO Systems (http://www.astelco.com). The optical scheme includes three mirrors: M1) 80 cm primary concave parabolic mirror (reflectivity >95%) which reflects and focuses the light on the secondary mirror; M2) secondary convex hyperbolic mirror also used for focusing; M3) a relatively small tertiary flat mirror that reflects the light to one of the two Nasmyth foci of the telescope at f⁄8, with a focal length of 6.4 m.

The OARPAF telescope can be repositioned to point an object at a velocity of 20°/s and an acceleration of 20°/s^2. Due to the alt-azimuthal mount, the image of the sky rotates in the focal plane during data acquisition, thus a derotator is also installed to capture long-exposure images. Careful positioning is crucial for accurate telescopic measurements. In this way, the different static, and dynamic intrinsic errors are compensated by pointing reference stars. Astelco Systems provides a dedicated software that allows creating new pointing models or improving the existing ones by adding more measurements. After refining our pointing model, pointing accuracy <10'' root mean square was obtained. Night tests showed that during a 30-min observation on the same target, the tracking precision is <1''. In addition, scientific acquisitions require precise site characterization. To this end, several measurements and calibrations were conducted including: i) determination of the average sky background; ii) determination of the typical seeing of the site; and iii) determination of the extinction coefficients and zero points.

OARPAF is able to conduct a wide range of scientific research activities, including analyses on active galactic nuclei, gravitationally lensed quasars, asteroids and exoplanets. In particular, exoplanets can be detected and studied through the transit photometry: the light emission by the host star is monitored for several hours and, when the planet transits in front of it, the depth and duration of the drop in the observed luminosity allows to determine the kinematic and dynamical properties of the planet transit (Figure 6.3B). During the last years numerous gaseous exoplanets have been studied with OARPAF, such as: WASP-58b, HAT-P-3b, HAT-P-12b and TrES-3b. Observations conducted on TrES-3b were combined with a series of measurements performed with Observatorio Astronomico Nacional de San Pedro Martir, Mexico, Observatorio de la Universidad de Monterrey, Mexico, and Telescopio Carlos Sanchez at the Observatorio del Teide, Spain, and combined to derive physical and orbital parameters of the planet (Ricci et al., 2017, Figure 6.3B). Systematic observations of exoplanet transits at OARPAF are currently carried on by students and researchers of the University of Genova and contribute to the ExoClock project (https://www.exoclock.space), a worldwide effort aimed at monitoring the ephemerides of transiting exoplanets for use by the future *Ariel* space mission (https://arielmission.space/): *Ariel*, or Atmospheric Remote-sensing Infrared Exoplanet Large-survey, will be a medium-class mission by the European Space Agency aimed at studying the formation, evolution and composition of exoplanets. Measuring the ephemerides of as many exoplanets as possible will be of fundamental importance for *Ariel*: the observations of TOI-3785b, TOI-1288b and TOI-4145Ab planets by students of the University of Genova can be seen at the following links, respectively: https://www.exoclock.space/database/observations/TOI-

3785b_1863_2023-11-06_andreadamonte_1386_R/, https://www.exoclock.space/database/observations/TOI-1288b_3227_2023-11-10_M4551001_1577_R, https://www.exoclock.space/database/observations/TOI-4145Ab_2143_2023-11-11_MORENO-MONTICELLI_1397_R.

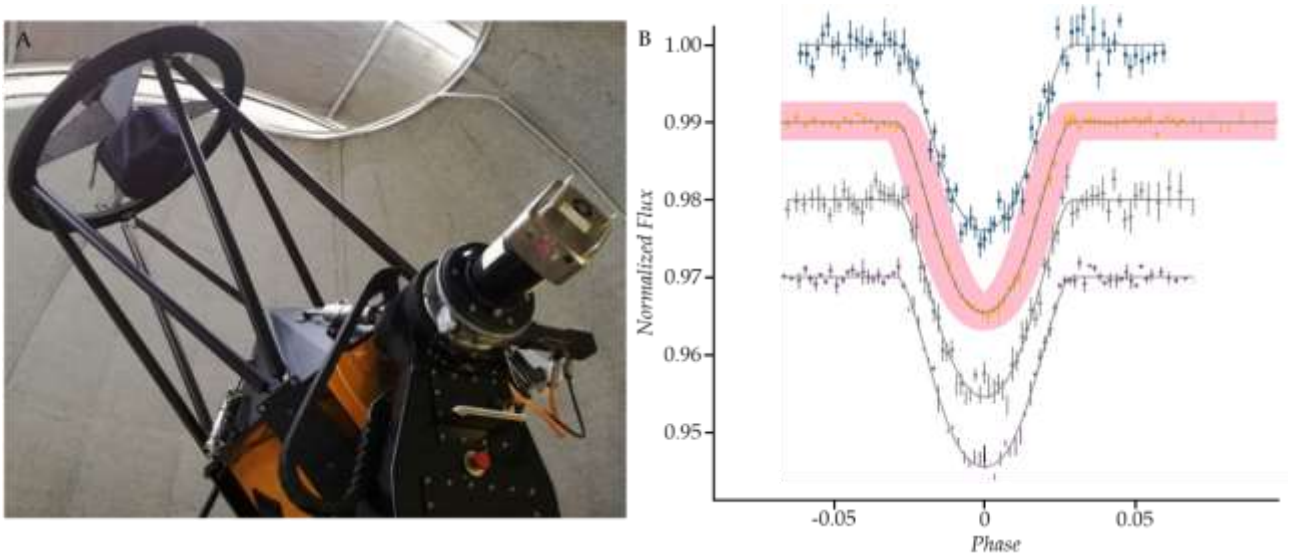

Figure 6.3 - A) The OARPAF telescope with the STL on the derotated Nasmyth focus. **B)** TrES-3b transit photometry results. The pink band indicates the OARPAF contribution. Redrawn from Ricci D., Tosi S., Balbi E., et al. (2021).

6.2 Measurements of spatial and temporal variations of Martian atmospheric CO_2 using strategies developed for exoplanets

While the statistics of exoplanets is ever increasing, new campaigns and experiments are planned for the next decade to better characterise exoplanet systems and build realistic formation and evolution models, ultimately aiming at precisely determining the chemical compositions and even the potential for hosting life. The *Ariel* space mission and the high-resolution optical and near-infrared spectrograph ANDES (https://elt.eso.org/instrument/ANDES/) which will be installed at the ELT, a new 40-m class optical telescope currently under construction in Chile (https://elt.eso.org), will have the capabilities to measure the properties of atmospheres with an unprecedented precision, identifying features linked to the possible presence of life. In order to achieve such an ambitious goal and derive unambiguous conclusions, the techniques used must be fully understood and tested on known systems. The collaborations established at OARPAF allowed to participate not only in the global efforts to characterize exoplanet systems using the currently available facilities but also to prepare the tools and techniques to boost the scientific output of those future missions, an example being the study of Mars as an exoplanet analogue.

Although the Solar System might seem to be "atypical", the ever-improving knowledge in planetary sciences allowed considering the major bodies that orbit the Sun as proxy to better frame the setting of other planetary systems. In particular, Mars represents a good analogue of terrestrial exoplanets and a great laboratory to investigate their global-scale geologic properties. Its surface hosts numerous regional scale fracture zones such as the CF that, as discussed in the previous chapters, could represent a preferential pathway for fluid migration able to connect the inner planet and its atmosphere. In this way, the recent and present-day tectonic (and seismic) and volcanic activity highlighted on the Red Planet (e.g. Hauber et al., 2011; Sita & van der Lee, 2022; Fernando et al., 2023; Pieterek et al., 2024; Andrews-Hanna & Broquet, 2023) could suggest that signatures of planetary geodynamic evolution might be hosted (and detected) in the Martian atmosphere. In the frame of this thesis, temporal and spatial variations, both in strength and dynamics, of the atmospheric signal of the Martian CO_2 are investigated through astrophysical observational techniques and analytical strategies usually used to investigate exoplanets. The CO_2 is here considered a crucial molecule for geodynamic investigations due to i) its high concentration in the Martian atmosphere (>95%), and ii) its possible linkage, such as on Earth, with multiple geologic processes (e.g. volcanic activity). The identified signatures cover a key role in exoplanetary research since they can be sought in the atmospheric spectra of terrestrial exoplanets to look for geologic activity. This will be of particular interest in the near future with the new generation telescopes which will be able to analyse exoplanets with dimensions similar to Mars. Indeed, one of the main scientific goal of ANDES will be the study of terrestrial planets in reflected light, an observational technique recently applied also in exoplanetary research. Commonly, exoplanet atmospheres are analysed through transmitted and emitted light. The first one can be used only for transiting exoplanets, the second one only with "hot" exoplanets. In this way, the advantage of observing Mars from Earth is that the Red Planet can be analysed only thought reflected light, since it is external to the orbit of Earth (i.e. it never transits between Earth and Sun) and it is too cold for analysing the emitted visible light with optical telescopes.

Measurements on the Martian CO_2 were conducted thanks to the observing program A46TAC_22 obtained at the Telescopio Nazionale Galileo (TNG) operated by the Fundación Galileo Galilei of the Italian Istituto Nazionale di Astrofisica (INAF) at the Observatorio del Roque de los Muchachos in La Palma, Canary Islands, Spain. PI of the project Dr. Monica Rainer, INAF-Osservatorio Astronomico di Brera.

6.2.1 Instrumentation and Method

6.2.1.1 Observing Strategy

Mars was observed using the high-resolution near-infrared slit spectrograph of GIANO-B (Oliva et al., 2012; Origlia et al., 2014; Claudi et al., 2018) at the TNG. GIANO-B covers 950-2450 nm of spectral range with a nominal resolution of 50 000 and can perform observations in two modes: nodding mode, used for point-like astronomical objects, and stare mode, used for extended (i.e. covering the entire slit) astronomical objects. In the case of this study, Mars was observed in stare mode. In order to optimize the observational strategy to i) identify possible CO_2 temporal variations, and ii) ensure the observation of both the northern and southern hemispheres independently, six observations were planned before, around and after the spring (autumn) equinox of the Martian northern (southern) hemisphere (i.e. 26 December 2022). This time interval was selected to follow the winter-spring (summer-autumn) transition and to observe Mars during a period close to its opposition phase in order to take advantage of an apparent angular diameter larger than the slit. The size of the slit of GIANO-B is 6×0.5 arcsec (length×width), therefore, to observe the two hemispheres independently regardless of the slit inclination on the planetary disk (an uncontrollable variable) the angular diameter of Mars needed to be larger at least twice than the slit length (i.e. 12 arcsec). Each visit consisted of six pointing on different Martian regions. Each pointing was composed of five 10 seconds exposures. The short exposure time was used to keep the signal below the saturation threshold. Then, the five signals were summed up to increase the Signal-to-Noise Ratio (SNR). The position of the slit is registered at the beginning and at the end of each pointing to evaluate the drift of each pointing and to confirm their stability (Figure 6.4).

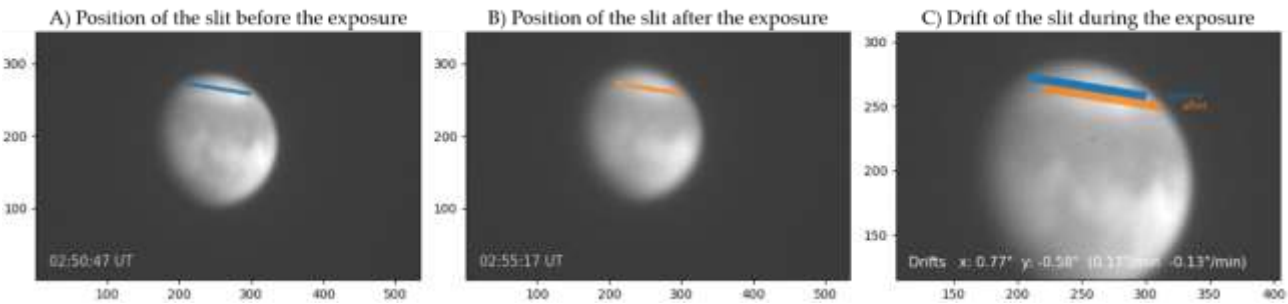

Figure 6.4 - Position of the slit **A)** before (blue line) and **B)** after (orange line) the pointing to evaluate the drift **C)**. The low drift allows confirming the stability of the pointing in order to sum up the five exposures to increase the SNR (Redrawn after Rainer, Balbi et al., in prep.).

6.2.1.2 Data reduction

Raw data obtained with GIANO-B are firstly processed through the online Data Reduction Software (DRS) (Harutyunyan et al., 2018) at the telescope. However, an issue of persistence of the signal of the wavelength calibrating UNe (Uranium-Neon) lamp on the detector forces to perform this particular calibration step at the end of the night, to avoid contaminating the scientific data with the residuals of the emission lines of the UNe lamp. Due to this issue, the online DRS performs the wavelength calibration on the fly with archival data, in order to allow the observer an immediate check of the data quality, knowing that the online wavelength calibration may not always be optimal. Thus, a second reduction of the data offline is recommended using the UNe lamp observed immediately after the scientific observations, to ensure a correct wavelength calibration for the specific observing night. The freely available software *Gofio* (Rainer et al., 2018, https://atreides.tng.iac.es/monica.rainer/gofio), which is an integral part of the online DRS, allows performing the reduction of the raw data offline. For each stare mode spectrum, *Gofio* provides two final outputs: i) a wavelength calibrated, barycentric corrected mono-dimensional spectrum with the echelle orders merged and a constant step in wavelength, and ii) a wavelength calibrated, not barycentric corrected spectrum with the echelle orders separated and the original constant step in pixel. Following the tradition of precise exoplanet studies, the second output with a spectrum less manipulated is more suitable to analyse Mars "as if it was an exoplanet".

6.2.1.3 Telluric contamination removal

Raw data obtained through ground-based telescopes are always affected by signals related to Earth's atmosphere (namely, telluric bands). Exoplanetary spectra are also typically blended with their host star spectra: aside for the very few cases where it is possible to detect the planets with direct imaging, host star and exoplanets are observed at the same time, and the resulting data carry both the spectra superimposed. The same situation is not present in the Solar System objects. However, the light observed from Mars, in the IR spectral range, is mostly the reflected solar light, that penetrates the Martian atmosphere and then it is reflected back from the ground thus carrying contribution of both Martian surface reflectance and the signature of the Martian atmosphere. Therefore, the Solar spectrum should be still considered. The light reflected from Mars is subsequently observed by telescopes on Earth after passing through terrestrial atmosphere, where further scattering and absorption occur resulting in additional absorption lines. To analyse temporal and spatial variation of atmospheric Martian CO_2, a very careful removal of the CO_2 telluric bands is necessary also

considering that near-infrared spectra are more susceptible to significative telluric contaminations. Telluric removal is conducted through the European Southern Observatory's (ESO) software *molecfit* (Smette et al., 2015; Kausch et al., 2015). GIANO-B is an echelle spectrograph: echelle grating is a type of diffraction grating characterized by a relatively low groove density, optimized for use at high angles of incidence and thus resulting in high diffraction orders. In GIANO-B each echelle order is independently wavelength calibrated (Oliva et al., 2018). However, this calibration is not equally accurate for all orders depending on the number and strength of the Une lamp emission lines that fall in each order, yielding a non-homogeneous precision in the results. This may lead to incorrect telluric removals if the telluric lines are removed in a single step from the whole merged spectrum. This is due to a misalignment between the observed spectra and the computed telluric transmission spectrum. To bypass this issue, each single order is corrected by itself using *esoreflex*, the graphical interface of *molecfit*. For each order, the molecules to be removed and the regions where to compute the atmospheric model are defined separately. Nevertheless, the Martian CO_2 signal is almost overlapped to that of the Earth. In this way, *molecfit* would consider together both signal thus estimating excessively high contents of CO_2 and removing both contributions. To avoid removing the Martian features, *molecfit* is used to adjust the abundance of telluric CO_2 by modelling another molecule existing in the same processed orders and that is absent or very little abundant on Mars (typically H_2O). This last molecule is thus used to scale the CO_2 abundance and to remove the telluric contamination. Figure 6.5 shows the results of the telluric removal in a region of the spectrum rich in CO_2 lines.

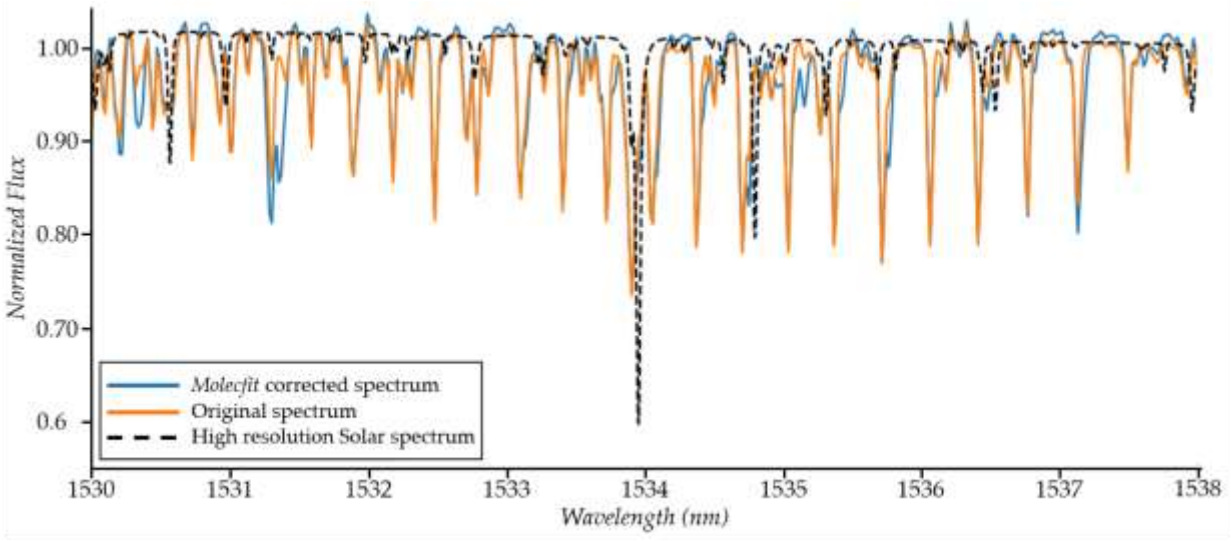

Figure 6.5 - Martian spectrum before (orange) and after (blue) the telluric removal. Telluric contaminations are blended with the Martian spectrum, removal as accurate as possible is fundamental to obtain precise data on CO_2 variation in the Martian atmosphere. Black dashed line indicates the high resolution Solar spectrum in the same wavelength range (Solar spectrum lacks CO_2 signal) (Redrawn after Rainer, Balbi et al., in prep.).

6.2.1.4 Data analysis and Equivalent Width (EW) computation

In the case of bodies close to Earth such as Mars, spectra can be thoroughly analysed by isolating the single lines of chemical elements or molecules (CO_2 in the case of this study, Figure 6.5). On the other hand, exoplanets signals are several times smaller. Thus, masks which allow locating that chemical element or molecule within the spectrum are made. As stated at the beginning of Section 6.2, analysing Mars "as if it was an exoplanet" makes necessary to treat the data obtained through the observation with the same technique used in exoplanetary studies. Therefore, a cross-correlation technique is here applied to sum up in a single profile all the identified lines of the atmospheric Martian CO_2 in the wavelength range of 1200-2300 nm (that is the mask used in the case of this study). Despite the removal of the telluric contamination, Martian spectrum is also influenced by the reflected solar spectrum, which falls almost at the same radial velocity (RV) of the Martian spectra (precise RVs of both spectra are obtained via the JPL Horizons service with the *astroquery* python package). The solar spectrum lacks CO_2, nevertheless other absorption lines falling in the same wavelength ranges can exist. To prevent any other contamination, all the spectral lines less than 15 km/s ($\pm$15 km/s is the range within which both CO2 and Solar absorption lines of the measurements fall) from any solar line are removed from the CO_2 mask (black dashed line in Figure 6.5 refers to the disk-integrated high-resolution solar spectrum - SOLAR-HRS5 from Meftah et al., 2023 - used as reference solar spectrum). In this way, the length of the mask decreases from 1428 to 1012 lines. An additional mask is applied by selecting all the local minima of the SOLAR-HRS spectrum in the same wavelength range of the main mask (i.e. 1200-2300 nm), this will allow us to compute a cross-correlation between the spectra and a solar mask and isolate the solar signal, to be used as a comparison for our variability studies. Then, all the lines contaminated by the Martian CO_2 are discarded eventually leaving around 16000 lines.

Normalized CO_2 profiles obtained for each observation are analysed through the Equivalent Width (EW) to highlight spatial CO_2 variations. EW is calculated with two different methods to exclude computation dependencies and thus to increase the reliability of the results. The first method involves the fit of the profile with a Gaussian. In this case, EW represents the area of the Gaussian and is given by:

$$EW = \sqrt{2\pi} \times \sigma \times d \qquad \text{(Eq. 5)}$$

Where σ is the standard deviation and d is the depth of the Gaussian. In the second method, EW is computed as the zero moment of the line profiles and represents the area of the observed data

instead of the fitting function (Briquet & Aerts, 2003). The Gaussian fit is still used to automatically define the limits of the profile as the centre of the line $\pm 3\sigma$.

6.2.2 Preliminary results and first considerations

Despite the great effort of the TNG operators, weather conditions between October 2022 and February 2023 allowed conducting only three observations out of the six planned. The time interval before the equinox was homogeneously covered (1st observation: 9 October 2022; 2nd observation: 11 November 2022; 3rd Observation: 16 December 2022 - Figure 6.6), however no observations were conducted after the 26 December 2022. This prevented monitoring any temporal (seasonal) variation of the atmospheric Martian CO_2. Although the details of the surface were slightly blurred during the observations, they were clear enough to allow the identification of the different Martian regions and global-scale physiographic features (e.g. Highlands, Lowlands, Tharsis, Thaumasia).

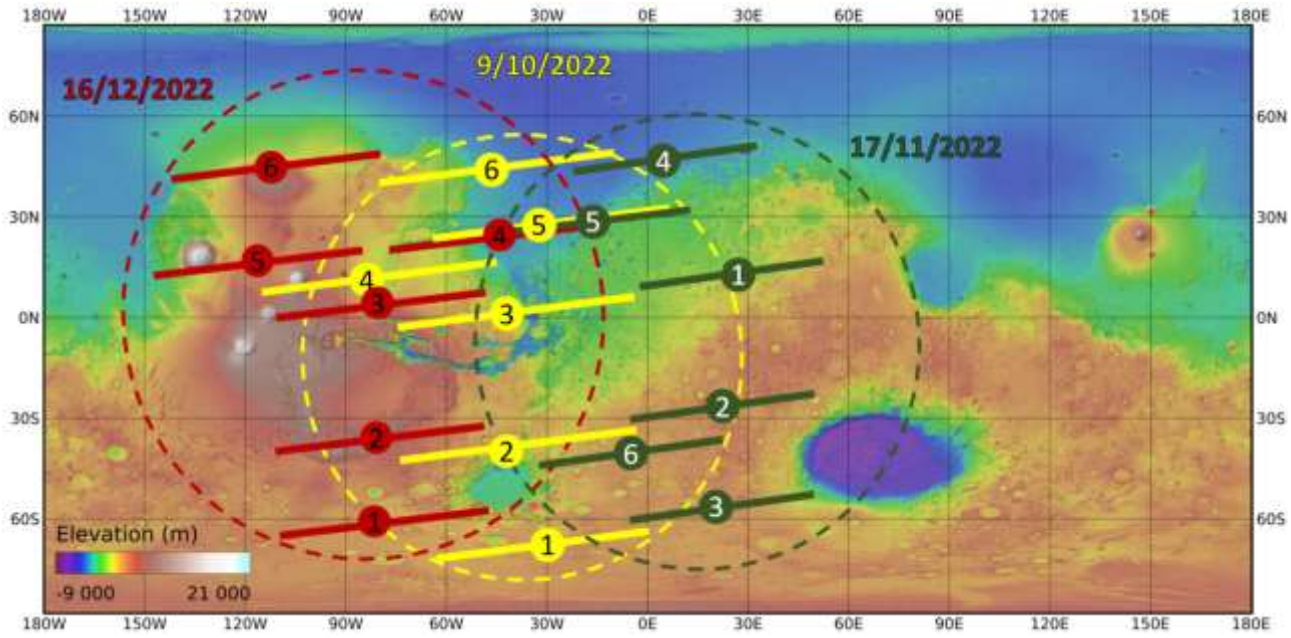

Figure 6.6 - Projection on the Martian surface of the slit position during the six pointing conducted at the three observations. Dashed circles indicate the observed portion of the Martian surface (yellow: 9 October 2022; green: 11 November 2022; red: 16 December 2022) (Redrawn after Rainer, Balbi et al., in prep.).

The accurate locations of the slit for each pointing (i.e. the average projection on the Martian surface of the slit at each pointing) were identified in a second time and reported in Table 6.1. All the pointing with the position of the slit before and after the exposure for the three conducted observations are included in Appendix 2.

Telluric contamination is successfully removed despite the heavy blending of the Martian and Terrestrial CO_2. In Figure 6.7 (upper panels) original CO_2 profiles of the first pointing of each observation are compared with *molecfit* corrected spectra to show the accuracy of the operation. As

stated in Section 6.2.1.2, spectra derived from *Gofio* are not barycentric corrected, thus the telluric signal falls always at 0 km/s. Lower panels of Figure 6.7 show some examples of the resulting solar profiles obtained with the SOLAR-HRS mask. The comparison between them with the Martian CO_2 profiles clearly highlights that both spectra have almost the same RV.

Pointing	Region	Central point
9 October 2022		
1	South polar cap	70°S 30°W
2	Argyre Planitia - Noachis Terra	40°S 45°W
3	Valles Marineris - Xante Terra - Arabia Terra	0°N 45°W
4	Tharsis Montes - Lunae Planum	10°N 85°W
5	Lunae Planum - Chryse Planitia - Arabia Terra	25°N 35°W
6	Tempe Terra - Acidalia Planitia	40°N 50°W
17 November 2022		
1	Arabia Terra - Terra Sabaea	10°N 25°E
2	Noachis terra - Terra Sabaea	25°S 25°E
3	Noachis Terra	55°S 20°E
4	Acidalia Planitia	45°N 5°E
5	Chryse Planitia - Arabia Terra	30°N 15°W
6	Noachis Terra	40°S 5°E
16 December 2022		
1	Aonia Terra	60°S 80°W
2	Claritas Fossae - Thaumasia Highlands	35°S 80°W
3	Tharsis Montes – Lunae Planum	5°N 80°W
4	Lunae Planum - Chryse Planitia - Arabia Terra	25°N 45°W
5	Olympus Mons – Tharsis	15°N 115°W
6	Alba Patera	45°N 110°W

Table 6.1 - Identified Martian regions for each pointing (numbers are referred to Figure 6.6) of the three conducted observations. To the right the coordinates of the slit centre are shown (Redrawn after Rainer, Balbi et al., in prep.).

In Figure 6.8 values of EW obtained through the Gaussian fitting (upper panels) and Moment methods (lower panels) are shown. Results of both methods are in agreement, thus confirming no computational dependencies. To estimate the errors on the zero moment the standard deviation of

the continuum outside the line is used. GIANO-B spectra are affected by a pseudo-sinusoidal fringing that heavily increase the standard deviation and accordingly the error. Since line profiles are quite clean and Gaussian-shaped, the Gaussian fit returns lower fitting errors. Therefore, data obtained through the Gaussian method are considered representative of the evaluation of the EW evaluated in this study (Table 6.2). Results show variations in the concentration of Martian atmospheric CO_2 in the different observed regions of Mars. This is visualized in Figure 6.9A where circles with size proportional to the estimated EW values are shown. An incorrect telluric removal that may have affected the results can be excluded since the comparison of the atmospheric parameters found by *molecfit* in the three nights are consistent for the entire time range. In particular, the second observation (11 November 2022) shows the highest absolute values and the largest spread of EWs. To ensure that no correlation between CO_2 variations and instrumental effects exists, the EWs of the solar profiles are computed as well (Figure 6.9B). It should be noted that during the second observation, although the EWs values are the highest and more spread, the solar EWs are still high, but very stable. This suggests that the detected variation of the Martian EWs is likely related to a real physical cause. If the variation was caused by computational bias or incorrect telluric removal this should be found also in the solar EWs.

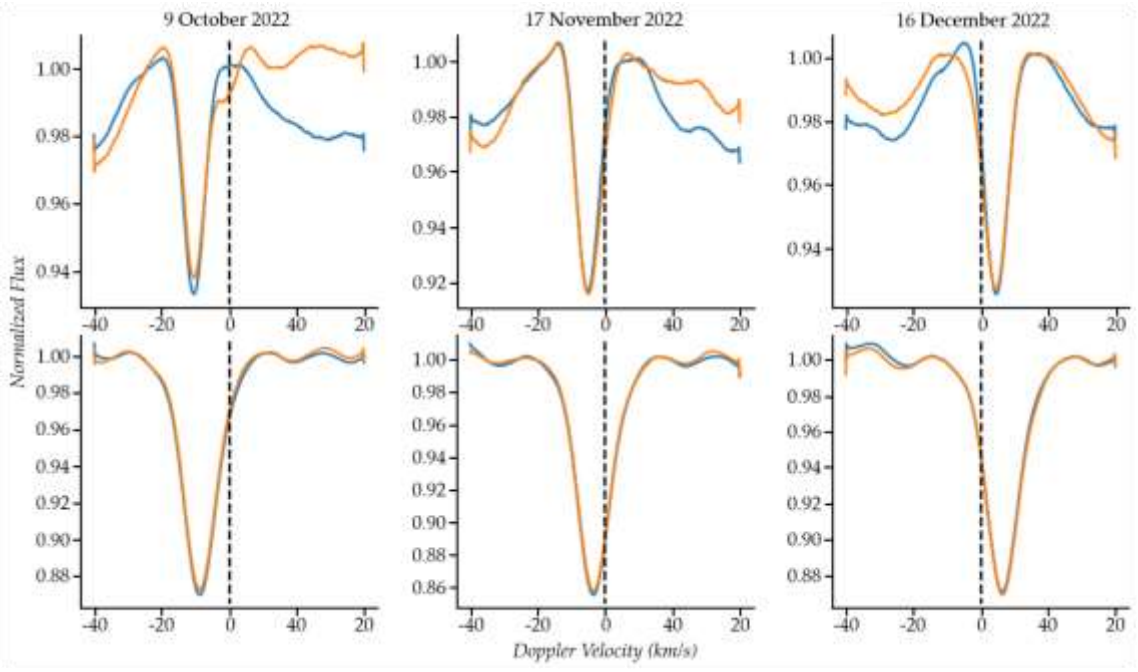

Figure 6.7 - Martian CO_2 and reflected solar light mean line profiles during the first pointing of the three observations. **Upper panels**: Comparison between CO_2 profiles before (orange) and after (blue) the telluric removal. Dashed vertical lines show where the telluric signal falls (0 km/s). Among the three observations, blending increases due to the different velocity of Mars relative to the Earth. Distortions on the line continuum are due to both the fringing that affects the GIANO-B spectra and the correlation with the CO2 lines that we excluded from our mask due to solar contamination. **Lower panels**: profiles of the solar reflected spectra. Lack of telluric molecules in the solar spectrum makes the telluric contamination in this case very faint (Redrawn after Rainer, Balbi et al., in prep.).

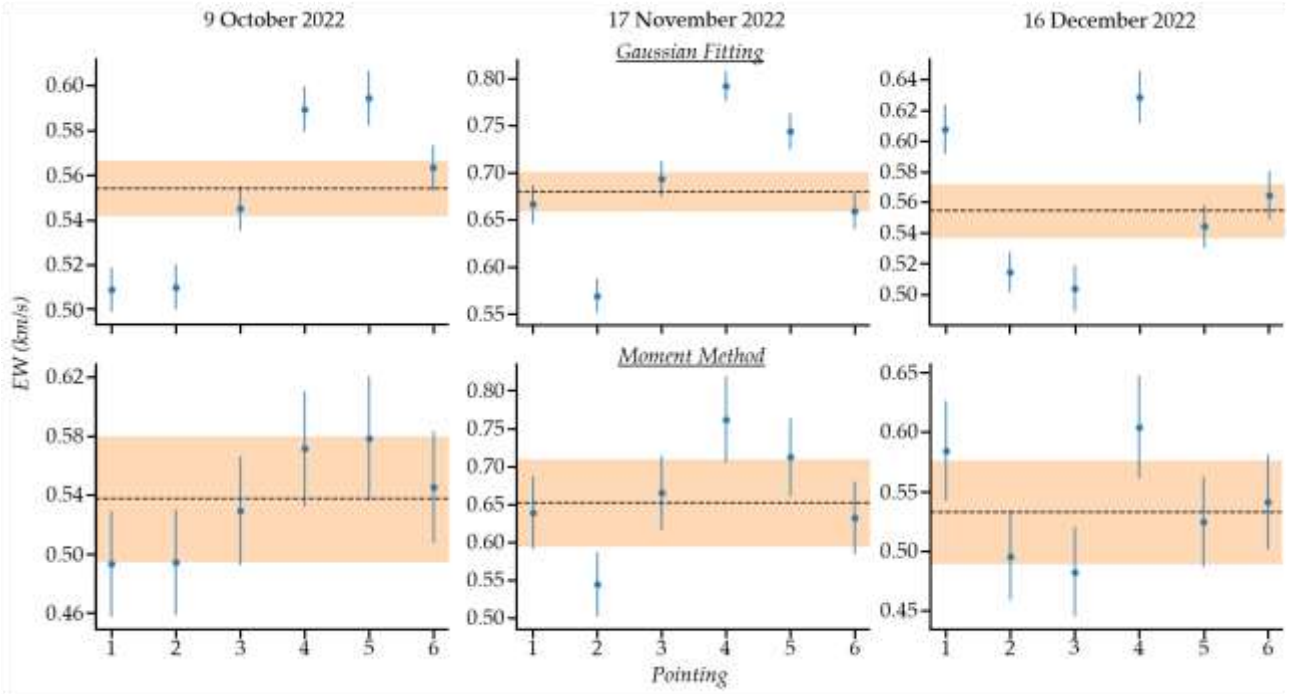

Figure 6.8 - Spatial variations of EW of the Martian CO_2 profiles calculated with the Gaussian fitting method **(upper panels)** and the Moment method **(lower panels)**. Dashed black line represents the median, the shaded orange area shows the region around the median within the maximum error computed on the measured EWs. Results of the Gaussian method are used as representative of the EW of the CO_2 spectra due to their considerably lower error (Redrawn after Rainer, Balbi et al., in prep.).

9 October 2022		*17 November 2022*		*16 December 2022*	
Pointing	**EW (km/s)**	**Pointing**	**EW (km/s)**	**Pointing**	**EW (km/s)**
1	0.508 ± 0.013	1	0.653 ± 0.019	1	0.609 ± 0.018
2	0.512 ± 0.013	2	0.553 ± 0.018	2	0.518 ± 0.015
3	0.548 ± 0.013	3	0.675 ± 0.018	3	0.507 ± 0.018
4	0.588 ± 0.013	4	0.773 ± 0.015	4	0.632 ± 0.020
5	0.601 ± 0.013	5	0.721 ± 0.018	5	0.549 ± 0.016
6	0.563 ± 0.013	6	0.633 ± 0.018	6	0.568 ± 0.019

Table 6.2 - Mean value of the EWs obtained through the Gaussian method for each pointing during the three conducted observations. Results highlight spatial variation in the concentration of the Martian atmospheric CO_2 (Redrawn after Rainer, Balbi et al., in prep.).

Due to the inclination of Mars respectively to the Earth during the observations, the majority of the pointing occurred in correspondence of the highlands. Nevertheless, a few pointing captured the crustal dichotomy. It is interesting to note that some of the highest EW values are right in correspondence of the transition highlands-lowlands, precisely between Arabia Terra, Acidalia Planitia and the easternmost part of Tharsis. In addition, latitudinal CO_2 variations can be observed

also over Tharsis and surrounding areas from north to south (Figure 6.9A). This is of particular interest since Tharsis includes a huge variety of regional- and global-scale volcano-tectonic features such as Claritas Fossae, Valles Marineris, and Noctis Labyrinthus. Previous studies analysed the relation that exists between CO_2 surface pressure changes and the topography on Mars mainly yielded by the different atmospheric path length (Chamberlain et al., 2005, 2006). Nevertheless, at present a direct relationship between the major volcano-tectonic features on Mars and the measured spatial variation in the atmospheric CO_2 concentration cannot be proposed. Possible contributions to the CO_2 concentrations might also derive from seasonal/climatic variations related/associated to release from the polar ice cap and/or mid-latitude permafrost layers affected by (ice)tectonic features where CO2 pockets are present (Kieffer et al., 2006; Phillips et al., 2011; Pilorget & Forget, 2016; Dickson et al., 2023). These last processes deserve to be further investigated planning new, extended observational campaigns also to assess the contribution of seasonal variations.

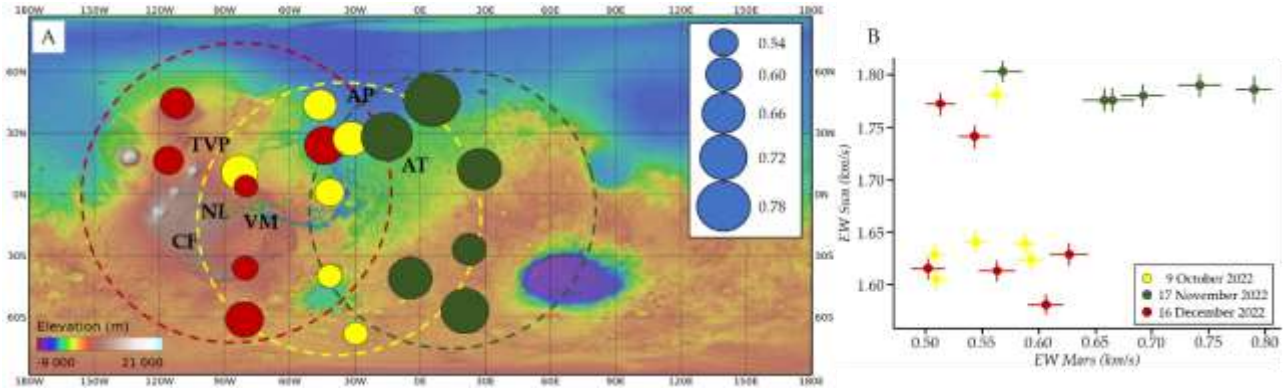

Figure 6.9 - A) Circles represent the central point of the slit for each pointing of the three observations (yellow: 9 October 2022; green: 11 November 2022; red: 16 December 2022, see also Figure 6.6). Size of the circles are proportional to the values of EW of the Martian CO_2 profiles (Table 6.2). TVP: Tharsis Volcanic Province; NL Noctis Labyrinthus; CF: Claritas Fossae; VM: Valles Marineris; AP: Acidalia Planitia; AT: Arabia Terra **B)** Comparison between EWs of Sun and Mars for each pointing (Redrawn after Rainer, Balbi et al., in prep.).

6.3 Conclusive Remarks

Observing Mars by applying techniques and analytical strategies usually used to investigate exoplanets represents an original approach that allowed successfully detecting spatial CO_2 variations in the atmosphere. Further in-depth analyses are necessary to understand the origin (endogenous Vs exogenous, including a possible climatic contribution) of the observed spatial variation of CO_2 atmospheric concentration. Nevertheless, the proposed method is truly promising and will be applied to other bodies of the Solar System and to other molecules of particular interest for bio/geo-investigations in exoplanetary research, such as hydrocarbons, ammonia, or phosphate. This will be fundamental to develop models to be compared with exoplanetary measurements,

especially with data that will come in the near future from the new generation telescopes. That is the case of the ANDES spectrograph of the ELT that will analyse terrestrial exoplanet through the reflected light spectra. In particular, the combination of high-resolution spectrographic data and the analysis of atmospheric molecules of particular relevance (e.g. CO2) could represent a pioneering tool to map the topographic surface of terrestrial exoplanets.

Chapter 7

General Conclusions

This thesis proposes an original workflow capable of providing significative insights on the evolution and on the present-day setting of terrestrial planets and exoplanets. The proposed workflow consists of i) an initial detailed characterization of terrestrial planets through the combination of geological and geophysical approaches (Chapter 3, 4, and 5), and ii) the challenging task of finding a robust method to link geological/geophysical and astronomical/astrophysical investigations to characterize exoplanets and exoplanetary systems (Chapter 6). The combination of kinematic numerical modelling, structural mapping, clustering analysis, and lineament domain analysis in the first part of the workflow revealed effective in unravelling the tectonic setting and highlighting complex, polyphase history of tectonically controlled regions. Independent analyses pointed to similar results thus making them robust and strengthening the reliability of findings and interpretations. In detail, the twofold approach presented in Chapter 3 combining kinematic numerical modelling and structural mapping has allowed proposing a detailed kinematic evolution of the CF. A polyphase scenario has been advanced consisting of a Noachian to Early Hesperian right-lateral strike-slip event characterised by fault-parallel extension and a Late Hesperian/Early Amazonian reactivation in right-lateral transtensional regime characterised by a fault-perpendicular extension. This approach has highlighted a significative underestimation of the extensional strain in the area of the CF, and likely more in general on Mars, and has provided important constraints about the architecture of the crust beneath the study region. These do not allow constraining between isostatic compensation or flexural elastic deformation models associated to the Tharsis induced stress. Nevertheless, they will inform future geodynamic modelling on planetary thermal evolution, cooling processes, and tectonic styles that a planets with a rigid outer shell can experience since its formation. The subdivision in azimuthal sets found through the regional scale structural mapping has been confirmed by the clustering workflow presented in Chapter 4. This method has allowed objectively categorizing the tectonic lineaments outcropping at the CF based on their characteristics and accurately reproducing the distribution of the azimuthal sets. The strength of the proposed clustering workflow lies in its high capability of finding subsets not recognized by more widely used geostatistical analyses. This has allowed highlighting areas characterized by different deformation thus confirming that the ESc, modelled as the superficial manifestation of a crustal-scale listric fault,

represents the area of the CF where the deformation most concentrated. Results of the structural mapping have been further strengthened by the lineament domain analysis. In particular, both the manual and the automatic approaches conducted to identify lineament domains in the CF have highlighted the existence of two main domains. Their spatial distribution and angular relationship suggest their development within a right-lateral transtensional deformation corridor. As highlighted for the results of the other methods, also in this application the relationship between the two domains and the different aged terrains of the CF support the polyphase tectonic scenario. The second part of the workflow has been focussed on studying Mars as "if it was an exoplanet". This represents an original perspective to look to an object close to the Earth for which ever more detailed and high resolution data are usually sought. In the study presented in this thesis, astrophysical observational techniques and analytical strategies usually used to investigate exoplanets are applied to detect spatial and temporal variation of peculiar molecules in the Martian atmosphere. Although analysis of the data are still in progress at the time of writing this thesis, preliminary results are promising. Spatial variations of the Martian CO_2 have been detected with very interesting data coming from the crustal dichotomy and Tharsis, the two most important geological feature at the global scale on Mars. Spatial variations of the atmospheric CO_2 may reflect topographic variations at the surface. In this way, finding a connection between concentration variations of specific molecules and geological features would be of outmost importance to infer the topography based on atmospheric data. This will be crucial in exoplanetary studies in which direct images of the surface of terrestrial exoplanets are (still) out of reach. Therefore, the ambitious goal of this study is to use CO_2, or other peculiar molecules, as a proxy to indirectly map the surface of exoplanets with a rigid outer shell and an atmosphere as well as to infer the existence of some kind of active geological features.

To conclude, the workflow presented in this thesis is viable and represents a novel tool for geological studies in planetary sciences. In particular, the combination of different geological, geophysical, and astrophysical principles proved to be a common (scientific) ground between geologists, trained to analyse changes of a phenomenon at all scales by monitoring a given object through time, and astrophysicists, used to infer the evolution of a phenomenon from the observation of various different objects, each representing a different stage. In the near future this common ground will be further investigated to explore structurally complex planetary bodies, such as the icy and rocky natural satellite of Jupiter and Saturn (e.g. Enceladus, Io, or Ganymede and Europa that will be

visited by the NASA's Europa Clipper mission and ESA's JUICE mission, respectively) or Venus, target of several missions in the incoming years. In this way, this workflow will be able to develop planetary models to be compared with exoplanets to better characterise them and their system. This will be crucial when space and ground-based campaign and experiments planned for the next decade (e.g. ARIEL, ELT) will provide precise data on the chemical composition of the atmosphere of terrestrial exoplanets. In this perspective, the interdepartmental and widely multidisciplinary collaboration established at OARPAF results of outmost importance to include the presented PhD project in the global efforts to characterize exoplanets and their systems.

Appendices

Appendix 1: Supplementary materials of Chapter 3

A.1.1 Tectonic numerical modelling

Different results of the modelling obtained by varying geometries and displacements of the fault (Figure A.1) and crustal thickness (Figure A.2) are shown. The best fit between the Martian topography (blue) and the modelled one (black) is achieved by tuning the different parameters with a trial-and-error procedure and several attempts.

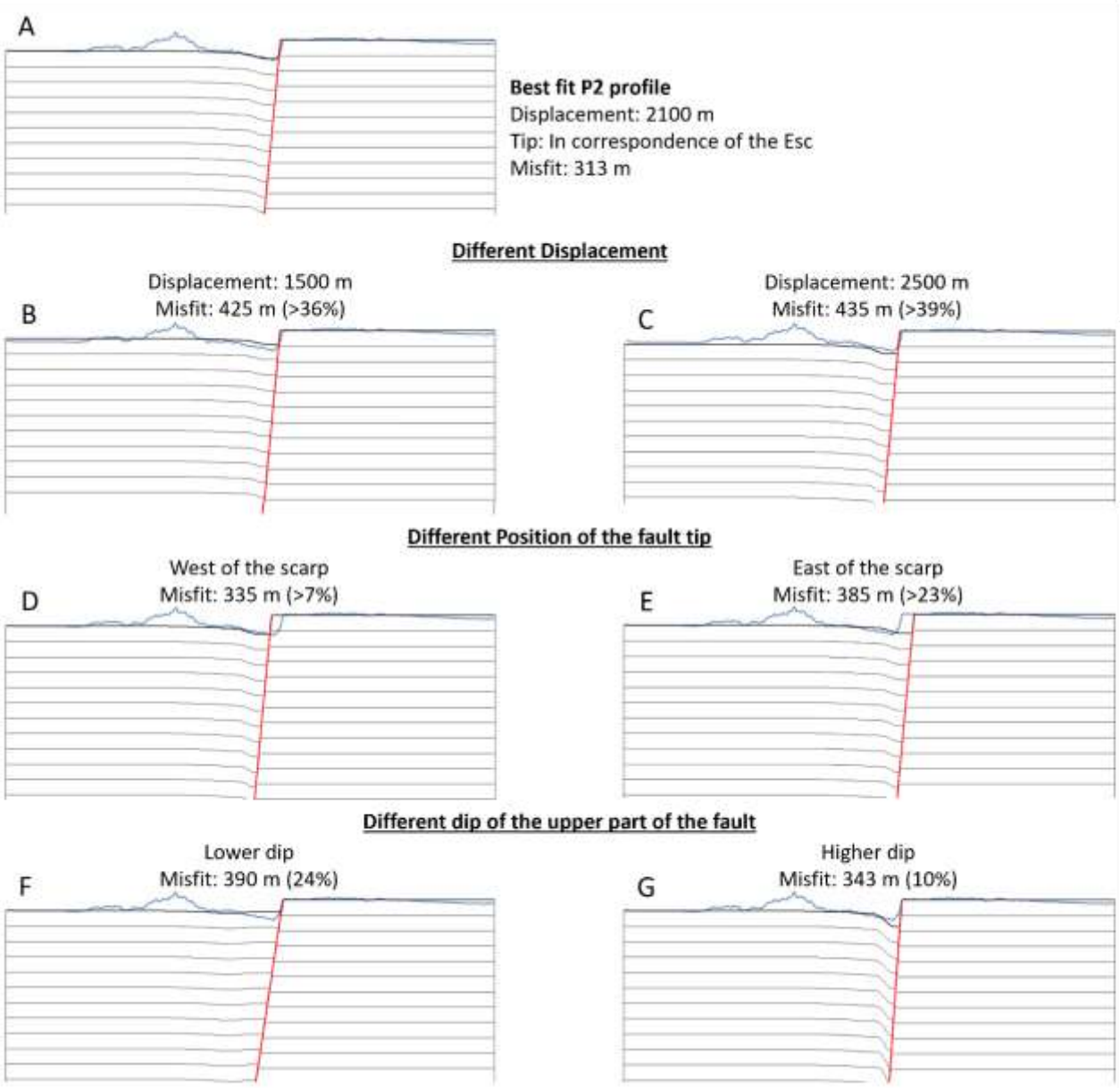

Figure A.1 - Examples of the different morphologies of the hangingwall resulting from different displacements of the fault (B - C), different position of the fault tip (D - E), and different initial dip of the fault (F-G). Vertical exaggeration of the profiles 10:1.

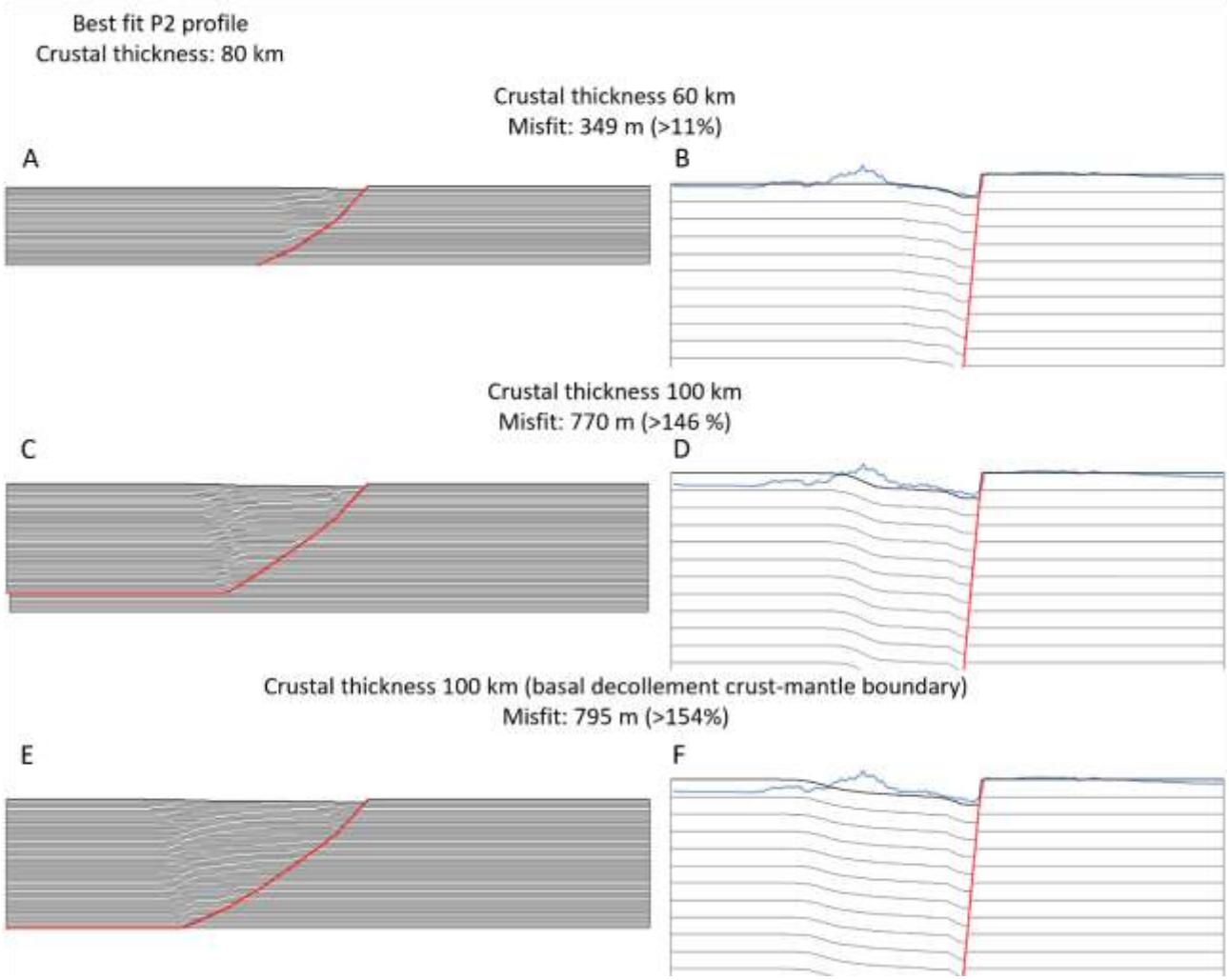

Figure A.2 - Examples of the different morphologies of the hangingwall resulting from different values of crustal thickness: 60 km (A-B). Profiles on the left have no vertical exaggeration. Profiles on the right have vertical exaggeration 10:1.

A.1.2 Mapped tectonic lineaments

Different morphologies represented by the identified tectonic lineaments belonging to the four identifies sets (figures A.3 and A.4) and evidence of right-lateral offset related to Set2 (figures A5, A6, and A7) in high resolution images (CTX mosaic 5 m/px).

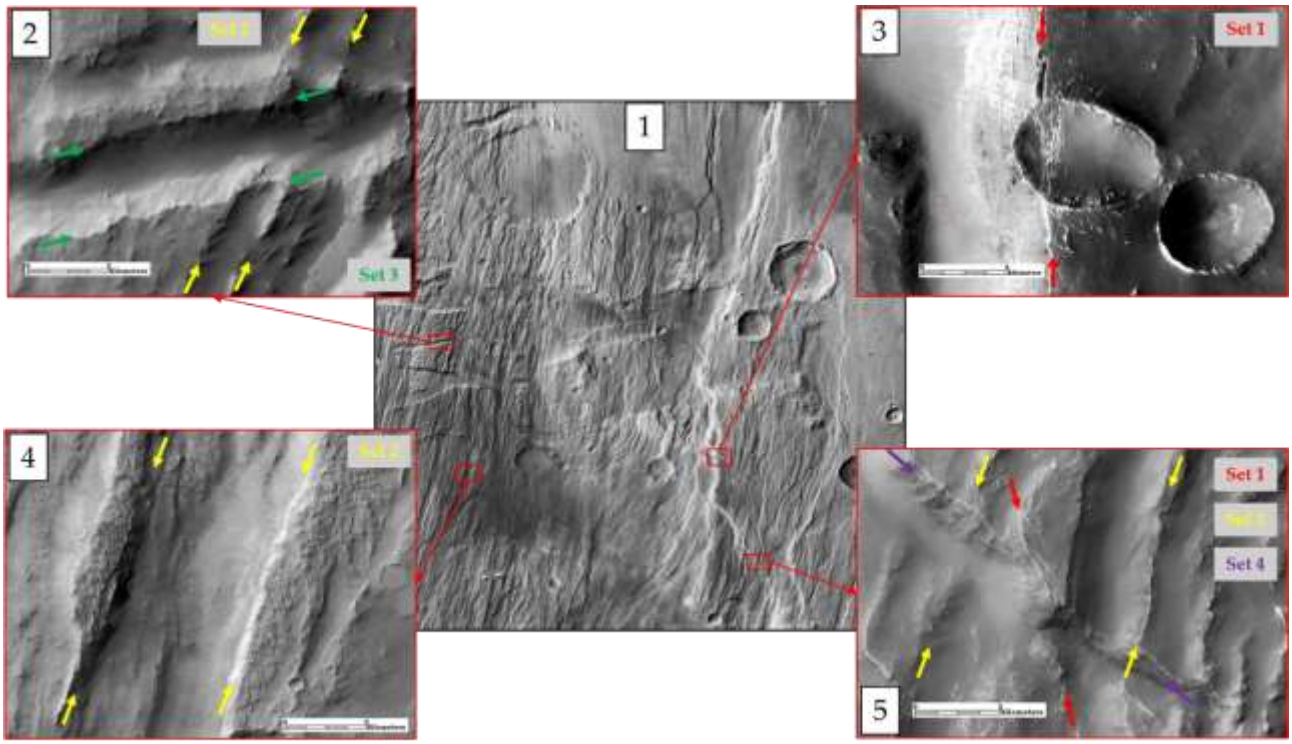

Figure A.3 - 1) THEMIS DayIR Controlled Mosaic v2 (100 m/px); **2 to 5)** Examples of graben-like depressions (2, green arrow, 3, 4 and 5) and elongated reliefs (yellow arrow in 2) belonging to the four identified sets. Global CTX Mosaic of Mars - V01 - E-108_N-24 (Bruce Murray Laboratory for Planetary Visualization).

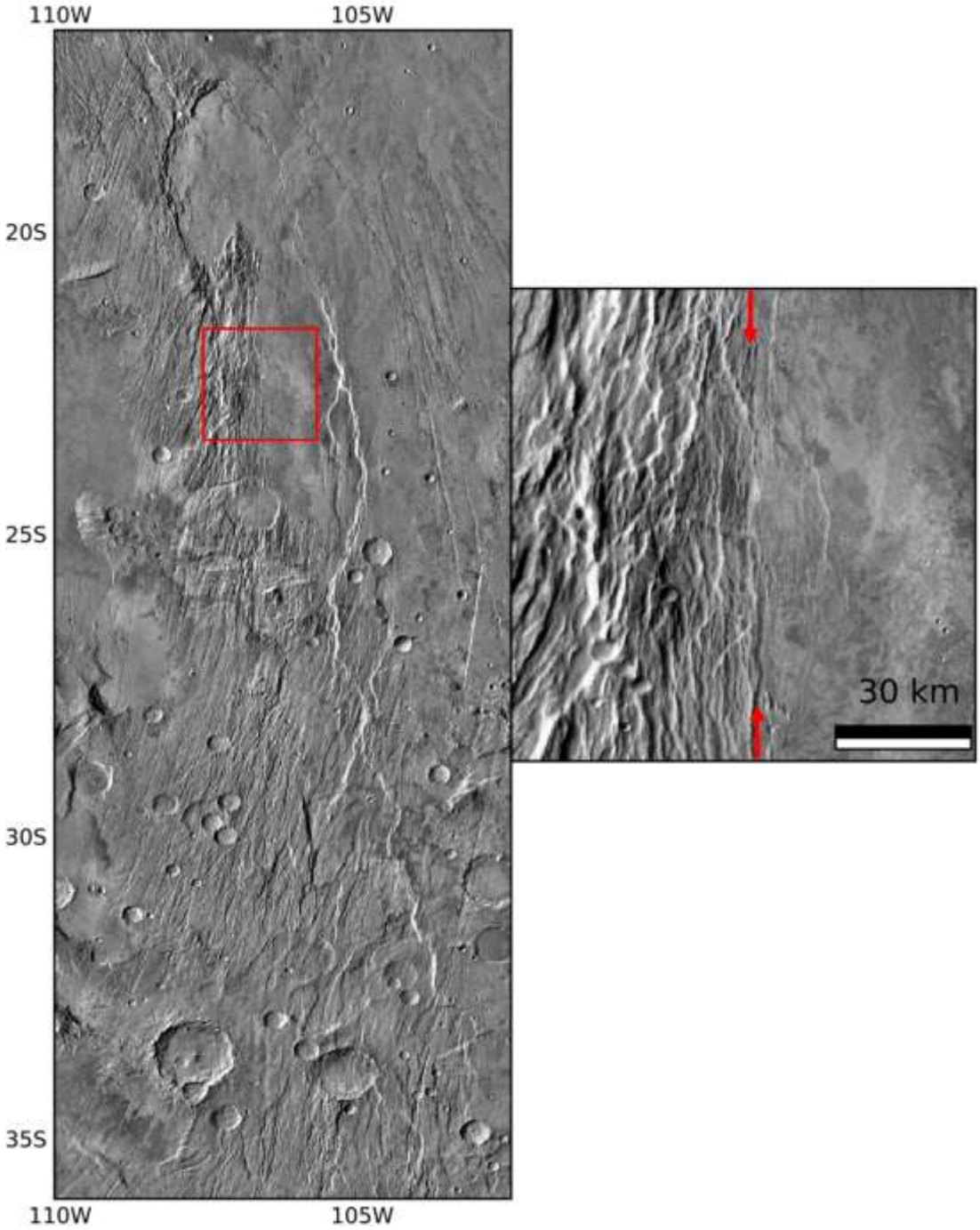

Figure A.4 - Subset of THEMIS DayIR Controlled Mosaic v2 (100 m/px) showing example of the juxtaposition of terrains with different roughness/texture (Set 1 represented with red arrows).

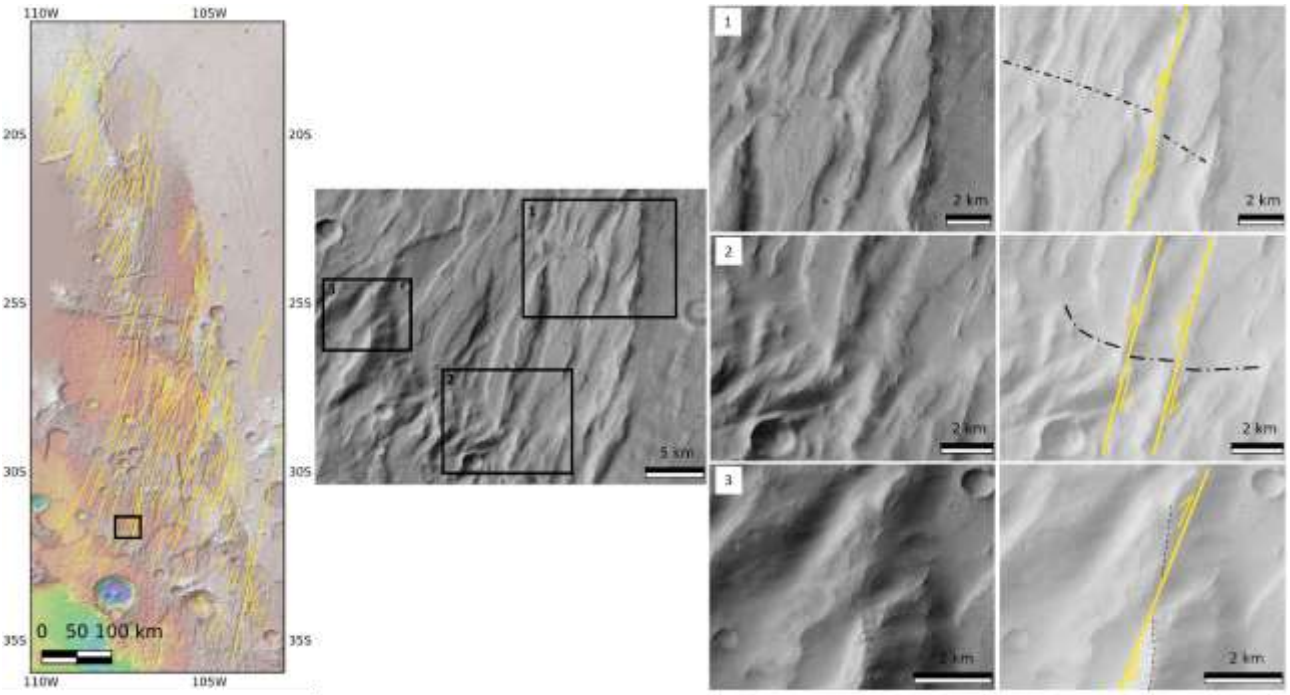

Figure A.5 - Right-lateral offset of crater rim due to the activity of Set2 faults (Global CTX Mosaic of Mars, 5 m/px).

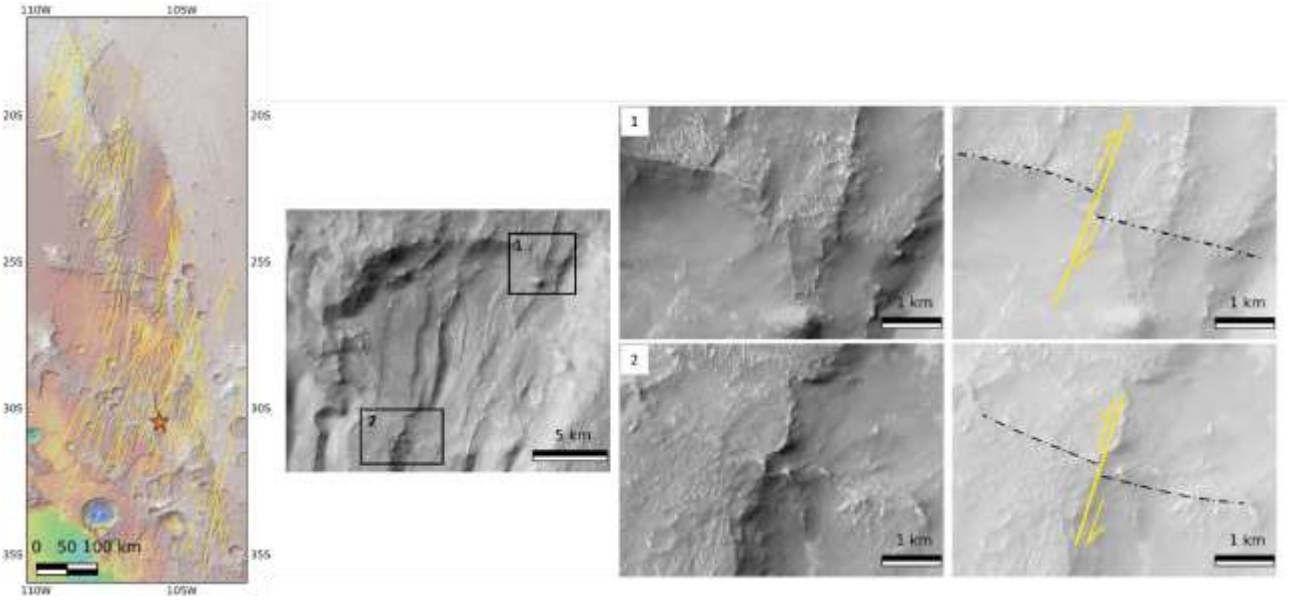

Figure A.6 - Right-lateral offset of crater rim due to the activity of Set2 faults (Global CTX Mosaic of Mars, 5 m/px).

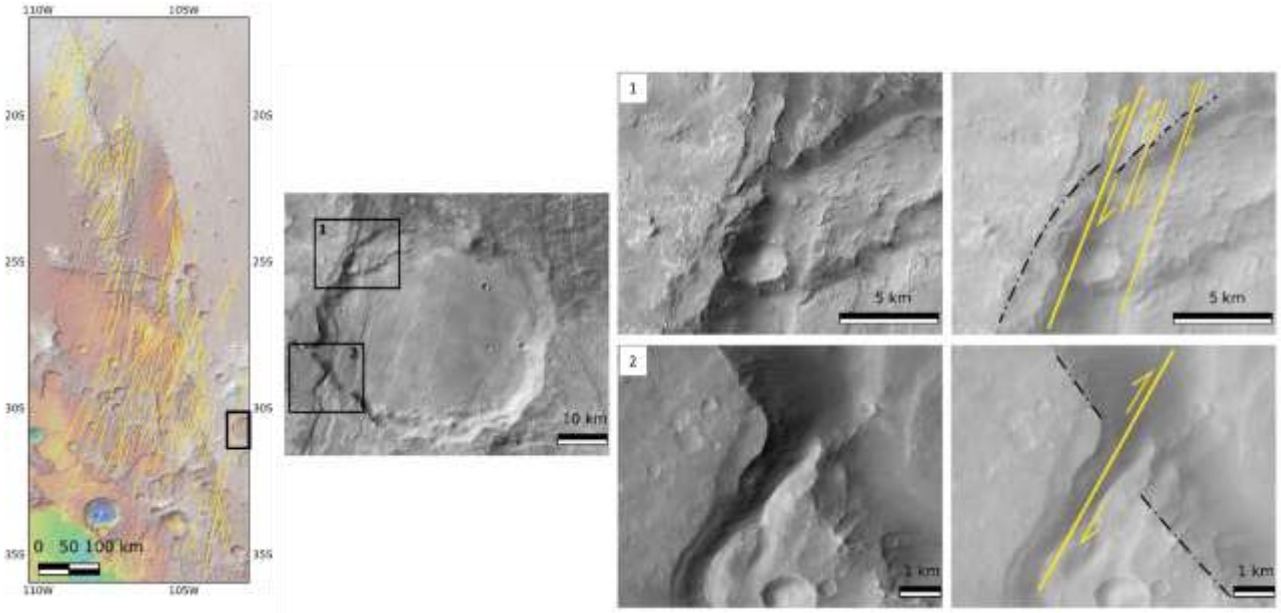

Figure A.7 - Right-lateral offset of crater rim due to the activity of Set2 faults (Global CTX Mosaic of Mars, 5 m/px).

A.1.3 Geostatistical analysis

The geostatistical analysis of the mapped lineaments was performed with the *Daisy3* software (v. 5.58.3.231121, Rome, Italy). Below histograms of the azimuth by frequency are shown. Histograms are smoothed to reduce the statistic noise component by a selected number of moving weighted averages (Wise and Mccrory, 1982) and then histogram peaks are fitted with a function sum of Gaussian curves through a best-fit algorithm derived from Frazer &Suzuki(1966), based on the methodology derived from Wise et al. (1985).

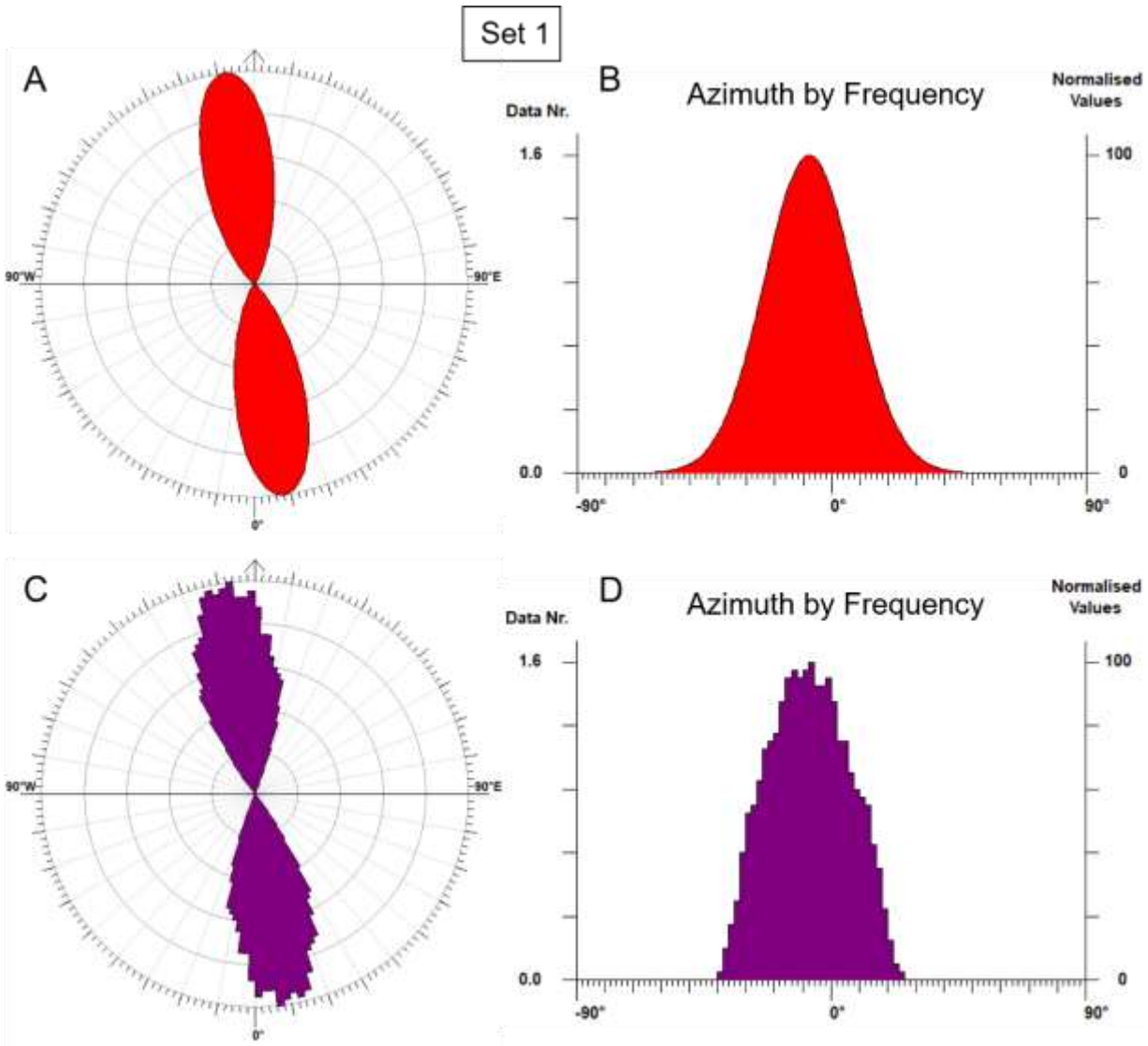

Figure A.8 - Rose diagrams in A and C represent the azimuthal distribution by frequency of Set 1 shown in B and D. In A and B histogram are fitted with a function sum of Gaussian curves through the best-fit algorithm of Frazer and Suzuki (1966). Petal thus represents the Gaussian peak resulting from the azimuthal analysis of the structures belonging to Set 1.

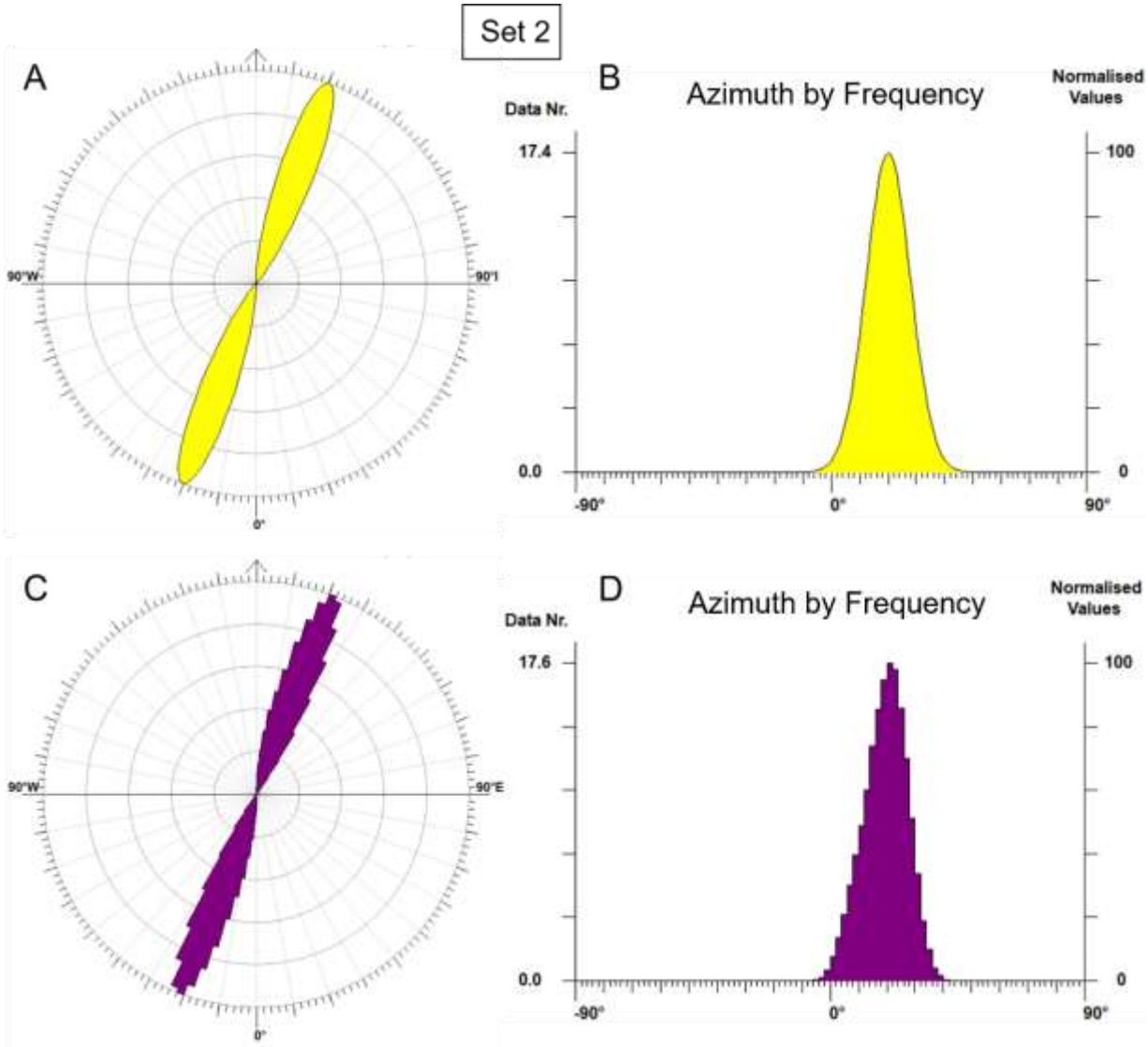

Figure A.9 - Rose diagrams in A and C represent the azimuthal distribution by frequency of Set 2 shown in B and D. In A and B histogram are fitted with a function sum of Gaussian curves through the best-fit algorithm of Frazer and Suzuki (1966). Petal thus represents the Gaussian peak resulting from the azimuthal analysis of the structures belonging to Set 2.

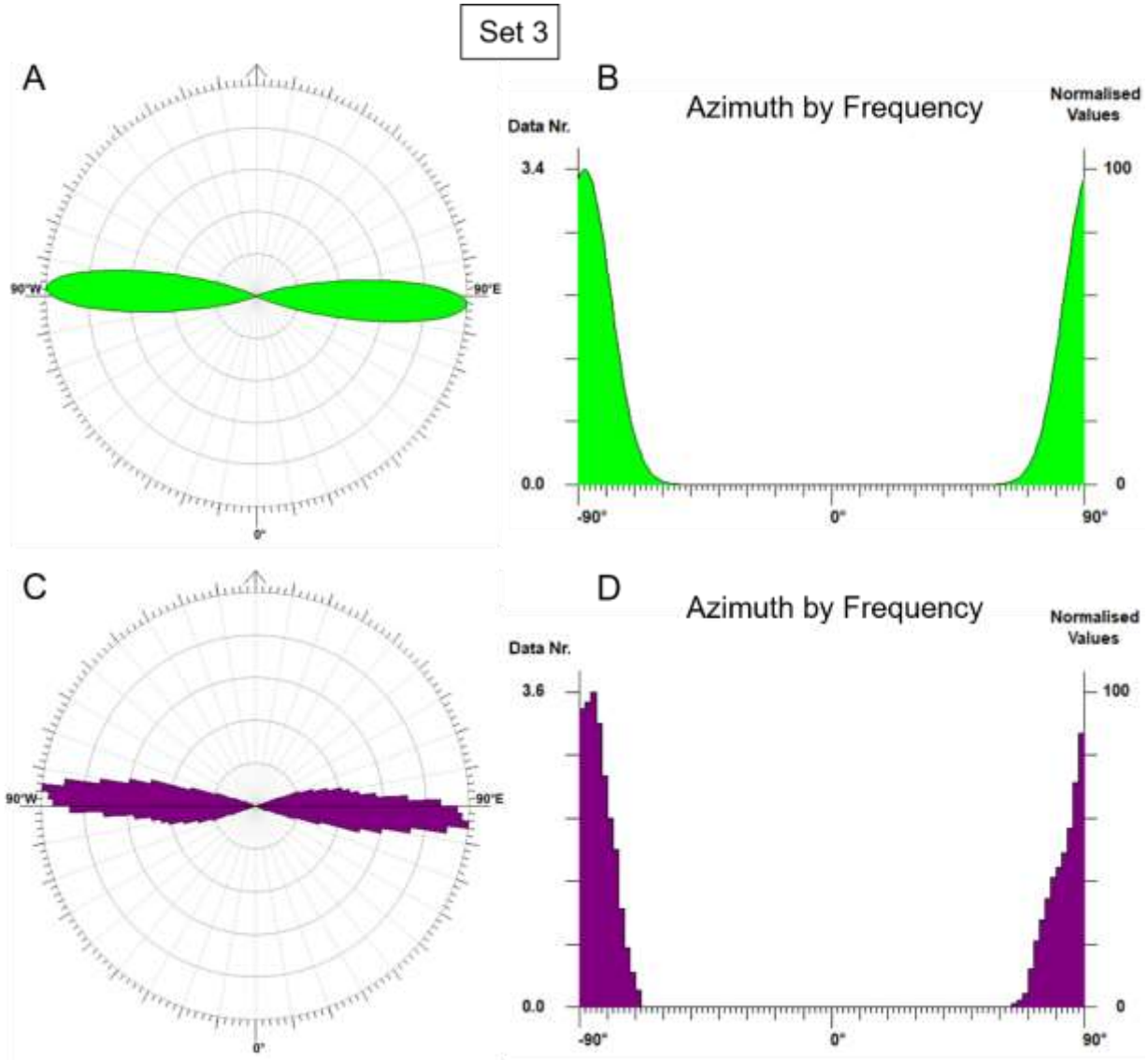

Figure A.10 - Rose diagrams in A and C represent the azimuthal distribution by frequency of Set 3 shown in B and D. In A and B histogram are fitted with a function sum of Gaussian curves through the best-fit algorithm of Frazer and Suzuki (1966). Petal thus represents the Gaussian peak resulting from the azimuthal analysis of the structures belonging to Set 3.

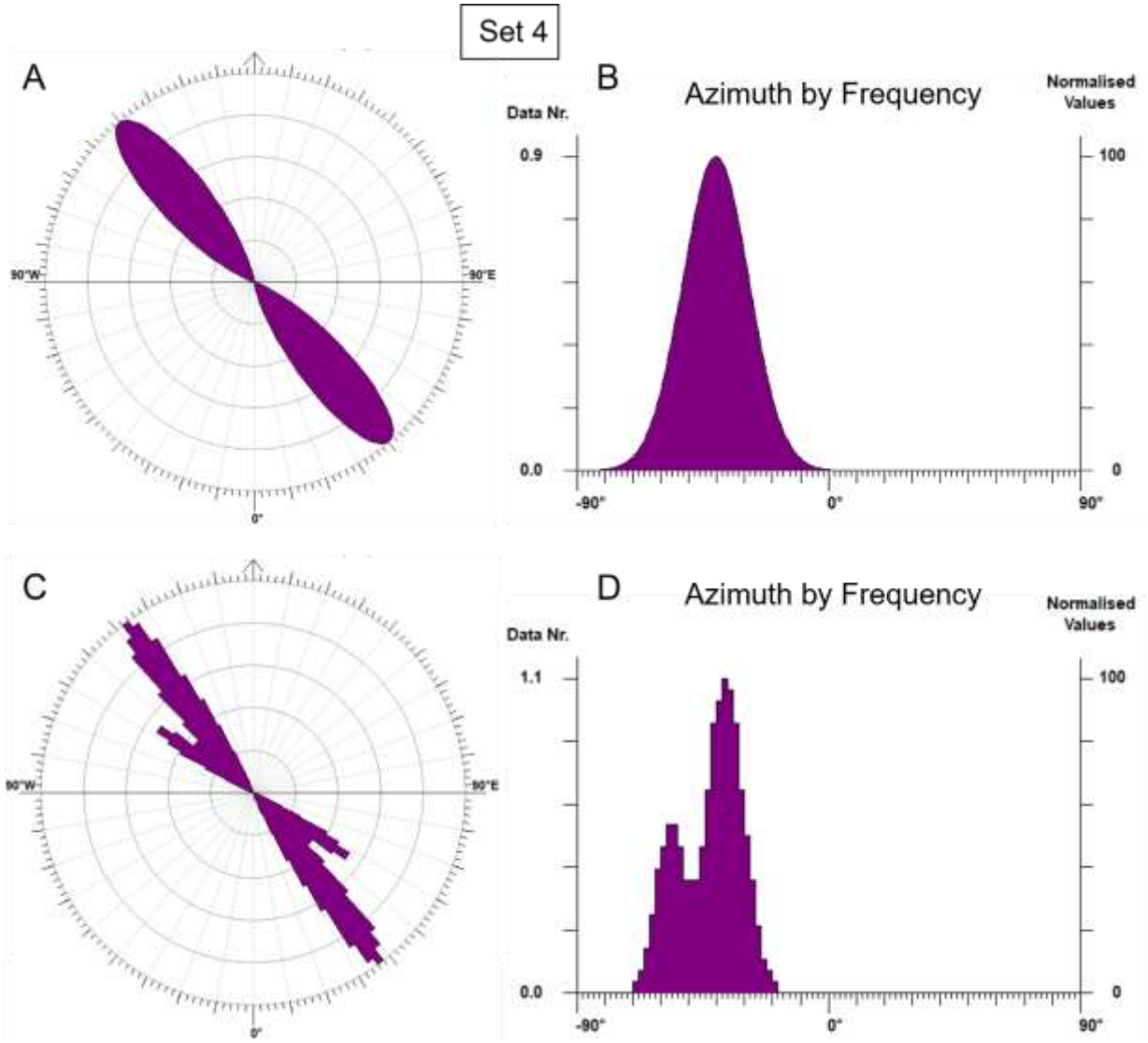

Figure A.11 - Rose diagrams in A and C represent the azimuthal distribution by frequency of Set 4 shown in B and D. In A and B histogram are fitted with a function sum of Gaussian curves through the best-fit algorithm of Frazer and Suzuki (1966). Petal thus represents the Gaussian peak resulting from the azimuthal analysis of the structures belonging to Set 4.

Appendix 2: Supplementary materials of Chapter 6

Position of the slit before and after the exposures during the six pointing of the three visits.

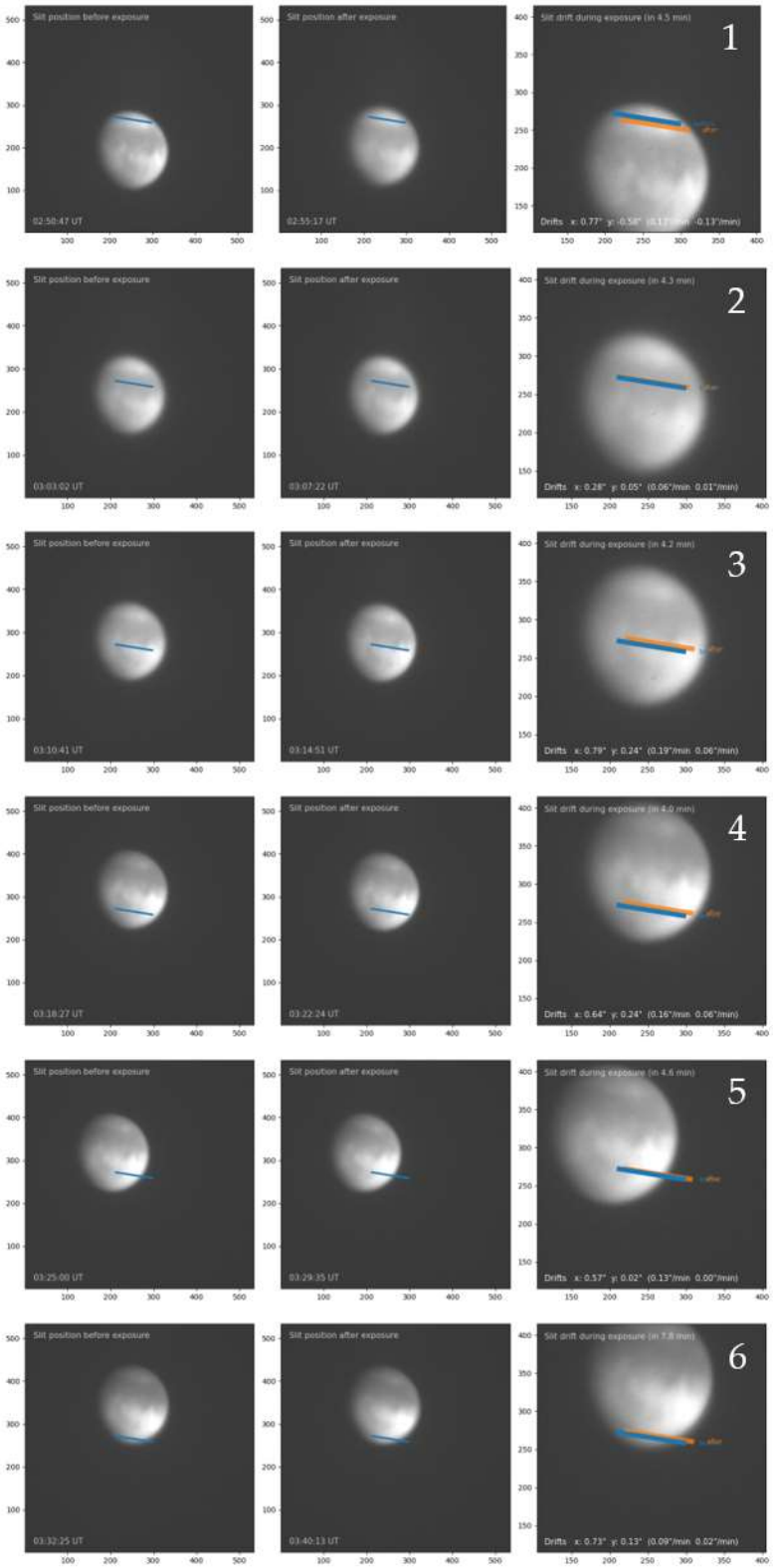

Figure A.12 - Position of the slit before and after (drift) the exposures during the 9 October 2022 observation. North is downwards oriented.

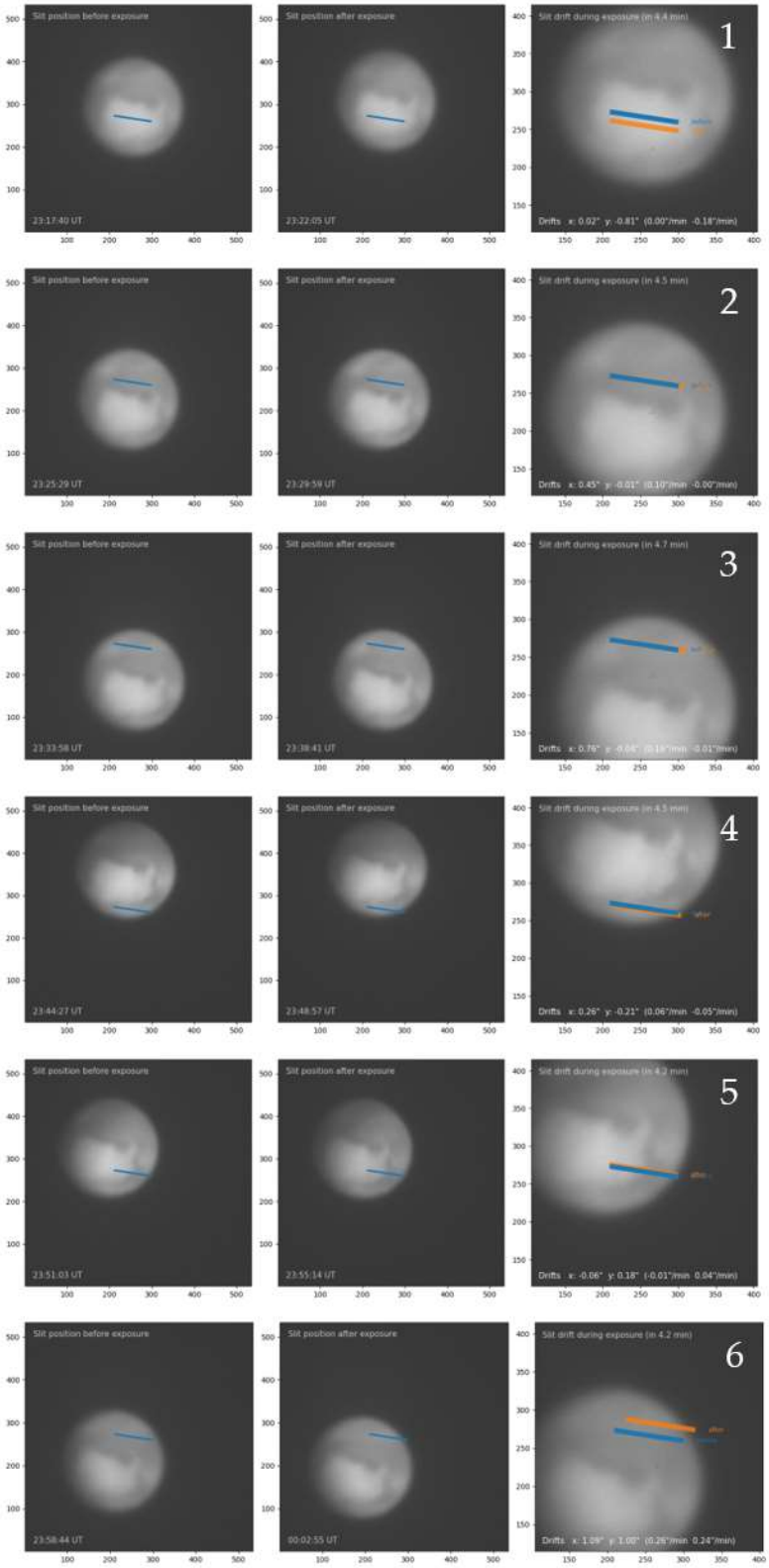

Figure A.13 - Position of the slit before and after (drift) the exposures during the 11 November 2022 observation. North is downwards oriented.

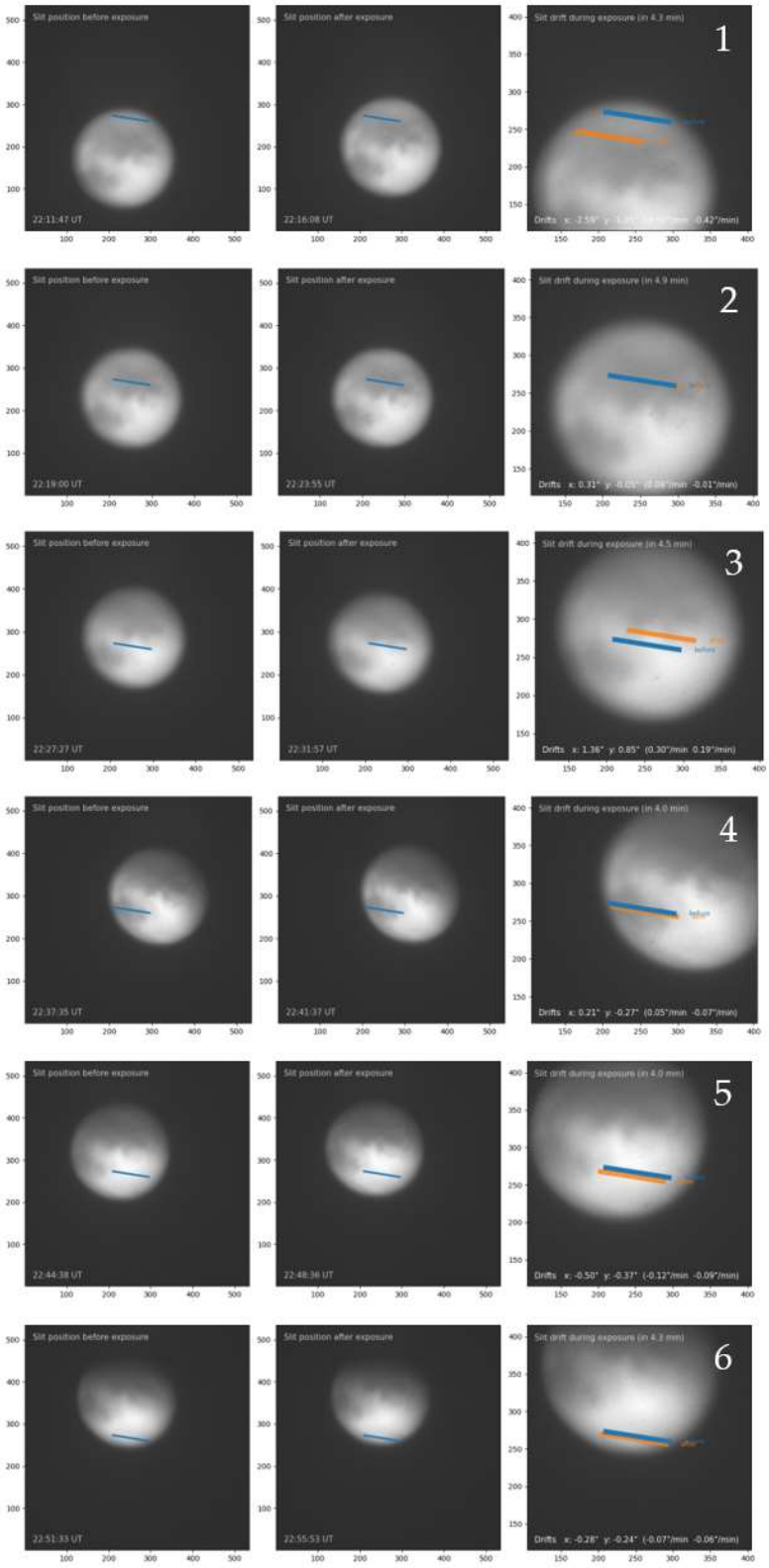

Figure A.14 - Position of the slit before and after (drift) the exposures during the 16 December 2022 observation. North is downwards oriented.

Acknowledgements

This journey has come to an end. These have been three intense years full of dedication, efforts and, most importantly, great gratifications. Studying Mars and what lies beyond the human "line of sight" has been one of my dreams for a long time. I must thank above all my supervisors, Paola Cianfarra, Gabriele Ferretti and Silvano Tosi, who first gave me the chance to undertake this path. I thank them for their ever-present support, for always encouraging me, for teaching and guiding me with so much passion and trust even in challenging times. A special thanks also to Laura Crispini for her efforts in bringing light to this project and for her invaluable advice and suggestions from even before these three years. I owe so much of my personal and scientific growth to all of you, so…thank you.

A special thanks to Prof. Francesco Salvini and Dott. Ernst Hauber who carefully revised this thesis and whose comments allowed to improve the clarity and the thoroughness of the manuscript.

My thanks also go to the people with whom I collaborated during these three years. Thank you to Monica Rainer, Avet Harutyunyan and Francesco Borsa for their "astronomical" support; Davide Scafidi for his endless patience with my software requests and problems; Francesco Faccini, Martino Terrone, Simone Barani, and Andrea Ferrando for the "interferometric collaboration"; and Alba Domi for our exciting and promising space project! Thank you also to Laura Federico for the insightful scientific discussions during these three years.

Many thanks are also due to my friends inside and outside the university and to my family. In particular a special thanks to Michele Locatelli, my "roommate" at DISTAV, with whom I shared many laughs and interesting scientific discussions; to Mattia La Fortezza, my teammate in this PhD journey, I will always remember this thesis writing during 2023-24 winter "holidays"; to Davide and Emanuele who supported and tolerated me in the most difficult moments of this last incredible and strange year.

Last but definitely not least, Nymeria. My dog, who has been my crutch since she arrived. I cannot even explain how important you have been and are for me. You allowed me to see the light again, laugh again, and joy again. You are and will remain forever an essential, vital part of me.

Evandro

References

Aghaee, A., Shamsipour, P., Hood, S., & Haugaard, R. (2021). A convolutional neural network for semi-automated lineament detection and vectorisation of remote sensing data using probabilistic clustering: A method and a challenge. Computers & Geosciences, 151, 104724. https://doi.org/10.1016/j.cageo.2021.104724

Aharonson, O., Zuber, M. T., & Rothman, D. H. (2001). Statistics of Mars' topography from the Mars Orbiter Laser Altimeter: Slopes, correlations, and physical models. Journal of Geophysical Research: Planets, 106(E10), 23723-23735. https://doi.org/10.1029/2000JE001403

Anderson, D. L. (1995). Lithosphere, asthenosphere, and perisphere. Reviews of Geophysics, 33(1), 125-149. https://doi.org/10.1029/94RG02785

Anderson, E.M., 1951. The Dynamics of Faulting and Dyke Formation with Applications to Britain, 2nd ed. Oliver and Boyd, Edinburgh.

Anderson, R. C., Dohm, J. M., Golombek, M. P., Haldemann, A. F., Franklin, B. J., Tanaka, K. L., ... & Peer, B. (2001). Primary centres and secondary concentrations of tectonic activity through time in the western hemisphere of Mars. Journal of Geophysical Research: Planets, 106(E9), 20563-20585. https://doi.org/10.1029/2000JE001278

Anderson, R. C., Dohm, J. M., Williams, J. P., Robbins, S. J., Siwabessy, A., Golombek, M. P., & Schroeder, J. F. (2019). Unravelling the geologic and tectonic history of the Memnonia-Sirenum region of Mars: Implications on the early formation of the Tharsis rise. Icarus, 332, 132-150. https://doi.org/10.1016/j.icarus.2019.06.010

Andrews-Hanna, J. C., & Broquet, A. (2023). The history of global strain and geodynamics on Mars. Icarus, 395, 115476. https://doi.org/10.1016/j.icarus.2023.115476

Andrews-Hanna, J. C., Zuber, M. T., & Banerdt, W. B. (2008). The Borealis basin and the origin of the Martian crustal dichotomy. Nature, 453(7199), 1212-1215. https://doi.org/10.1038/nature07011

Anguita, F., Farelo, A. F., López, V., Mas, C., Muñoz-Espadas, M. J., Márquez, Á., & Ruiz, J. (2001). Tharsis dome, Mars: New evidence for Noachian-Hesperian thick-skin and Amazonian thin-skin tectonics. Journal of Geophysical Research: Planets, 106(E4), 7577-7589. https://doi.org/10.1029/2000JE001246

Ansari, A., Noorzad, A., & Zafarani, H. (2009). Clustering analysis of the seismic catalog of Iran. Computers & Geosciences, 35(3), 475-486. https://doi.org/10.1016/j.cageo.2008.01.010

Arabie, P., Hubert, L., & De Soete, G. (Eds.). (1996). Clustering and classification. World Scientific.

Arragoni, S., Maggi, M., Cianfarra, P., & Salvini, F. (2016). The Cenozoic fold-and-thrust belt of Eastern Sardinia: Evidence from the integration of field data with numerically balanced geological cross section. Tectonics, 35(6), 1404-1422. https://doi.org/10.1002/2015TC004004

Atmaoui, N., & Hollnack, D. (2003). Neotectonics and extension direction of the Southern Kenya Rift, Lake Magadi area. Tectonophysics, 364(1-2), 71-83. https://doi.org/10.1016/S0040-1951(03)00051-9

Aydin, A. (2006). Failure modes of the lineaments on Jupiter's moon, Europa: Implications for the evolution of its icy crust. Journal of structural geology, 28(12), 2222-2236. https://doi.org/10.1016/j.jsg.2006.08.003

Bai, T., & Pollard, D. D. (2000a). Closely spaced fractures in layered rocks: initiation mechanism and propagation kinematics. Journal of structural geology, 22(10), 1409-1425. https://doi.org/10.1016/S0191-8141(00)00062-6

Bai, T., Pollard, D. D., & Gao, H. (2000b). Explanation for fracture spacing in layered materials. Nature, 403(6771), 753-756. https://doi.org/10.1038/35001550

Balbi E., Cianfarra P., Ferretti G., Crispini L. & Tosi S. (2021). Tectonic styles of the Martian crust: insights from Cerberus Fossae and Thaumasia Highlands – 90° Congress of the Italian Geological Society (September 13 – 16, 2021), session S24: The contribution of geology to the knowledge of solar system bodies. https://www.geoscienze.org/trieste2021/index.php/abstracts/elenco-abstracts

Balbi E., Cianfarra P., Tosi S., Crispini L. & Ferretti G. (2023) - Clustering analysis to unravel polyphase tectonics settings on planetary surfaces: the case of the Claritas Fossae, Mars. SIMP, SGI, SOGEI, AIV Joint Congress, Potenza, Italy, 18-22 Sept 2023. https://www.socgeol.it/files/download/pubblicazioni/Abstract%20Book/Abstract%20Book%20Congresso%20SGI-SIMP%202023.pdf

Balbi, E., Cianfarra, P., Ferretti, G., Crispini, L., & Tosi, S. (2022a). The Claritas Fossae region, an example of polyphasic deformation on Mars? (No. EPSC2022-1041). Copernicus Meetings. https://doi.org/10.5194/epsc2022-1041

Balbi, E., Cianfarra, P., Ferretti, G., Crispini, L., & Tosi, S. (2022b). Modelling the extensional tectonic setting of the Claritas Fossae. In EGU General Assembly Conference Abstracts (pp. EGU22-7683). https://doi.org/10.5194/egusphere-egu22-7683

Balbi, E., Cianfarra, P., Ferretti, G., Crispini, L., & Tosi, S. (2021). Analysis of tectonic structures on the Martian surface: a contribution to the understanding of the crustal dichotomy (No. EPSC2021-838). Copernicus Meetings. https://doi.org/10.5194/epsc2021-838

Balbi, E., Cianfarra, P., Ferretti, G., Crispini, L., and Tosi, S. (2023). Structural mapping and stress analysis to unravel the polyphasic tectonic history of the Claritas Fossae, Mars. XVIII National Congress of Planetary Sciences, Perugia, Italy, 6-10 Feb 2023. https://www.scienzeplanetarie.it/wp-content/uploads/2023/02/Abstracts_Book_Oral_CNSP2023.pdf

Balbi, E., Cianfarra, P., Ferretti, G., Crispini, L., and Tosi, S. (2022). The Claritas Fossae Fault System (Mars): a potential enhanced pathway for fluids exchange between the inner planet and the Martian atmosphere. Chianti Topics: Atmospheres International Congress 2022, Antico Spedale del Bigallo (Fi), Italy, 20 – 22, 2022 http://chiantitopics.it/wp-content/uploads/2022/04/Abstract-Book-5th-Chianti-Topics.pdf

Balbi, E., Ferretti, G., Tosi, S., Crispini, L., and Cianfarra, P. (2024). Polyphase tectonics on Mars: Insight from the Claritas Fossae. Icarus, 411, 115972 https://doi.org/10.1016/j.icarus.2024.115972

Banerdt, W. B., & Golombek, M. P. (2000). Tectonics of the Tharsis region of Mars: Insights from MGS topography and gravity. Lunar and Planetary Science XXXI. https://ntrs.nasa.gov/citations/20000080557

Baptista, A. R., Mangold, N., Ansan, V., Baratoux, D., Lognonné, P., Alves, E. I., ... & Neukum, G. (2008). A swarm of small shield volcanoes on Syria Planum, Mars. Journal of Geophysical Research: Planets, 113(E9). https://doi.org/10.1029/2007JE002945

Baratoux, D., Samuel, H., Michaut, C., Toplis, M. J., Monnereau, M., Wieczorek, M., ... & Kurita, K. (2014). Petrological constraints on the density of the Martian crust. Journal of Geophysical Research: Planets, 119(7), 1707-1727. https://doi.org/10.1002/2014JE004642

Basri, G. (2000). Observations of brown dwarfs. Annual Review of Astronomy and Astrophysics, 38(1), 485-519. https://doi.org/10.1146/annurev.astro.38.1.485

Bate, M. R., Bonnell, I. A., & Bromm, V. (2002). The formation mechanism of brown dwarfs. Monthly Notices of the Royal Astronomical Society, 332(3), L65-L68. https://doi.org/10.1046/j.1365-8711.2002.05539.x

Ben-Avraham, Z., Garfunkel, Z., & Lazar, M. (2008). Geology and evolution of the southern Dead Sea fault with emphasis on subsurface structure. Annu. Rev. Earth Planet. Sci., 36, 357-387. https://doi.org/10.1146/annurev.earth.36.031207.124201

Binder, A. B., & McCarthy Jr, D. W. (1972). Mars: The lineament systems. Science, 176(4032), 279-281. https://doi.org/10.1126/science.176.4032.279

Bistacchi, N., Massironi, M., & Baggio, P. (2004). Large-scale fault kinematic analysis in Noctis Labyrinthus (Mars). Planetary and Space Science, 52(1-3), 215-222. https://doi.org/10.1016/j.pss.2003.08.015

Bland, M. T., & McKinnon, W. B. (2016). Mountain building on Io driven by deep faulting. Nature Geoscience, 9(6), 429-432. https://doi.org/10.1038/ngeo2711

Bonnet Gibet, V., Michaut, C., Wieczorek, M., & Lognonné, P. (2022). A positive feedback between crustal thickness and melt extraction for the origin of the Martian dichotomy. Journal of Geophysical Research: Planets, 127(12), e2022JE007472. https://doi.org/10.1029/2022JE007472

Bouley, S., Baratoux, D., Paulien, N., Missenard, Y., & Saint-Bézar, B. (2018). The revised tectonic history of Tharsis. Earth and Planetary Science Letters, 488, 126-133. https://doi.org/10.1016/j.epsl.2018.02.019

Briquet, M., & Aerts, C. (2003). A new version of the moment method, optimized for mode identification in multiperiodic stars. Astronomy & Astrophysics, 398(2), 687-696. https://doi.org/10.1051/0004-6361:20021683

Brož, P., & Hauber, E. (2012). A unique volcanic field in Tharsis, Mars: Pyroclastic cones as evidence for explosive eruptions. Icarus, 218(1), 88-99. https://doi.org/10.1016/j.icarus.2011.11.030

Burbank, D. W., & Anderson, R. S. (2013). Tectonic geomorphology. Second Edition. Environmental & Engineering Geoscience 2013; 19 (2): 198–200. https://doi.org/10.2113/gseegeosci.19.2.198

Burke, C. J., Christiansen, J. L., Mullally, F., Seader, S., Huber, D., Rowe, J. F., ... & Still, M. (2015). Terrestrial planet occurrence rates for the Kepler GK dwarf sample. The Astrophysical Journal, 809(1), 8. http://dx.doi.org/10.1088/0004-637X/809/1/8

Cardinale, M., Vaz, D. A., D'Incecco, P., Mari, N., Filiberto, J., Eggers, G. L., & Di Achille, G. (2023). Morphostructural mapping of Borealis Planitia, Mercury. Journal of Maps, 19(1), 2223637. https://doi.org/10.1080/17445647.2023.2223637

Carr, M. H. (2013). Geologic exploration of the planets: The first 50 years. Eos, Transactions American Geophysical Union, 94(3), 29-30. https://doi.org/10.1002/2013EO030001

Carr, M. H., & Head III, J. W. (2010). Geologic history of Mars. Earth and Planetary Science Letters, 294(3-4), 185-203. https://doi.org/10.1016/j.epsl.2009.06.042

Cassanelli, J. P., & Head, J. W. (2019). Glaciovolcanism in the Tharsis volcanic province of Mars: Implications for regional geology and hydrology. Planetary and Space Science, 169, 45-69. https://doi.org/10.1016/j.pss.2019.02.006

Ceccato, A., Tartaglia, G., Antonellini, M., & Viola, G. (2022). Multiscale lineament analysis and permeability heterogeneity of fractured crystalline basement blocks. Solid Earth, 13(9), 1431-1453. https://doi.org/10.5194/se-13-1431-2022

Chabot, N. L., Hoppa, G. V., & Strom, R. G. (2000). Analysis of lunar lineaments: Far side and polar mapping. Icarus, 147(1), 301-308. https://doi.org/10.1006/icar.2000.6433

Chamberlain, S. A., Bailey, J. A., & Crisp, D. (2006). Mapping Martian atmospheric pressure with ground-based near infrared spectroscopy. Publications of the Astronomical Society of Australia, 23(3), 119-124. https://doi.org/10.1071/AS05028

Chamberlain, S., Bailey, J., Crisp, D., & Walter, M. (2005, January). Near-Infrared Spectral Observations of Mars. In 5th NSSA Australian Space Science Conference: 14 to 16 September 2005 Hosted by RMIT University, Melbourne, Australia (pp. 124-128). Melbourne, Vic.: RMIT University.

Chao, K. H., deGraffenried, R., Lach, M., Nelson, W., Truax, K., & Gaidos, E. (2021). Lava worlds: From early earth to exoplanets. Geochemistry, 81(2), 125735. https://doi.org/10.1016/j.chemer.2020.125735

Charbonneau, D., Brown, T. M., Latham, D. W., & Mayor, M. (1999). Detection of planetary transits across a sun-like star. The Astrophysical Journal, 529(1), L45. https://doi.org/10.1086/312457

Charbonneau, D., Brown, T. M., Noyes, R. W., & Gilliland, R. L. (2002). Detection of an extrasolar planet atmosphere. The Astrophysical Journal, 568(1), 377. https://doi.org/10.1086/338770

Chorowicz, J. (2005). The east African rift system. Journal of African Earth Sciences, 43(1-3), 379-410. https://doi.org/10.1016/j.jafrearsci.2005.07.019

Christensen, P. R., Jakosky, B. M., Kieffer, H. H., Malin, M. C., McSween, H. Y., Nealson, K., ... & Ravine, M. (2004). The thermal emission imaging system (THEMIS) for the Mars 2001 Odyssey Mission. Space Science Reviews, 110, 85-130. https://doi.org/10.1023/B:SPAC.0000021008.16305.94

Cianfarra, P., & Maggi, M. (2017). Cenozoic extension along the reactivated Aurora fault system in the East Antarctic Craton. Tectonophysics, 703, 135-143. https://doi.org/10.1016/j.tecto.2017.02.019

Cianfarra, P., & Salvini, F. (2014). Ice sheet surface lineaments as nonconventional indicators of East Antarctica bedrock tectonics. Geosphere, 10(6), 1411-1418. https://doi.org/10.1130/GES01074.1

Cianfarra, P., & Salvini, F. (2015). Lineament domain of regional strike-slip corridor: Insight from the Neogene transtensional De Geer transform fault in NW Spitsbergen. Pure and Applied Geophysics, 172, 1185-1201. https://doi.org/10.1007/s00024-014-0869-9

Cianfarra, P., & Salvini, F. (2016b). Quantification of fracturing within fault damage zones affecting Late Proterozoic carbonates in Svalbard. Rendiconti Lincei, 27, 229-241. https://doi.org/10.1007/s12210-016-0527-5

Cianfarra, P., Forieri, A., Salvini, F., Tabacco, I. E., & Zirizotti, A. (2009). Geological setting of the Concordia trench-lake system in East Antarctica. Geophysical Journal International, 177(3), 1305-1314. https://doi.org/10.1111/j.1365-246X.2009.04123.x

Cianfarra, P., Locatelli, M., Capponi, G., Crispini, L., Rossi, C., Salvini, F., & Federico, L. (2022). Multiple reactivations of the Rennick Graben Fault system (northern Victoria Land, Antarctica): new evidence from paleostress analysis. Tectonics, 41(6), e2021TC007124. https://doi.org/10.1029/2021TC007124

Claudi, R., Benatti, S., Carleo, I., Ghedina, A., Guerra Sr, J., Ghinassi, F., ... & Riverol, C. (2018). GIARPS: commissioning and first scientific results. In Ground-based and Airborne Instrumentation for Astronomy VII (Vol. 10702, pp. 282-295). SPIE. https://doi.org/10.1117/12.2312555

Crane, K., & Rich, J. (2023). Lithospheric strength and elastic properties for Mars from InSight geophysical data. Icarus, 400, 115581. https://doi.org/10.1016/j.icarus.2023.115581

Davey, S. C., Ernst, R. E., Samson, C., & Grosfils, E. B. (2013). Hierarchical clustering of pit crater chains on Venus. Canadian Journal of Earth Sciences, 50(1), 109-126. https://doi.org/10.1139/cjes-2012-0054

de Arruda Passos, V. S., de Miranda, T. S., Oliveira, J. T. C., Celestino, M. A. L., Corrêa, R., Topan, J. G., & da Cruz Falcão, T. (2022). Quantification of the spatial arrangement of structural lineaments and deformation bands: Implications for the tectonic evolution of the eastern border of the Araripe Basin, NE Brazil. Journal of South American Earth Sciences, 118, 103934. https://doi.org/10.1016/j.jsames.2022.103934

De Pater, I., & Lissauer, J. J. (2015). Planetary sciences. Cambridge University Press.

Dickson, J. L., Palumbo, A. M., Head, J. W., Kerber, L., Fassett, C. I., & Kreslavsky, M. A. (2023). Gullies on Mars could have formed by melting of water ice during periods of high obliquity. Science, 380(6652), 1363-1367. https://doi.org/10.1126/science.abk2464

Dohm, J. M., & Tanaka, K. L. (1999). Geology of the Thaumasia region, Mars: Plateau development, valley origins, and magmatic evolution. Planetary and Space Science, 47(3-4), 411-431. https://doi.org/10.1016/S0032-0633(98)00141-X

Dohm, J. M., Anderson, R. C., Williams, J. P., Ruiz, J., McGuire, P. C., Buczkowski, D. L., ... & Miyamoto, H. (2009). Claritas rise, Mars: Pre-Tharsis magmatism?. Journal of Volcanology and Geothermal Research, 185(1-2), 139-156. https://doi.org/10.1016/j.jvolgeores.2009.03.012

Dohm, J. M., Maruyama, S., Kido, M., & Baker, V. R. (2018). A possible anorthositic continent of early Mars and the role of planetary size for the inception of Earth-like life. Geoscience Frontiers, 9(4), 1085-1098. https://doi.org/10.1016/j.gsf.2016.12.003

Dohm, J. M., Spagnuolo, M. G., Williams, J. P., Viviano-Beck, C. E., Karunatillake, S., Álvarez, O., ... & Maruyama, S. (2015). The Mars plate-tectonic-basement hypothesis. In Lunar and planetary science conference (p. 1741). https://www.hou.usra.edu/meetings/lpsc2015/pdf/1741.pdf

Dohm, J.M., Tanaka, K.L., and Hare, T.M. (2001). Geologic map of the Thaumasia region, Mars: U.S. Geological Survey Geologic Investigations Series I–2650, 3 sheets. https://pubs.usgs.gov/imap/i2650/.

Donzé, F. V., Klinger, Y., Bonilla-Sierra, V., Duriez, J., Jiao, L., & Scholtès, L. (2021). Assessing the brittle crust thickness from strike-slip fault segments on Earth, Mars and Icy moons. Tectonophysics, 805, 228779. https://doi.org/10.1016/j.tecto.2021.228779

Drury, S. A. (2004). Image interpretation in geology.

Durney, D. W., & Kisch, H. J. (1994). A field classification and intensity scale for first-generation cleavages. AGSO Journal of Australian Geology & Geophysics, 15(3), 257-295.

Duxbury, T. C., Kirk, R. L., Archinal, B. A., & Neumann, G. A. (2002). Mars Geodesy/Cartography Working Group recommendations on Mars cartographic constants and coordinate systems. International Archives of Photogrammetry Remote Sensing and Spatial Information Sciences, 34(4), 743-748.

Dzurisin, D. (1978). The tectonic and volcanic history of Mercury as inferred from studies of scarps, ridges, troughs, and other lineaments. Journal of Geophysical Research: Solid Earth, 83(B10), 4883-4906. https://doi.org/10.1029/JB083iB10p04883

Edwards, B., Changeat, Q., Mori, M., Anisman, L. O., Morvan, M., Yip, K. H., ... & Tinetti, G. (2020). Hubble WFC3 spectroscopy of the habitable-zone super-earth LHS 1140 b. The Astronomical Journal, 161(1), 44. https://doi.org/10.3847/1538-3881/abc6a5

Edwards, C. S., Nowicki, K. J., Christensen, P. R., Hill, J., Gorelick, N., & Murray, K. (2011). Mosaicking of global planetary image datasets: 1. Techniques and data processing for Thermal Emission Imaging System (THEMIS) multi-spectral data. Journal of Geophysical Research: Planets, 116(E10). https://doi.org/10.1029/2010JE003755

Enoh, M. A., Okeke, F. I., & Okeke, U. C. (2021). Automatic lineaments mapping and extraction in relationship to natural hydrocarbon seepage in Ugwueme, South-Eastern Nigeria. Geodesy and Cartography, 47(1), 34-44. https://doi.org/10.3846/gac.2021.12099

Exon, N. F., Moore, A. M. G., & Hill, P. J. (1997). Geological framework of the South Tasman Rise, south of Tasmania, and its sedimentary basins. Australian Journal of Earth Sciences, 44(5), 561-577. https://doi.org/10.1080/08120099708728337

Faraj, F., & Ortiz, J. M. (2021). A simple unsupervised classification workflow for defining geological domains using multivariate data. Mining, Metallurgy & Exploration, 38(3), 1609-1623. https://doi.org/10.1007/s42461-021-00428-5

Fassett, C. I., & Head III, J. W. (2008). The timing of Martian valley network activity: Constraints from buffered crater counting. Icarus, 195(1), 61-89. https://doi.org/10.1016/j.icarus.2007.12.009

Fergason, R. L, Hare, T. M., & Laura, J. (2018). HRSC and MOLA Blended Digital Elevation Model at 200m v2. Astrogeology PDS Annex, U.S. Geological Survey. http://bit.ly/HRSC_MOLA_Blend_v0

Fernando, B., Daubar, I. J., Charalambous, C., Grindrod, P. M., Stott, A., Al Ateqi, A., ... & Banerdt, W. B. (2023). A tectonic origin for the largest marsquake observed by InSight. Geophysical Research Letters, 50(20), e2023GL103619. https://doi.org/10.1029/2023GL103619

Fischer, D. A., Howard, A. W., Laughlin, G. P., Macintosh, B., Mahadevan, S., Sahlmann, J., & Yee, J. C. (2015). Exoplanet detection techniques. https://doi.org/10.48550/arXiv.1505.06869

Fortney, J. J., Dawson, R. I., & Komacek, T. D. (2021). Hot jupiters: Origins, structure, atmospheres. Journal of Geophysical Research: Planets, 126(3), e2020JE006629. https://doi.org/10.1029/2020JE006629

Fossen, H. (2016). Structural geology. Cambridge university press.

Foucher, F., Hickman-Lewis, K., Hutzler, A., Joy, K. H., Folco, L., Bridges, J. C., ... & Westall, F. (2021). Definition and use of functional analogues in planetary exploration. Planetary and Space Science, 197, 105162. https://doi.org/10.1016/j.pss.2021.105162

Franceschini, Z., Cioni, R., Scaillet, S., Corti, G., Sani, F., Isola, I., ... & Brune, S. (2020). Recent volcano-tectonic activity of the Ririba rift and the evolution of rifting in South Ethiopia. Journal of Volcanology and Geothermal Research, 403, 106989. https://doi.org/10.1016/j.jvolgeores.2020.106989

Frazer, R. D., & Suzuki, E. (1966). Resolution of overlapping absorption bands by least squares procedures. Analytical Chemistry, 38(12), 1770-1773.

Fressin, F., Torres, G., Charbonneau, D., Bryson, S. T., Christiansen, J., Dressing, C. D., ... & Batalha, N. M. (2013). The false positive rate of Kepler and the occurrence of planets. The Astrophysical Journal, 766(2), 81. https://doi.org/10.1088/0004-637X/766/2/81

Fressin, F., Torres, G., Désert, J. M., Charbonneau, D., Batalha, N. M., Fortney, J. J., ... & Uddin, K. (2011). Kepler-10 c: A 2.2 Earth radius transiting planet in a multiple system. The Astrophysical Journal Supplement Series, 197(1), 5. https://doi.org/10.1088/0067-0049/197/1/5

Frey, H., & Schultz, R. A. (1988). Large impact basins and the mega-impact origin for the crustal dichotomy on Mars. Geophysical Research Letters, 15(3), 229-232. https://doi.org/10.1029/GL015i003p00229

Frey, H., Sakimoto, S. E., & Roark, J. (1998). The MOLA topographic signature at the crustal dichotomy boundary zone on Mars. Geophysical research letters, 25(24), 4409-4412. https://doi.org/10.1029/1998GL900095

Gardner, M. (1970). The fantastic combinations of John Conway's new solitaire game life. Mathematical Games. Scientific American. Vol. 223, no. 4. pp. 120–123. doi:10.1038/scientificamerican1070-120. JSTOR 24927642

Genova, A., Goossens, S., Lemoine, F. G., Mazarico, E., Neumann, G. A., Smith, D. E., & Zuber, M. T. (2016). Seasonal and static gravity field of Mars from MGS, Mars Odyssey and MRO radio science. Icarus, 272, 228-245. https://doi.org/10.1016/j.icarus.2016.02.050

Gerya, T. V. (2014). Plume-induced crustal convection: 3D thermomechanical model and implications for the origin of novae and coronae on Venus. Earth and Planetary Science Letters, 391, 183-192. https://doi.org/10.1016/j.epsl.2014.02.005

Giardini, D., Lognonné, P., Banerdt, W. B., Pike, W. T., Christensen, U., Ceylan, S., ... & Yana, C. (2020). The seismicity of Mars. Nature Geoscience, 13(3), 205-212. https://doi.org/10.1038/s41561-020-0539-8

Gleeson, T., & Novakowski, K. (2009). Identifying watershed-scale barriers to groundwater flow: Lineaments in the Canadian Shield. Geological Society of America Bulletin, 121(3-4), 333-347. https://doi.org/10.1130/B26241.1

Golombek, M. P., & Bridges, N. T. (2000). Erosion rates on Mars and implications for climate change: Constraints from the Pathfinder landing site. Journal of Geophysical Research: Planets, 105(E1), 1841-1853. https://doi.org/10.1029/1999JE001043

Golombek, M. P., & Phillips, R. J. (2010). Mars tectonics. Planetary tectonics, 11, 183-232.

Golombek, M. P., Grant, J. A., Crumpler, L. S., Greeley, R., Arvidson, R. E., Bell III, J. F., ... & Squyres, S. W. (2006). Erosion rates at the Mars Exploration Rover landing sites and long-term climate change on Mars. Journal of Geophysical Research: Planets, 111(E12). https://doi.org/10.1029/2006JE002754

Gordon, A. D. (1999). Classification. CRC Press.

Gower, J. C. (1971). A general coefficient of similarity and some of its properties. Biometrics, 857-871.

Grindrod, P. M., & Hoogenboom, T. (2006). Venus: the corona conundrum. Astronomy & Geophysics, 47(3), 3-16. https://doi.org/10.1111/j.1468-4004.2006.47316.x

Grott, M., Hauber, E., Werner, S. C., Kronberg, P., & Neukum, G. (2005). High heat flux on ancient Mars: Evidence from rift flank uplift at Coracis Fossae. Geophysical Research Letters, 32(21). https://doi.org/10.1029/2005GL023894

Grott, M., Hauber, E., Werner, S. C., Kronberg, P., & Neukum, G. (2007). Mechanical modeling of thrust faults in the Thaumasia region, Mars, and implications for the Noachian heat flux. Icarus, 186(2), 517-526. https://doi.org/10.1016/j.icarus.2006.10.001

Grott, M., Kronberg, P., Hauber, E., & Cailleau, B. (2007). Formation of the double rift system in the Thaumasia Highlands, Mars. Journal of Geophysical Research: Planets, 112(E6). https://doi.org/10.1029/2006JE002800

Gutiérrez, F., & Gutiérrez, M. (2016). Landforms of the earth: an illustrated guide. Springer.

Hargitai, H. (Ed.). (2019). Planetary Cartography and GIS. Berlin/Heidelberg, Germany: Springer International Publishing. https://doi.org/10.1007/978-3-319-62849-3

Hartmann, W. K. (1999). Martian cratering VI: Crater count isochrons and evidence for recent volcanism from Mars Global Surveyor. Meteoritics & Planetary Science, 34(2), 167-177. https://doi.org/10.1111/j.1945-5100.1999.tb01743.x

Harutyunyan, A., Rainer, M., Hernandez, N., Oliva, E., Guerra, J., Lodi, M., ... & Sozzi, M. (2018). GIANO-B online data reduction software at the TNG. In Advances in Optical and Mechanical Technologies for Telescopes and Instrumentation III (Vol. 10706, pp. 1167-1172). SPIE. https://doi.org/10.1117/12.2312690

Hauber, E., & Kronberg, P. (2001). Tempe Fossae, Mars: A planetary analogon to a terrestrial continental rift?. Journal of Geophysical Research: Planets, 106(E9), 20587-20602. https://doi.org/10.1029/2000JE001346

Hauber, E., & Kronberg, P. (2005). The large Thaumasia graben on Mars: Is it a rift?. Journal of Geophysical Research: Planets, 110(E7). https://doi.org/10.1029/2005JE002407

Hauber, E., Brož, P., Jagert, F., Jodłowski, P., & Platz, T. (2011). Very recent and wide-spread basaltic volcanism on Mars. Geophysical Research Letters, 38(10). https://doi.org/10.1029/2011GL047310

Hauber, E., Grott, M., & Kronberg, P. (2010). Martian rifts: Structural geology and geophysics. Earth and Planetary Science Letters, 294(3-4), 393-410. https://doi.org/10.1016/j.epsl.2009.11.005

Hauber, E., Mège, D., Platz, T., & Brož, P. (2018). Endogenic processes. Planetary Geology, 147-183.

Heap, M. J., Villeneuve, M., Albino, F., Farquharson, J. I., Brothelande, E., Amelung, F., ... & Baud, P. (2020). Towards more realistic values of elastic moduli for volcano modelling. Journal of Volcanology and Geothermal Research, 390, 106684. https://doi.org/10.1016/j.jvolgeores.2019.106684

Heller, D. A., & Janle, P. (1999). Lineament analysis and geophysical modelling of the Alba Patera Region on Mars. Earth, Moon, and Planets, 84, 1-22. https://doi.org/10.1023/A:1026578305434

Hobbs, W. H. (1904). Lineaments of the Atlantic border region. Bulletin of the Geological Society of America, 15(1), 483-506. https://doi.org/10.1130/GSAB-15-483

Hood, D. R., Judice, T., Karunatillake, S., Rogers, D., Dohm, J. M., Susko, D., & Carnes, L. K. (2016). Assessing the geologic evolution of Greater Thaumasia, Mars. Journal of Geophysical Research: Planets, 121(9), 1753-1769. https://doi.org/10.1002/2016JE005046

Howard, A. W., Marcy, G. W., Johnson, J. A., Fischer, D. A., Wright, J. T., Isaacson, H., ... & Ida, S. (2010). The occurrence and mass distribution of close-in super-Earths, Neptunes, and Jupiters. Science, 330(6004), 653-655. https://doi.org/10.1126/science.1194854

Howell, S. M., & Pappalardo, R. T. (2020). NASA's Europa Clipper—A mission to a potentially habitable ocean world. Nature Communications, 11(1), 1311. https://doi.org/10.1038/s41467-020-15160-9

Jaeger, J. C., Cook, N. G., & Zimmerman, R. (2009). Fundamentals of rock mechanics. John Wiley & Sons.

Kaas, O., Šilhavý, J., Kolingerová, I., & Čada, V. (2023). Accelerated multi-hillshade hierarchic clustering for automatic lineament extraction. Journal of Geographical Systems, 1-18. https://doi.org/10.1007/s10109-023-00423-y

Kattenhorn, S. A., & Prockter, L. M. (2014). Evidence for subduction in the ice shell of Europa. Nature Geoscience, 7(10), 762-767. https://doi.org/10.1038/ngeo2245

Kaufman, L., & Rousseeuw, P. J. (1990). Finding groups in data: an introduction to cluster analysis. John Wiley & Sons. https://doi.org/10.1002/9780470316801

Kausch, W., Noll, S., Smette, A., Kimeswenger, S., Barden, M., Szyszka, C., ... & Kerber, F. (2015). Molecfit: A general tool for telluric absorption correction-II. Quantitative evaluation on ESO-VLT/X-Shooterspectra. Astronomy & Astrophysics, 576, A78. https://doi.org/10.1051/0004-6361/201423909

Kedar, S., Panning, M. P., Smrekar, S. E., Stähler, S. C., King, S. D., Golombek, M. P., ... & Banerdt, W. B. (2021). Analyzing low frequency seismic events at Cerberus Fossae as long period volcanic quakes. Journal of Geophysical Research: Planets, 126(4), e2020JE006518. https://doi.org/10.1029/2020JE006518

Kerrich, R. (1986). Fluid transport in lineaments. Philosophical Transactions of the Royal Society of London. Series A, Mathematical and Physical Sciences, 317(1539), 219-251. https://doi.org/10.1098/rsta.1986.0033

Kieffer, H. H., Christensen, P. R., & Titus, T. N. (2006). CO2 jets formed by sublimation beneath translucent slab ice in Mars' seasonal south polar ice cap. Nature, 442(7104), 793-796. https://doi.org/10.1038/nature04945

Kirchoff, M. R., McKinnon, W. B., & Schenk, P. M. (2011). Global distribution of volcanic centers and mountains on Io: Control by asthenospheric heating and implications for mountain formation. Earth and Planetary Science Letters, 301(1-2), 22-30. https://doi.org/10.1016/j.epsl.2010.11.018

Klimczak, C. (2014). Geomorphology of lunar grabens requires igneous dikes at depth. Geology, 42(11), 963-966. https://doi.org/10.1130/G35984.1

Klimczak, C., Beddingfield, C. B., Byrne, P. K., Cheng, H. C., Crane, K. T., & Annex, A. (2021). Opportunities and Challenges for Structural Geology and Tectonics in the Planetary Sciences. Bulletin of the American Astronomical Society, 53(4), 133. https://doi.org/10.3847/25c2cfeb.4a4657ca

Knapmeyer-Endrun, B., Panning, M. P., Bissig, F., Joshi, R., Khan, A., Kim, D., ... & Banerdt, W. B. (2021). Thickness and structure of the martian crust from InSight seismic data. Science, 373(6553), 438-443. https://dor.org/10.1126/science.abf8966

Komolafe, A. A., Kuria, Z. N., Woldai, T., Noomen, M., & Anifowose, A. Y. B. (2012). Integrated remote sensing and geophysical investigations of the geodynamic activities at Lake Magadi, Southern Kenyan rift. International Journal of Geophysics, 2012. https://doi.org/10.1155/2012/318301

Kouider, M. H., Dahou, M. E. A., Nezli, I. E., Dehmani, S., Touahri, A., Séverin, P., & Antonio, P. B. (2023). Fractures and lineaments mapping and hydrodynamic impacts on surface and groundwater occurrence and quality in an arid region, Oued M'ya basin–Southern Sahara, Algeria. Environmental Earth Sciences, 82(22), 1-28. https://doi.org/10.1007/s12665-023-11128-2

Kreslavsky, M. A., Head, J. W., Neumann, G. A., Zuber, M. T., & Smith, D. E. (2017). Low-amplitude topographic features and textures on the Moon: Initial results from detrended Lunar Orbiter Laser Altimeter (LOLA) topography. Icarus, 283, 138-145. https://doi.org/10.1016/j.icarus.2016.07.017

Krishnan, V., & Kumar, P. S. (2023). Long-Lived and Continual Volcanic Eruptions, Tectonic Activity, Pit Chains Formation, and Boulder Avalanches in Northern Tharsis Region: Implications for Late Amazonian Geodynamics and Seismo-Tectonic Processes on Mars. Journal of Geophysical Research: Planets, 128(1), e2022JE007511. https://doi.org/10.1029/2022JE007511

Lachenbruch, A. H. (1961). Depth and spacing of tension cracks. Journal of Geophysical Research, 66(12), 4273-4292.

Langlais, B., Purucker, M. E., & Mandea, M. (2004). Crustal magnetic field of Mars. Journal of Geophysical Research: Planets, 109(E2). https://doi.org/10.1029/2003JE002048

Lee, M. D., & Morris, W. A. (2010). Lineament analysis as a tool for hydrocarbon and mineral exploration: a Canadian case study. ASEG Extended Abstracts, 2010(1), 1-5. https://doi.org/10.1071/ASEG2010ab049

Leopold, Luna B., Wolman, M.G., and Miller, J.P., 1964, Fluvial Processes in Geomorphology, San Francisco, W.H. Freeman and Co., 522p.

Lucchetti, A., Rossi, C., Mazzarini, F., Pajola, M., Pozzobon, R., Massironi, M., & Cremonese, G. (2021). Equatorial grooves distribution on Ganymede: Length and self-similar clustering analysis. Planetary and Space Science, 195, 105140. https://doi.org/10.1016/j.pss.2020.105140

Lucchitta, B. K. (1987). Valles Marineris, Mars: Wet debris flows and ground ice. Icarus, 72(2), 411-429. https://doi.org/10.1016/0019-1035(87)90183-7

Lucianetti, G., Cianfarra, P., & Mazza, R. (2017). Lineament domain analysis to infer groundwater flow paths: Clues from the Pale di San Martino fractured aquifer, Eastern Italian Alps. Geosphere, 13(5), 1729-1746. https://doi.org/10.1130/GES01500.1

Maggi, M., Cianfarra, P., & Salvini, F. (2016). Erosion by tectonic carving in the Concordia subglacial fault zone, East Antarctica. Earth and Planetary Science Letters, 433, 99-108. https://doi.org/10.1016/j.epsl.2015.10.045

Man, B., Rothery, D. A., Balme, M. R., Conway, S. J., & Wright, J. (2023). Widespread small grabens consistent with recent tectonism on Mercury. Nature Geoscience, 16(10), 856-862. https://doi.org/10.1038/s41561-023-01281-5

Mann, P. (2007). Global catalogue, classification and tectonic origins of restraining-and releasing bends on active and ancient strike-slip fault systems. Geological Society, London, Special Publications, 290(1), 13-142. https://doi.org/10.1144/SP290.2

Mansfield, M., Line, M. R., Bean, J. L., Fortney, J. J., Parmentier, V., Wiser, L., ... & Roudier, G. M. (2021). A unique hot Jupiter spectral sequence with evidence for compositional diversity. Nature Astronomy, 5(12), 1224-1232. https://doi.org/10.1038/s41550-021-01455-4

Marois, C., Zuckerman, B., Konopacky, Q. M., Macintosh, B., & Barman, T. (2010). Images of a fourth planet orbiting HR 8799. Nature, 468(7327), 1080-1083. https://doi.org/10.1038/nature09684

Martin, R. G., & Livio, M. (2015). The solar system as an exoplanetary system. The Astrophysical Journal, 810(2), 105. https://doi.org/10.1088/0004-637X/810/2/105

Mason, J. W. (2008). Exoplanets.

Mayor, M., & Queloz, D. (1995). A Jupiter-mass companion to a solar-type star. nature, 378(6555), 355-359. https://doi.org/10.1038/378355a0

Mayor, M., Marmier, M., Lovis, C., Udry, S., Ségransan, D., Pepe, F., ... & Santos, N. C. (2011). The HARPS search for southern extra-solar planets XXXIV. Occurrence, mass distribution and orbital properties of super-Earths and Neptune-mass planets. https://doi.org/10.48550/arXiv.1109.2497

Mazzarini, F. (2004). Volcanic vent self-similar clustering and crustal thickness in the northern Main Ethiopian Rift. Geophysical Research Letters, 31(4). https://doi.org/10.1029/2003GL018574

Mazzarini, F. (2007). Vent distribution and crustal thickness in stretched continental crust: The case of the Afar Depression (Ethiopia). Geosphere, 3(3), 152-162. https://doi.org/10.1130/GES00070.1

Mazzarini, F., & D'Orazio, M. (2003). Spatial distribution of cones and satellite-detected lineaments in the Pali Aike Volcanic Field (southernmost Patagonia): insights into the tectonic setting of a Neogene rift system. Journal of Volcanology and Geothermal Research, 125(3-4), 291-305. https://doi.org/10.1016/S0377-0273(03)00120-3

Mazzarini, F., & Isola, I. (2010). Monogenetic vent self-similar clustering in extending continental crust: Examples from the East African Rift System. Geosphere, 6(5), 567-582. https://doi.org/10.1130/GES00569.1

Mazzarini, F., & Isola, I. (2021). Vent distribution and structural inheritance in an embryonic rift: The example of the Chyulu Hills off-rift magmatic range (South Kenya). Journal of Volcanology and Geothermal Research, 416, 107268. https://doi.org/10.1016/j.jvolgeores.2021.107268

Mazzarini, F., & Isola, I. (2022). Quaternary off-rift volcanism along a section of the East African Rift System (EARS), from the south Ethiopia to the south Kenya. Italian Journal of Geosciences, 141(3), 334-347. https://doi.org/10.3301/IJG.2022.19

Mazzarini, F., & Salvini, F. (1994). Tectonic blocks in northern Victoria Land (Antarctica): Geological and structural constraints by satellite lineament domain analysis. Terra Antartica, 1(1), 74-77.

McKenzie, D., Barnett, D. N., & Yuan, D. N. (2002). The relationship between Martian gravity and topography. Earth and Planetary Science Letters, 195(1-2), 1-16. https://doi.org/10.1016/S0012-821X(01)00555-6

Meftah, M., Sarkissian, A., Keckhut, P., & Hauchecorne, A. (2023). The SOLAR-HRS New High-Resolution Solar Spectra for Disk-Integrated, Disk-Center, and Intermediate Cases. Remote Sensing, 15(14), 3560. https://doi.org/10.3390/rs15143560

Mirkin, B. (2013). Mathematical classification and clustering (Vol. 11). Springer Science & Business Media.

Mojena, R. (1977). Hierarchical grouping methods and stopping rules: an evaluation. The Computer Journal, 20(4), 359-363. https://doi.org/10.1093/comjnl/20.4.359

Montgomery, D. R., Som, S. M., Jackson, M. P., Schreiber, B. C., Gillespie, A. R., & Adams, J. B. (2009). Continental-scale salt tectonics on Mars and the origin of Valles Marineris and associated outflow channels. Geological Society of America Bulletin, 121(1-2), 117-133. https://doi.org/10.1130/B26307.1

Moore, W. B., & Webb, A. A. G. (2013). Heat-pipe earth. Nature, 501(7468), 501-505. https://doi.org/10.1038/nature12473

Moore, W. B., Simon, J. I., & Webb, A. A. G. (2017). Heat-pipe planets. Earth and Planetary Science Letters, 474, 13-19. https://doi.org/10.1016/j.epsl.2017.06.015

Morelli, D., Locatelli, M., Corradi, N., Cianfarra, P., Crispini, L., Federico, L., & Migeon, S. (2022). Morpho-Structural Setting of the Ligurian Sea: The Role of Structural Heritage and Neotectonic Inversion. Journal of Marine Science and Engineering, 10(9), 1176. https://doi.org/10.3390/jmse10091176

Morelli, D., Locatelli, M., Crispini, L., Corradi, N., Cianfarra, P., Federico, L., & Brandolini, P. (2023). 3D Modelling of Late Quaternary coastal evolution between Albenga and Loano (Western Liguria, Italy). Journal of Maps, 19(1), 2227211. https://doi.org/10.1080/17445647.2023.2227211

Morelli, M., & Piana, F. (2006). Comparison between remote sensed lineaments and geological structures in intensively cultivated hills (Monferrato and Langhe domains, NW Italy). International Journal of Remote Sensing, 27(20), 4471-4493. https://doi.org/10.1080/01431160600784200

Morschhauser, A., Lesur, V., & Grott, M. (2014). A spherical harmonic model of the lithospheric magnetic field of Mars. Journal of Geophysical Research: Planets, 119(6), 1162-1188. https://doi.org/10.1002/2013JE004555

Moustafa, S. S., Abdalzaher, M. S., & Abdelhafiez, H. E. (2022). Seismo-lineaments in egypt: analysis and implications for active tectonic structures and earthquake magnitudes. Remote Sensing, 14(23), 6151. https://doi.org/10.3390/rs14236151

Müllner, D. (2013). fastcluster: Fast hierarchical, agglomerative clustering routines for R and Python. Journal of Statistical Software, 53, 1-18. https://doi.org/10.18637/jss.v053.i09

Murtagh, F., & Legendre, P. (2014). Ward's hierarchical agglomerative clustering method: which algorithms implement Ward's criterion?. Journal of classification, 31, 274-295. https://doi.org/10.1007/s00357-014-9161-z

Musiol, S., Holohan, E. P., Cailleau, B., Platz, T., Dumke, A., Walter, T. R., ... & Van Gasselt, S. (2016). Lithospheric flexure and gravity spreading of Olympus Mons volcano, Mars. Journal of Geophysical Research: Planets, 121(3), 255-272. https://doi.org/10.1002/2015JE004896

Nahm, A. L., & Schultz, R. A. (2010). Evaluation of the orogenic belt hypothesis for the formation of the Thaumasia Highlands, Mars. Journal of Geophysical Research: Planets, 115(E4). https://doi.org/10.1029/2009je003327

Nahm, A. L., & Schultz, R. A. (2010). Evaluation of the orogenic belt hypothesis for the formation of the Thaumasia Highlands, Mars. Journal of Geophysical Research: Planets, 115(E4). https://doi.org/10.1029/2009JE003327

Neumann, G. A., Rowlands, D. D., Lemoine, F. G., Smith, D. E., & Zuber, M. T. (2001). Crossover analysis of Mars Orbiter Laser Altimeter data. Journal of Geophysical Research, 106(E10), 23753–23768. https://doi.org/10.1029/2000JE001381

Neumann, G. A., Smith, D. E., & Zuber, M. T. (2003). Two Mars years of clouds detected by the Mars Orbiter Laser Altimeter. Journal of Geophysical Research, 108(E4), 5023. https://doi.org/10.1029/2002JE001849

Neumann, G. A., Zuber, M. T., Wieczorek, M. A., McGovern, P. J., Lemoine, F. G., & Smith, D. E. (2004). Crustal structure of Mars from gravity and topography. Journal of Geophysical Research: Planets, 109(E8). https://doi.org/10.1029/2004JE002262

Nimmo, F., Hart, S. D., Korycansky, D. G., & Agnor, C. B. (2008). Implications of an impact origin for the martian hemispheric dichotomy. Nature, 453(7199), 1220-1223. https://doi.org/10.1038/nature07025

O'leary, D. W., Friedman, J. D., & Pohn, H. A. (1976). Lineament, linear, lineation: some proposed new standards for old terms. Geological Society of America Bulletin, 87(10), 1463-1469. https://doi.org/10.1130/0016-7606(1976)87%3C1463:LLLSPN%3E2.0.CO;2

Oliva, E., Origlia, L., Maiolino, R., Baffa, C., Biliotti, V., Bruno, P., ... & Tozzi, A. (2012). The GIANO spectrometer: towards its first light at the TNG. In Ground-based and Airborne Instrumentation for Astronomy IV (Vol. 8446, pp. 1307-1315). SPIE. https://doi.org/10.1117/12.925274

Oliva, E., Sanna, N., Rainer, M., Massi, F., Tozzi, A., & Origlia, L. (2018). GIANO, the high-resolution IR spectrograph of the TNG: geometry of the echellogram and strategies for the 2D reduction of the spectra. In Ground-based and Airborne Instrumentation for Astronomy VII (Vol. 10702, pp. 2118-2130). SPIE. https://doi.org/10.1117/12.2309927

Olson, S. L., Jansen, M., & Abbot, D. S. (2020). Oceanographic considerations for exoplanet life detection. The Astrophysical Journal, 895(1), 19. https://doi.org/10.3847/1538-4357/ab88c9

Origlia, L., Oliva, E., Baffa, C., Falcini, G., Giani, E., Massi, F., ... & Lodi, M. (2014). High resolution near IR spectroscopy with GIANO-TNG. In Ground-based and Airborne Instrumentation for Astronomy V (Vol. 9147, pp. 522-530). SPIE. https://doi.org/10.1117/12.2054743

Ouillon, G., Castaing, C., & Sornette, D. (1996). Hierarchical geometry of faulting. Journal of Geophysical Research: Solid Earth, 101(B3), 5477-5487. https://doi.org/10.1029/95JB02242

Paasche, H., & Eberle, D. G. (2009). Rapid integration of large airborne geophysical data suites using a fuzzy partitioning cluster algorithm: a tool for geological mapping and mineral exploration targeting. Exploration Geophysics, 40(3), 277-287. https://doi.org/10.1071/EG08028

Palin, R. M., Santosh, M., Cao, W., Li, S. S., Hernández-Uribe, D., & Parsons, A. (2020). Secular change and the onset of plate tectonics on Earth. Earth-Science Reviews, 207, 103172. https://doi.org/10.1016/j.earscirev.2020.103172

Pardo, N., Macias, J. L., Giordano, G., Cianfarra, P., Avellán, D. R., & Bellatreccia, F. (2009). The~ 1245 yr BP Asososca maar eruption: The youngest event along the Nejapa–Miraflores volcanic fault, Western Managua, Nicaragua. Journal of Volcanology and Geothermal Research, 184(3-4), 292-312. https://doi.org/10.1016/j.jvolgeores.2009.04.006

Perrin, C., Jacob, A., Lucas, A., Myhill, R., Hauber, E., Batov, A., ... & Fuji, N. (2022). Geometry and segmentation of Cerberus Fossae, Mars: Implications for marsquake properties. Journal of Geophysical Research: Planets, 127(1), e2021JE007118. https://doi.org/10.1029/2021JE007118

Perryman, M. (2018). The exoplanet handbook. Cambridge university press.

Phillips, R. J., Davis, B. J., Tanaka, K. L., Byrne, S., Mellon, M. T., Putzig, N. E., ... & Seu, R. (2011). Massive CO2 ice deposits sequestered in the south polar layered deposits of Mars. Science, 332(6031), 838-841. https://doi.org/10.1126/science.1203091

Phillips, R. J., Zuber, M. T., Solomon, S. C., Golombek, M. P., Jakosky, B. M., Banerdt, W. B., ... & Hauck II, S. A. (2001). Ancient geodynamics and global-scale hydrology on Mars. Science, 291(5513), 2587-2591. https://doi.org/10.1126/science.1058701

Pieterek, B., Brož, P., & Hauber, E. (2023). Low-voluminous, mafic-dominated volcanism in Claritas Fossae, Thaumasia region on Mars (No. EGU23-11093). Copernicus Meetings. https://doi.org/10.5194/egusphere-egu23-11093

Pieterek, B., Brož, P., Hauber, E., & Stephan, K. (2024). Insight from the Noachian-aged fractured crust to the volcanic evolution of Mars: A case study from the Thaumasia graben and Claritas Fossae. Icarus, 407, 115770. https://doi.org/10.1016/j.icarus.2023.115770

Pieterek, B., Laban, M., Ciążela, J., & Muszyński, A. (2022). Explosive volcanism in Noctis fossae on Mars. Icarus, 375, 114851. https://doi.org/10.1016/j.icarus.2021.114851

Pilorget, C., & Forget, F. (2016). Formation of gullies on Mars by debris flows triggered by CO2 sublimation. Nature Geoscience, 9(1), 65-69. https://doi.org/10.1038/ngeo2619

Pinheiro, M. R., Cianfarra, P., Villela, F. N. J., & Salvini, F. (2019). Tectonics of the Northeastern border of the Parana Basin (Southeastern Brazil) revealed by lineament domain analysis. Journal of South American Earth Sciences, 94, 102231. https://doi.org/10.1016/j.jsames.2019.102231

Pischiutta, M., Anselmi, M., Cianfarra, P., Rovelli, A., & Salvini, F. (2013). Directional site effects in a non-volcanic gas emission area (Mefite d'Ansanto, southern Italy): Evidence of a local transfer fault transversal to large NW–SE extensional faults?. Physics and Chemistry of the Earth, Parts A/B/C, 63, 116-123. https://doi.org/10.1016/j.pce.2013.03.008

Platz, T., Byrne, P. K., Massironi, M., & Hiesinger, H. (2015). Volcanism and tectonism across the inner solar system: an overview. Geological Society, London, Special Publications, 401(1), 1-56. https://doi.org/10.1144/SP401.22

Plesa, A. C., Grott, M., Tosi, N., Breuer, D., Spohn, T., & Wieczorek, M. A. (2016). How large are present-day heat flux variations across the surface of Mars?. Journal of Geophysical Research: Planets, 121(12), 2386-2403. https://doi.org/10.1002/2016JE005126

Plesa, A. C., Padovan, S., Tosi, N., Breuer, D., Grott, M., Wieczorek, M. A., ... & Banerdt, W. B. (2018). The thermal state and interior structure of Mars. Geophysical Research Letters, 45(22), 12-198. https://doi.org/10.1029/2018GL080728

Plesa, A. C., Wieczorek, M., Knapmeyer, M., Rivoldini, A., Bozdag, E., Walterova, M., ... & Banerdt, B. (2023). InSight's Constraints on the Interior of Mars: Geodynamical Models and Observations. https://www.hou.usra.edu/meetings/lpsc2023/pdf/2212.pdf

Plescia, J. B. (2003). Cerberus Fossae, Elysium, Mars: A source for lava and water. Icarus, 164(1), 79-95. https://doi.org/10.1016/S0019-1035(03)00139-8

Plescia, J. B., & Saunders, R. S. (1982). Tectonic history of the Tharsis region, Mars. Journal of Geophysical Research: Solid Earth, 87(B12), 9775-9791. https://doi.org/10.1029/JB087iB12p09775

Pondrelli, M., Baker, V. R., & Hauber, E. (2018). Geologic tools. Planetary geology, 15-31.

Pozzobon, R., Mazzarini, F., & Isola, I. (2023). Deep and shallow crustal structure control on the late-stage volcanism in Syria Planum (Mars). Journal of Volcanology and Geothermal Research, 107830. https://doi.org/10.1016/j.jvolgeores.2023.107830

Prabhakaran, R., Bertotti, G., Urai, J., & Smeulders, D. (2021). Investigating spatial heterogeneity within fracture networks using hierarchical clustering and graph distance metrics. Solid Earth, 12(10), 2159-2209. https://doi.org/10.5194/se-12-2159-2021

Rainer, M., Harutyunyan, A., Carleo, I., Oliva, E., Benatti, S., Bignamini, A., ... & Sozzi, M. (2018). Introducing GOFIO: a DRS for the GIANO-B near-infrared spectrograph. In Ground-based and Airborne Instrumentation for Astronomy VII (Vol. 10702, pp. 1855-1864). SPIE. https://doi.org/10.1117/12.2312130

Ramli, M. F., Yusof, N., Yusoff, M. K., Juahir, H., & Shafri, H. Z. M. (2010). Lineament mapping and its application in landslide hazard assessment: a review. Bulletin of engineering Geology and the Environment, 69, 215-233. https://doi.org/10.1007/s10064-009-0255-5

Reese, C. C., Solomatov, V. S., & Moresi, L. N. (1999). Non-newtonian stagnant lid convection and magmatic resur facing on venus. Icarus, 139(1), 67-80. https://doi.org/10.1006/icar.1999.6088

Ricci, D., Sada, P. V., Navarro-Meza, S., López-Valdivia, R., Michel, R., Machado, L. F., ... & Deeg, H. (2017). Multi-filter transit observations of HAT-P-3b and TrES-3b with multiple northern hemisphere telescopes. Publications of the Astronomical Society of the Pacific, 129(976), 064401. https://doi.org/10.1088/1538-3873/aa6b54

Ricci, D., Tosi, S., Cabona, L., Righi, C., La Camera, A., Marini, A., Domi, A., Santostefano, M., Balbi E., Nicolosi, F., Ancona, M., Boccacci, P., Bracco, G., Cardinale, R., Dellacasa, A., Landoni, M., Pallavicini, M., Petrolini, A., Schiavi, C., Zappatore, S., & Zerbi, F. M. (2021). Commissioning and improvements of the instrumentation and launch of the scientific exploitation of OARPAF, the Regional Astronomical Observatory of the Antola Park. Journal of Astronomical Telescopes, Instruments, and Systems, 7(2), 025003-025003. https://doi.org/10.1117/1.JATIS.7.2.025003

Riedel, W. (1929). Zur Mechanik geologischer Brucherscheinungen ein Beitrag zum Problem der Fiederspatten. Zentbl. Miner. Geol. Palaont. Abt., 354-368.

Rodriguez, M., Chamot-Rooke, N., Fournier, M., Huchon, P., & Delescluse, M. (2013). Mode of opening of an oceanic pull-apart: The 20° N basin along the Owen fracture zone (NW Indian Ocean). Tectonics, 32(5), 1343-1357. https://doi.org/10.1002/tect.20083

Rossi, A. P., & Van Gasselt, S. (2010). Geology of Mars after the first 40 years of exploration. Research in Astronomy and Astrophysics, 10(7), 621. https://doi.org/10.1088/1674-4527/10/7/003

Rossi, A.P., van Gasselt Editors, S., 2018. Planetary Geology.

Rossi, C., Cianfarra, P., Salvini, F., Bourgeois, O., & Tobie, G. (2020). Tectonics of Enceladus' South Pole: Block Rotation of the Tiger Stripes. Journal of Geophysical Research: Planets, 125(12), e2020JE006471. https://doi.org/10.1029/2020JE006471

Rossi, C., Cianfarra, P., Salvini, F., Mitri, G., & Massé, M. (2018). Evidence of transpressional tectonics on the Uruk Sulcus region, Ganymede. Tectonophysics, 749, 72-87. https://doi.org/10.1016/j.tecto.2018.10.026

Rousseeuw, P. J. (1987). Silhouettes: a graphical aid to the interpretation and validation of cluster analysis. Journal of computational and applied mathematics, 20, 53-65.

Salvini, F. (2013). The fault zone deformation architecture. In 40th Workshop of the International School of Geophysics on properties and processes of crustal fault zones, Erice, Italy (pp. 18-24). ftp://ingv.it/pro/web_ingv/Erice2013_40th%20Course.pdf/Salvini_Erice2013.pdf

Salvini, F., & Storti, F. (1999). Cenozoic tectonic lineaments of the Terra Nova Bay region, Ross embayment, Antarctica. Global and Planetary Change, 23(1-4), 129-144. https://doi.org/10.1016/S0921-8181(99)00054-5

Salvini, F., & Storti, F. (2004). Active-hinge-folding-related Deformation and its Role in Hydrocarbon Exploration and DevelopmentInsights from HCA Modeling.

Salvini, F., Ambrosetti, P., Carraro, F., Conti, M. A., Funicello, R., Ghisetti, F., ... & Vezzani, L. (1979). Tentativi di correlazione tra distribuzioni statistiche di lineamenti geomorfologici ed elementi di neotettonica.

Salvini, F., Billi, A., & Wise, D. U. (1999). Strike-slip fault-propagation cleavage in carbonate rocks: the Mattinata Fault Zone, Southern Apennines, Italy. Journal of Structural Geology, 21(12), 1731-1749. https://doi.org/10.1016/S0191-8141(99)00120-0

Salvini, F., Storti, F., & McClay, K. (2001). Self-determining numerical modeling of compressional fault-bend folding. Geology, 29(9), 839-842. https://doi.org/10.1130/0091-7613(2001)029%3C0839:SDNMOC%3E2.0.CO;2

Sander, P. (2007). Lineaments in groundwater exploration: a review of applications and limitations. Hydrogeology journal, 15(1), 71-74. https://doi.org/10.1007/s10040-006-0138-9

Schultz, R. A. (1998). Multiple-process origin of Valles Marineris basins and troughs, Mars. Planetary and space science, 46(6-7), 827-834. https://doi.org/10.1016/S0032-0633(98)00030-0

Schultz, R. A., & Frey, H. V. (1990). A new survey of multiring impact basins on Mars. Journal of Geophysical Research: Solid Earth, 95(B9), 14175-14189. https://doi.org/10.1029/JB095iB09p14175

Schultz, R.A., Soliva, R., Okubo, C.H., Ege, D.M., Watters, T.R. (2009). Fault populations. Planetary tectonics, 457-510.

Schwenker, F., & Trentin, E. (2014). Pattern classification and clustering: A review of partially supervised learning approaches. Pattern Recognition Letters, 37, 4-14. https://doi.org/10.1016/j.patrec.2013.10.017

Showman, A. P., Tan, X., & Parmentier, V. (2020). Atmospheric dynamics of hot giant planets and brown dwarfs. Space Science Reviews, 216, 1-83. https://doi.org/10.1007/s11214-020-00758-8

Šilhavý, J., Minár, J., Mentlík, P., & Sládek, J. (2016). A new artefacts resistant method for automatic lineament extraction using Multi-Hillshade Hierarchic Clustering (MHHC). Computers & Geosciences, 92, 9-20. https://doi.org/10.1016/j.cageo.2016.03.015

Silva, A. T., Lopes, M. R. F., Salvini, F., & Cianfarra, P. (2009). HCA methodology applied to model the interaction of faulting and salt movement in Campos Basin, Brazilian Atlantic Margin. In 11th International Congress of the Brazilian Geophysical Society & EXPOGEF 2009, Salvador, Bahia, Brazil, 24-28 August 2009 (pp. 1855-1858). Society of Exploration Geophysicists and Brazilian Geophysical Society. https://doi.org/10.1190/sbgf2009-390

Sita, M., & van der Lee, S. (2022). Potential Volcano-Tectonic Origins and Faulting Mechanisms of Three Low-Frequency Marsquakes Detected by a Single InSight Seismometer. Journal of Geophysical Research: Planets, 127(10), e2022JE007309. https://doi.org/10.1029/2022JE007309

Sleep, N. H. (1994). Martian plate tectonics. Journal of Geophysical Research: Planets, 99(E3), 5639-5655. https://doi.org/10.1029/94JE00216

Smette, A., Sana, H., Noll, S., Horst, H., Kausch, W., Kimeswenger, S., ... & Taylor, J. (2015). Molecfit: A general tool for telluric absorption correction-I. Method and application to ESO instruments. Astronomy & Astrophysics, 576, A77. https://doi.org/10.1051/0004-6361/201423932

Smit, J., Brun, J. P., Cloetingh, S. A. P. L., & Ben-Avraham, Z. (2010). The rift-like structure and asymmetry of the Dead Sea Fault. Earth and Planetary Science Letters, 290(1-2), 74-82. https://doi.org/10.1016/j.epsl.2009.11.060

Smith, D. E., Zuber, M. T., Frey, H. V., Garvin, J. B., Head, J. W., Muhleman, D. O., ... & Duxbury, T. C. (1998). Topography of the northern hemisphere of Mars from the Mars Orbiter Laser Altimeter. Science, 279(5357), 1686-1692. https://doi.org/10.1126/science.279.5357.1686

Smith, D. E., Zuber, M. T., Frey, H. V., Garvin, J. B., Head, J. W., Muhleman, D. O., ... & Sun, X. (2001). Mars Orbiter Laser Altimeter: Experiment summary after the first year of global mapping of Mars. Journal of Geophysical Research: Planets, 106(E10), 23689-23722. https://doi.org/10.1029/2000JE001364

Smith, D. E., Zuber, M. T., Solomon, S. C., Phillips, R. J., Head, J. W., Garvin, J. B., ... & Duxbury, T. C. (1999). The global topography of Mars and implications for surface evolution. science, 284(5419), 1495-1503. https://doi.org/10.1126/science.284.5419.1495

Smith, M. R., Gillespie, A. R., Montgomery, D. R., & Batbaatar, J. (2009). Crater–fault interactions: A metric for dating fault zones on planetary surfaces. Earth and Planetary Science Letters, 284(1-2), 151-156. https://doi.org/10.1016/j.epsl.2009.04.025

Sneath, P. H., & Sokal, R. R. (1973). Numerical taxonomy. The principles and practice of numerical classification.

Snyder, C. W., & Moroz, V. I. (1992). Spacecraft exploration of Mars. Mars, 71-119.

Solomatov, V. S., & Moresi, L. N. (1996). Stagnant lid convection on Venus. Journal of Geophysical Research: Planets, 101(E2), 4737-4753. https://doi.org/10.1029/95JE03361

Stähler, S. C., Khan, A., Banerdt, W. B., Lognonné, P., Giardini, D., Ceylan, S., ... & Smrekar, S. E. (2021). Seismic detection of the martian core. Science, 373(6553), 443-448. https://doi.org/10.1126/science.abi7730

Stern, R. J., Gerya, T., & Tackley, P. J. (2018). Stagnant lid tectonics: Perspectives from silicate planets, dwarf planets, large moons, and large asteroids. Geoscience Frontiers, 9(1), 103-119. https://doi.org/10.1016/j.gsf.2017.06.004

Storti, F., Holdsworth, R. E., & Salvini, F. (2003). Intraplate strike-slip deformation belts. Geological Society, London, Special Publications, 210(1), 1-14. https://doi.org/10.1144/GSL.SP.2003.210.01.01

Storti, F., Rossetti, F., Läufer, A. L., & Salvini, F. (2006). Consistent kinematic architecture in the damage zones of intraplate strike-slip fault systems in North Victoria Land, Antarctica and implications for fault zone evolution. Journal of Structural Geology, 28(1), 50-63. https://doi.org/10.1016/j.jsg.2005.09.004

Struyf, A., Hubert, M., & Rousseeuw, P. (1997). Clustering in an object-oriented environment. Journal of Statistical Software, 1, 1-30. https://doi.org/10.18637/jss.v001.i04

Sugan, M., Jel, W., & McClay, K. (2014). 3D analogue modelling of transtensional pull-apart basins: comparison with the Cinarcik basin, Sea of Marmara, Turkey. Bollettino Di Geofisica Teorica E Applicata, 55, 699-716. https://doi.org/10.4430/bgta0129

Swanson, M. T. (1988). Pseudotachylyte-bearing strike-slip duplex structures in the Fort Foster Brittle Zone, S. Maine. Journal of Structural Geology, 10(8), 813-828. https://doi.org/10.1016/0191-8141(88)90097-1

Swift, D. C., Eggert, J. H., Hicks, D. G., Hamel, S., Caspersen, K., Schwegler, E., ... & Ackland, G. J. (2011). Mass–radius relationships for exoplanets. The Astrophysical Journal, 744(1), 59. https://doi.org/10.1088/0004-637X/744/1/59

Takahashi, A., Hashimoto, M., Hu, J. C., Takeuchi, K., Tsai, M. C., & Fukahata, Y. (2019). Hierarchical cluster analysis of dense GPS data and examination of the nature of the clusters associated with regional tectonics in Taiwan. Journal of Geophysical Research: Solid Earth, 124(5), 5174-5191. https://doi.org/10.1029/2018JB016995

Tanaka, K. L., & Davis, P. A. (1988). Tectonic history of the Syria Planum province of Mars. Journal of Geophysical Research: Solid Earth, 93(B12), 14893-14917. https://doi.org/10.1029/JB093iB12p14893

Tanaka, K. L., Golombek, M. P., & Banerdt, W. B. (1991). Reconciliation of stress and structural histories of the Tharsis region of Mars. Journal of Geophysical Research: Planets, 96(E1), 15617-15633. https://doi.org/10.1029/91JE01194

Tanaka, K. L., Scott, D. H., & Greeley, R. (1992). Global stratigraphy. Mars, 345-382.

Tanaka, K.L., Skinner, J.A., Dohm, J.M., Irwin, R.P., Kolb, E.J., Fortezzo, C.M., Platz, T., Michael, G.G., Hare, T.M. (2014). Geologic map of Mars: U.S. Geological Survey Scientific Investigations Map 3292, scale 1:20,000,000, pamphlet 43 p. https://doi.org/10.3133/sim3292

Tapponnier, P., & Molnar, P. (1979). Active faulting and Cenozoic tectonics of the Tien Shan, Mongolia, and Baykal regions. Journal of Geophysical Research: Solid Earth, 84(B7), 3425-3459. https://doi.org/10.1029/JB084iB07p03425

Tavani, S., Storti, F., Fernández, O., Muñoz, J. A., & Salvini, F. (2006). 3-D deformation pattern analysis and evolution of the Añisclo anticline, southern Pyrenees. Journal of structural geology, 28(4), 695-712. https://doi.org/10.1016/j.jsg.2006.01.009

Taylor, N. C., Johnson, J. H., Herd, R. A., & Regan, C. E. (2020). What can Olympus Mons tell us about the Martian lithosphere?. Journal of Volcanology and Geothermal Research, 402, 106981. https://doi.org/10.1016/j.jvolgeores.2020.106981

ten Brink, U. S., & Taylor, M. H. (2002). Crustal structure of central Lake Baikal: Insights into intracontinental rifting. Journal of Geophysical Research: Solid Earth, 107(B7), ETG-2. https://doi.org/10.1029/2001jb000300

Turcotte, D. L., and Schubert G. Geodynamics. (2014). Third Edition, Cambridge University Press

van Gasselt, S., & Nass, A. (2011). Planetary mapping—The datamodel's perspective and GIS framework. Planetary and space science, 59(11-12), 1231-1242. https://doi.org/10.1016/j.pss.2010.09.012

Vaz, D. A. (2011). Analysis of a Thaumasia Planum rift through automatic mapping and strain characterization of normal faults. Planetary and Space Science, 59(11-12), 1210-1221. https://doi.org/10.1016/j.pss.2010.07.008

Vaz, D. A., Di Achille, G., Barata, M. T., & Alves, E. I. (2012). Tectonic lineament mapping of the Thaumasia Plateau, Mars: Comparing results from photointerpretation and a semi-automatic approach. Computers & geosciences, 48, 162-172. https://doi.org/10.1016/j.cageo.2012.05.008

Vaz, D. A., Di Achille, G., Barata, M. T., & Alves, E. I. (2012). Tectonic lineament mapping of the Thaumasia Plateau, Mars: Comparing results from photointerpretation and a semi-automatic approach. Computers & geosciences, 48, 162-172. https://doi.org/10.1016/j.cageo.2012.05.008

Vaz, D. A., Spagnuolo, M. G., & Silvestro, S. (2014). Morphometric and geometric characterization of normal faults on Mars. Earth and Planetary Science Letters, 401, 83-94. https://doi.org/10.1016/j.epsl.2014.05.022

Walsh, J.J., Watterson, J., 1988. Analysis of the relationship between displacements and dimensions of faults, Journal of Structural Geology. https://doi.org/10.1016/0191-8141(88)90057-0

Ward Jr, J. H. (1963). Hierarchical grouping to optimize an objective function. Journal of the American statistical association, 58(301), 236-244. https://doi.org/10.1080/01621459.1963.10500845

Watters, T. R. (2003a). Lithospheric flexure and the origin of the dichotomy boundary on Mars. Geology, 31(3), 271-274. https://doi.org/10.1130/0091-7613(2003)031%3C0271:LFATOO%3E2.0.CO;2

Watters, T. R. (2003b). Thrust faults along the dichotomy boundary in the eastern hemisphere of Mars. Journal of Geophysical Research: Planets, 108(E6). https://doi.org/10.1029/2002JE001934

Watters, T. R., & Schultz, R. A. (Eds.). (2010). Planetary tectonics (Vol. 11). Cambridge University Press.

Watters, T. R., McGovern, P. J., & Irwin Iii, R. P. (2007). Hemispheres apart: The crustal dichotomy on Mars. Annu. Rev. Earth Planet. Sci., 35, 621-652. https://doi.org/10.1146/annurev.earth.35.031306.140220

Weller, M. B., & Lenardic, A. (2018). On the evolution of terrestrial planets: Bi-stability, stochastic effects, and the non-uniqueness of tectonic states. Geoscience Frontiers, 9(1), 91-102. https://doi.org/10.1016/j.gsf.2017.03.001

Wenzel, M. J., Manga, M., & Jellinek, A. M. (2004). Tharsis as a consequence of Mars' dichotomy and layered mantle. Geophysical research letters, 31(4). https://doi.org/10.1029/2003GL019306

Wilhelms, D. E., & Squyres, S. W. (1984). The Martian hemispheric dichotomy may be due to a giant impact. Nature, 309(5964), 138-140. https://doi.org/10.1038/309138a0

Williams, J. P., Nimmo, F., Moore, W. B., & Paige, D. A. (2008). The formation of Tharsis on Mars: What the line-of-sight gravity is telling us. Journal of Geophysical Research: Planets, 113(E10). https://doi.org/10.1029/2007JE003050

Wise, D. U. (1979). Domini di lineamenti e di fratture in Italia. Università di Roma. Istituto di geologia e paleontologia.

Wise, D. U. (1982). Linesmanship and the practice of linear geo-art. Geological Society of America Bulletin, 93(9), 886-888. https://doi.org/10.1130/0016-7606(1982)93%3C886:LATPOL%3E2.0.CO;2

Wise, D. U., & McCrory, T. A. (1982). A new method of fracture analysis: azimuth versus traverse distance plots. Geological Society of America Bulletin, 93(9), 889-897.

Wise, D. U., Funiciello, R., Parotto, M., & Salvini, F. (1985). Topographic lineament swarms: Clues to their origin from domain analysis of Italy. Geological Society of America Bulletin, 96(7), 952-967. https://doi.org/10.1130/0016-7606(1985)96%3C952:TLSCTT%3E2.0.CO;2

Wise, D. U., Golombek, M. P., & McGill, G. E. (1979). Tectonic evolution of Mars. Journal of Geophysical Research: Solid Earth, 84(B14), 7934-7939. https://doi.org/10.1029/JB084iB14p07934

Wise, D. U., Golombek, M. P., & McGill, G. E. (1979). Tharsis province of Mars: Geologic sequence, geometry, and a deformation mechanism. Icarus, 38(3), 456-472. https://doi.org/10.1016/0019-1035(79)90200-8

Wolfram, S. (1986). Theory and application of cellular automata. Singapore, World Scientific.

Woodward, N. B., Boyer, S. E., & Suppe, J. (1989). Balanced geological cross-sections. Short course in geology, 6, 132.

Wu, J. E., McClay, K., Whitehouse, P., & Dooley, T. (2009). 4D analogue modelling of transtensional pull-apart basins. Marine and Petroleum Geology, 26(8), 1608-1623. https://doi.org/10.1016/j.marpetgeo.2008.06.007

Yang, J., Grunsky, E., & Cheng, Q. (2019). A novel hierarchical clustering analysis method based on Kullback–Leibler divergence and application on dalaimiao geochemical exploration data. Computers & Geosciences, 123, 10-19. https://doi.org/10.1016/j.cageo.2018.11.003

Yin, A. (2012). An episodic slab-rollback model for the origin of the Tharsis rise on Mars: Implications for initiation of local plate subduction and final unification of a kinematically linked global plate-tectonic network on Earth. Lithosphere, 4(6), 553-593. https://doi.org/10.1130/L195.1

Yusof, N., Ramli, M. F., Pirasteh, S., & Shafri, H. Z. M. (2011). Landslides and lineament mapping along the Simpang Pulai to Kg Raja highway, Malaysia. International journal of remote sensing, 32(14), 4089-4105. https://doi.org/10.1080/01431161.2010.484434

Zienkiewicz, O. C. and Taylor, R. L. (1991). The finite element method: solid and fluid mechanics and nonlinearity. London, McGraw-Hill Book Company, 648 p

Zuber, M. T. (2001). The crust and mantle of Mars. Nature, 412(6843), 220-227. https://doi.org/10.1038/35084163

Zuber, M. T., Solomon, S. C., Phillips, R. J., Smith, D. E., Tyler, G. L., Aharonson, O., ... & Zhong, S. (2000). Internal structure and early thermal evolution of Mars from Mars Global Surveyor topography and gravity. science, 287(5459), 1788-1793. https://doi.org/10.1126/science.287.5459.1788